Multicomponent Reynolds-Averaged Navier–Stokes Modeling of Reshocked Richtmyer–Meshkov Instability-Induced Turbulent Mixing Using the Weighted Essentially Nonoscillatory Method

by

J. Tiberius Morán-López

A dissertation submitted in partial fulfillment
of the requirements for the degree of
Doctor of Philosophy
(Nuclear Engineering and Radiological Sciences)
in The University of Michigan
2013

Doctoral Committee:

Associate Dean James P. Holloway, Co-Chair
Oleg Schilling, Co-Chair, Lawrence Livermore National Laboratory
Professor William R. Martin
Professor Kenneth G. Powell
Assistant Professor Alexander G. R. Thomas

To my parents, Juan M. and M. Laura Morán-López

ACKNOWLEDGEMENTS

This dissertation was completed with much help and support from many individuals. I would like to express my sincere appreciation to my co-advisors and mentors, Professor James P. Holloway and Dr. Oleg Schilling, for their guidance, instruction, and support throughout the development of the dissertation. I would also like to thank the committee members, Professors William R. Martin, Kenneth Powell, and Alexander Thomas, for their support and participation in completing the dissertation. Many thanks to the University of Michigan Department of Nuclear Engineering and Radiological Sciences for their support and flexibility in allowing me to pursue this research topic in nonclassical nuclear engineering. Thank you, also, to the Lawrence Livermore National Laboratory (LLNL) for granting me the opportunity to participate in the high-energy-density physics summer program in 2007, where I first met one of my mentors, Dr. Oleg Schilling, with whom I still perform collaborative work. Many thanks also to Emeritus Professor Terry Kammash and Professor John E. Foster for the enthusiasm and motivation over the years.

I would like to express since my appreciation, gratitude, and love to my parents, Juan M. and M. Laura Morán-López, as well as to my brother and sister, Juan M. and Julia O. Morán-López, for their enduring support, encouragement, and motivation throughout the years. Please know that this achievement could not have been realized without any of you. Many thanks to my friends and colleagues. Thank you for the friendship, advice, and energy that has contributed to this success. Special thanks to Dr. Jinan Yang, Peggy Jo Gramer, Michael Nazareth, Tizoc Cruz–González, Cherilyn

Davis, Linda Peterson, Jan Beltran, and Edward Birdsall.

This work was funded by the U.S. Department of Energy National Nuclear Security Administration under the Predictive Science Academic Alliances Program by grant DE-FC52-08NA28616 and performed under the auspices of the U.S. Department of Energy by Lawrence Livermore National Laboratory under contract number DE-AC52-07NA27344.

TABLE OF CONTENTS

LIST OF FIGURES

Figure

LIST OF TABLES

Table

ABSTRACT

Multicomponent Reynolds-Averaged Navier–Stokes Modeling of Reshocked Richtmyer–Meshkov Instability-Induced Turbulent Mixing Using the Weighted Essentially Nonoscillatory Method

by

J. Tiberius Morán-López

Co-chairs: James P. Holloway, Oleg Schilling

Hydrodynamic instability-induced turbulent mixing has a primary role in many science and engineering applications. Elucidating reshocked Richtmyer–Meshkov instability is important for improving current techniques in predicting turbulence in complex flows and advancing many areas of high-energy-density physics. Shock-driven turbulent mixing induced by reshocked Richtmyer–Meshkov instability is investigated here using a multicomponent Reynolds-averaged Navier–Stokes (RANS) model including mixture molecular transport and thermodynamic coefficients closed with a two-equation K–ϵ turbulence model. The model is implemented in a hydrodynamics code using a third-order weighted essentially nonoscillatory (WENO) finite-difference method for the advection terms and a second-order centered WENO method for the gradients in the source and diffusion terms.

Turbulent mixing generated by a shock accelerated perturbed air–sulfur hexafluoride interface with Atwood numbers $At = \pm 0.67$ is simulated for a variety of experiments with incident shock Mach numbers $1.20 \leq Ma_s \leq 1.98$. Parametric studies are conducted to study the model sensitivity to variations in buoyancy production

model coefficients, initial conditions, and incident shock Mach number. The time-evolution of the predicted mixing layer widths corresponding to different reshock times by variations in shock tube test section lengths is also considered. The RANS model results are compared with experimental data, previous large-eddy simulation (LES) and turbulence model predictions, and the early-time analytical self-similar mixing layer width. Sets of model coefficients that provide very good agreement with various sets of experiments are established, together with a general coefficient set that provides generally good agreement with data from all of these experiments.

The model is also applied to reshocked Richtmyer–Meshkov instability with Atwood numbers $At = \pm 0.21$, ± 0.67, and ± 0.87 (corresponding to gas pairs air–CO_2, air–SF_6, and air–H_2, respectively) and $Ma_s = 1.50$, as experimental and numerical simulation data for Atwood numbers different from $At = \pm 0.67$ are sparse. The mixing layer widths are compared with LES data. Early-time and post-reshock growth rates of the mixing layer width are considered for the different Atwood numbers. Shock-driven instabilities are also considered with larger incident shock Mach numbers $Ma_s = 3.00$ and 5.00, as limited turbulent mixing investigations with larger Ma_s values have been conducted. These studies are considered for cases with negative Atwood numbers, $At = -0.21$, -0.67, and -0.87.

The budgets of the turbulent kinetic energy and turbulent kinetic energy dissipation rate transport equations are investigated to determine the key mechanisms in turbulent mixing. The shear and buoyancy production, diffusion, and dissipation contributions to the budgets are considered for the various cases above. Results for convergence under grid refinement for mixing layer widths, mean density, mean pressure, mean heavy mass fraction, mean velocity, turbulent kinetic energy, turbulent kinetic energy dissipation rate, and turbulent viscosity are also presented. These investigations are considered for early-time and post-reshock mixing, as well as for changes in the mixing due to secondary expansion, rarefaction, and reshock waves.

CHAPTER I

Introduction

The effects of multifluid hydrodynamic instabilities and turbulent mixing are of critical importance to a large number of science and engineering applications, and elucidating the impact of these effects has been considered for various applications. Turbulence is manifested in numerous familiar situations and is perhaps often overlooked as its presence is ubiquitous. Turbulence is present in geophysical flows such as rivers and oceans, where density fluctuations develop due to temperature and salinity effects. Atmospheric motions are also turbulent, and the effects of these unsteady flows are especially common in aviation. Other examples include the flow over a baseball in motion, the mixing of cream in coffee, and smoke rising from a cigarette shows the transition from laminar to turbulent flow. Engineering examples ranging from low-speed to supersonic regimes include high-speed flight and supersonic combustion ramjet engines (1). Figure 1.1 illustrates examples of turbulent flows in familiar situations. Gas dynamics typically involves large Reynolds numbers and viscosity has an important effect on the motion of gases, where perturbations at any point will grow throughout (45). The generation and evolution of turbulence from variable-density and compressible hydrodynamic instabilities play a significant role in these processes.

In addition to the wide range of applicability, these examples also show that hydrodynamic instabilities are present in multiphase flows of liquids, gases, and plasmas.

Figure 1.1: Illustrations of turbulent flows in familiar situations.

Important characteristics of turbulence are the effective transport and mixing of fluids, irregular flows, dissipation of energy into heat, and a large range of spatial scales (33). However, despite the many observable characteristics of turbulence, it is still difficult to give a precise definition of turbulence despite its long history of investigation. In a general sense, turbulence can be defined as an irregular condition of flow in which the various quantities show a random variation with time and space, so that statistically distinct average values can be discerned (47).

1.1 Hydrodynamic Instabilities and Turbulence in High-Energy-Density Physics

Of particular interest are turbulent flows and mixing in high-energy-density physics (HEDP), as hydrodynamic instability-induced turbulence has important effects in these environments (2), where shocks and blast waves are generated by large and instantaneous releases of energy. Astrophysical examples are supernovae, stellar evolution, and molecular cloud interactions with the interstellar medium. Other examples include inertial confinement fusion (ICF), high-energy laser and shock tube experiments, and laboratory astrophysics experiments.

1.1.1 Astrophysical investigations

Turbulent mixing occurs during stellar core-collapse, where shock waves generated propagate outward, and traverse and accelerate multiple perturbed gas interfaces. Stellar convection zones also experience enhanced turbulent mixing processes due to large and rapid changes in pressure and temperature as gases of different densities diffuse and mix across interfaces (see Fig. 1.2). In supernovae dynamics, ionizing radiation and turbulence from blast and shock wave instabilities (3) are processes found in stellar and galaxy formation. During supernova detonation, stellar matter is ejected with densities 2–3 $\times$ 10^9 g/cm^3, temperatures 10^8–10^9 K, and velocities 10^9 cm/s (63; 64; 65). Molecular clouds in the interstellar medium (ISM), such as the Horse head nebula (see Fig. 1.2) and the three pillars of creation, are sources of ionizing radiation and turbulence strong enough to support gravitational collapse, which are responsible for star formation (66). Hydrodynamical models for SNe Ia are still poorly understood and controversial (67). Moreover, improved methods for modeling such instabilities are critical for developing more reliable estimates for the rate of cosmological expansion (65).

Figure 1.2: Illustrations of convection and radiation zones within a star (left) and the Horse head nebula (right).

1.1.2 Inertial confinement fusion and related high-energy studies

Reproducing astrophysical-type events in the laboratory is difficult due to the high pressures and temperatures involved (68). High-energy implosions, such as those in thermonuclear fuel compression in inertial confinement fusion (ICF), are inherently unstable and susceptible to shock-induced hydrodynamic instabilities. Over the past decades, experiments with various ICF capsule targets have demonstrated the important role fluid instabilities and mixing have in determining the efficiency of target implosion and neutron yield or the limiting of thermonuclear fuel compression (7). The National Ignition Facility (NIF) at the Lawrence Livermore National Laboratory (LLNL) consists of 192 40 cm square laser beams and a 10 m diameter chamber housing the thermonuclear fuel target; it is designed to deliver 1.8 MJ of energy (69) to rapidly heat and compress deuterium–tritium fuel to achieve thermonuclear fusion. During the compression process a sequence of inward-driven shock waves are generated that compress the fuel target. The first NIF experiment successfully sustained a blast wave speed corresponding to a 14 Mbar pressure held for 3 ns (70). Due to the extreme energies, pressures, and velocities involved, turbulent instabilities develop during the compression process.

High-energy density experiments are crucial to linking scaled models in controlled environments to astrophysical observations (71). Shock tube experiments are used to generate scaled shocks representative of those found in astrophysical environments, by separating a low-pressure gas from a high-pressure gas with a thin membrane having perturbations. As the diaphragm ruptures, the gas expands from high pressure (driver section) to low pressure (driven section), creating a shock wave (42).

In the context of ICF, even small amounts of mixing can have large effects on the energy released (72), and the application of Reynolds-averaged models to high-energy-density experiments has been considered to better understand turbulent mixing (see Sec. 1.3.3 for the description and application of several Reynolds-averaged models).

Until recently, simulations were performed without mixing effects, and even now modeling is usually applied in one dimension; high-resolution two-dimensional simulations have been considered, but they cannot model any fully developed turbulence that is present (73). Hurricane *et al.* (72) applied the K–L model in the multidimensional radiation hydrodynamics code ARES developed at the Lawrence Livermore National Laboratory and assumed negligible molecular viscosity, diffusivity, and conductivity. Amendt *et al.* (74) solved the ICF equations using the CALE code to assess the evolution of mixing and its effect on target performance, and estimate the yield degradation from short-wavelength perturbations growing on the inner shell surface. Bradley *et al.* (73) applied the BHR-2 turbulence model in an adaptive mesh refinement (AMR) Eulerian hydrodynamics code xRAGE (see Ref. (29)). The *turbulent* kinetic energy used to initiate turbulence was 0.1% of the *mean* kinetic energy, and the model was activated until the shock begins to pass through the gas interface. In these studies, the experimental widths were larger than the simulation predicted widths. Additional discussion on simulation and modeling studies is provided in Secs. 1.3.2 and 1.3.3.

1.1.3 Turbulent mixing

The present investigation is dedicated to advancing turbulence modeling relevant to the aforementioned applications. The further development and assessment of turbulence models validated against experimental data, theoretical predictions, and computational models are important areas of contemporary hydrodynamics and turbulence research. An important mechanism for the production of shock-induced turbulent mixing in high-energy-density systems is Richtmyer–Meshkov instability, in which the impulsive acceleration of a perturbed gas interface induces interfacial perturbation growth and eventually turbulent mixing at sufficiently large Reynolds numbers. In many applications, the evolving interface and resulting mixing layer are *reshocked* by a reflected shock. Reshocked Richtmyer–Meshkov instability is impor-

tant to better understand physically and model accurately, as it is a central mechanism for turbulent mixing in diverse applications (6; 17). Sections 1.2 and 1.3 discuss reshocked Richtmyer–Meshkov instability and previous experimental, theoretical, and computational endeavors to elucidate this phenomenon.

1.2 Reshocked Richtmyer–Meshkov Instability and Mixing

Initially predicted by Richtmyer in 1960 (48) and later experimentally verified by Meshkov in 1969 (49), Richtmyer–Meshkov instability occurs when the impulsive acceleration of a perturbed interface initially separating fluids with different densities results in the growth of perturbations. As the shock wave interacts with the first fluid it accelerates the interface and amplifies distortions on both the shock and interface (11; 10). These perturbations are manifested by the penetration of *bubbles* of light fluid into the heavy fluid and penetration of *spikes* of heavy fluid into the light fluid (4; 5). Eventually, turbulent mixing within the layer generated by this interpenetration occurs at sufficiently large Reynolds numbers. *Reshock*, in which the mixing layer is subjected to multiple shock–interface interactions rather than a single interaction (9), also occurs in many applications affected by Richtmyer–Meshkov instability.

Shock tubes are often used to experimentally investigate this instability. In describing the multi-stage evolution of reshocked Richtmyer–Meshkov instability in a shock tube, the incident shock wave is generated in the driver section, which contains either the lighter or heavier gas. The shock then impulsively accelerates the first gas towards the second gas situated in the test section. The incident shock and accelerated interface propagate downstream, with the shock traveling ahead of the interface. Gases behind the shock front can still be supersonic, but remain subsonic relative to the shock. Upon reflecting from the endwall of the test section, the shock propagates backwards. Reshock occurs when the reflected shock interacts with the evolving layer,

and results in enhanced turbulent mixing manifested by an increased growth rate of the mixing layer width. Following reshock, a transmitted wave continues upstream and a rarefaction wave is reflected in the direction of the test section endwall. Figure 1.3 shows Schlieren images from an air–SF_6 shock tube experiment conducted by Leinov *et al.* (12). Abbreviations for images (a)–(d) in the figure are: initial shock wave (ISW), mixing zone (MZ), reflected shock wave (RSW), transmitted–reflected shock wave (TRSW), and rarefaction wave (RRW); images (e)–(h) demonstrate the enhancement of turbulent mixing after reshock. Reshocked Richtmyer–Meshkov instability is also important in ICF as it can enhance turbulent mixing and limit thermonuclear fuel compression and ignition by mixing ablative shell material with the deuterium–tritium fuel in the capsule (7; 8).

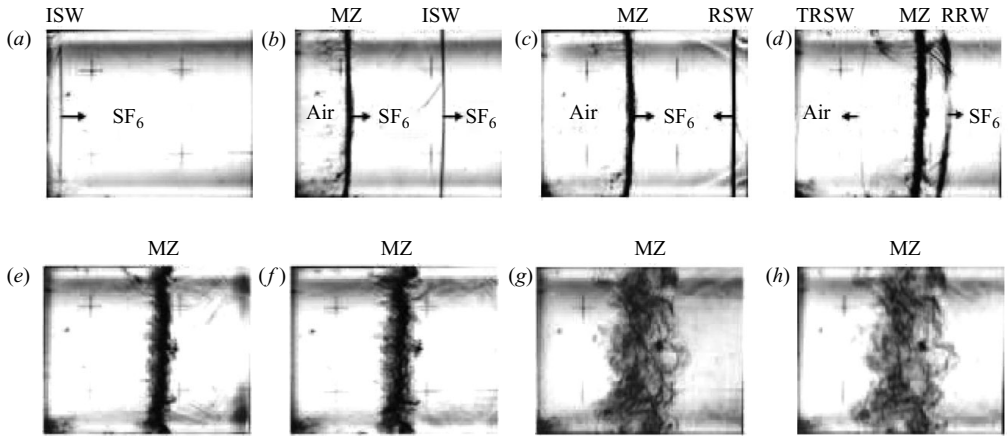

Figure 1.3: Evolution of reshocked Richtmyer–Meshkov instability for an air–SF_6 experiment conducted by Leinov *et al.* (12).

Experiments (10; 11; 12; 13; 14) and numerical simulations (15; 16; 17; 18; 19; 20; 21) show that reshock significantly increases the growth rate of the mixing layer, enhancing turbulent mixing. For example, Vetter and Sturtevant (10) found that turbulent mixing was amplified by a factor of six after the mixing layer was reshocked in experiments with incident shock Mach numbers ranging from $Ma_s = 1.24$ to 1.98. A summary of previous experimental work, numerical simulations, and Reynolds-

averaged modeling of reshocked Richtmyer–Meshkov instability and mixing is provided in Sec. 1.3.

1.3 Previous Experimental, Simulation, and Modeling Studies of Reshocked Richtmyer–Meshkov Instability

Turbulent mixing induced by shock–interface interactions, as occurs in reshocked Richtmyer–Meshkov instability, is challenging to diagnose in experiments and numerically simulate and model. The mixing involves two or more gases, so that advanced diagnostic methods and numerical methods that accurately describe the evolution of the instability, transition to turbulence, and turbulent mixing are necessary. This section discusses previous experimental, numerical, and modeling of reshocked Richtmyer–Meshkov instability.

1.3.1 Experiments

A total of ten different experiments were simulated for various investigations in the present work and initial condition calibration. Table 1.1 provides specifications for each of the studies conducted including incident shock Mach number $Ma_s = \sqrt{\overline{\gamma}\,\overline{p}/\overline{\rho}}$, gases, Atwood number $At = (\rho_2 - \rho_1)/(\rho_2 + \rho_1)$, and length of the test section δ. Experimental measurements with other gas combinations or shock Mach numbers larger than 1.98 are sparse and not as readily available.

Shock tube experiments provide mostly Schlieren visualizations for the turbulent mixing layer width, where x-rays, differential interferometry, and infrared absorption and emission are used for average density measurements (11). The three Vetter and Sturtevant experiments (1995) (10) listed in Table 1.1 were performed in the GALCIT 17-inch diameter horizontal shock tube (50). A thin 0.5 μm nitrocellulose membrane formed the initial interface separating air and SF_6, while a wire mesh supported

	Ma_s	Gas order	At	Test section length, δ [cm]
Vetter–Sturtevant (1995)	1.98	air–SF_6	0.67	49
	1.50	air–SF_6	0.67	61
	1.24	air–SF_6	0.67	110
Poggi *et al.* (1998)	1.45	SF_6–air	-0.67	30
Leinov *et al.* (2009)	1.20	air–SF_6	0.67	8, 9.8, 13.1, 17.2, 19.9, 23.5

Table 1.1: Experiments by Vetter and Sturtevant (10), Poggi *et al.* (11), and Leinov *et al.* (12) simulated in the present study. Specifications include incident shock Mach number Ma_s, gas order, Atwood number At, and test section length δ.

the membrane for most of the experiments. To achieve high-resolution imaging, a single spark-Schlieren photograph with a $0.5\,\mu$s spark-initiated flash of light was taken during each run. Due to the single-photograph limitation of Schlieren imaging, there is significant dependence on the repeatability of flow conditions as many runs are required to experimentally assemble the mixing layer width evolution (10). This limitation can be circumvented by capturing several images in one experimental run using low-resolution imaging; spark Schlieren images are still needed to facilitate interpretation of the mixing layer width.

Poggi *et al.* (1998) directly characterized the turbulence intensity with the hypothesis of a global turbulent field (11). Laser Doppler anemometry (LDA) was used to make instantaneous axial velocity measurements and obtain profiles of the axial contribution of the turbulent kinetic energy when the turbulent mixing layer swept past the measurement location. A vertical shock tube with SF_6 in the driver section and air in a 30 cm test section separated by a $0.3\,\mu$m thick membrane was used in the experiment. The gases were impulsively accelerated by an upward propagating shock with $Ma_s = 1.45$. The membrane did not induce any measurable turbulence and was ruptured by the incident shock. As discontinuous interfaces are usually generated by separating gases with a membrane, a thin wire mesh was placed directly above it. The spacing and diameter of the wire mesh were $1010\,\mu$m and $80\,\mu$m, respectively.

The LDA probe was positioned at 5.1, 12.6, 16.1, 16.9, and 17.9 cm ahead of the initial interface location in order to measure turbulence levels in the turbulent mixing layer before and after reshock. In order to achieve statistical convergence, approximately forty runs were necessary at almost every location of the LDA probe. This additionally required reproducing nearly identical initial experimental conditions.

The six reshocked Richtmyer–Meshkov instability experiments conducted by Leinov *et al.* were performed at the Ben-Gurion University using a horizontal shock tube with 550 cm length and constant 8 cm $\times$ 8 cm internal cross-section (12). Air and SF_6 were situated in the driver and test sections, respectively, resulting in Atwood number $At = 0.67$. A shock with incident shock Mach number $Ma_s = 1.20$ was generated in the air and progressed into the SF_6 test section. The gases were separated by a thin nitrocellulose membrane with randomly-distributed small-scale perturbations with mean wavelength $\langle\lambda\rangle = 0.10$ cm. To ensure $<1\%$ variation in the incident shock Mach number, an electrically actuated striking pin mounted on a rod inside the driver section was used to rupture the diaphragm separating the gases in the driver and test sections. In these experiments, the endwall of the test section was positioned at $\delta = 8.0$, 9.8, 13.1, 17.2, 19.9, and 23.5 cm downstream from the membrane to achieve different times of reshock corresponding to different degrees of nonlinearity of the mixing layer initially generated by the first shock passage through the interface. Schlieren photography was used to visualize the evolution of the reshocked turbulent mixing layer. The Schlieren images were digitized and the locations of the shock waves, mixing layer edges, and endwall positions were measured digitally. Physical quantities were obtained from the images using a suitable calibration. For each test section length considered, instantaneous mixing layer widths were plotted as a function of time from an ensemble of experiments.

1.3.2 Numerical simulations

The presence of shocks in numerical simulations introduces stringent resolution requirements. Typically an Eulerian shock-capturing or a Lagrangian method with artificial viscosity is used to represent the shock over several grid points (52). Material discontinuities, such as gas interfaces, pose similar difficulties for numerical methods. Except in particular cases, grid resolutions needed to fully resolve a shock, as would be required in a direct numerical simulation (DNS), are generally impractical (53).

Therefore, large-eddy simulation (LES) has been applied to shock-driven mixing more recently, in which explicit subgrid-scale models are implemented in the resolved-scale equations. However, there has been very little validation of subgrid-scale models applied to Richtmyer–Meshkov unstable flows in comparison to other more widely studied turbulent flows. Initially proposed by Smagorinsky (75), LES is a simulation method used in computational fluid dynamics that models the smallest (unresolved) scales of the flow (33), rather than resolving them directly as in DNS. The vast majority of multimaterial shock-driven flows have been simulated using implicit large-eddy simulation (ILES) (54) and monotone implicit large-eddy simulation (MILES), in which the Euler equations are solved with truncation errors of the numerical method providing intrinsic dissipation and diffusion that regularize the discrete solution. Implicit LES methods use finite-volume schemes to capture the inviscid cascade of kinetic energy through the inertial range, while the inherent numerical dissipation acts as an implicit subgrid model, providing another form of LES (76). The intrinsic dissipation and diffusion are very difficult to quantify for complex hydrodynamic flows. Investigations of such flows using LES, ILES, and MILES in three dimensions is highly computationally intense, as present resources limit these simulations to grid resolutions that cannot resolve all of the salient structures present in shocked flows. This limitation is exacerbated when simulating experiments with large Reynolds numbers and a wide range of spatial scales. Furthermore, because the

grids presently used are already at the size limit of available resources, numerical convergence studies cannot be performed and most simulations are likely underresolved.

Hill, Pantano and Pullin (15) performed LES of the $Ma_s = 1.24$, 1.50, and 1.98 Vetter–Sturtevant experiments using a hybrid tuned center-difference/fifth-order WENO scheme and the stretched vortex subgrid-scale model. Grid resolutions were 616×128^2 and 327×128^2 for the smallest and largest Mach numbers, respectively, and 388×128^2 and 776×256^2 for the intermediate Mach number simulations. Binary mixture relations were used to compute transport coefficients and thermodynamic quantities. The LES overpredicted the mixing layer growth rates prior to reshock but compared favorably with experimental measurements after reshock for all Mach numbers. They argued that due to the uncertainty in the initial conditions, the actual width of the mixing layer is not expected to compare well prior to reshock (15); measured widths prior to reshock were $\approx 50\%$ of the widths from the simulations. The post-reshock widths agreed well with the experimental data, with differences of $\approx 4\%$ for the $Ma_s = 1.50$ and 1.98 cases and $\approx 10\%$ for the $Ma_s = 1.24$ case.

Ukai *et al.* (55) performed LES of the $Ma_s = 1.50$ Vetter–Sturtevant experiment at a resolution of 746×140^2 using a one-equation model for the subgrid-scale kinetic energy. A finite-volume method with a fourth-order central scheme in smooth flow regions was used. While the mixing growth rate before reshock was overestimated, the growth rate following reshock was in good agreement with experimental data. However, the predicted mixing layer width was notably larger than the experimental measurements before and after reshock.

Schilling and Latini (18) performed ILES of the $Ma_s = 1.50$ Vetter–Sturtevant experiment at a resolution of 513×257^2 using a ninth-order WENO method. The predicted growth rate of the mixing layer before and after reshock agreed well with experimental measurements. However, the simulation mixing layer width overpredicted the experimental width before reshock due to the limited spatial resolution

and large initial perturbation amplitudes, but was in good agreement with the data after reshock. Grinstein, Gowardhan and Wachtor (19) also performed ILES of the $Ma_s = 1.50$ Vetter–Sturtevant experiment using adaptive mesh refinement with base resolutions $240^2 \times 820$ and $480^2 \times 1640$. The mixing layer growth rates were relatively insensitive to the initial conditions before reshock, and were more sensitive following reshock. Growth rates for all of the different initial perturbations considered agreed well with the experimental growth rates before and after reshock, but the mixing layer widths were overestimated.

1.3.3 Reynolds-averaged modeling

Reynolds-averaged Navier–Stokes (RANS) modeling is a complementary approach to the simulations discussed above. This method is widely used in modeling turbulence and mixing in engineering and scientific applications (33) and may be the only current practical means of estimating the effects of turbulence on mean flows in complex high-energy-density physics applications such as ICF. In RANS modeling, ensemble-averaged Navier–Stokes equations are solved with closures for the correlations introduced through averaging of the nonlinear terms. When flow symmetries permit, such as in shock propagation where most of the transport occurs in the direction of shock propagation, RANS models can be run in fewer than three spatial dimensions. Unlike for multidimensional numerical simulations, this also permits numerical convergence studies to be performed. However, RANS models also have relative disadvantages. Compared to LES where only the subgrid scales are modeled, all flow scales are modeled in RANS simulations and additional modeled turbulent transport equations are necessary. Model coefficients in these transport equations can be numerous and require calibration, or otherwise must be specified using theoretical considerations, e.g., self-similarity constraints (see Sec. 2.3). Specifying the initial conditions of the turbulent fields must also be addressed.

One Reynolds-averaged model that has been used to perform these studies is the K–L turbulence model; K is the turbulent kinetic energy in the flow and the turbulent lengthscale L is characteristic of the largest eddy size. The *turbulent* kinetic energy is often taken as a fraction of the *mean* kinetic energy ($\approx 0.1\% - 10\%$). Dimonte and Tipton (27) applied a K–L turbulence model implemented in an arbitrary Lagrangian–Eulerian (ALE) code to model the $Ma_s = 1.50$ Vetter–Sturtevant and $Ma_s = 1.45$ Poggi–Thorembey–Rodriguez experiments. This two-equation transport model for the turbulent kinetic energy and turbulent lengthscale is based on a buoyancy–drag model for the Rayleigh–Taylor and Richtmyer–Meshkov instabilities. Good agreement with the data before and after reshock was obtained for both cases by adjusting a model coefficient C_P and the initial turbulent lengthscale L_0 between these cases. Chiravalle (28) used a similar K–L model implemented in a Lagrangian code with a von Neumann–Richtmyer artificial viscosity, and showed similarly good agreement with both experiments by adjusting model coefficients and initial conditions. Furthermore, Mügler and Gauthier (51) also performed ALE simulations of the $Ma_s = 1.45$ Poggi–Thorembey–Rodriguez experiment. The two-dimensional Navier–Stokes equations using a two-species formulation were simulated with the Baldwin–Lomax turbulence model for near-wall boundary layers. Predicted mixing layer widths were slightly larger than experimental measurements, but better agreement was achieved after reshock. In addition to conducting experiments for various reshock times, Leinov *et al.* also performed three-dimensional numerical simulations using the arbitrary Lagrangian–Eulerian LEEOR3D code for $\delta = 8.0$, 17.2, and 23.5 cm (12; 31). Simulation mixing layer widths matched experimental widths with good accuracy.

Another Reynolds-averaged model often used is the K–ϵ model, where the turbulent kinetic energy dissipation rate, ϵ, is modeled instead of the turbulent lengthscale, L. The turbulent lengthscale and the turbulent kinetic energy dissipation rate can

be related by $\epsilon = C_D\, K^{3/2}/L$ (74), where $C_D \approx 1.25$ (27) is the bubble drag coefficient. Gauthier and Bonnet (25) developed a K–ϵ model for turbulent mixing, where the closure relations were supplemented with algebraic relations in order to provide reasonable predictions under strong gradients. A fully turbulent state was assumed for closing the turbulent fluxes by gradient-diffusion models using the corresponding mean quantities. The model was applied to two experiments for instability-induced turbulent mixing with incident shock Mach numbers $1.00 \leq Ma_s \leq 1.30$. However, a constant coefficient set was not established as the two experiments were modeled using three different combinations of σ_ρ and $C_{\epsilon 0}$. Valerio *et al.* (61) developed a one-dimensional Reynolds-averaged model (an early version of the BHR model) for simulating reshocked Richtmyer–Meshkov instability-induced turbulent mixing. Calibrations were made against results from the impulsive acceleration of an air–He interface by a $Ma_s = 1.3$ incident shock. The model was applied to experiments with gas configurations CO_2–He, CO_2–Ar and CO_2–Kr with corresponding Atwood numbers $At = -0.73$, -0.05, and 0.31; the incident shock Mach numbers considered in the studies were $Ma_s = 2.4$, 3.1, and 4.5. The model also predicted multiple reshocks for the various studies. Except for small Atwood numbers, the predictions agreed quantitatively with theoretical estimates and experimental results. Gauthier and Bonnet (25) and Valerio *et al.* (61) solved the equations using a Lagrangian method.

Banerjee, Gore and Andrews (29) applied the three-equation Besnard–Harlow–Rauenzahn (BHR) model to the $Ma_s = 1.24$, 1.50, and 1.98 Vetter–Sturtevant and $Ma_s = 1.45$ Poggi–Thorembey–Rodriguez experiments. This model is also based on a K–L turbulence model. However, an additional transport equation is modeled for the averaged fluctuating velocity, $\overline{v_j''}$. Agreement with the pre-reshock experimental data was good, but the model generally predicted less turbulent mixing following reshock, resulting in smaller growth rates of the mixing layer widths.

Grégoire, Souffland and Gauthier (26) applied a second-order Reynolds-averaged

Euler model to simulate the $Ma_s = 1.45$ Poggi–Thorembey–Rodriguez experiment. The components of the Reynolds stress equation (instead of the turbulent kinetic energy) were solved together with an equation for the modeled turbulent kinetic energy dissipation rate. These equations were coupled to modeled transport equations for the averaged Favre fluctuating velocity $\overline{v_j''}$ and density variance $\overline{\rho'^2}$. The model was implemented in a Lagrangian finite-volume code using a second-order staggered spatial discretization and shock-capturing was achieved using a von Neumann–Richtmyer artificial viscosity. The model showed some inaccuracy prior to reshock as a smaller width was predicted. However, agreement with experimental data improved following reshock as the growth of the turbulent mixing layer was well predicted.

In this thesis, a multicomponent (two species) Reynolds-averaged Navier–Stokes (RANS) model based on a two-equation K–ϵ turbulence model is used to simulate reshocked Richtmyer–Meshkov instability. The model equations are solved using a third-order conservative finite-difference weighted essentially nonoscillatory (WENO) shock-capturing method and a characteristic projection formulation. The governing equations include heat conduction, viscous effects, mass diffusion, and enthalpy diffusion, unlike previous studies (25; 26; 27; 28; 29) in which the Reynolds-averaged Euler equations were considered. Rather than using an arbitrary lengthscale, the linear Richtmyer growth rate is used as a relevant timescale to relate the initial values of K and ϵ.

1.4 Outline of the Thesis

The multicomponent Reynolds-averaged Navier–Stokes equations coupled to a two-equation K–ϵ turbulence model are introduced in Chapter II. Mixture molecular transport and thermodynamic contributions are discussed, followed by the closures for the Reynolds stress and averaged fluctuating velocity. Definitions for the mixing layer width and the analytical self-similar solution are presented. A discussion of the

numerical method used to solve these equations is also given.

The model predictions are evaluated in Chapter III by simulating four reshocked Richtmyer–Meshkov instability experiments. The first three experiments were conducted by Vetter and Sturtevant (1995) (10) for $Ma_s = 1.24$, 1.50, and 1.98 with $At = 0.67$. The fourth experiment was conducted by Poggi, Thorembey, and Rodriguez (1998) (11) for $Ma_s = 1.45$ with $At = -0.67$. In addition to experimental measurements, results are compared with predictions from the BHR model (29), LES data (15), and self-similar solutions. Parametric studies are conducted to test the sensitivity of the model to changes in initial conditions and key model coefficients.

The model is applied to study the effects of variations in reshock timing by adjusting the test section length δ in Chapter IV. A set of six experiments conducted by Leinov *et al.* (12) with $\delta = 8$, 9.8, 13.1, 17.2, 19.9, and 23.5 cm are considered to evaluate the predicted mixing layer widths using an optimal set of coefficients. Results from three-dimensional simulations (31) for $\delta = 8$, 17.2, and 23.5 cm are also available for additional comparison. A second set of general coefficients applicable to a broader range of Ma_s, At, and δ was also determined; comparisons are made between the mixing layer widths obtained using the optimal and general coefficients for the ten experiments just discussed. To the author's knowledge, this is the first published application of a RANS model to simulate these experiments.

Reshocked Richtmyer–Meshkov instability is investigated in Chapter V for different Atwood numbers. Combinations of air with CO_2, SF_6, and H_2 resulting in $At = \pm 0.21$, ± 0.67, and ± 0.87, respectively, are considered for both light-to-heavy and heavy-to-light configurations. Although experimental data are not available for these investigations, results from perviously performed LES are compared to the model predictions. Mixing rates following reshock are compared between gas pairs for the positive and negative Atwood numbers. RANS modeling of reshocked Richtmyer–Meshkov instability is considered in Chapter VI for larger incident shock Mach num-

bers, $Ma_s = 3.00$ and 5.00. Comparisons are also made for early-time and post-reshock mixing between Atwood numbers for larger Ma_s values. Finally, conclusions and future work are given in Chapter VII.

The principal contribution of this research to the field is the systematic application of a multicomponent RANS turbulence model to reshocked Richtmyer–Meshkov instability. The present work addresses the following questions and new contributions to this field:

- How is reshocked Richtmyer–Meshkov instability modeled differently in this RANS study?

  A multicomponent (two species) RANS model including mixture molecular transport and thermodynamic contributions coupled with a K–ϵ turbulence model is used. The linear Richtmyer growth rate is used as a relevant timescale in initializing K and ϵ instead of an arbitrary turbulent lengthscale. The model is used to *systematically* investigate a broad range of reshocked Richtmyer–Meshkov instability cases.

- How is confidence established in the model?

  This work entails comparisons to a variety of experimental and numerical simulation data and the analytical self-similar solution for early-time mixing. Parametric studies were conducted to test the model sensitivity to variations in key model coefficients, initial conditions, and experimental uncertainty. Numerical convergence under grid refinement for the mixing layer width, the mean density, mean pressure, mean heavy mass fraction, mean velocity, turbulent kinetic energy, turbulent kinetic energy dissipation rate, and turbulent viscosity was considered for each of the cases. Converged results show good agreement with the experimental data, and also suggest the possibility of underresolved results from other Reynolds-averaged models and LES.

- How do variations in model coefficients and initial conditions affect turbulent mixing predictions?

  Turbulent budgets for the turbulent kinetic energy and turbulent kinetic energy dissipation rate transport equations and how they correlate with features observed in the mixing layer growth are considered; see also Ref. (62) for a similar analysis of these budgets for Rayleigh–Taylor turbulent mixing. The buoyancy and shear production, diffusion, and dissipation contributions to the budgets are evaluated for early-time and post-reshock mixing. These studies elucidate changes in the mixing layer growth rates, shock speeds, turbulence intensities, and general mixing processes as initial conditions, model coefficients, and experimental parameters are varied.

- What areas of reshocked Richtmyer–Meshkov instability relevant to high-energy-density physics are elucidated?

  As the model shows good agreement with various experimental data and the analytical self-similar solution, its application is extended to cases for which experimental and numerical simulation data are either not available or sparse: reshocked Richtmyer–Meshkov instability for Atwood numbers $At = \pm 0.21$, ± 0.67, and ± 0.87 corresponding to combinations of air with CO_2, SF_6, and H_2, respectively. Comparisons of the mixing layer growth rate and turbulent budgets are made between Atwood numbers. Furthermore, reshocked Richtmyer–Meshkov instability-induced turbulent mixing is also considered for larger incident shock Mach numbers, $Ma_s = 3.00$ and 5.00. These regimes are relevant to high-energy-density applications, and experimental and numerical simulation data is very limited.

CHAPTER II

Turbulence Modeling and Numerical Method

2.1 Turbulence Modeling

2.1.1 The multicomponent Reynolds-averaged Navier–Stokes model

The multicomponent RANS model including mixture molecular transport and thermodynamic coefficients describes the transport of mean density $\overline{\rho}$, velocity $\widetilde{v}_i$, total energy $\widetilde{e}$, and heavy gas mass fraction $\widetilde{m}_H$ (22; 24). All quantities are in cgs units. The mean transport equations are

$$\frac{\partial \overline{\rho}}{\partial t} + \frac{\partial}{\partial x_j}(\overline{\rho}\,\widetilde{v}_j) = 0\,, \tag{2.1}$$

$$\frac{\partial}{\partial t}(\overline{\rho}\,\widetilde{v}_i) + \frac{\partial}{\partial x_j}(\overline{\rho}\,\widetilde{v}_i\,\widetilde{v}_j) = -\frac{\partial \overline{p}}{\partial x_i} - \frac{\partial \tau_{ij}}{\partial x_j} + \frac{\partial \overline{\sigma}_{ij}}{\partial x_j}\,, \tag{2.2}$$

$$\begin{aligned}\frac{\partial}{\partial t}(\overline{\rho}\,\widetilde{e}) + \frac{\partial}{\partial x_j}(\overline{\rho}\,\widetilde{e}\,\widetilde{v}_j) &= -\frac{\partial}{\partial x_j}(\overline{p}\,\widetilde{v}_j) - \frac{\partial}{\partial x_j}\left(\overline{p}\,\overline{v_j''}\right) - \frac{\partial}{\partial x_j}(\tau_{ij}\,\widetilde{v}_i) + \frac{\partial \overline{H}_j}{\partial x_j} \\ &\quad + \frac{\partial}{\partial x_j}\left(\overline{\kappa}\,\frac{\partial \widetilde{T}}{\partial x_j} + \frac{\mu_t}{\sigma_U}\,\frac{\partial \widetilde{U}}{\partial x_j}\right) + \frac{\partial}{\partial x_j}\left[\left(\overline{\mu} + \frac{\mu_t}{\sigma_K}\right)\frac{\partial K}{\partial x_j}\right],\end{aligned} \tag{2.3}$$

$$\frac{\partial}{\partial t}(\overline{\rho}\,\widetilde{m}_H) + \frac{\partial}{\partial x_j}(\overline{\rho}\,\widetilde{m}_H\,\widetilde{v}_j) = \frac{\partial}{\partial x_j}\left[\left(\overline{\rho}\,\overline{D} + \frac{\mu_t}{\sigma_m}\right)\frac{\partial \widetilde{m}_H}{\partial x_j}\right], \tag{2.4}$$

where overbars and tildes denote Reynolds and Favre averaged fields, respectively (see Appendix A for the derivation of these equations and the approximations used in the present study). The mean total energy includes the mean kinetic, mean internal, and turbulent kinetic energies, respectively,

$$\widetilde{e} = \frac{\widetilde{v}^2}{2} + \widetilde{U} + K \,. \tag{2.5}$$

The gases are assumed to satisfy the ideal gas equation of state relating the mean internal energy $\widetilde{U}$, pressure $\overline{p}$, and temperature $\widetilde{T}$,

$$\widetilde{U} = \frac{\overline{p}}{(\overline{\gamma} - 1)\,\overline{\rho}} = \overline{c}_v\,\widetilde{T} \,. \tag{2.6}$$

The mixture ratio of specific heats

$$\overline{\gamma} = \frac{\overline{c}_p}{\overline{c}_v} = \frac{c_{pH}\,\widetilde{m}_H + c_{pL}\,(1 - \widetilde{m}_H)}{c_{vH}\,\widetilde{m}_H + c_{vL}\,(1 - \widetilde{m}_H)} \tag{2.7}$$

depends on the heavy mass fraction, $\widetilde{m}_H$, and light mass fraction, $\widetilde{m}_L = 1 - \widetilde{m}_H$. Specific heats at constant pressure and volume are $c_{pH,L}$ and $c_{vH,L}$, respectively, and are assumed constant for each gas. Subscripts H and L denote the heavy and light fluids, respectively. The mean viscous stress tensor is

$$\overline{\sigma}_{ij} = \overline{\mu}\left(\frac{\partial \widetilde{v}_i}{\partial x_j} + \frac{\partial \widetilde{v}_j}{\partial x_i} - \frac{2}{3}\,\delta_{ij}\,\frac{\partial \widetilde{v}_k}{\partial x_k}\right) \tag{2.8}$$

and bulk viscosity is neglected. Molecular transport coefficients and thermodynamic quantities, $\overline{\kappa}$, $\overline{\mu}$, $\overline{D}$, and $\overline{H}_j$, are discussed in Sec. 2.1.2. Closures for the Reynolds stress tensor τ_{ij} and averaged fluctuating velocity $\overline{v_j''}$ are discussed in Sec. 2.1.4. The model coefficients σ_m, σ_U, σ_K are discussed in Sec. 2.3.

The second and third terms on the right side of Eq. (2.3) are the buoyancy

production (pressure work) and shear production, respectively, of the mean total energy followed by the mean enthalpy diffusion. The last two terms in Eq. 2.3 are the internal energy and turbulent kinetic energy diffusion, which account for both molecular and turbulent contributions. Diffusive terms in Eq. 2.4 for the heavy mass fraction similarly account for molecular and turbulent transport processes.

2.1.2 Mixture molecular transport coefficients and thermodynamic quantities

The binary mixture relation (15; 38; 40)

$$\overline{\phi} = \frac{\phi_H \, \widetilde{m}_H / \sqrt{MW_H} + \phi_L \left(1 - \widetilde{m}_H\right) / \sqrt{MW_L}}{\widetilde{m}_H / \sqrt{MW_H} + \left(1 - \widetilde{m}_H\right) / \sqrt{MW_L}} \tag{2.9}$$

is used for the molecular transport coefficients, where $\phi = \mu$, D, and κ are the dynamic viscosity, mass diffusivity, and thermal conductivity, respectively; these quantities are assumed constant for each gas. The molecular weights for the heavy and light gases are $MW_{H,L}$.

The mean enthalpy diffusion term in the mean total energy equation (2.3),

$$\overline{H}_j = -\sum_{r=1}^{2} \widetilde{h}_r \overline{J}_{r,j} \ , \tag{2.10}$$

depends on the mean enthalpy and diffusive flux of gas r,

$$\widetilde{h}_r = \widetilde{U}_r + \frac{\overline{p}_r}{\overline{\rho}_r} \tag{2.11}$$

$$\overline{J}_{r,j} = -\overline{\rho} \left(D_r \frac{\partial \widetilde{m}_r}{\partial x_j} - \widetilde{m}_r \sum_{s=1}^{2} D_s \frac{\partial \widetilde{m}_s}{\partial x_j} \right) \tag{2.12}$$

respectively. Indices 1 and 2 refer to H and L.

2.1.3 The K–ϵ turbulence model

The transport equations for the turbulent kinetic energy K and turbulent kinetic energy dissipation rate ϵ (22; 24; 32; 33) are

$$\begin{aligned}\frac{\partial}{\partial t}(\overline{\rho}\,K)+\frac{\partial}{\partial x_j}(\overline{\rho}\,K\,\widetilde{v}_j) &= -\overline{v_j''}\,\frac{\partial \overline{p}}{\partial x_j}-\tau_{ij}\,\frac{\partial \widetilde{v}_i}{\partial x_j}-\overline{\rho}\,\epsilon+\Pi_K \\ &\quad +\frac{\partial}{\partial x_j}\left[\left(\overline{\mu}+\frac{\mu_t}{\sigma_K}\right)\frac{\partial K}{\partial x_j}\right],\end{aligned} \tag{2.13}$$

$$\begin{aligned}\frac{\partial}{\partial t}(\overline{\rho}\,\epsilon)+\frac{\partial}{\partial x_j}(\overline{\rho}\,\epsilon\,\widetilde{v}_j) &= -C_{\epsilon 0}\,\frac{\epsilon}{K}\,\overline{v_j''}\,\frac{\partial \overline{p}}{\partial x_j}-C_{\epsilon 1}\,\frac{\epsilon}{K}\,\tau_{ij}^{d}\,\frac{\partial \widetilde{v}_i}{\partial x_j}-\frac{2}{3}\,C_{\epsilon 3}\,\overline{\rho}\,\epsilon\,\frac{\partial \widetilde{v}_j}{\partial x_j} \\ &\quad -C_{\epsilon 2}\,\frac{\overline{\rho}\,\epsilon^2}{K}+C_{\epsilon 4}\,\frac{\epsilon}{K}\,\Pi_K+\frac{\partial}{\partial x_j}\left[\left(\overline{\mu}+\frac{\mu_t}{\sigma_\epsilon}\right)\frac{\partial \epsilon}{\partial x_j}\right],\end{aligned} \tag{2.14}$$

respectively (1; 25; 32). The first two terms on the right side of Eq. 2.13 represent the production of turbulent kinetic energy through buoyancy (pressure work) and shear, respectively. The third term is the dissipation of turbulent kinetic energy, followed by the pressure–dilatation Π_K, which generally behaves as an additional dissipation term. The last term in Eq. 2.13 is the diffusion of turbulent kinetic energy, which is the same as that in Eq. 2.3. The right side of the turbulent kinetic energy dissipation equation is proportional to the right side of the turbulent kinetic energy equation by the inverse of the turbulent timescale K/ϵ and dimensionless model coefficients $C_{\epsilon 0}$–$C_{\epsilon 4}$. The physical interpretation of the mechanisms in Eq. 2.14 is similar to those in Eq. 2.13. These equations are closed using the expressions in Sec. 2.1.4.

2.1.4 Turbulence model closures and principal model coefficients

Contributions from the Reynolds stress tensor are found in the mean momentum transport in Eq. 2.2 and in the shear production in Eqs. 2.3, 2.13, and 2.14. The classical Boussinesq closure (32; 33) for the Reynolds stress is (the summation convention

is used for repeated indices)

$$\tau_{ij} = \frac{2}{3}\,\overline{\rho}\,K\,\delta_{ij} - 2\,\mu_t\left(\widetilde{S}_{ij} - \delta_{ij}\,\frac{\widetilde{S}_k^{\,k}}{3}\right). \tag{2.15}$$

The isotropic part is often expressed in terms of the turbulent pressure $\overline{p}_T = (2/3)\,\overline{\rho}\,K$, while the deviatoric part of the Reynolds stress tensor (with zero trace, and not included in the present work) is $\tau_{ij}^d = -2\mu_t\left(\widetilde{S}_{ij} - \delta_{ij}\widetilde{S}_k^{\,k}/3\right)$, where the mean strain-rate tensor is $\widetilde{S}_{ij} = (1/2)(\partial\widetilde{v}_i/\partial x_j + \partial\widetilde{v}_j/\partial v_i)$.

The turbulent viscosity has the standard form (32; 33; 60)

$$\nu_T = \frac{\mu_t}{\overline{\rho}} = C_\mu\,\frac{K^2}{\epsilon} \tag{2.16}$$

with its magnitude related to the intensity of turbulent mixing within the core of the layer. The averaged fluctuating velocity $\overline{v_j''}$ contributes to the buoyancy production (pressure work) in Eqs. 2.3, 2.13, and 2.14. The algebraic closure used here is (34; 35)

$$\overline{v_j''} = -\frac{\overline{\rho'\,v_j''}}{\overline{\rho}} = \frac{\nu_t}{\sigma_\rho\,\overline{\rho}}\left(\frac{\partial\overline{\rho}}{\partial x_j} - \frac{\overline{\rho}}{\overline{p}}\,\frac{\partial\overline{p}}{\partial x_j}\right), \tag{2.17}$$

which accounts for the mean pressure gradient in addition to the mean density gradient. The standard expression in variable-density and compressible turbulence includes only the mean density gradient (1).

As turbulence is dissipative, it requires a source of energy to be sustained (60). Otherwise, the turbulent kinetic energy is dissipated rapidly due to viscous effects as eddies transfer this energy to the internal energy of the medium. The volumetric rate at which the turbulent kinetic energy dissipates is

$$\overline{\rho}\,\epsilon = \overline{\sigma_{ij}\,\frac{\partial v_i''}{\partial x_j}} \tag{2.18}$$

with viscous stress tensor σ_{ij}. The pressure–dilatation correlation, $\Pi_K = \overline{p'\partial v_j''/\partial x_j}$, behaves as an additional dissipative term, but is not currently included in the simulations as it is expected to be small compared to the other terms. This term is often neglected in compressible turbulence modeling.

Diffusion of turbulent kinetic energy is composed of three unclosed terms: molecular diffusion $\overline{\sigma_{ij} v_i''}$, which is a process in which molecular transport of the gas causes turbulent energy to diffuse; the rate at which energy is transported through the fluid due to turbulent fluctuations is the turbulent transport, $-\overline{\frac{1}{2}\rho v''^2 v_j''}$; the last component is another form of turbulent diffusion due to pressure and velocity fluctuations, $-\overline{p' v_j''}$. In some cases molecular diffusion is neglected and this term is approximated as the combination of turbulent transport and pressure diffusion (32). The molecular diffusion and turbulent transport are modeled by a single term as

$$\overline{\frac{\rho\, v''^2\, v_j''}{2}} + \overline{p'\, v_j''} - \overline{\sigma_{ij}\, v_i''} = -\left(\overline{\mu} + \frac{\mu_t}{\sigma_K}\right)\frac{\partial K}{\partial x_j} \tag{2.19}$$

and the internal energy flux is modeled by an analogous expression

$$\overline{\rho\, U''\, v_j''} = -\frac{\mu_t}{\sigma_U}\,\frac{\partial \widetilde{U}}{\partial x_j}\,. \tag{2.20}$$

The model coefficients held constant in all of the simulations in this study are (22; 24)

$$C_{\epsilon 1} = 1.44\ ,\ C_{\epsilon 2} = 1.92\ ,\ C_{\epsilon 3} = 2.00\,, \tag{2.21}$$

$$\sigma_m = \sigma_U = \sigma_K = \sigma_\epsilon = 0.50\,.$$

The values of $C_{\epsilon 1}$ and $C_{\epsilon 2}$ are standard values for shear turbulence (33; 32), while the value of $C_{\epsilon 3}$ is chosen to be consistent with shockless rapid compression [see Ref. (27) for a derivation corresponding to the K–L model]. As current simulations do not include the pressure–dilatation, $C_{\epsilon 4} = 0$. The two coefficients varied in the sim-

ulations are σ_ρ and $C_{\epsilon 0}$, which are associated with the buoyancy (shock) production mechanisms in Eqs. (2.13) and (2.14). The coefficient σ_ρ affects the magnitude of the K and ϵ buoyancy production terms while $C_{\epsilon 0}$ scales the dissipation of turbulent kinetic energy generated by buoyancy (shock) production. Note that self-similarity (see Sec. 2.3) requires $\sigma_m = \sigma_U = \sigma_K = \sigma_\epsilon$, and these coefficients are chosen here to be smaller than their typical values close to unity (32).

2.1.5 Initialization of the mean and turbulent fields

The initial pressure and temperature for the quiescent gases in the driver and test sections are held constant at $p = 23$ kPa and $T = 70^o$ F $= 294$ K, respectively. The equation for an ideal gas is used to calculate the initial density, $\rho = p\, M_W/(R\, T)$, where M_W is the molecular weight and R is the universal gas constant. The test section length is adjusted for each case by placing the interface a distance δ from the endwall. In all cases considered in this study, the shock is generated a distance 0.25 cm away from the interface. The Rankine–Hugoniot relations (41; 42) used to calculate the initial mean post-shock density, pressure, and velocity are

$$\overline{\rho}_0(x,0) = \frac{\rho_1\, Ma_s^2\,(\gamma_1+1)}{Ma_s^2\,(\gamma_1-1)+2}\,, \tag{2.22a}$$

$$\overline{p}_0(x,0) = \frac{p_1[2\,\gamma_1\,\, Ma_s^2-(\gamma_1-1)]}{\gamma_1+1}\,, \tag{2.22b}$$

$$\widetilde{v}_0(x,0) = \frac{2\,c_s(Ma_s^2-1)}{Ma_s(\gamma_1+1)}\,, \tag{2.22c}$$

respectively, where Ma_s and $c_s = \sqrt{\overline{\gamma}\,(\overline{p}+\overline{p}_T)/\overline{\rho}}$ are the incident shock Mach number and initial sound speed, respectively. Subscripts 1 and 2 denote the gas where the shock is initiated (driver section) and the (test section) gas that is impulsively accelerated by the first gas; the subscript 0 denotes the post-shock region of gas 1. Figure 2.1 shows the conditions in the post-shock, driver, and test sections at the onset of

the simulation for a study with $At = 0.67$ and $Ma_s = 1.50$.

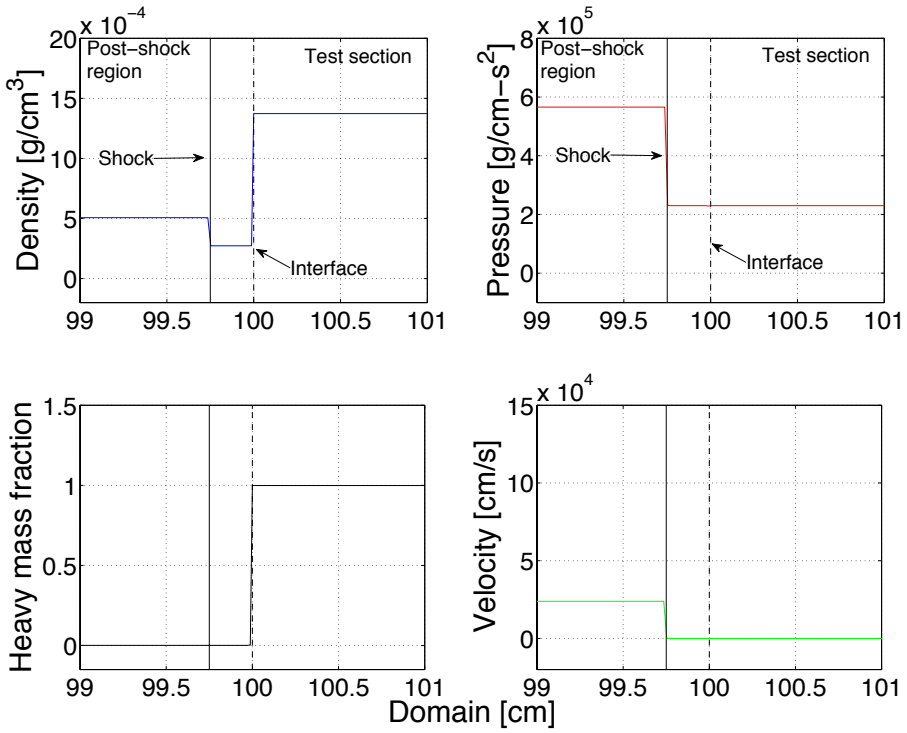

Figure 2.1: Initial mean density, pressure, heavy mass fraction, and velocity in the post-shock, driver, and test regions for $At = 0.67$ with $Ma_s = 1.50$. The locations of the interface and shock are denoted by the dashed and solid lines.

Two important degrees of freedom in RANS modeling are the initial turbulent kinetic energy and turbulent kinetic energy dissipation rate. Predictions of unsteady RANS models can generally depend on the initial values of the turbulent fields. Defining the turbulent kinetic energy seed K_0 as a small fraction of the initial mean kinetic energy, the turbulent kinetic energy is initialized as

$$K(x,0) = K_0 \left(At\, \widetilde{v}_0\right)^2 . \tag{2.23}$$

The initial condition for the turbulent kinetic energy is proportional to the initial post-shock mean kinetic energy, $\widetilde{v}_0^2$. The dependence on the Atwood number, $At = (\rho_2 - \rho_1)/(\rho_2 + \rho_1)$, allows $K(x,0)$ to approach zero in the limit of equal gas densities.

The turbulent kinetic energy dissipation rate is initialized as

$$\epsilon(x,0) = K(x,0)\,\omega \tag{2.24}$$

and depends on $K(x,0)$ and the linear Richtmyer growth rate $\omega = k_{rms}\,|At|\,\Delta v$ for an rms perturbation wavenumber $k_{rms} = 2\pi/\lambda_{rms}$ and initial rms perturbation wavelength λ_{rms} (22; 24). The linear Richtmyer growth rate is a relevant timescale that relates $K(x,0)$ and $\epsilon(x,0)$ at the initial shock–interface interaction. The change in velocity due to the passage of the shock is Δv (36). This method is different from other approaches that introduce arbitrary values when initializing the turbulent kinetic energy dissipation rate. For example, the K–L model introduces a value based on a 'turbulent' lengthscale through $\epsilon(x,0) = C_\epsilon K(x,0)^{3/2}/L(x,0)$, where C_ϵ and $L(x,0)$ must be specified (see Sec. 1.3.3).

2.2 Defining the Time-Dependent Mixing Layer Width

The mixing layer width $h(t)$ is a fundamental hydrodynamic instability-induced quantity associated with the mixing of two fluids. This quantity is typically measured or inferred in experiments and computed in numerical simulations (22). There is no unique definition of this quantity. In the mixing process the light and heavy fluids interpenetrate in the form of *bubbles* and *spikes* (24), respectively, thus generating the mixing layer. As the turbulent mixing process develops following the shock–interface interaction during reshock, the growth rate of the mixing layer becomes correspondingly steeper as the mixing increases.

Several approaches exist to calculate the mixing layer width. The mean heavy gas mole fraction (16) is used here,

$$\widetilde{X}_H(x,t) = \frac{MW_L\,\widetilde{m}_H(x,t)}{(MW_L - MW_H)\,\widetilde{m}_H(x,t) + MW_H}\,, \tag{2.25}$$

where MW is the molecular weight and subscripts L and H differentiate the light and heavy gases, respectively; $\widetilde{m}_H(x,t)$ is the mean heavy mass fraction. The time-dependent bubble location $h_b(t)$ is determined by the point on the plane where $\widetilde{X}_H(x,t) \leq 1-\eta$. Similarly, the spike location $h_s(t)$ is the point where $\widetilde{X}_H(x,t) \geq \eta$. The mole fraction limit $\eta = 0.02$ is held constant for all simulations. Other commonly used mole fraction limits include $\eta = 0.01$ and 0.05. The mixing layer width, $h(t)$, is then calculated as the difference between the spike and bubble locations,

$$h(t) = h_s(t) - h_b(t)\,. \tag{2.26}$$

2.3 The Pre-Reshock Analytical Self-Similar Solution

The analytical self-similar mixing layer width prior to reshock is

$$h(t) = h_0 \left(\frac{t}{t_0} + 1 \right)^{\theta} \tag{2.27}$$

with amplitude h_0, $t_0 = h_0/(\theta \Delta v)$, and power-law exponent (see Ref. (27) for a derivation of the self-similar mixing layer width corresponding to the K–L model),

$$\theta = \frac{2\,C_{\epsilon 2} - 3}{3\,C_{\epsilon 2} - 3} \approx 0.30\,. \tag{2.28}$$

The initial amplitude of the mixing layer width is compared with the $\approx t^{\,0.3}$ evolution of this quantity prior to reshock. The expression for $h(t)$ can be derived by solving a simplified form of the one-dimensional Reynolds-averaged equations, in which the shock–interface interaction is treated as an impulse at the initial time, and $\widetilde{v}_i = 0$, $\tau_{ij} = 0$, and $\overline{\mu} = 0$. The resulting K and ϵ equations include only the dissipation and turbulent diffusion terms, and can be solved analytically using the self-similar scaling variable $\eta = 2x/h(t)$ with $h(t) = h_0\,(t/t_0)^{\theta}$.

2.4 Implementation of the Model in a Third-Order WENO Shock-Capturing Code

The six RANS equations are implemented in a one-dimensional hydrodynamics code developed at the Lawrence Livermore National Laboratory (LLNL) and further modified at the University of Michigan to conduct the present investigations. Inviscid (advective) flux reconstruction is achieved using a conservative Eulerian finite-difference weighted essentially nonoscillatory (WENO) shock-capturing method and a characteristic projection formulation (43; 44). The numerical implementation includes four mean flow equations (see Sec. 2.1.1) and two turbulent transport equations (see Sec. 2.1.3; one or two additional scalar turbulent transport equations are also available, but are not considered in the present study). The 6×6 left and right eigenvector matrices resulting from the Jacobian of the inviscid fluxes are used to project the fluxes between characteristic and physical space, together with Lax–Friedrichs flux-splitting and Roe averaging generalized to multicomponent flow (*i.e.*, to include the mean mass fraction equation and a variable $\overline{\gamma}$) and to additional turbulent transport equations. The advection terms, numerical flux, Jacobian $\partial f(u)/\partial u$, eigenvalues, and Roe-averaged left and right eigenvectors for the 6×6 system of equations are given in Appendix A.6.

Following Refs. (43) and (44), first consider the spatial discretization for a conservative scalar equation of the form

$$\frac{du}{dt} + \frac{df(u)}{dx} = 0 \tag{2.29}$$

and assume a positive flux gradient with respect to the advective term, $\partial f(u)/\partial u \geq 0$: a positive wind direction. Defining the domain X and number of points n, $dx \approx \Delta x =$

X/n. An approximation $u_j(t)$ to the exact solution $u(x_j,t)$ with $f_j = f(u_j(t))$ satisfies

$$\frac{du_j(t)}{dt} + \frac{\hat{f}_{j+1/2} - \hat{f}_{j-1/2}}{\Delta x} = 0\,. \tag{2.30}$$

The numerical flux $\hat{f}_{j+1/2}$ for the third-order WENO scheme is

$$\hat{f}_{j+1/2} = \omega_1\,\hat{f}^{(1)}_{j+1/2} + \omega_2\,\hat{f}^{(2)}_{j+1/2}\,. \tag{2.31}$$

For cases with a positive wind direction, the stencils for the fluxes in Eq. (2.31) are biased to the left and are given by

$$\hat{f}^{(1)}_{j+1/2} = -\frac{1}{2}f_{j-1} + \frac{3}{2}f_j\;, \quad \hat{f}^{(2)}_{j+1/2} = -\frac{1}{2}f_j + \frac{3}{2}f_{j+1} \tag{2.32}$$

with the *nonlinear* weights

$$\omega_m = \frac{\widetilde{\omega}_m}{\sum_{n=1}^{2}\widetilde{\omega}_n}\;, \quad \widetilde{\omega}_n = \frac{\gamma_n}{(\epsilon+\beta_n)^2}\,. \tag{2.33}$$

In Eq. (2.33), the *linear* weights are

$$\gamma_1 = \frac{1}{3}\;, \quad \gamma_2 = \frac{2}{3} \tag{2.34}$$

and the smoothness indicators are

$$\beta_1 = (f_j - f_{j-1})^2\;, \quad \beta_2 = (f_{j+1} - f_j)^2\,. \tag{2.35}$$

The parameter $\epsilon = 10^{-6}$ in Eq (2.33) ensures that the denominator in the nonlinear weights does not equal zero. For cases with a negative wind direction, $\partial f(u)/\partial u \geq 0$, the numerical flux $\hat{f}_{j+1/2}$ is calculated in the exact mirror image with respect to $x_{j+1/2}$ and the stencils are biased to the right. If $\partial f(u)/\partial u$ changes sign, smooth flux

splitting is used: $f(u) = f^+(u) + f^-(u)$, where $\partial f^+(u)/\partial u \geq 0$ and $\partial f^-(u)/\partial u \leq 0$. The numerical flux is constructed using Lax–Friedrichs flux splitting in the present studies:

$$f^{\pm}(u) = \frac{f(u) + \alpha\, u}{2}\,, \quad \alpha = max_u \left| \frac{\partial f}{\partial u} \right| . \tag{2.36}$$

An explicit third-order TVD Runge–Kutta method is used for the time-evolution:

$$u^{(1)} = u^n + \Delta t\, L(u^n, t^n)\,, \tag{2.37a}$$

$$u^{(2)} = \frac{3}{4}\, u^n + \frac{1}{4}\, u^{(1)} + \frac{1}{4}\, \Delta t\, L(u^{(1)}, t^n + \Delta t)\,, \tag{2.37b}$$

$$u^{(n+1)} = \frac{1}{3}\, u^n + \frac{2}{3}\, u^{(2)} + \frac{2}{3}\, \Delta t\, L(u^{(2)}, t^n + \frac{1}{2}\Delta t)\,, \tag{2.37c}$$

where, L approximates the spatial derivatives $L(u,t) \approx -\partial f(u)/\partial x$.

The Courant-limited timestep determination for the RANS model with mixture molecular, thermodynamic, and turbulent terms is

$$\Delta t_{RANS} = \beta_{CFL}\, \frac{\Delta x}{\sqrt{(|\widetilde{v}| + c_s)^{\,2} + \Omega/(\Delta x)^{\,2}}}\,, \tag{2.38a}$$

$$\Omega = \left(\frac{\overline{\mu}}{\overline{\rho}} + \frac{\nu_T}{\sigma_K} \right)^2 + \left(\frac{\overline{\mu}}{\overline{\rho}} + \frac{\nu_T}{\sigma_\epsilon} \right)^2 + \left(\overline{D} + \frac{\nu_T}{\sigma_m} \right)^2 + \left(\overline{\kappa} + \frac{\nu_T}{\sigma_U} \right)^2 . \tag{2.38b}$$

For the Euler equations, the timestep condition reduces to

$$\Delta t_{Euler} = \beta_{CFL}\, \frac{\Delta x}{|\widetilde{v}| + c_s}\,. \tag{2.39}$$

A CFL number $\beta_{CFL} = 0.2$ is used for all simulations.

All first and second spatial derivatives are calculated using centered second-order accurate WENO derivatives. Although higher-order flux reconstruction is less dissipative and has greater resolving power than lower-order reconstruction (16), the present investigation considers third-order reconstruction, which is a good compromise for

solving the RANS equations. Good agreement is nevertheless obtained with experimental data and with the analytical self-similar solution prior to reshock. Shock-detection is not used to activate the turbulent production terms [the first terms on the right sides of Eqs. (2.13) and (2.14)] when a shock is present locally. No limiters (25) are imposed on the turbulent production terms or on any other terms in the discretized equations.

The velocity satisfied a reflecting boundary condition at the endwall of the test section, and the computational domain was chosen large enough to allow the mixing layers to evolve without waves traveling back from the left boundary and interacting with the interface. The computational grid was uniformly spaced in x, and the initial interface between the gases were sharp.

CHAPTER III

Application of the K–ϵ Model to the Vetter–Sturtevant and Poggi–Thorembey–Rodriguez Experiments

An essential component of establishing and building confidence in a RANS model is to compare its predictions with experimental, theoretical, and numerical results. However, as discussed in Chapter I, shock tube experimental measurements for Atwood numbers different from $At = \pm 0.67$ or incident shock Mach numbers greater than $Ma_s \approx 2.00$ are sparse. Theoretical models typically have a limited range of validity and may contain many simplifying assumptions. Comparisons with numerical results also present challenges as RANS, LES, and DNS simulations vary in grid resolution, initial conditions, numerical method, and other parameter settings. Another component of establishing confidence in model predictions is convergence investigations, which can include spatial and temporal refinement. This topic is often neglected in many turbulence-related investigations, as it is computationally expensive for three-dimensional simulations.

This chapter presents the application of the K–ϵ model described in Chapter II to four different air–SF_6 reshocked Richtmyer–Meshkov instability cases over a range of incident shock Mach numbers with Atwood numbers $At = \pm 0.67$. In the

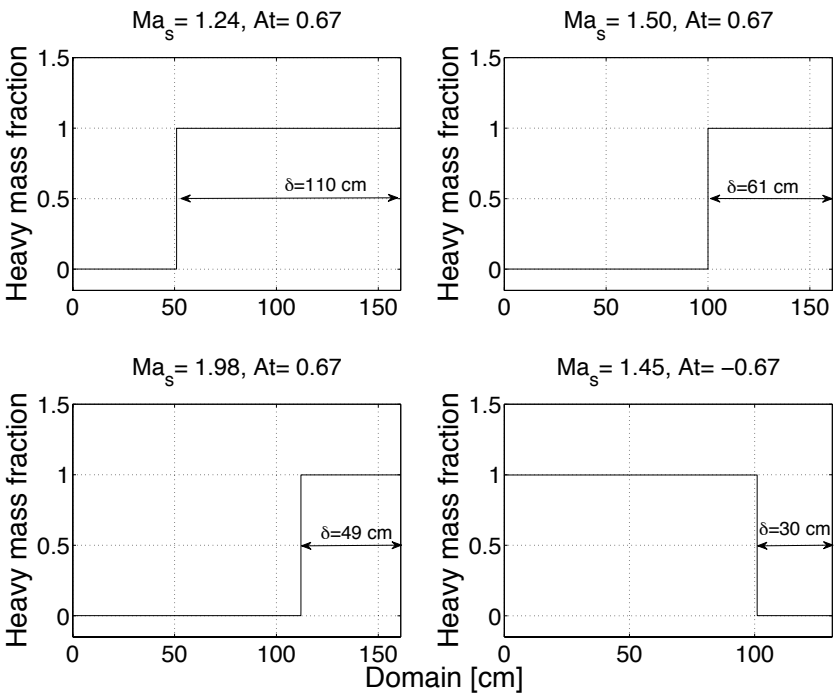

Ma_s		1.24	1.50	1.98	1.45
At		0.67	0.67	0.67	-0.67
δ	cm	110	61	49	30
X	cm	161	161	161	131
t_{end}	$\times 10^{-3}$ s	17	5.6	2.6	2.2

Figure 3.1: Mean heavy mass fractions, test section lengths δ, domain lengths X, and simulation times, t_{end}, for the $At = 0.67$ Vetter–Sturtevant (10) and $At = -0.67$ Poggi *et al.* (11) experiments.

light-to-heavy initial shock transition, where $At = 0.67$, mixing layer widths are compared with experimental data points for shock Mach numbers $Ma_s = 1.24$, 1.50, and 1.98 with test section lengths $\delta = 110$, 61, and 49 cm (10), respectively, and domain $X = 161$ cm. In the reversal of the gas order having $At = -0.67$, results are compared with data for $Ma_s = 1.45$ with $\delta = 30$ cm (11) and domain $X = 131$ cm. Comparisons are also made with BHR turbulence model predictions (29) and LES data (15). The K–ϵ model predictions are also compared to the power-law self-similar solution Eq. (2.27) prior to reshock. Parametric studies are performed to evaluate the sensitivity of the predictions to changes in model coefficients and initial conditions,

together with turbulent budget evaluations. Convergence under grid refinement of the mixing layer width and mean and turbulent fields is also considered. Ideally, it is desired to only modify initial conditions for the turbulent kinetic energy seed, K_0, and the initial perturbation wavelength, λ_{rms}, to establish a model applicable to various shock Mach numbers, Atwood numbers, and test section lengths. A general set of coefficients is established that predicts results agreeing well with experimental measurements of the mixing layer widths. An optimal set of model coefficients used throughout these studies are Eq. (2.21), $\sigma_\rho = 0.90$, and $C_{\epsilon 0} = 0.90$ in the K and ϵ buoyancy production terms.

3.1 $Ma_s = 1.24$: Model Sensitivity to the Turbulent Kinetic Energy Seed

Effects due to variations in the turbulent kinetic energy seed, K_0, are considered in the $Ma_s = 1.24$ study. Reshock and arrival of the expansion wave occur at $\tau_R \approx 9.25$ and $\tau_E \approx 14.70$ ms, respectively. Referring to Chapter II, this initial condition determines the percentage of *mean* kinetic energy used in initializing the *turbulent* kinetic energy. Figure 3.2 shows the sensitivity of the mixing layer width to variations in K_0 from 0.1 to 0.001. The turbulent kinetic energy seed affects turbulent mixing before and after reshock. In comparing the K–ϵ model results with experimental measurements, it is found that $K_0 = 0.01$ provides best agreement with the data. The BHR model (29) agrees well with the early-time mixing but predicts lower turbulent mixing after reshock. In comparison, LES (15) predicts larger mixing early, but provides better agreement with data following reshock. Note the order of magnitude difference in the spatial discretization between LES and RANS, $\Delta x_{LES}/\Delta x_{RANS} = 10.5$.

In evaluating the K–ϵ model predictions prior to reshock, larger values of K_0

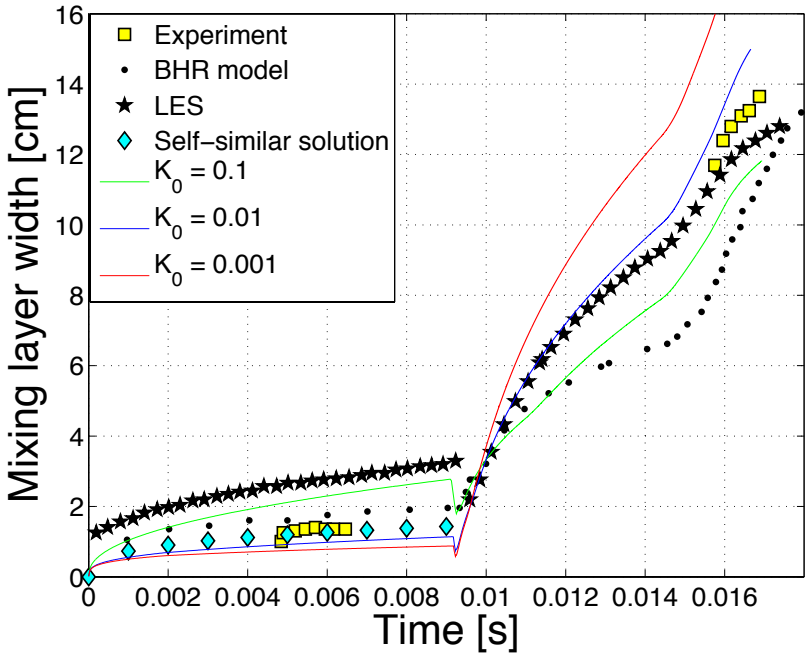

Figure 3.2: Converged mixing layer widths for $Ma_s = 1.24$, $At = 0.67$, $K_0 = 0.10$, 0.01, and 0.001, $\lambda_{rms} = 1.00$ cm, $\sigma_\rho = 0.90$, $C_{\epsilon 0} = 0.90$, and $n = 9600$ with $\Delta x = 0.02$ cm. The experimental data are from Ref. (10), the BHR results are from Ref. (29), the LES data with $\Delta x = 0.21$ cm are from (15), and the self-similar solution is from Eq. (2.27).

result in larger widths as more turbulent kinetic energy is available for early-time mixing. Differences in widths are more apparent between $K_0 = 0.1$ and 0.01 in comparison between $K_0 = 0.01$ and 0.001. Additionally, larger values of K_0 result in stronger compression of the gas interface during reshock. This indicates the relative energy expended in compressing the gases for each K_0 value. As more energy is deposited during compression, more turbulent kinetic energy is dissipated into heat as the shock passes through the mixing layer, leading to reduced turbulent mixing later. For example, using $K_0 = 0.1$ introduces more turbulent kinetic energy for early mixing and compresses the gas interface to a higher degree, but there is less turbulent mixing after reshock. In comparison, using $K_0 = 0.001$ leads to a smaller width and the shock compresses the layer to a lesser extent, but mixing continues at a higher rate following reshock. After the arrival of the expansion wave at $t \approx 15$ ms, which is

indicated by the change in the width curvature, additional turbulent kinetic energy is introduced principally through buoyancy production, which is spread by the diffusive term during turbulent mixing.

To further investigate the effects of K_0 variations on the turbulent kinetic energy production terms, the buoyancy production $-\overline{v_j''}\,\partial\overline{p}/\partial x_j$ and shear production $-\tau_{ij}\,\partial\widetilde{v}_i/\partial x_j = (2/3)\,\overline{\rho}\,K\partial\widetilde{v}_j/\partial x_j$ are considered at $t = 5$, 10, and 15 ms, corresponding to times before and after reshock, and in the proximity of the expansion wave, respectively (see Fig. 3.2). Figures 3.3 and 3.4 illustrate the evolution of the K buoyancy and shear production terms at these times. At $t = 5.00$ ms the shock is traveling towards the test section endwall, where it is evident that $K_0 = 0.1$ generates the most mixing at early times; both production mechanisms for $K_0 = 0.01$ and 0.001 are negligible in comparison. Furthermore, the production mechanisms are strongest in the vicinity of the shock with larger contributions from the buoyancy production by approximately one order of magnitude. Shortly after reshock at $t = 10$ ms, the shock in the $K_0 = 0.1$ case is traveling ≈ 1 cm ahead of the shocks in the $K_0 = 0.01$ and $K_0 = 0.001$ cases, as larger K_0 values result in larger turbulent pressures, and therefore larger sounds speeds. Due to the smaller compressions accompanying smaller K_0 values, less energy is dissipated into heat during reshock, and more turbulent mixing is observed for the cases with $K_0 = 0.01$ and 0.001. Approximately 5 ms after reshock at $t = 15$ ms, the expansion wave introduces additional turbulent kinetic energy via buoyancy production, as seen in the bottom plot of Fig. 3.3. From 10 to 15 ms, the mixing layer generated with $K_0 = 0.1$ has experienced more dissipation in comparison to the other two cases and demonstrates less mixing at later times, despite the contribution from the expansion wave. As the shear production is not augmented by the arrival of the expansion wave, the effects of dissipation are more apparent in the bottom plot of Fig. 3.4.

Figure 3.5 illustrates the evolution of the dissipation rate, $-\overline{\rho}\,\epsilon$, at the same times.

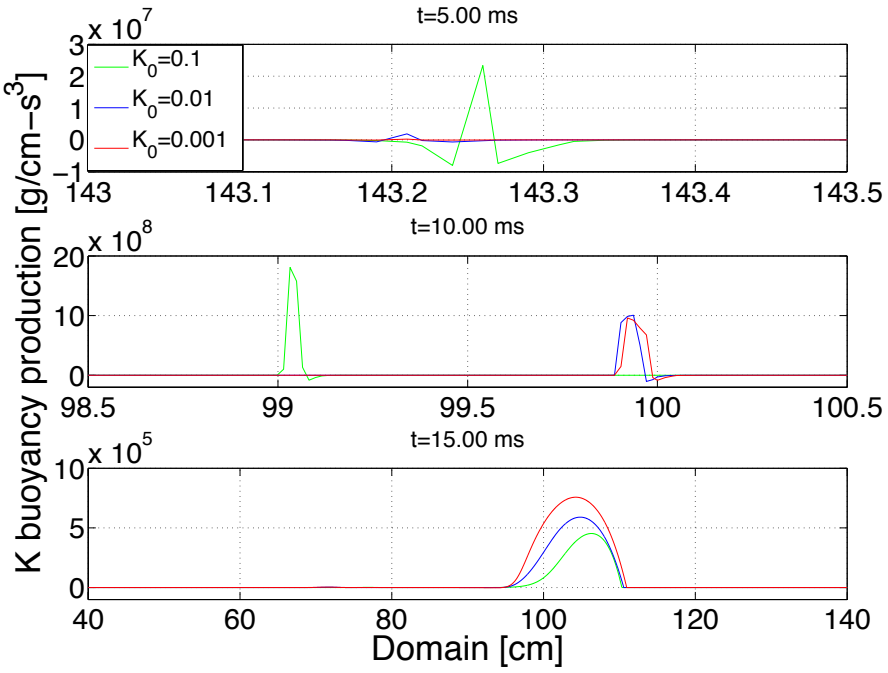

Figure 3.3: Evolution of turbulent kinetic energy buoyancy production for $Ma_s = 1.24$, $At = 0.67$, $K_0 = 0.1$, 0.01, and 0.001, $\lambda_{rms} = 1.00$ cm, $\sigma_\rho = 0.90$, $C_{\epsilon 0} = 0.90$, and $n = 9600$ with $\Delta x = 0.02$ cm.

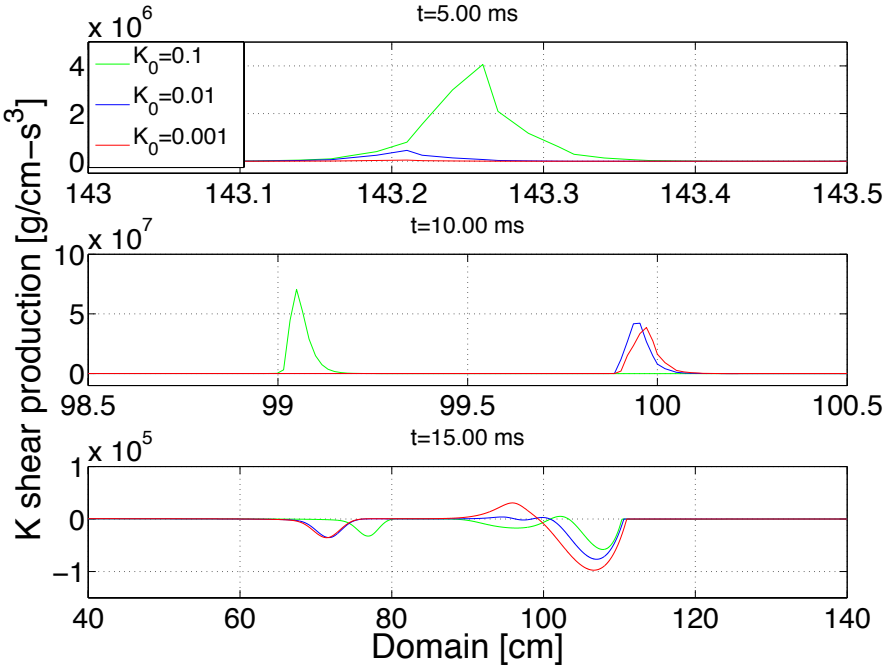

Figure 3.4: Evolution of turbulent kinetic energy shear production for $Ma_s = 1.24$, $At = 0.67$, $K_0 = 0.1$, 0.01, and 0.001, $\lambda_{rms} = 1.00$ cm, $\sigma_\rho = 0.90$, $C_{\epsilon 0} = 0.90$, and $n = 9600$ with $\Delta x = 0.02$ cm.

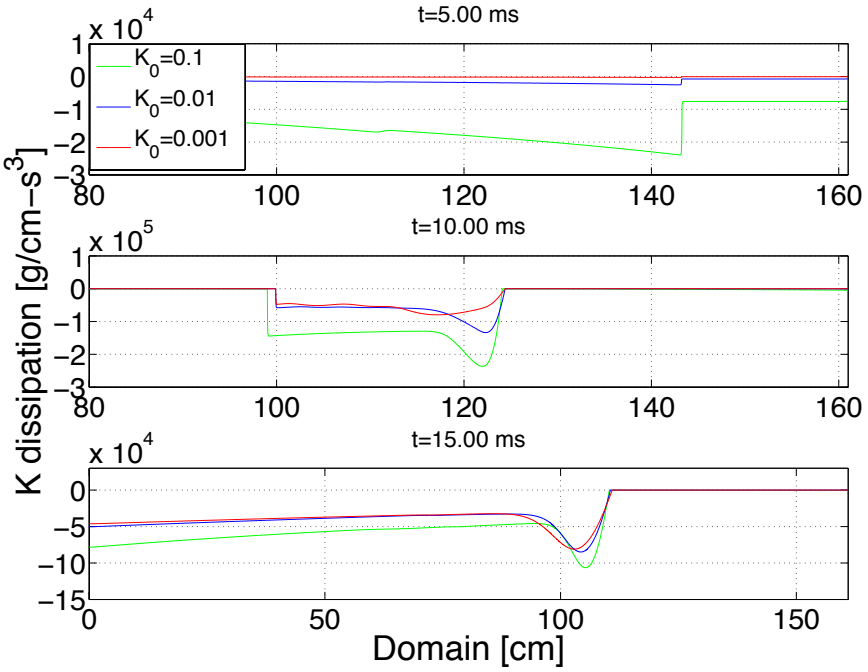

Figure 3.5: Evolution of turbulent kinetic energy dissipation for $Ma_s = 1.24$, $At = 0.67$, $K_0 = 0.1$, 0.01, and 0.001, $\lambda_{rms} = 1.00$ cm, $\sigma_\rho = 0.90$, $C_{\epsilon 0} = 0.90$, and $n = 9600$ with $\Delta x = 0.02$ cm.

Before reshock, the flow with $K_0 = 0.1$ is more susceptible to dissipation, while the $K_0 = 0.01$ and 0.001 cases exhibit smaller dissipative losses because the initial condition $\epsilon(x, 0)$ is proportional to $K(x, 0)$, and increases in K_0 also lead to larger dissipation. The top plot in Fig. 3.5 shows that dissipation is largest at the shock front and gradually decays behind the shock. Strong dissipative effects are still evident at the shock front after reshock at $t = 10$ ms, but dissipation also occurs in the mixing layer as the reflected wave travels towards the test section endwall. The dissipation is reduced by approximately one order of magnitude at $t = 15$ ms as the expansion wave introduces additional turbulent kinetic energy for mixing.

Turbulent kinetic energy diffusion, $\frac{\partial}{\partial x_j}\left[\left(\overline{\mu} + \frac{\mu_t}{\sigma_K}\right)\frac{\partial K}{\partial x_j}\right]$, is also considered and illustrated in Fig. 3.6. As with the production and dissipation mechanisms just discussed, diffusion is also largest for $K_0 = 0.1$. Prior to reshock, diffusive effects at smaller values of K_0 are negligible in comparison to the $K = 0.1$ case. Following reshock,

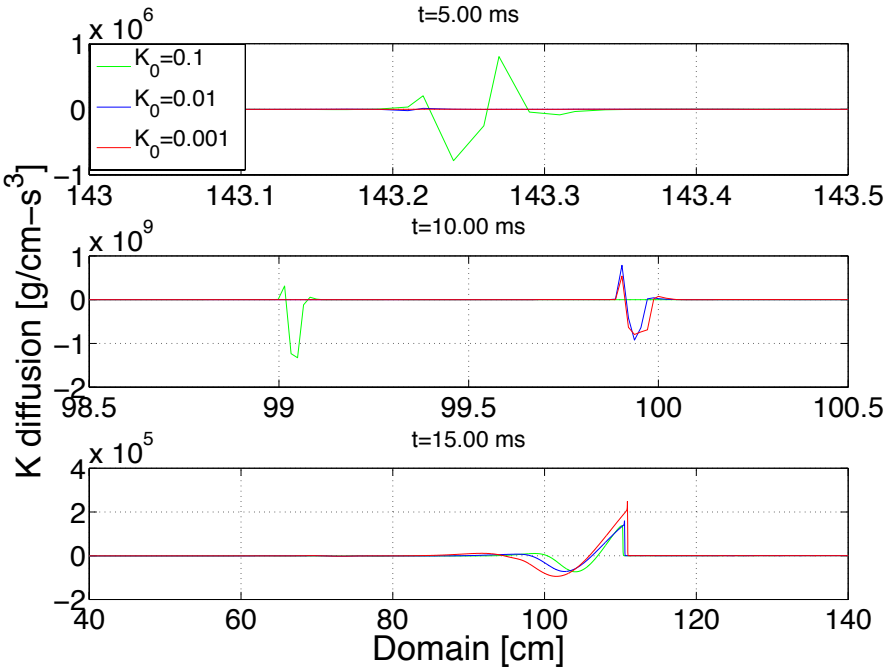

Figure 3.6: Evolution of turbulent kinetic energy diffusion for $Ma_s = 1.24$, $At = 0.67$, $K_0 = 0.1$, 0.01, and 0.001, $\lambda_{rms} = 1.00$ cm, $\sigma_\rho = 0.90$, $C_{\epsilon 0} = 0.90$, and $n = 9600$ with $\Delta x = 0.017$ cm.

diffusive effects increase in magnitude because buoyancy production increases the supply of turbulent kinetic energy for mixing. Diffusion of turbulent kinetic energy from the arrival of the expansion wave is weakly dependent on the initial condition, K_0, as shown by the similar diffusion profiles for the three K_0 values in Fig. 3.6: the arrival of the expansion wave results in an increase in turbulent kinetic energy due to changes in pressure and density, which principally affect the buoyancy production, and minimally affect the shear production. Conversely, the value of K_0 principally affects the shear production.

Figures 3.7–3.9 show the corresponding turbulent kinetic energy dissipation rate buoyancy production $-C_{\epsilon 0}(\epsilon/K)\ \overline{v_j''}\,\partial\overline{p}/\partial x_j$, shear production $-(2/3)\,C_{\epsilon 3}\,\overline{\rho}\,\epsilon\,\partial\widetilde{v}_j/\partial x_j$, dissipation $-C_{\epsilon 2}\,\overline{\rho}\,\epsilon^2/K$, and diffusion $\frac{\partial}{\partial x_j}\left[\left(\overline{\mu}+\frac{\mu_t}{\sigma_\epsilon}\right)\frac{\partial \epsilon}{\partial x_j}\right]$. These terms are qualitatively similar to those in Figs. 3.3–3.5 (recall that the turbulent kinetic energy dissipation rate is proportional to the turbulent kinetic energy). The difference in

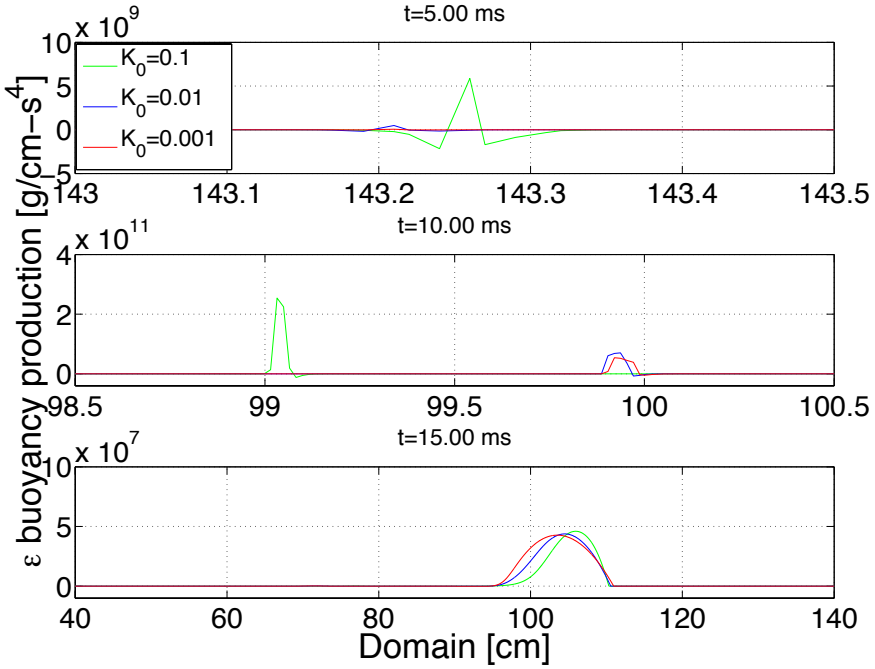

Figure 3.7: Buoyancy production of turbulent kinetic energy dissipation rate for $Ma_s = 1.24$, $At = 0.67$, $K_0 = 0.1$, 0.01, and 0.001, $\lambda_{rms} = 1.00$ cm, $\sigma_\rho = 0.90$, $C_{\epsilon 0} = 0.90$, and $n = 9600$ with $\Delta x = 0.02$ cm.

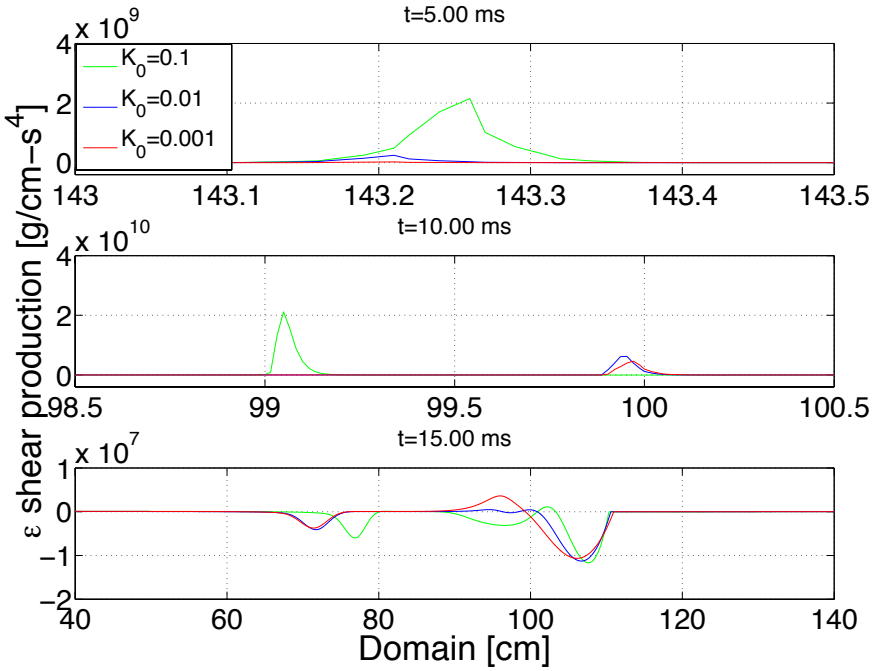

Figure 3.8: Shear production of turbulent kinetic energy dissipation rate for $Ma_s = 1.24$, $At = 0.67$, $K_0 = 0.1$, 0.01, and 0.001, $\lambda_{rms} = 1.00$ cm, $\sigma_\rho = 0.90$, $C_{\epsilon 0} = 0.90$, and $n = 9600$ with $\Delta x = 0.02$ cm.

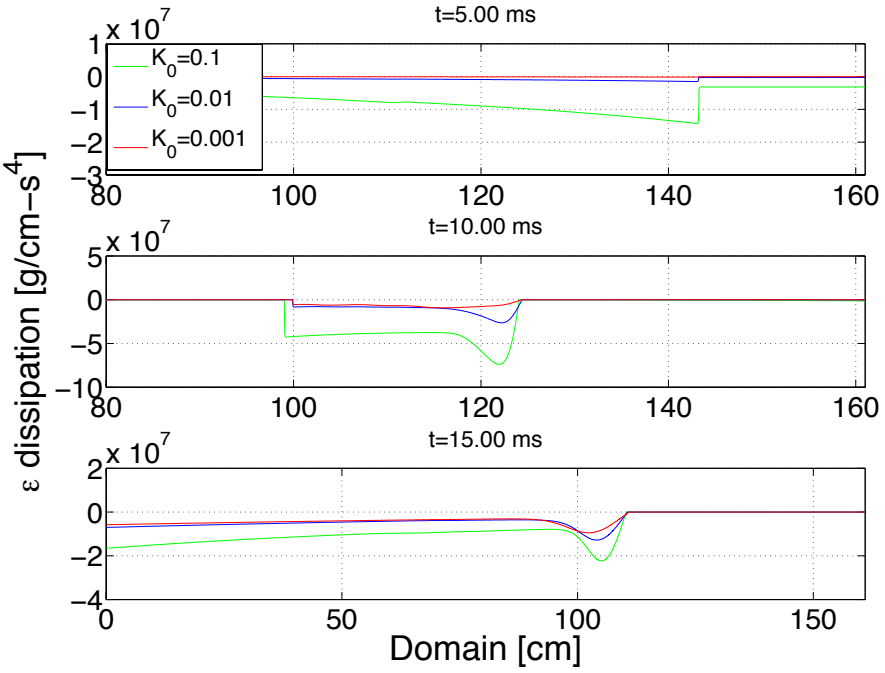

Figure 3.9: Dissipation of turbulent kinetic energy dissipation rate for $Ma_s = 1.24$, $At = 0.67$, $K_0 = 0.1$, 0.01, and 0.001, $\lambda_{rms} = 1.00$ cm, $\sigma_\rho = 0.90$, $C_{\epsilon 0} = 0.90$, and $n = 9600$ with $\Delta x = 0.02$ cm.

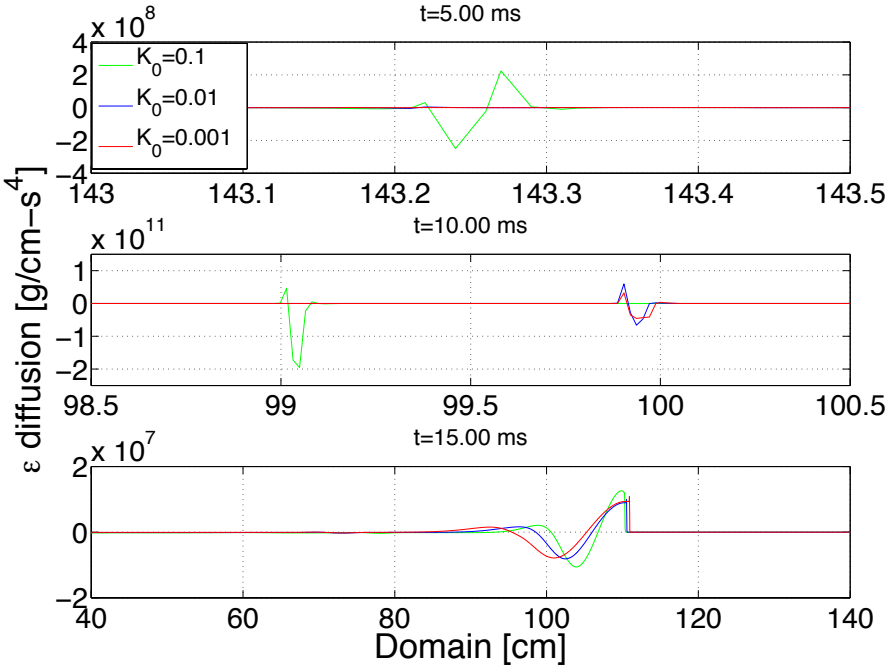

Figure 3.10: Diffusion of turbulent kinetic energy dissipation rate for $Ma_s = 1.24$, $At = 0.67$, $K_0 = 0.1$, 0.01, and 0.001, $\lambda_{rms} = 1.00$ cm, $\sigma_\rho = 0.90$, $C_{\epsilon 0} = 0.90$, and $n = 9600$ with $\Delta x = 0.02$ cm.

magnitudes is also due to the proportionality between K and ϵ.

3.2 $Ma_s = 1.50$: Effects of Shock Mach Number Variations on Turbulent Mixing

The $Ma_s = 1.50$ parametric study evaluates the effects on turbulent mixing due to variations in the incident shock Mach number, Ma_s, which indicates the speed with which the shock travels relative to the speed of sound. This investigation considers small parametric deviations, $Ma_s = 1.50 \pm 0.05$, corresponding to $\pm 3\%$ variation from 1.50. This variation is analogous to experimental uncertainty in the shock Mach number.

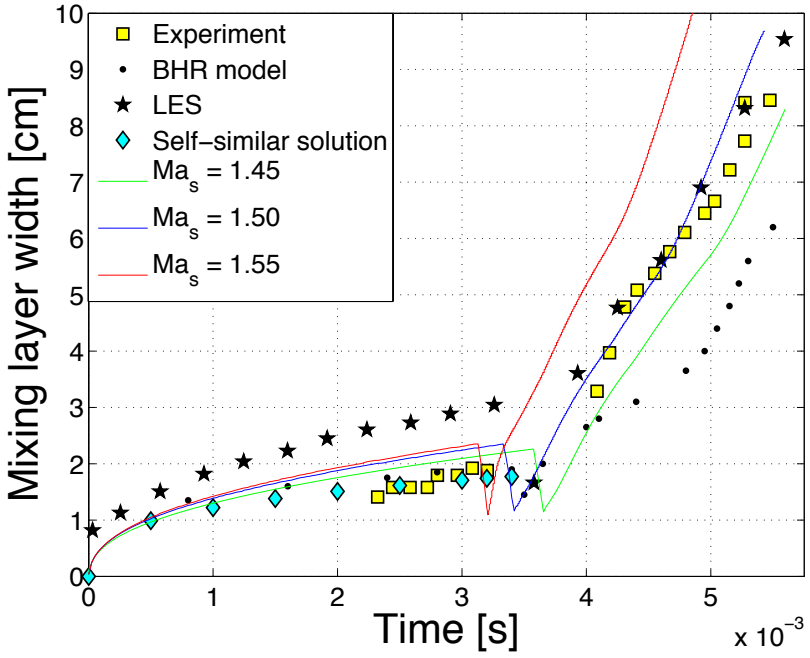

Figure 3.11: Mixing layer widths for $Ma_s = 1.45$, 1.50, and 1.55, $At = 0.67$, $K_0 = 0.10$, $\lambda_{rms} = 1.00$ cm, $\sigma_\rho = 0.90$, $C_{\epsilon 0} = 0.90$, and $n = 7200$ with $\Delta x = 0.02$ cm. The experimental data are from Ref. (10), the BHR results are from Ref. (29), the LES data with $\Delta x = 0.21$ cm are from (15), and the self-similar solution is from Eq. (2.27).

Figure 3.11 illustrates mixing layer width evolutions resulting from incident shocks

with, $Ma_s = 1.45$, 1.50 and 1.55, where experimental data for $Ma_s = 1.50$ (10) are included for comparison; results using $Ma_s = 1.45$ and 1.55 are not expected to agree with the experiment as these values deviate from the prescribed experimental value. The K–ϵ model overpredicts the experimental and self-similar amplitudes at early times by a small amount. After reshock, the model predictions agree well with experimental data for $Ma_s = 1.50$. The BHR model (29) agrees well with the data and self-similar solution prior to reshock. However, this three-equation RANS model predicts less turbulent mixing after reshock. Similarly, LES (15) demonstrates a deviation prior to reshock but predicts good agreement after reshock similar to the K–ϵ model predictions.

The early mixing prior to reshock is considered first in the current parametric investigation: small changes in shock Mach number have minimal influence on the mixing evolution as seen in the small differences in the early-time widths between cases. It was demonstrated in Sec. 3.1 that early mixing is influenced by the initial condition, K_0. Although effects due to changes in Ma_s are less notable, similar effects are evident: as Ma_s increases from 1.45 to 1.55, additional turbulence is introduced at early times and amplifies the mixing.

At the shock compression stage, a change in the time of reshock is also observed for the three different Ma_s values, which occurs at $\tau_R \approx 3.67$, 3.42 and 3.20 ms for $Ma_s = 1.45$, 1.50 and 1.55, respectively. The difference in reshock times can be explained by noting that as Ma_s increases, the shock speed correspondingly increases. Therefore, the shock reflects from the test section endwall at an earlier time and impacts the interface sooner.

Impulsively accelerating the gases with a stronger shock also impacts the evolution of the mixing layer to some extent after reshock. The approximate mixing layer growth rates following reshock are $\dot{h} = 3200$, 3820, and 4360 cm/s for $Ma_s = 1.45$ and 1.50, and 1.55, respectively (see Fig. 3.12). These differences in growth rate are

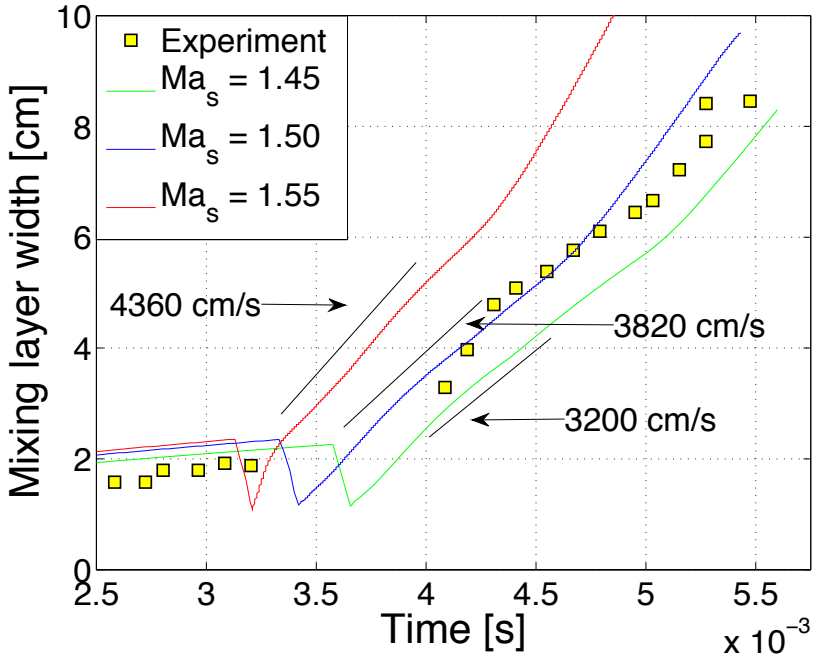

Figure 3.12: Approximate mixing layer growth rates for $Ma_s = 1.45$, 1.50, and 1.55, $At = 0.67$, $K_0 = 0.10$, $\lambda_{rms} = 1.00$ cm, $\sigma_\rho = 0.90$, $C_{\epsilon 0} = 0.90$, and $n = 7200$ with $\Delta x = 0.02$ cm. The experimental data are from Ref. (10).

$\approx 16\%$ and $\approx 12\%$ differences as Ma_s increases. Similar to mixing at early times, the production and dissipation terms following reshock demonstrate higher sensitivity to variations in shock Mach number as a more rapid evolution of gas mixing is observed for stronger shocks.

To further elucidate the effects of the Ma_s variations, the evolution of turbulence mechanisms is also considered in Figs. 3.13 and 3.14, which show the buoyancy and shear production, diffusion, and dissipation terms at $t = 2.00$ and 4.00 ms. These figures illustrate the relative turbulence intensity for each of the shock Mach number cases before and after reshock. Figure 3.13 compares contributions from the buoyancy production and turbulent kinetic energy diffusion. At $t = 2.00$ ms, the shock is traveling in the direction of the test section endwall and has not yet reflected. The strongest shock has traveled a farther distance and is more energetic. Although the buoyancy production typically has a secondary role in early mixing, the increase in

turbulent pressure $p_T = (2/3)\overline{\rho}\,K$ from larger turbulent kinetic energy as a result of larger Ma_s values (and shock speeds) increases the magnitude of this term. At $t = 4.00$ ms, the three cases have undergone reshock and are progressing to the left. The increase in magnitude and localizations in the vicinity of the shock indicate the increase in turbulent mixing due to reshock.

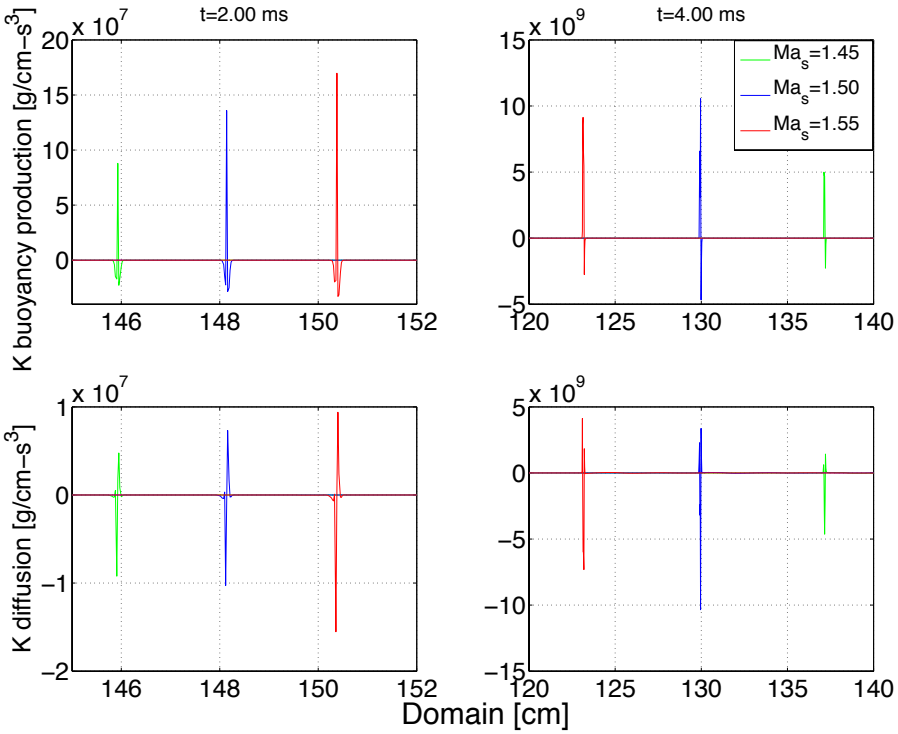

Figure 3.13: Turbulent kinetic energy buoyancy production and diffusion terms [g/cm-s^3] at $t = 2.00$ and 4.00 ms for $Ma_s = 1.45$, 1.50, and 1.55, $At = 0.67$, $K_0 = 0.10$, $\lambda_{rms} = 1.00$ cm, $\sigma_\rho = 0.90$, and $C_{\epsilon 0} = 0.90$.

The turbulent kinetic energy shear production and dissipation terms are presented in Fig. 3.14. Like the buoyancy production, the shear production becomes larger with increasing Ma_s values due to the higher turbulent pressure. After reshock, the shear production has a secondary role in turbulent mixing as the rate of generating turbulent kinetic energy is approximately one order of magnitude lower than the buoyancy production. The dissipation of turbulent kinetic energy is strongest at the shock front prior to reshock and rapidly decays as the shock heats the gas. The domain

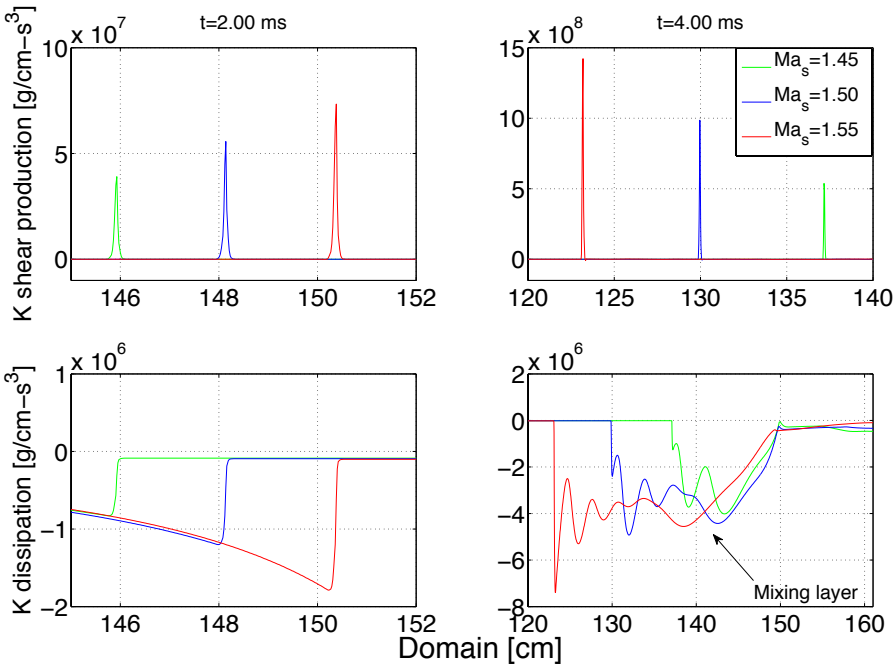

Figure 3.14: Turbulent kinetic energy shear production and dissipation terms [g/cm-s^3] at $t = 2.00$ and 4.00 ms for $Ma_s = 1.45$, 1.50, and 1.55, $At = 0.67$, $K_0 = 0.10$, $\lambda_{rms} = 1.00$ cm, $\sigma_\rho = 0.90$, and $C_{\epsilon 0} = 0.90$.

for the dissipation term after reshock is extended to show that although dissipative effects are still large behind the shock, dissipation of turbulent kinetic energy is also strong in the mixing layer after it is compressed and the mixing is enhanced, as is seen in the behavior behind the shock.

Corresponding plots for the turbulent kinetic energy dissipation rate are provided in Figs. 3.15 and 3.16; similar behavior is observed as in Figs. 3.13 and 3.14 for the turbulent kinetic energy. Therefore, to better compare the magnitudes and behavior between production terms, the buoyancy and shear production are plotted together in Fig. 3.15. The dissipation and diffusion terms are shown in Fig. 3.16.

To further explain the behavior and evolution of the turbulent budgets, the $Ma_s = 1.55$ and 1.50 cases are investigated together at $t = 3.25$ ms (see Fig. 3.17). At this time the shock in the former case has just reshocked the interface while the latter is approaching the interface for reshock. The transmitted and reflected waves

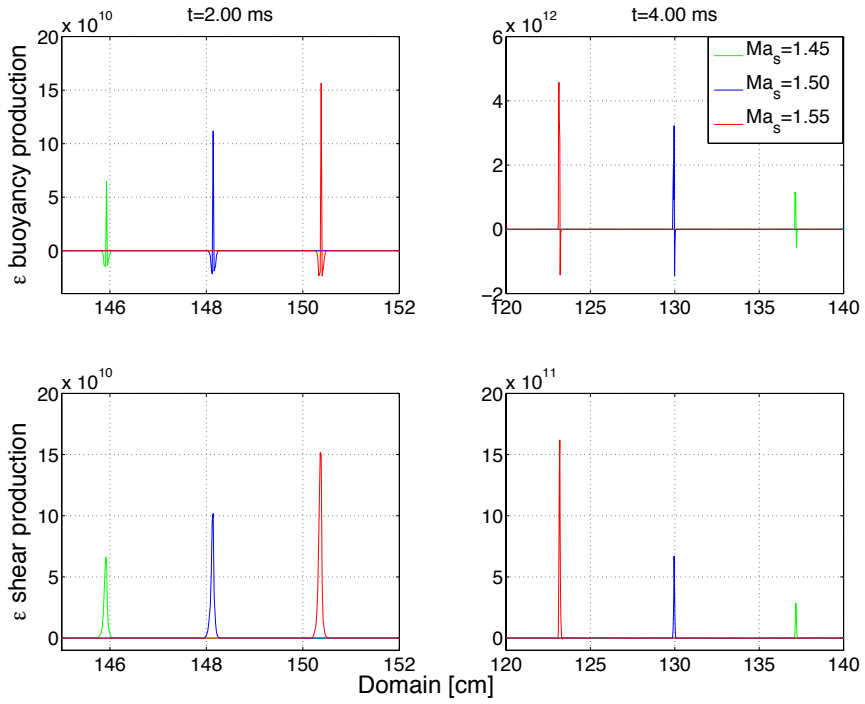

Figure 3.15: Turbulent kinetic energy dissipation rate buoyancy and shear production terms [g/cm-s^4] at $t = 2.00$ and 4.00 ms for $Ma_s = 1.45$, 1.50, and 1.55 with $At = 0.67$, $K_0 = 0.10$, $\lambda_{rms} = 1.00$ cm, $\sigma_\rho = 0.90$, and $C_{\epsilon 0} = 0.90$.

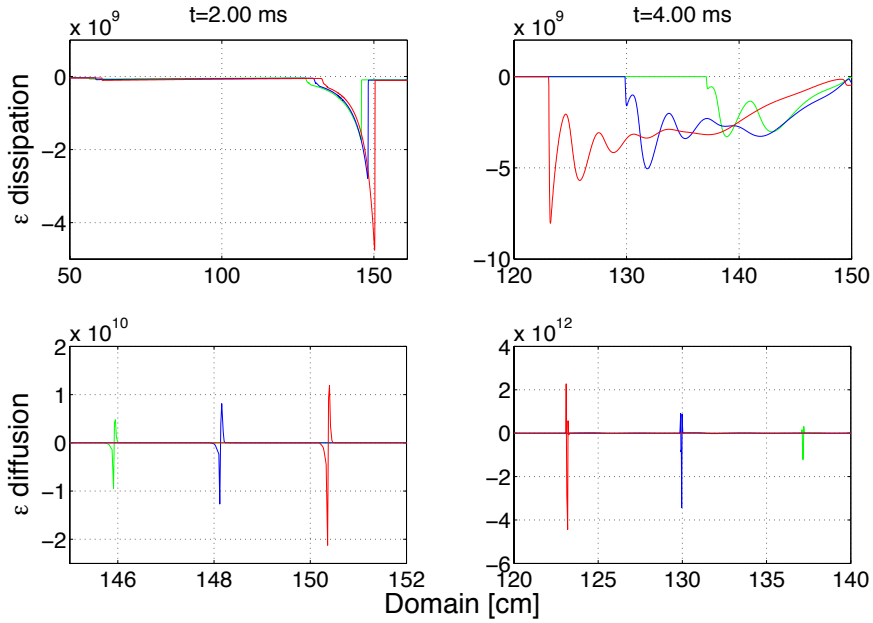

Figure 3.16: Turbulent kinetic energy dissipation rate dissipation and diffusion terms [g/cm-s^4] at $t = 2.00$ and 4.00 ms for $Ma_s = 1.45$, 1.50, and 1.55 with $At = 0.67$, $K_0 = 0.10$, $\lambda_{rms} = 1.00$ cm, $\sigma_\rho = 0.90$, and $C_{\epsilon 0} = 0.90$.

resulting from the $Ma_s = 1.55$ reshock are evident by the buoyancy production spikes and diffusion terms as the mixing evolves. The bottom plot in the figure minimizes the range to better see the structure of the reflected and transmitted waves. This also better visualizes contributions from the shear production, which are small in comparison to diffusion and buoyancy production; dissipation is relatively small. There is a significant increase of turbulent mixing due to reshock. The comparable mixing layer widths from the $Ma_s = 1.50$ and 1.55 cases before reshock in Figs. 3.11 and 3.12 show that early mixing is minimally affected by the incident shock Mach number. Thus, Fig. 3.17 illustrates the rapid increase of mixing due to the arrival of the shock. Finally, the mixing layer at this time is still undergoing shock compression, and further spreading of the mixing layer is occurring, as demonstrated by the buoyancy production and diffusion terms.

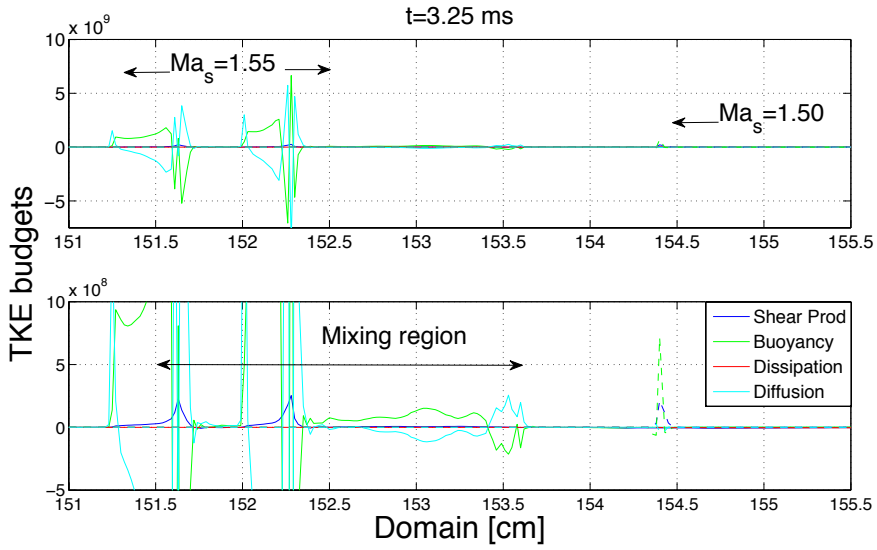

Figure 3.17: Turbulent kinetic energy budgets [g/cm-s^3] for $Ma_s = 1.50$ (dashed lines) and 1.55 (solid lines), $At = 0.67$, $K_0 = 0.10$, $\lambda_{rms} = 1.00$ cm, $\sigma_\rho = 0.90$, and $C_{\epsilon 0} = 0.90$.

Figure 3.18 shows the corresponding terms for the turbulent kinetic energy dissipation rate. Unlike the turbulent kinetic energy, where a significant difference is apparent before and after reshock for the buoyancy production, the dissipation rate

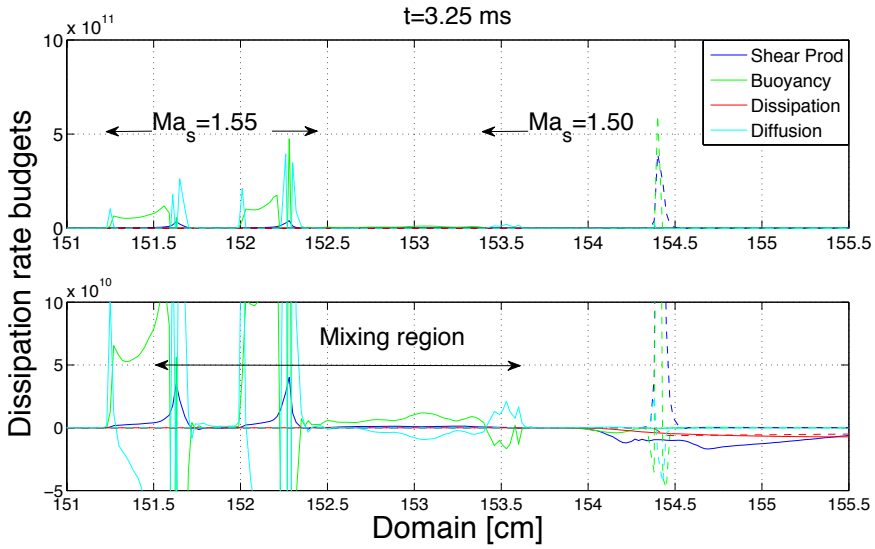

Figure 3.18: Turbulent kinetic energy dissipation rate budgets [g/cm-s^4] for $Ma_s = 1.50$ (dashed lines) and 1.55 (solid lines), $At = 0.67$, $K_0 = 0.10$, $\lambda_{rms} = 1.00$ cm, $\sigma_\rho = 0.90$, and $C_{\epsilon 0} = 0.90$.

terms maintain comparable contributions throughout, showing relatively constant dissipation. Diffusion makes similar contributions through the transmitted and reflected waves, while the shear production is larger prior to reshock because in compressing the mixing layer, some of the energy is dissipated and converted into heat. This can be seen starting at $x \approx 154$ cm, where the dissipation causes a sink in shear production. The budget has the same structure as in Fig. 3.17, with comparable contributions from buoyancy production and diffusion.

3.3 $Ma_s = 1.98$: Effects of Buoyancy Production on Turbulent Mixing

Sections 3.1 and 3.2 have discussed the effects on turbulent mixing due to variations in the initial conditions, K_0 and λ_{rms}, and the incident shock Mach number Ma_s; changes in these quantities influence production and dissipation mechanisms before and after reshock. In addition, the buoyancy production has a primary role in post-reshock mixing. This section focuses on the buoyancy production (pressure

work) mechanism to show how variations in this term affect turbulent mixing. As discussed in Chapter II, this term generates turbulence via pressure and density gradients and is a source that increases the turbulent viscosity, which increases diffusion of turbulent kinetic energy during mixing. Thus, changes in the buoyancy production model coefficients can strongly affect reshocked Richtmyer–Meshkov mixing predictions. The two model coefficients in these production terms found in Eqs. (2.3), (2.13), and (2.14) are σ_ρ and $C_{\epsilon 0}$. To elucidate the sensitivity of the K–ϵ model to changes in σ_ρ and $C_{\epsilon 0}$, parametric studies are performed for each of these coefficients.

3.3.1 Variations in σ_ρ

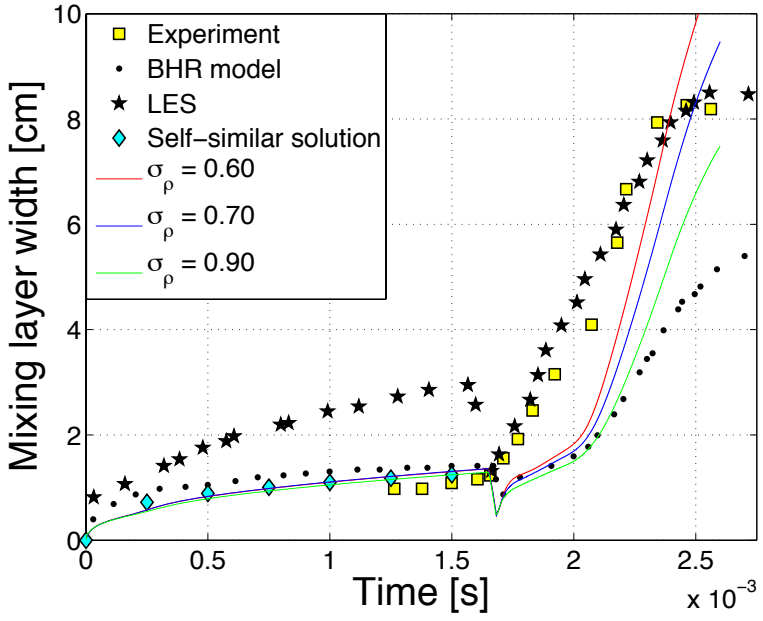

Figure 3.19: Mixing layer widths for $Ma_s = 1.98$, $At = 0.67$, $K_0 = 0.10$, $\lambda_{rms} = 0.50$ cm, $\sigma_\rho = 0.60$, 0.70, and 0.90, $C_{\epsilon 0} = 0.90$, and $n = 9600$ with $\Delta x = 0.02$ cm. The experimental data are from Ref. (10), the BHR results are from Ref. (29), the LES data with $\Delta x = 0.21$ cm are from (15), and the self-similar solution is from Eq. (2.27).

Figure 3.19 illustrates the sensitivity of the mixing layer width for $Ma_s = 1.98$ (with reshock time $\tau_R \approx 1.67$ ms) to changes in the coefficient values $\sigma_\rho = 0.60$, 0.70, and 0.90 with $C_{\epsilon 0} = 0.90$. The initial widths agree well with experimental data and

follow the $\approx t^{0.3}$ self-similar solution closely. Shortly after reshock, a small deviation can be observed from the experiment but more accurate predictions are achieved at later times, ≈ 0.50 ms after reshock. The BHR model (29) predicts a similar width prior to reshock but substantially underpredicts the mixing layer width after reshock. Conversely, LES (15) overpredicts the width at early times, but good agreement is established with experimental data following reshock. Figure 3.19 also indicates that variations in σ_ρ have minimal influence on model predictions for the early-time width, and that the shock compression strength and reshock time remain the same. Thus, unlike changes in K_0 and Ma_s resulting in different shock compression strengths and reshock times, respectively (see Secs. 3.1 and 3.2), σ_ρ does not influence these strengths and times.

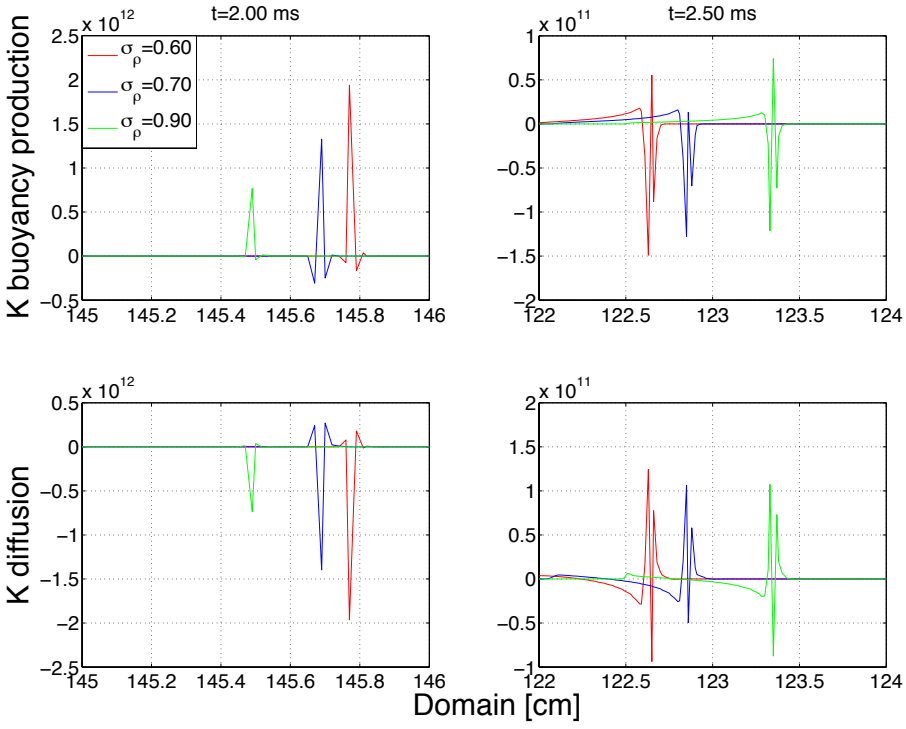

Figure 3.20: Turbulent kinetic energy buoyancy production and diffusion terms [g/cm-s^3] at $t = 2.00$ and 4.00 ms for $Ma_s = 1.98$, $At = 0.67$, $K_0 = 0.10$, $\lambda_{rms} = 0.50$ cm, $\sigma_\rho = 0.60$, 0.70, and 0.90, and $C_{\epsilon 0} = 0.90$.

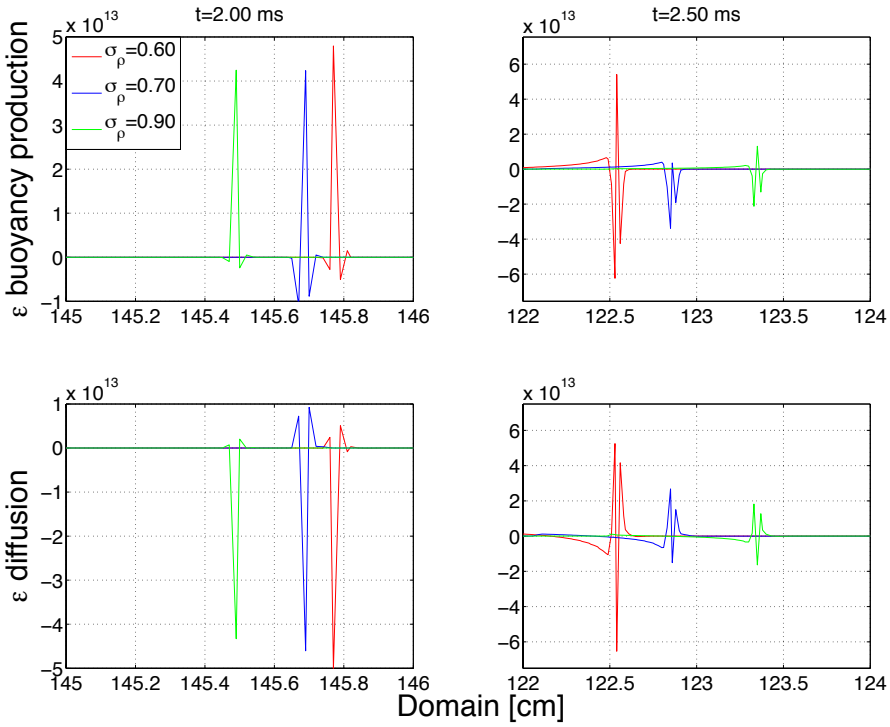

Figure 3.21: Turbulent kinetic energy dissipation rate buoyancy production and diffusion terms [g/cm-s^4] at $t = 2.00$ and 4.00 ms for $Ma_s = 1.98$, $At = 0.67$, $K_0 = 0.10$, $\lambda_{rms} = 0.50$ cm, $\sigma_\rho = 0.60$, 0.70, and 0.90, and $C_{\epsilon 0} = 0.90$.

However, effects due to changes in σ_ρ become more apparent following reshock. As σ_ρ decreases from 0.90 to 0.60, a corresponding growth in turbulent mixing via buoyancy production is observed. This coefficient appears reciprocally in the buoyancy production so that smaller σ_ρ values result in larger production of turbulent kinetic energy and its dissipation rate. Figures 3.20 and 3.21 illustrate the buoyancy production and diffusion terms for the turbulent kinetic energy and dissipation rate, respectively, at $t = 2.00$ and 2.50 ms, where the interface has been reshocked at $\tau_R \approx 1.67$ ms. Two observations can be made from Fig. 3.20. First, note the evolution of the buoyancy production along with the turbulent kinetic energy diffusion. At 2.00 ms, more turbulent kinetic energy is produced with smaller values of σ_ρ as indicated by the larger magnitudes of buoyancy production. As times progresses, turbulent mixing enhances (see Fig. 3.19) and the amount of turbulent kinetic en-

ergy reduces as noted by the decrease in magnitudes between $t = 2.00$ and 2.50 ms. Turbulent kinetic energy diffusion is plotted below the buoyancy production at the same times. Correspondingly, the rate at which turbulent kinetic energy is spread by the diffusion term grows as post-reshock mixing evolves. Moreover, more diffusion occurs for $\sigma_\rho = 0.60$ due to the larger amount of turbulent kinetic energy produced via buoyancy production. In comparison, using $\sigma_\rho = 0.90$ results in lower rates of turbulent kinetic energy production and diffusion after reshock.

Second, the speed with which the shock travels for each σ_ρ value in the 0.50 ms interval can be estimated. As buoyancy production and diffusion contributions are largest in the vicinity of the shock, the shock locations can be determined by the locations of the peaks. This was further verified by the mean field profiles (not shown). Noting the distance each peak travels in the same 0.50 ms interval, the average shock velocity for each case can be estimated. Smaller values of σ_ρ result in larger shock speeds following reshock as more turbulent kinetic energy is generated via buoyancy production. These findings are in agreement with the mixing layer behavior in Fig. 3.19 and with results from Sec. 3.2, where larger amounts of turbulent kinetic energy result in larger mixing layer growth rates. These results also demonstrate that turbulent mixing evolution can be influenced at later times through σ_ρ without modifying the initial conditions or shock strengths. Approximate shock speeds for $\sigma_\rho = 0.60$, 0.70, and 0.90 are provided in Table 3.1.

σ_ρ	Shock speed after reshock [cm/s]
0.60	$\approx 4.63 \times 10^4$
0.70	$\approx 4.58 \times 10^4$
0.90	$\approx 4.43 \times 10^4$

Table 3.1: Estimated shock speeds for $\sigma_\rho = 0.60$, 0.70, and 0.90 with $Ma_s = 1.98$, $At = 0.67$, $K_0 = 0.1$, $\lambda_{rms} = 0.50$ cm, and $C_{\epsilon 0} = 0.90$ after reshock.

3.3.2 Variations in $C_{\epsilon 0}$

The second parametric study focuses on the model sensitivity to variations in $C_{\epsilon 0}$. This coefficient scales the buoyancy production in Eq. (2.14) for the turbulent kinetic energy dissipation rate. Larger values in $C_{\epsilon 0}$ result in larger dissipation of turbulent kinetic energy and smaller growth of the mixing layer width. Figure 3.22 demonstrates that predictions of the mixing layer width are substantially more sensitive to variations in $C_{\epsilon 0}$ in comparison to σ_ρ. By increasing this value from 0.90 to 0.95, sufficient dissipation is introduced to considerably decrease the amount of turbulent mixing after reshock. For example, at $t = 2.60$ ms where the mixing width is largest, the width is approximately three times larger for $C_{\epsilon 0} = 0.90$ in comparison to 0.95. As $C_{\epsilon 0}$ is decreased further to 1.00, the post-reshock mixing evolution is highly suppressed. Like variations in σ_ρ, changes in $C_{\epsilon 0}$ similarly do not influence early-time mixing, shock compression, or reshock times.

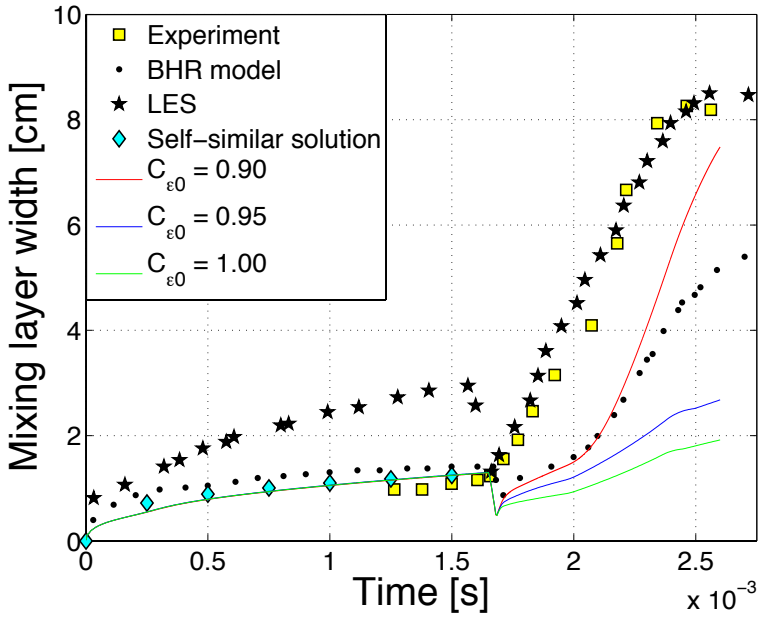

Figure 3.22: Mixing layer width for $Ma_s = 1.98$, $At = 0.67$, $K_0 = 0.10$, $\lambda_{rms} = 0.50$ cm, $\sigma_\rho = 0.90$, and $C_{\epsilon 0} = 0.90$, 0.95, and 1.00, and $n = 9600$ with $\Delta x = 0.02$ cm. The experimental data are from Ref. (10), the BHR results are from Ref. (29), the LES data with $\Delta x = 0.21$ cm are from (15), and the self-similar solution is from Eq. (2.27).

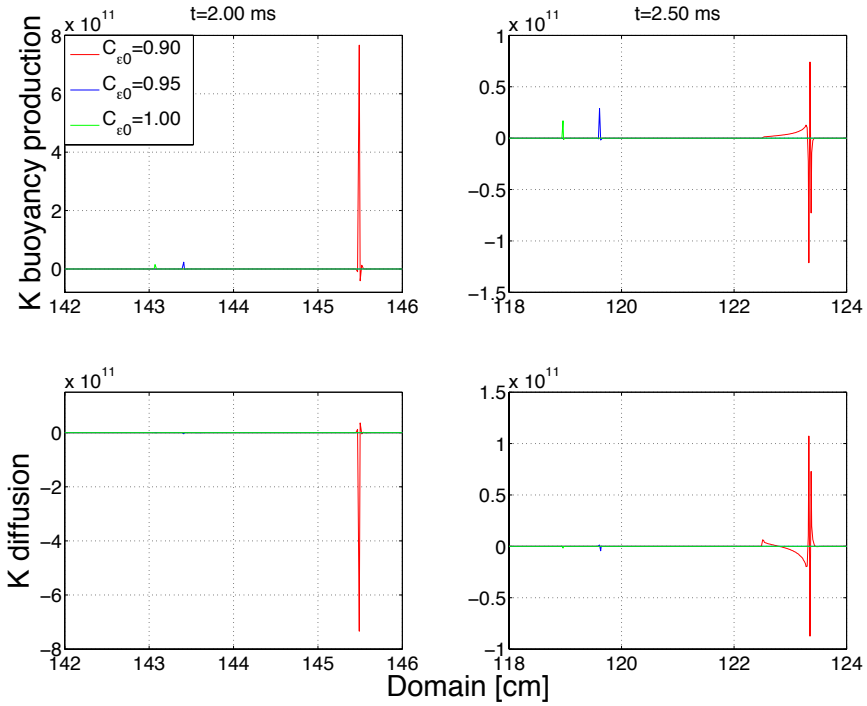

Figure 3.23: Turbulent kinetic energy buoyancy production and diffusion terms [g/cm-s^3] at times $t = 2.00$ and 2.50 ms for $Ma_s = 1.98$, $At = 0.67$, $K_0 = 0.10$, $\lambda_{rms} = 0.50$ cm, $\sigma_\rho = 0.90$, and $C_{\epsilon 0} = 0.90$, 0.95, and 1.00.

The turbulent kinetic energy and dissipation rate buoyancy production and diffusion budgets are presented in Figs. 3.23 and 3.24, respectively, at $t = 2.00$ and 2.50 ms. The K buoyancy production and diffusion terms demonstrate a relatively large rate of production and diffusion of turbulent kinetic energy for $C_{\epsilon 0} = 0.90$ in comparison to $C_{\epsilon 0} = 0.95$ and 1.00, where the model predicts stronger dissipation of turbulent kinetic energy. The small increase in turbulent kinetic energy observed at later times is due to changes in pressure from the arrival of the expansion wave at $\tau_E \approx 1.98$ ms. The rate at which turbulent kinetic energy is spread by the diffusion term is also substantially reduced for $C_{\epsilon 0} = 0.95$ and 1.00. This is due to the larger dissipation in the buoyancy production and reduced supply of turbulent kinetic energy for post-reshock mixing, and is in agreement with the post-reshock mixing in Fig. 3.22 as minimal turbulent mixing is observed at these stages. These strong

dissipative effects are further illustrated in Fig. 3.24 for ϵ. Larger dissipation in the buoyancy production term is predicted for larger $C_{\epsilon 0}$ values. When $C_{\epsilon 0}$ is smaller, dissipative effects decrease and diffusion is larger.

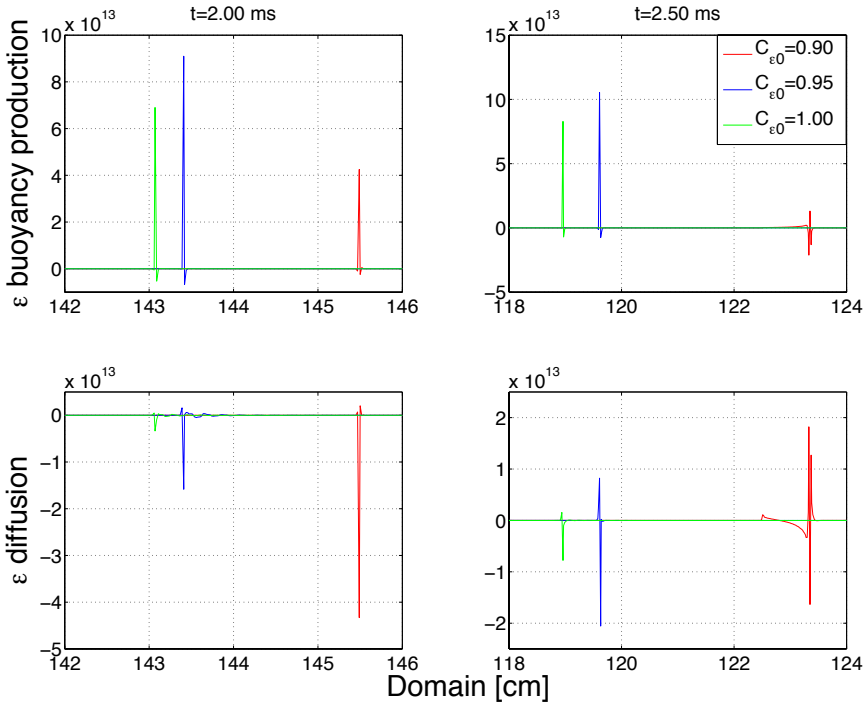

Figure 3.24: Turbulent kinetic energy dissipation rate buoyancy production and diffusion terms [g/cm-s^4] at times $t = 2.00$ and 2.50 ms for $Ma_s = 1.98$, $At = 0.67$, $K_0 = 0.10$, $\lambda_{rms} = 0.50$ cm, $\sigma_\rho = 0.90$, and $C_{\epsilon 0} = 0.90$, 0.95, and 1.00.

Finally, it was shown that variations in σ_ρ and $C_{\epsilon 0}$ have minimal influence on early-time mixing, shock compression strength, and reshock timing. However, variations in the buoyancy production of the turbulent kinetic energy and dissipation rate through σ_ρ influence the speed with which the shock travels in the post-reshock regime. Table 3.1 gives estimated shock speeds for different values of σ_ρ after reshock; as the rate of turbulent kinetic energy increases via buoyancy production by decreasing σ_ρ, the transmitted shock travels at a higher speed due to the larger supply of energy. However, as $C_{\epsilon 0}$ increases and dissipative effects become stronger, transmitted shocks following reshock also travel faster as $C_{\epsilon 0}$ decreases the rate at which turbulent kinetic

energy is generated for mixing through buoyancy production. Table 3.2 compares estimated shock speeds for different values of $C_{\epsilon 0}$. As the mixing layer growth rate is reduced for larger $C_{\epsilon 0}$ values, the width also grows to a lesser extent. Therefore, the region of compressed gas the shock has to traverse, which is at a higher pressure and density, is shorter. In effect, the shock loses less energy as it exits the compressed region sooner and increases speed as it enters a region of lower density.

$C_{\epsilon 0}$	Shock speed after reshock [cm/s]
0.90	$\approx 4.43 \times 10^4$
0.95	$\approx 4.75 \times 10^4$
1.00	$\approx 4.81 \times 10^4$

Table 3.2: Estimated shock speeds for $C_{\epsilon 0} = 0.90$, 0.95, and 1.00 with $Ma_s = 1.98$, $K_0 = 0.1$, and $\sigma_\rho = 0.90$ after reshock.

3.4 $Ma_s = 1.45$: Variations in the Initial Perturbation Wavelength with a Negative Atwood Number

The initial perturbation wavelength, λ_{rms}, which determines the initial turbulent kinetic energy dissipation rate can also be adjusted. Like the turbulent kinetic energy seed K_0, variations in λ_{rms} similarly influence the early mixing prior to reshock. However, unlike for K_0, the sensitivity of the model to variations in λ_{rms} is small following reshock because the dissipation rate principally affects the shear production, which contributes less to turbulent mixing than the buoyancy production after reshock. Thus, a reduction of turbulent kinetic energy from shear production after reshock has a smaller effect on the mixing layer width.

To illustrate these effects, an experiment conducted by Poggi *et al.* (11) is considered (see Sec. 1.1). The length of the test section is $\delta = 30$ cm and a shock with $Ma_s = 1.45$ is introduced in SF_6 a distance 0.25 cm away from the interface. In this experiment the gas interface experienced a secondary reshock: the first and

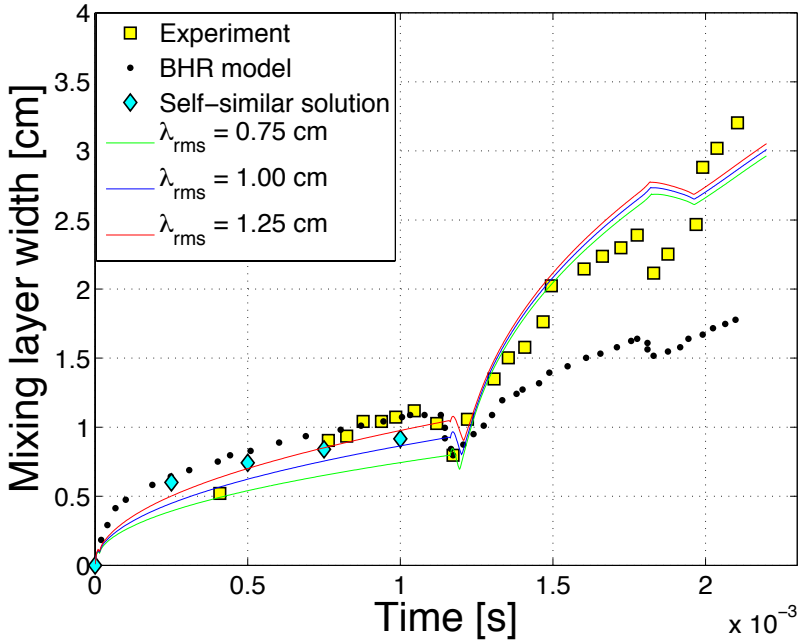

Figure 3.25: Mixing layer widths for $Ma_s = 1.45$, $At = -0.67$, $K_0 = 0.10$, $\lambda_{rms} = 0.75$, 1.00, and 1.25 cm, $\sigma_\rho = 0.90$, $C_{\epsilon 0} = 0.90$, and $n = 14400$ with $\Delta x = 0.01$ cm. The experimental data are from Ref. (11), the BHR results are from Ref. (29), and the self-similar solution is from Eq. (2.27).

second reshocks occur at $\tau_R \approx 1.2$ and $\tau_{R2} \approx 1.8$ ms, respectively. Figure 3.25 shows predicted mixing layer widths for wavelengths $\lambda_{rms} = 0.75$, 1.00, and 1.25 cm with $K_0 = 0.1$. Also shown are experimental measurements, BHR model predictions, and the self-similar prediction prior to reshock. In decreasing the initial perturbation wavelength, dissipative effects become stronger and early-time mixing is decreased. Based on results in Fig. 3.4, an initial wavelength of $\lambda_{rms} = 0.75$ cm introduces excessive dissipation and the initial profile underpredicts the experimental data. Conversely, as λ_{rms} reaches 1.25 cm, dissipative effects become weaker and the resulting increase in turbulent mixing agrees better with experimental data.

As an additional aid in understanding the effects of λ_{rms} on the production and dissipation mechanisms shortly before and after reshock, Fig. 3.26 shows the turbulent kinetic energy budgets at $t = 1.0$ and 1.5 ms. The first two rows in Fig. 3.26 illustrate the evolution of the buoyancy production and the turbulent kinetic energy

diffusion. The magnitude and structure of the buoyancy production are minimally affected by changes in λ_{rms} before reshock because the buoyancy production makes small contributions to early-time mixing. After reshock, where the buoyancy production is the dominant term for mixing, a decrease in turbulent kinetic energy occurs as it is spread by diffusion.

The bottom two rows in Fig. 3.26 show the evolution of the shear production and dissipation terms. Unlike the buoyancy production at $t = 1.0$ ms, the shear production is more sensitive to changes in λ_{rms}. As dissipative effects become stronger with smaller λ_{rms} values, the turbulent kinetic energy correspondingly decreases. Dissipative effects are strong in the vicinity of the shock as it heats the gas with dissipated energy evident in the shocked region. Following reshock, the profile of the shear production remains similar, indicating that this term in not strongly sensitive to diffusive effects and has a secondary role in post-reshock mixing. The change in magnitude is due to dissipative losses into heat during reshock. The dissipation rate following reshock demonstrates that most energy is expended in compressing and heating the mixing layer, as illustrated by the large decrease of turbulent kinetic energy in this region. Similar effects were noted in Sec. 3.1, where larger values of K_0 resulted in larger compression of the layer. Dissipative effects behind the transmitted and reflected waves after reshock are of much smaller magnitude. Figure 3.27 shows the corresponding budgets for the turbulent kinetic energy dissipation rate. As in the $Ma_s = 1.24$ case in Sec. 3.1, these results are qualitatively similar to those in Fig. 3.26.

Recall that effects due to variations in the initial perturbation wavelength are strongest during early mixing prior to reshock, while those observed after reshock (including the second reshock) are relatively insensitive to changes in this initial condition. It is instructive to consider the second reshock in more detail. The second reshock occurs because upon reshock, the reflected wave (evident in Figs. 3.26 and

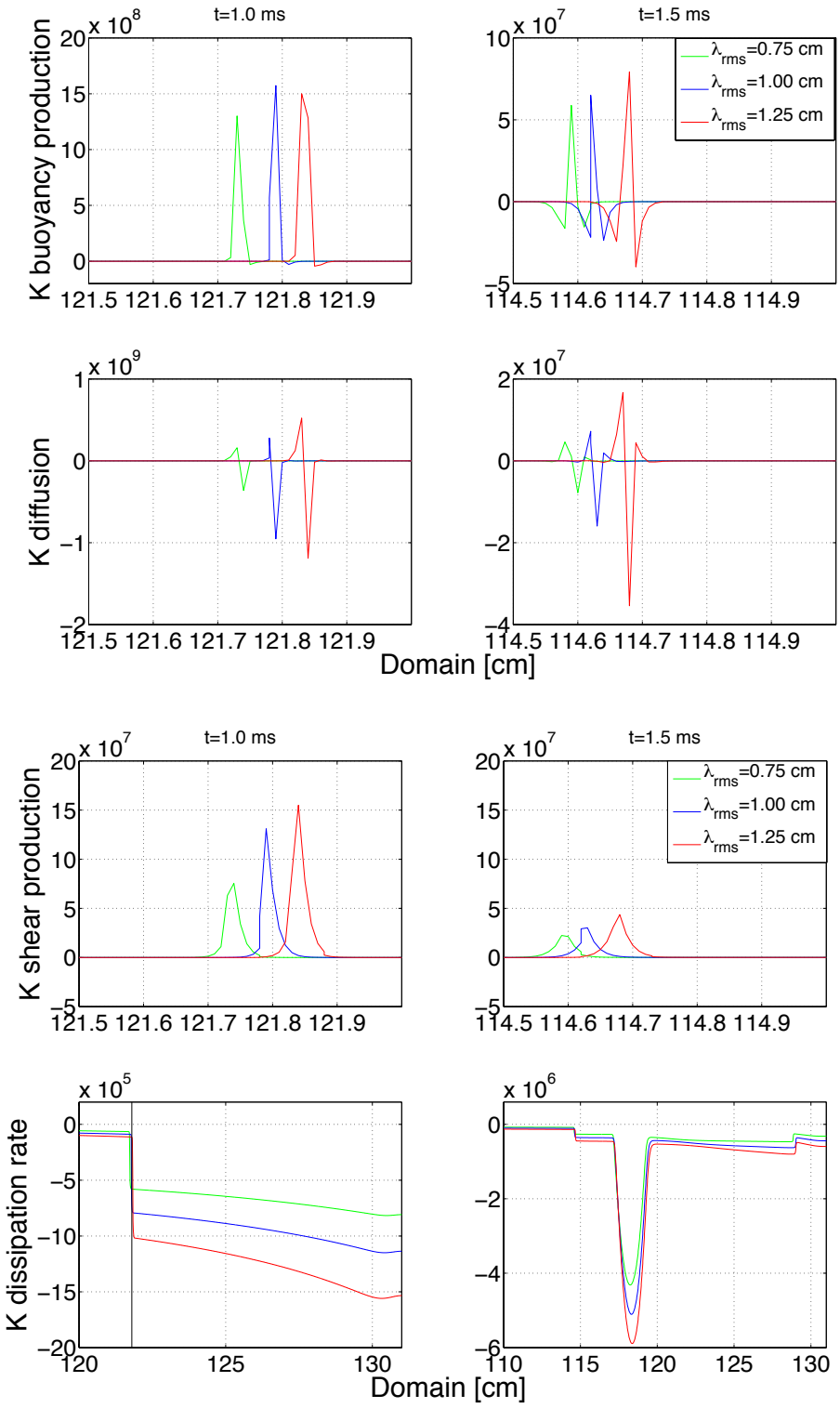

Figure 3.26: Turbulent kinetic energy budgets [g/cm-s^3] at $t = 1.0$ and 1.5 ms for $Ma_s = 1.45$, $At = -0.67$, $K_0 = 0.10$, $\lambda_{rms} = 0.75$, 1.00, and 1.25 cm, $\sigma_\rho = 0.90$, $C_{\epsilon 0} = 0.90$, and $n = 14400$ with $\Delta x = 0.01$ cm.

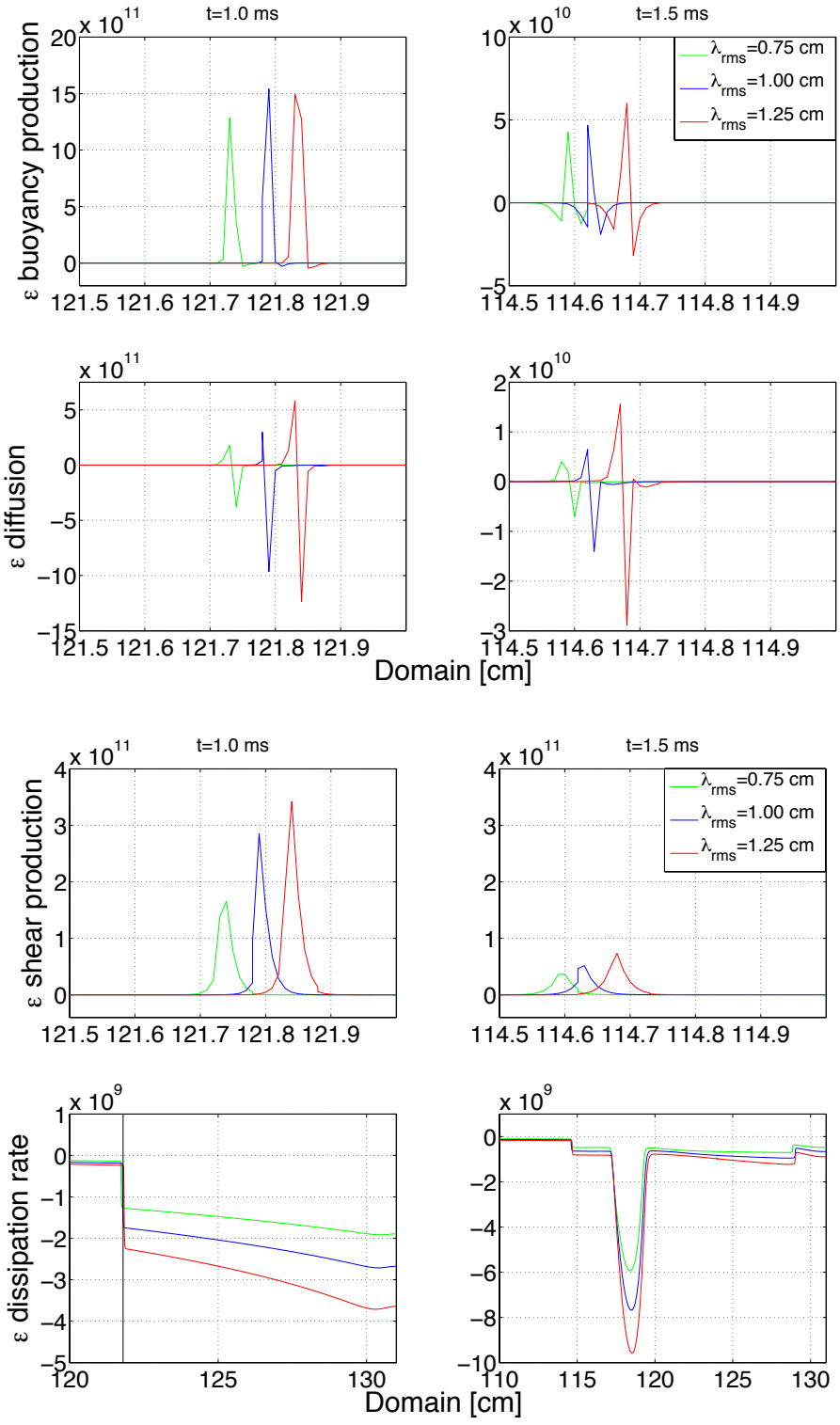

Figure 3.27: Turbulent kinetic energy dissipation rate budgets [g/cm-s^4] at $t = 1.0$ and 1.5 ms for $Ma_s = 1.45$, $At = -0.67$, $K_0 = 0.10$, $\lambda_{rms} = 0.75$, 1.00, and 1.25 cm, $\sigma_\rho = 0.90$, $C_{\epsilon 0} = 0.90$, and $n = 14400$ with $\Delta x = 0.01$ cm.

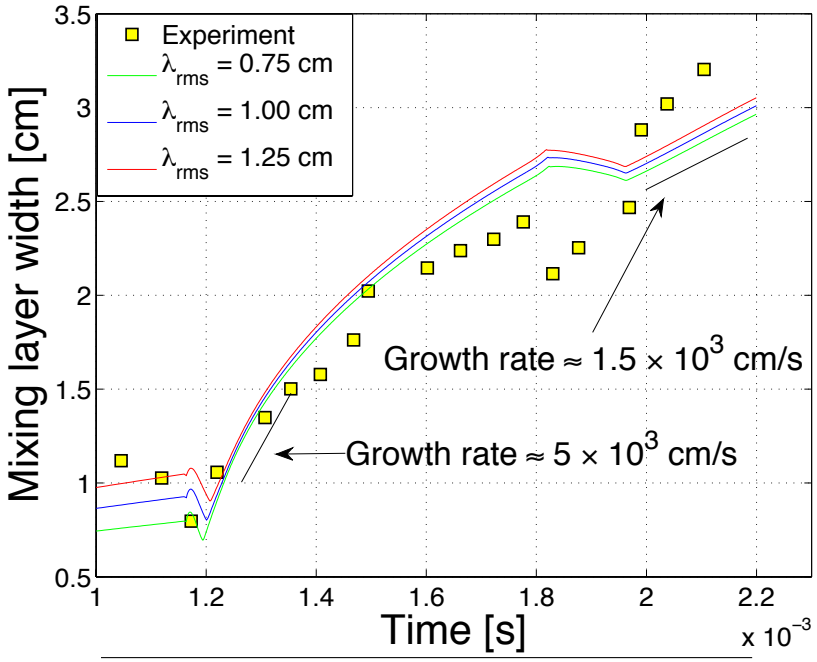

Growth rate	Units	τ_{R1}	τ_{R2}
$\dot{h}$ (experiment)	cm/s	3.3×10^3	5.8×10^3
$\dot{h}$ (RANS)	cm/s	5×10^3	1.5×10^3

Figure 3.28: Comparison of experimental and RANS mixing layer growth rates following first and second reshock for $Ma_s = 1.45$ and $At = -0.67$, $K_0 = 0.10$, $\lambda_{rms} = 0.75$, 1.00, and 1.25 cm, $\sigma_\rho = 0.90$, $C_{\epsilon 0} = 0.90$, and $n = 14400$ with $\Delta x = 0.01$ cm. The experimental data are from Ref. (11).

3.27) travels away from the mixing layer, reflects from the test section endwall, and again compresses the mixing layer. In this process, this secondary wave loses kinetic energy as it heats the gas and compresses the layer at a lower energetic state, resulting in a lower rate of turbulent mixing. Figure 3.28 considers an interval of time when both reshocks can be observed more closely. The approximate growth rates of the mixing layer after τ_{R1} and τ_{R2} are $\dot{h}_1 \approx 5 \times 10^3$ and $\dot{h}_2 \approx 1.5 \times 10^3$ cm/s, respectively, which are estimated as the difference in the mixing layer width over an interval of time. However, there is some deviation between the model predictions and experimental measurements of the growth rate after the compression of the layer. After the first reshock the model predicts a slightly larger mixing rate than the experimental

data. Following the second reshock, the opposite is observed, where the experiment shows a more rapid growth rate. Included with Fig. 3.28 are comparisons between experimental and RANS mixing layer growth rates following τ_{R1} and τ_{R2}.

3.5 Convergence Under Grid Refinement

Demonstration of numerical convergence of Reynolds-averaged model predictions for reshocked Richtmyer–Meshkov instability-induced mixing is important for several reasons. Achieving convergence can be problematic in shocked flows as compared to flows without shocks and other discontinuities. Unless shown otherwise, it is reasonable to assume that the predictions of Reynolds-averaged models are grid-dependent. In particular, unconverged results may suggest a set of model coefficients and initial conditions that provide apparently good predictions, but only for a particular grid resolution or underlying numerical implementation of the model equations.

Convergence properties under grid refinement are considered for the mixing layer widths, mean density, mean pressure, mean velocity, mean heavy mass fraction, turbulent kinetic energy, turbulent kinetic energy dissipation rate, and turbulent viscosity. In the preceding sections, predicted mixing layer widths were compared with experimental measurements (10; 11), LES (15), BHR model predictions (29), and the self-similar solution in Eq. (2.27). However, convergence studies were not presented or discussed for either the LES or BHR model studies. The grid spacings for the present Vetter–Sturtevant studies with $n = 2400$, 4800, 7200, and 9600 points were $\Delta x = 0.07$, 0.03, 0.02, and 0.01 cm, respectively. For the Poggi *et al.* study, the grid spacings for $n = 4800$, 7200, 9600, 14400, and 19200 points were $\Delta x = 0.03$, 0.02, 0.01, 0.009, and 0.007 cm, respectively. The grid spacings for the LES were $\Delta = 0.21$ cm (15).

3.5.1 Mixing layer widths

Simulations with grid refinement were considered starting with $n = 2400$ points for a coarse mesh and systematically increased to $n = 4800$, 7200, and 9600 points. For $Ma_s = 1.24$, similar results were obtained using $n = 7200$ and 9600 points. Figure 3.29 shows that the widths nearly overlap prior to reshock; following reshock, a small deviation is noted shortly before and after the arrival of the expansion wave. Using $n = 2400$ points provides a poor representation of the mixing layer evolution. However, the early-time width and the magnitude of the reshock compression at this resolution agree well with LES (15). It is possible that insufficient resolution may explain the LES deviations from the experiment at early times. In the post-reshock region, grid refined K–ϵ and LES predictions agree well with experimental measurements. In comparison, the BHR model (29) matches experimental data well at early times, but predicts a smaller mixing width after reshock.

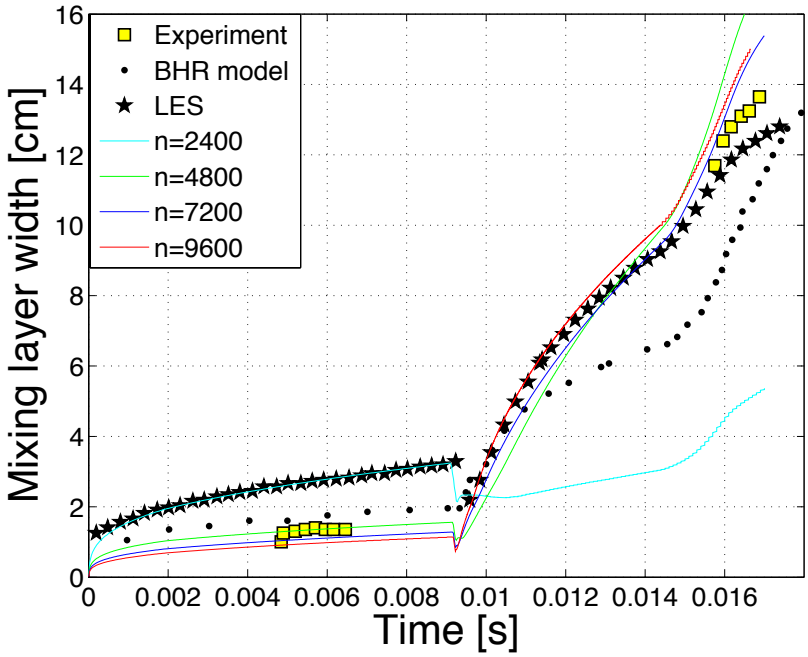

Figure 3.29: Convergence of mixing layer width for $Ma_s = 1.24$ and $At = 0.67$. The experimental data are from Ref. (10), the BHR results are from Ref. (29), and the LES data are from (15).

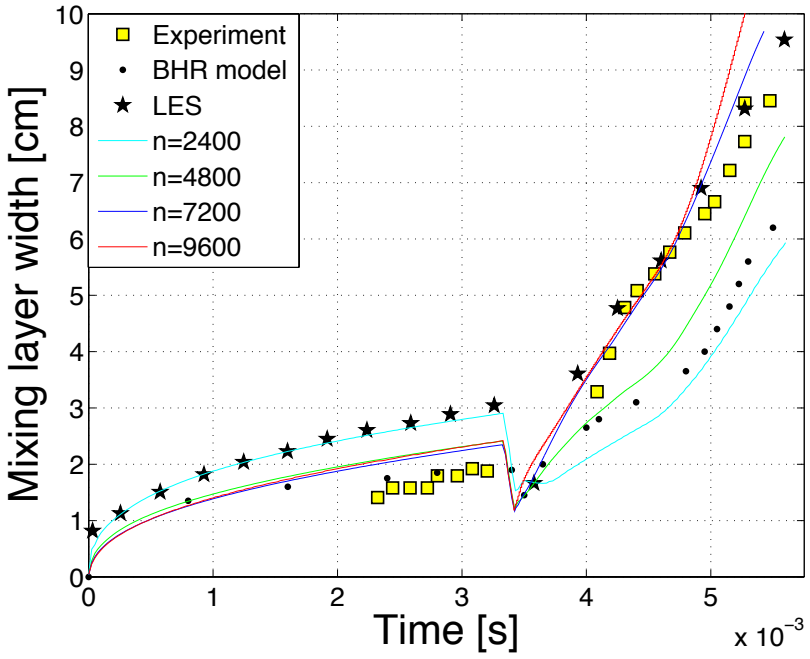

Figure 3.30: Convergence of mixing layer width for $Ma_s = 1.50$ and $At = 0.67$. The experimental data are from Ref. (10), the BHR results are from Ref. (29), and the LES data are from (15).

Similarly, Fig. 3.30 shows that convergence is achieved for $Ma_s = 1.50$ between $n = 7200$ and 9600 points. A small discrepancy is observed shortly after reshock due to the arrival of the expansion wave, but convergence is recovered shortly thereafter. Furthermore, some divergence begins at times near the end of the simulation, starting at $t \approx 5$ ms due to rarefaction wave interactions. As in the preceding convergence study, using $n = 2400$ points does not adequately represent the mixing layer evolution. At this coarse resolution, K–ϵ model predictions agree with those of LES (15) prior to reshock as well as with the BHR model (29) after reshock. The widths using $n = 7200$ and 9600 points agree with experimental and LES data after reshock.

Convergence studies for $Ma_s = 1.98$ reveal that $n = 7200$ and 9600 points produce comparable results. The widths overlap at early times and agree well with experimental data. After reshock, some deviation between the two resolutions is present, as seen in Fig. 3.31. Unlike the previous two cases, LES (15) gives a larger early-time

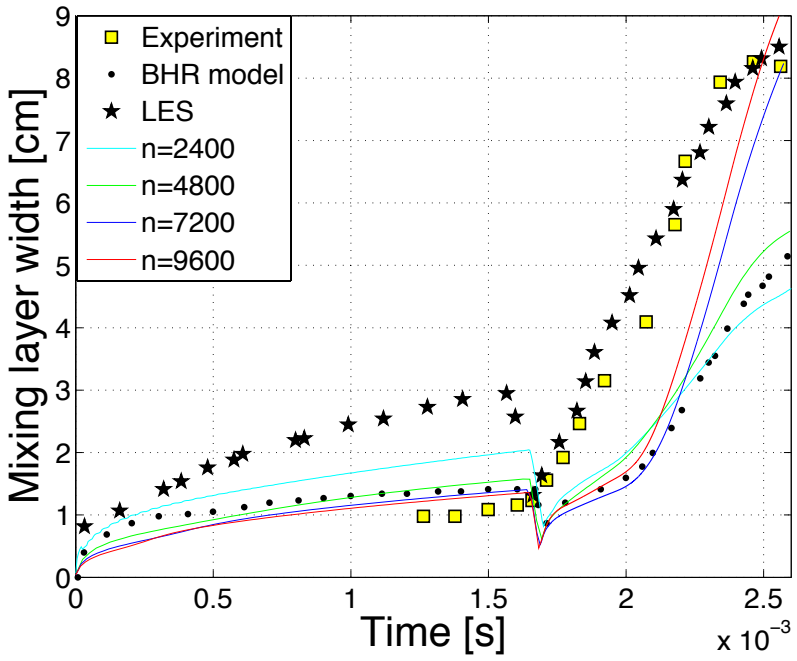

Figure 3.31: Convergence of mixing layer width for $Ma_s = 1.98$ and $At = 0.67$. The experimental data are from Ref. (10), the BHR results are from Ref. (29), and the LES data are from (15).

width and shock compression magnitude. Results obtained using $n = 4800$ points are in close agreement with BHR model predictions (29) throughout.

Finally, the study with $Ma_s = 1.45$ and $At = -0.67$ required a finer grid to achieve convergence. Figure 3.32 shows that good convergence is achieved prior to reshock and for a short time after. However, as time progresses and the second wave reflects from the endwall and approaches the interface to initiate the second reshock, the predicted mixing layer widths begin to diverge. It is possible that oscillations are introduced due to interactions between the secondary wave and the reflecting boundary conditions at the test section endwall. It is also demonstrated in the refinement studies for the mean and turbulent fields that convergence is difficult to achieve in the vicinity of the gas interface where mixing is strongest. Thus, as the test section decreases in length (and therefore the distance to the interface is shorter), convergence for cases with smaller test sections requires more grid refinement. This is further demonstrated in

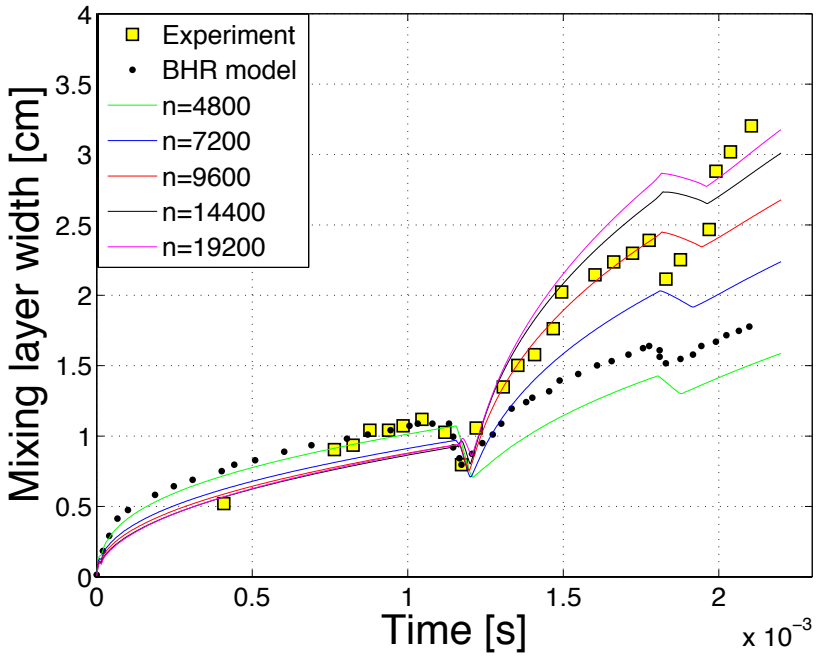

Figure 3.32: Convergence of mixing layer width for $Ma_s = 1.45$ and $At = -0.67$. The experimental data are from Ref. (11) and the BHR results are from Ref. (29).

Chapter IV.

3.5.2 Convergence of the mean fields

Convergence of the mean fields is evaluated at time, $t = 10$ and 12 ms for the $Ma_s = 1.24$ case in Fig. 3.33, shortly after reshock and before the arrival of the expansion wave, $\tau_R \approx 9.25$ and $\tau_E \approx 14.70$ ms, respectively. The locations of the transmitted and reflected shocks are denoted by solid and dashed vertical lines, respectively, while the arrows indicate the direction of shock propagation. At each time, mean field convergence is achieved between $n = 7200$ and 9600 points. Using $n = 2400$ points results in deviations near the shock and mixing layer, where material discontinuities are present. Using $n = 4800$ provides a reasonable representation with some loss of accuracy. Despite the small loss of accuracy for coarser grids, convergence is maintained throughout the domain.

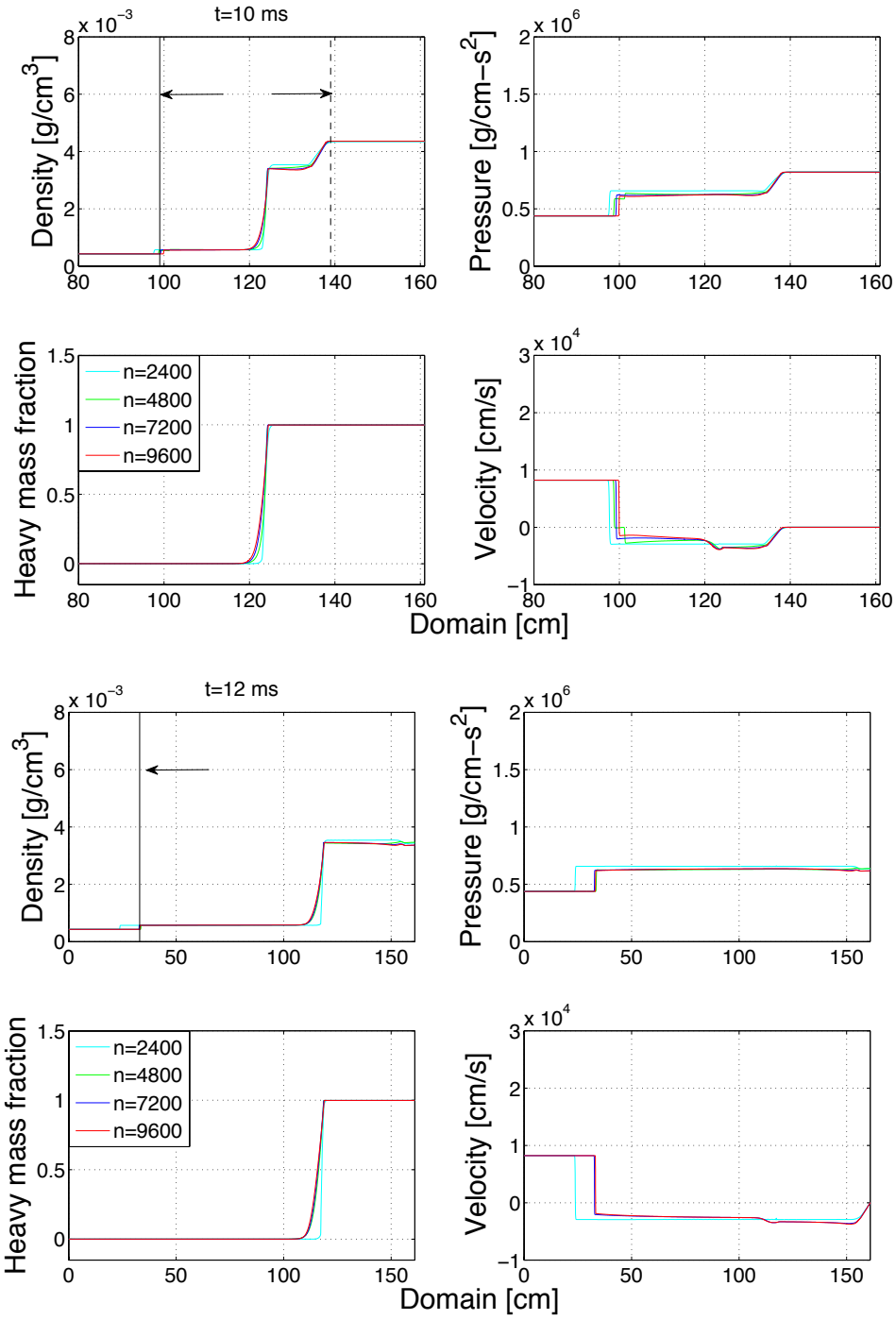

Figure 3.33: Mean field convergence for $Ma_s = 1.24$ and $At = 0.67$ at 10 ms (top) and 12 ms (bottom).

Similar findings are presented for $Ma_s = 1.50$ in Fig. 3.34 at times $t = 4.50$ and 5.00 ms, respectively. In the vicinity of the shock and the mixing region, small deviations are evident for coarser grids with $n = 2400$ and 4800 points. Convergence is achieved between $n = 7200$ and 9600 points. Moreover, deviations between profiles manifested by the rarefaction–layer interaction are not present in the mean fields.

Convergence behavior is evaluated for $Ma_s = 1.98$ at times $t = 1.70$ and 2.20 ms in Fig. 3.35. These times correspond to time of reshock at $\tau_R \approx 1.69$ ms, and shortly after the expansion wave arrival, $\tau_E \approx 1.98$ ms. The results indicate that mean field convergence is achieved even at reshock. Pressure and velocity profiles show that simulations using coarser grids have difficulty capturing the behavior of the pressure and velocity near the shock and interface, but using $n = 7200$ and 9600 points is adequate. Figure 3.35 also shows that the expansion wave introduces some numerical oscillations behind the shock in the pressure and velocity profiles. Some deviation is also seen in the density and heavy mass fraction profiles near the mixing layer, which decreases as the grid is refined. Unlike the $Ma_s = 1.24$ and 1.50 cases, lack of convergence for coarser grids is more apparent in the vicinity of the shock and mixing region for this case.

Finally, Fig. 3.36 illustrates mean field convergence results for $Ma_s = 1.45$ with $At = -0.67$. As the interface experiences a second reshock, convergence was examined shortly after the first and second reshock at $t = 1.20$ and 2.00 ms, respectively. At $t = 1.20$ ms following the first reshock, the transmitted and reflected waves are represented by solid and dashed black lines, respectively, with arrows indicating the direction of propagation. Similarly, the transmitted wave from the second reshock is also discernible. In this case, the density and heavy mass fraction achieve convergence between $n = 14400$ and 19200 points with small deviations at the edges of the layer. The pressure and velocity converge well with small deviations evident at the shock front. Convergence is generally achieved throughout the domain (i.e., in pure gas

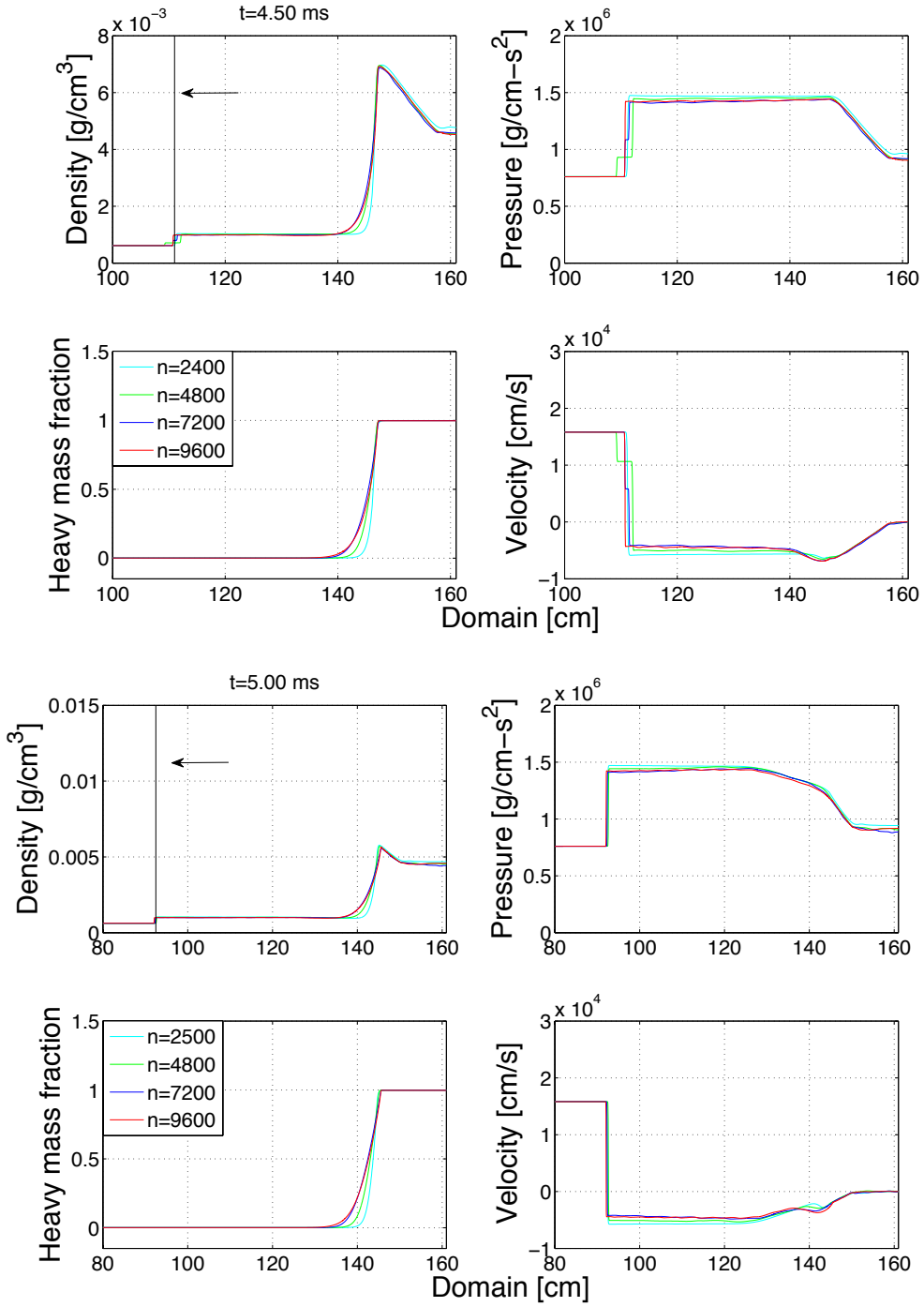

Figure 3.34: Mean field convergence for $Ma_s = 1.50$ and $At = 0.67$ at 4.50 ms (top) and 5.00 ms (bottom).

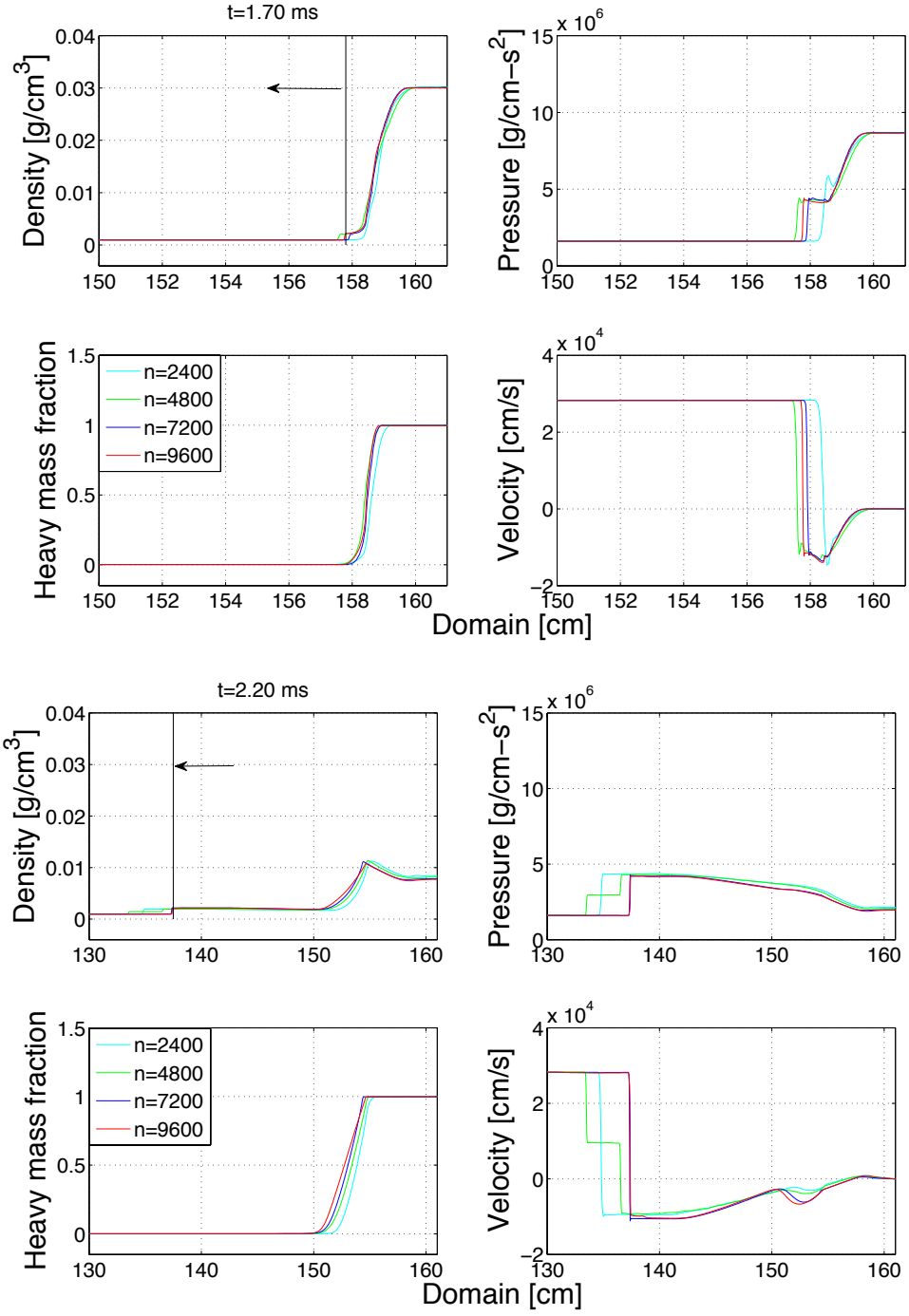

Figure 3.35: Mean field convergence for $Ma_s = 1.98$ and $At = 0.67$ at 1.70 ms (top) and 2.20 ms (bottom).

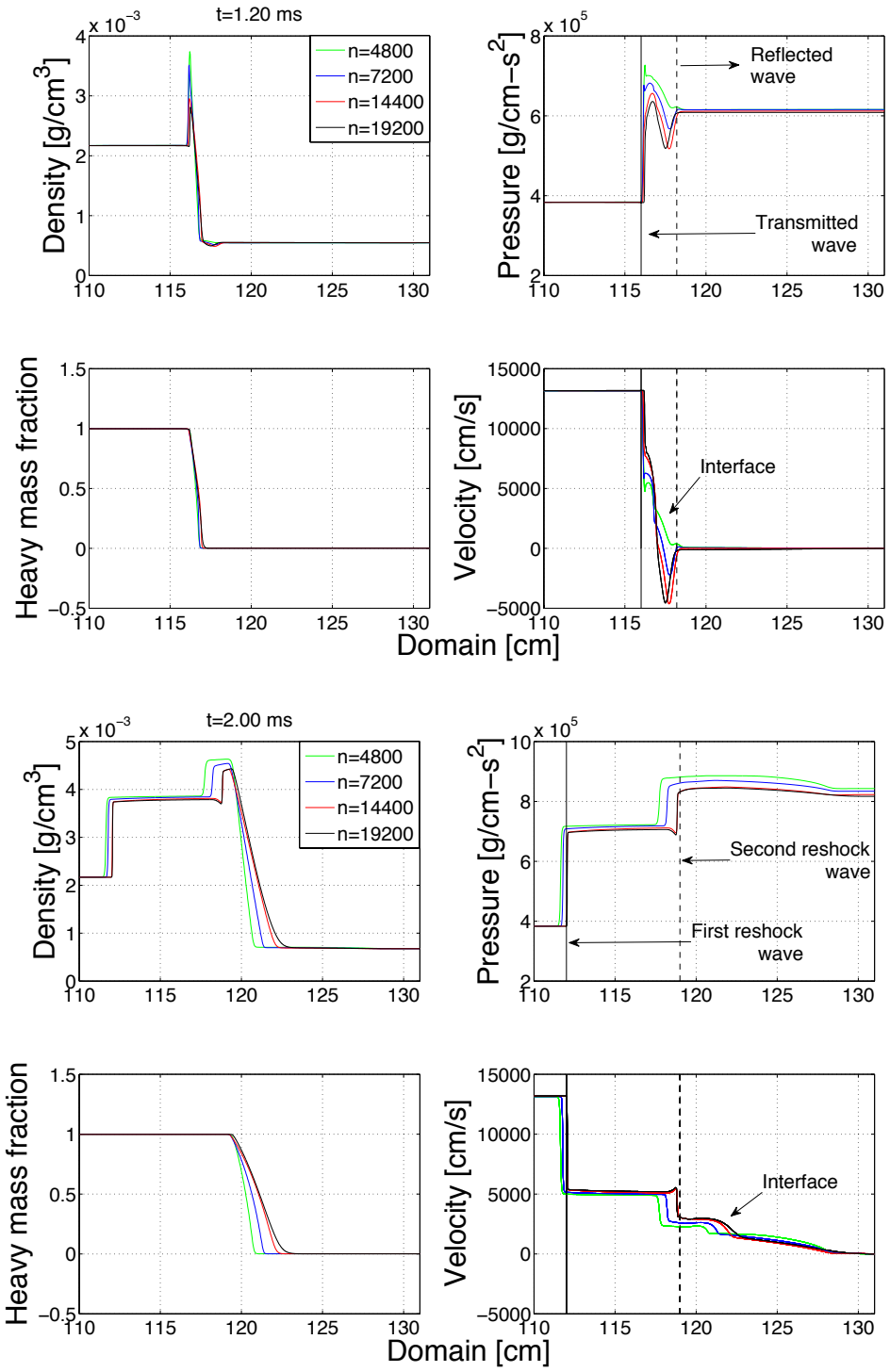

Figure 3.36: Mean field convergence for $Ma_s = 1.45$ and $At = -0.67$ at 1.20 ms (top) and 2.00 ms (bottom).

regions), but it is slower to achieve across the layer where material discontinuities exist and turbulent mixing occurs.

3.5.3 Convergence of the turbulent fields

Studies of the convergence of the turbulent fields demonstrate that the turbulent kinetic energy, turbulent kinetic energy dissipation rate, and turbulent viscosity are more sensitive to oscillations, particularly in the vicinity of the mixing layer. Convergence is slowest near the interface where mixing is most active, or in the vicinity of secondary expansion and rarefaction waves. Evaluation of turbulent field convergence is performed at the same times as for the mean fields above.

For $Ma_s = 1.24$, reshock occurs shortly before $t = 10$ ms. Figures 3.37–3.39 show that the turbulent kinetic energy, turbulent kinetic energy dissipation rate, and turbulent viscosity convergence rates are slower principally in the vicinity of the interface where reshock has just occurred. However, the fields appear converged ahead of the shock and in the test section away from the interface. The dissipation rate and turbulent viscosity approach convergence at a slower rate. At $t = 12$ ms, when the transmitted wave from reshock is farther away from the interface, the turbulent kinetic energy has converged throughout the domain with small perturbations at the interface. The dissipation rate and turbulent viscosity again demonstrate a slower rate of convergence.

The $Ma_s = 1.50$ case provides an example of how secondary waves also affect the convergence of the turbulent fields. Times $t = 4.50$ and 5.00 ms form a time interval over which the rarefaction wave is developing and the gas behind the shock expands. Although the mean fields in Fig. 3.34 demonstrate convergence, strong oscillations can be observed in the same region for the turbulent kinetic energy, dissipation rate, and turbulent viscosity in Figs. 3.40, 3.41, and 3.42, respectively. However, as time progresses, the shock travels farther from the interface and perturbations become

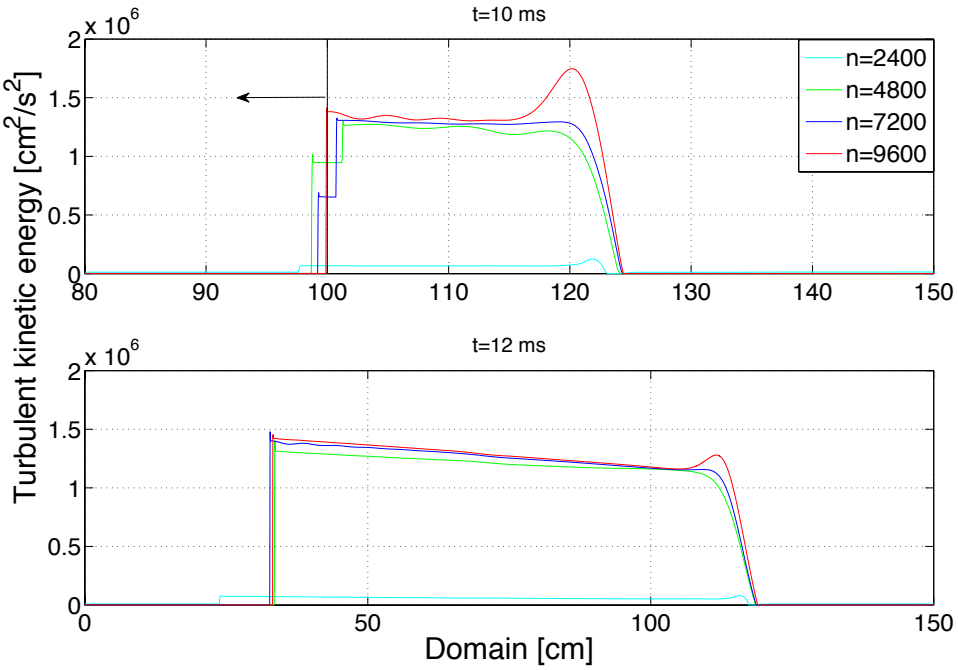

Figure 3.37: Turbulent kinetic energy convergence for $Ma_s = 1.24$ and $At = 0.67$ at $t = 10$ and 12 ms.

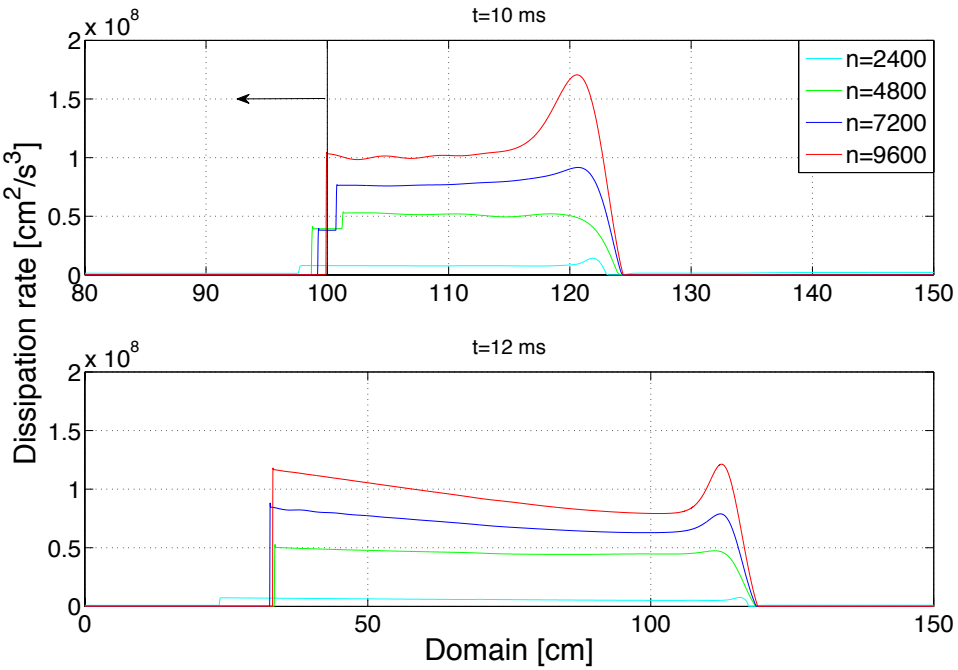

Figure 3.38: Turbulent kinetic energy dissipation rate convergence for $Ma_s = 1.24$ and $At = 0.67$ at $t = 10$ and 12 ms.

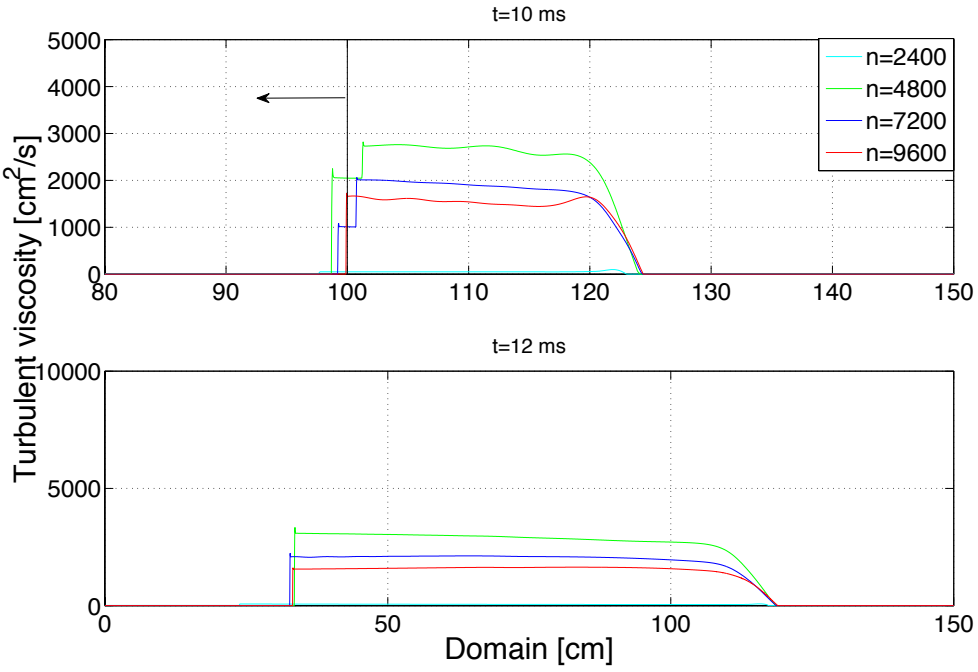

Figure 3.39: Turbulent viscosity convergence for $Ma_s = 1.24$ and $At = 0.67$ at $t = 10$ and 12 ms.

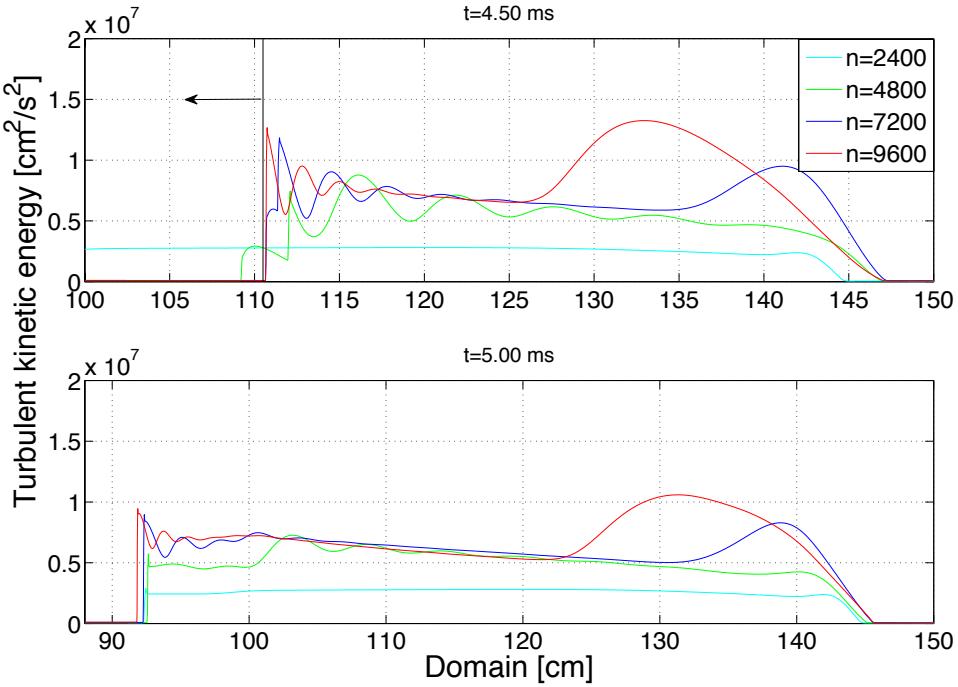

Figure 3.40: Turbulent kinetic energy convergence for $Ma_s = 1.50$ and $At = 0.67$ at $t = 4.50$ and 5.00 ms.

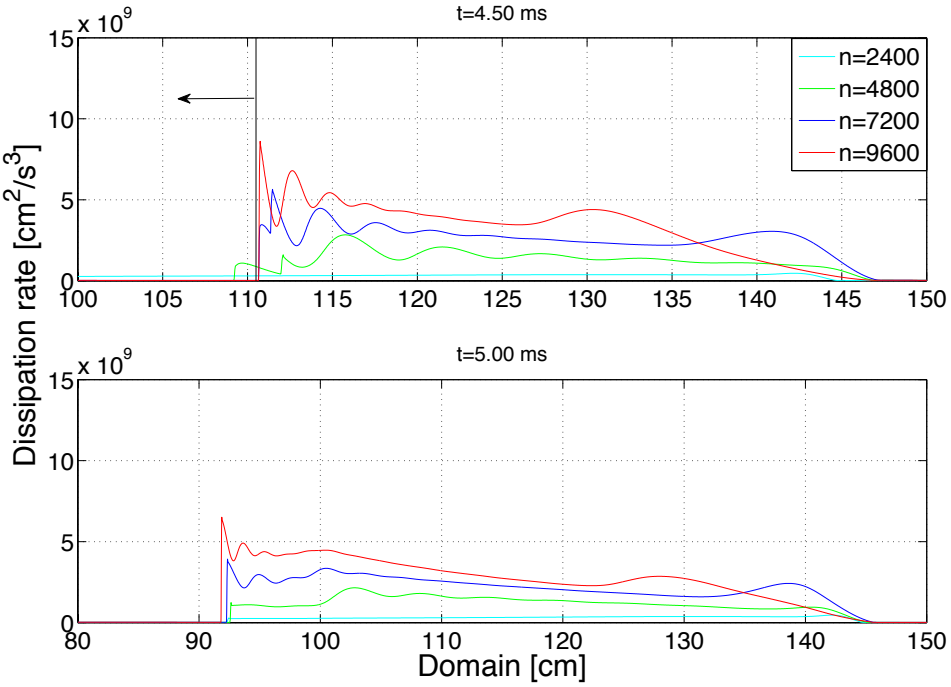

Figure 3.41: Turbulent kinetic energy dissipation rate convergence for $Ma_s = 1.50$ and $At = 0.67$ at $t = 4.50$ and 5.00 ms.

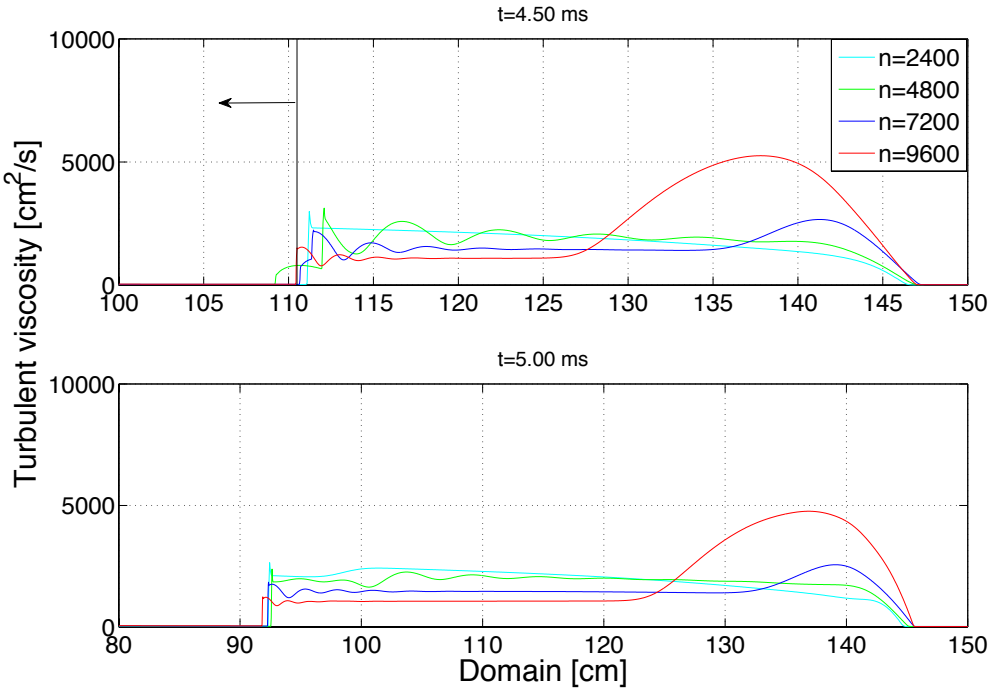

Figure 3.42: Turbulent viscosity convergence for $Ma_s = 1.50$ and $At = 0.67$ at $t = 4.50$ and 5.00 ms.

weaker; slow convergence is more readily observed in the turbulent kinetic energy and turbulent viscosity. Notable perturbations are still apparent across the mixing layer width.

A coarser grid does not adequately represent the mean field behavior for the $Ma_s = 1.98$ case, particularly for the pressure and velocity. A finer grid is necessary to obtain results where loss of accuracy is minimal with $n = 7200$ and 9600 points. Similar observations can be made for the turbulent fields in Figs. 3.43–3.45. Using $n = 2400$ and 4800 points represents the behavior of the turbulent fields poorly, especially the dissipation rate. Although some loss of accuracy is still observed as the shock compresses the interface $n = 7200$ and 9600 points, the turbulent fields show slow convergence.

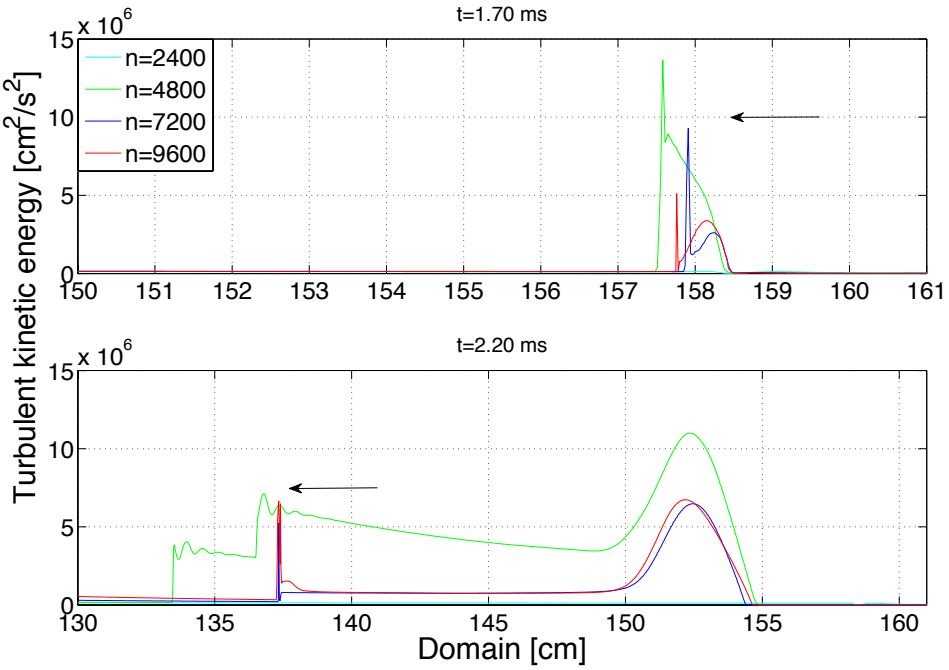

Figure 3.43: Turbulent kinetic energy convergence for $Ma_s = 1.98$ and $At = 0.67$ at $t = 1.70$ and 2.20 ms.

The last set of results for convergence of turbulent fields corresponds to the $Ma_s = 1.45$ case with $At = -0.67$. At $t = 1.20$ ms, the turbulent viscosity achieves convergence in front of the shock and at the interface. However, the reflected shock–

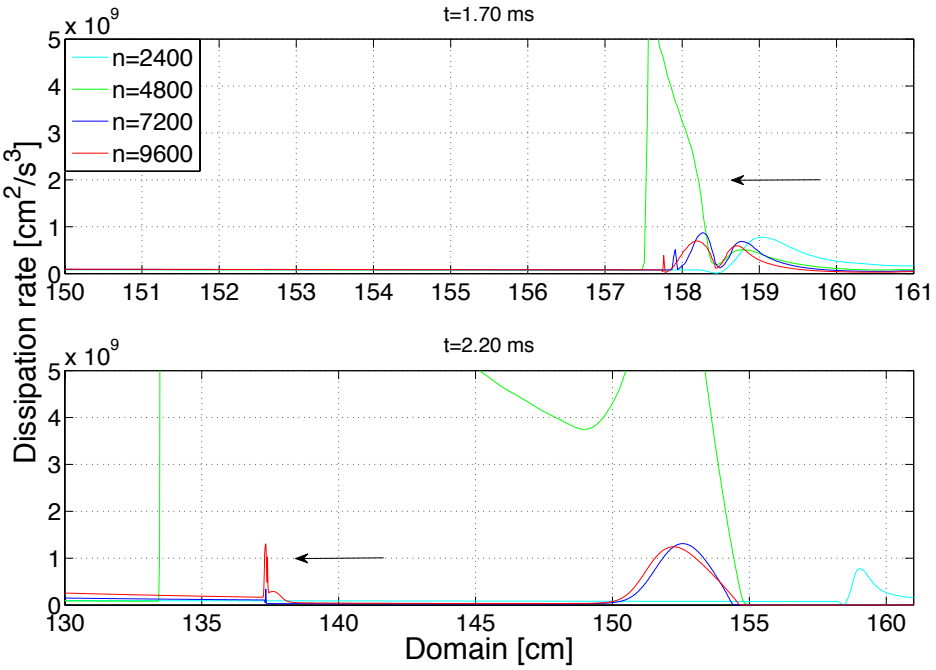

Figure 3.44: Turbulent kinetic energy dissipation rate convergence for $Ma_s = 1.98$ and $At = 0.67$ at $t = 1.70$ and 2.20 ms.

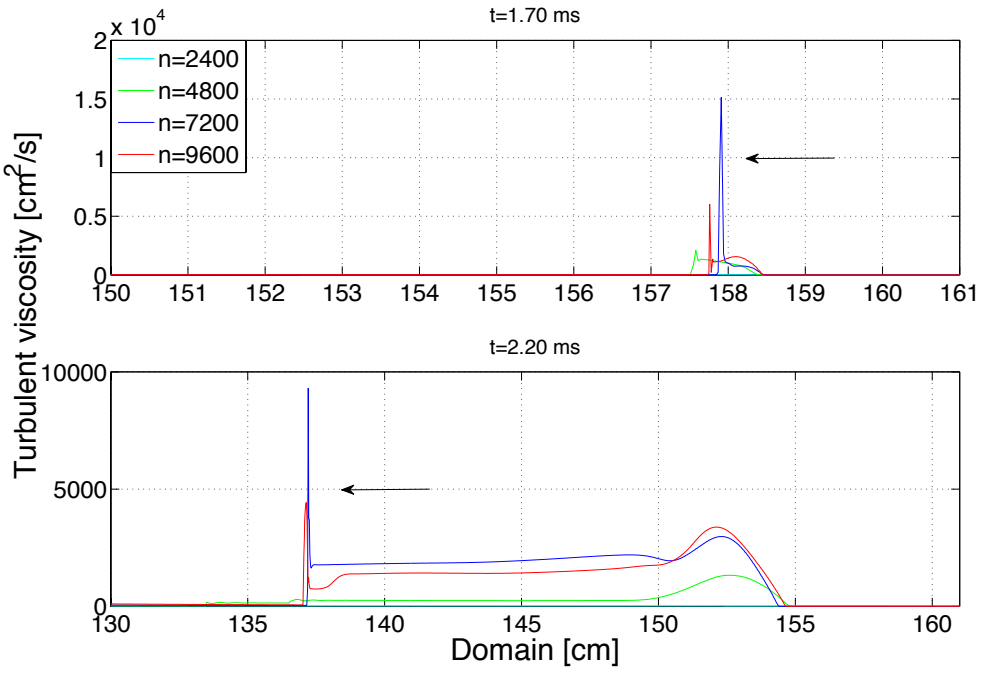

Figure 3.45: Turbulent viscosity convergence for $Ma_s = 1.98$ and $At = 0.67$ at $t = 1.70$ and 2.20 ms.

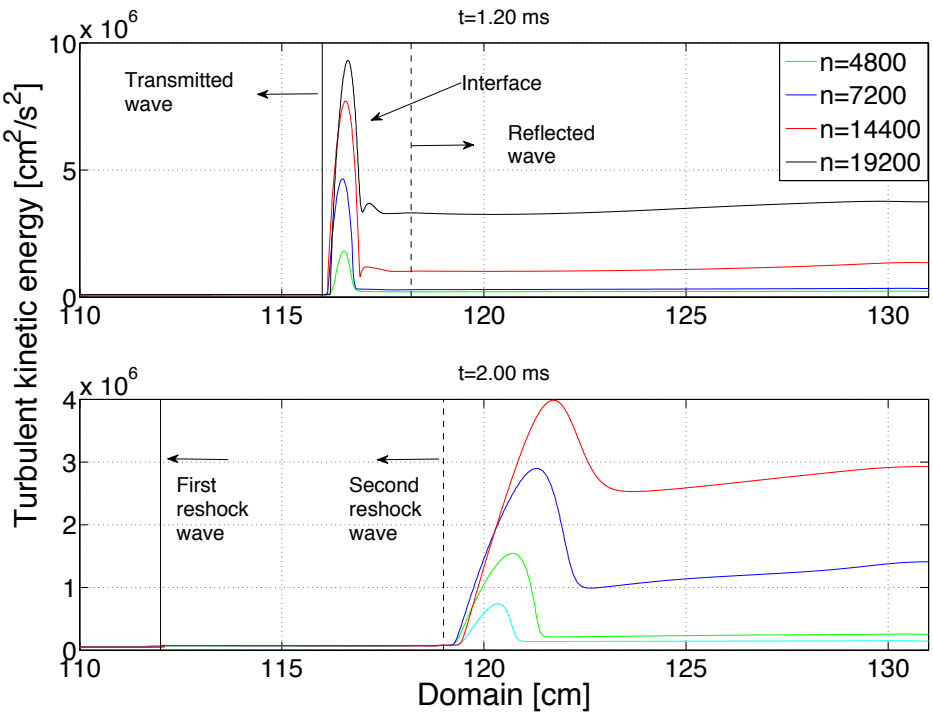

Figure 3.46: Turbulent kinetic energy convergence for $Ma_s = 1.45$ and $At = -0.67$ at $t = 1.20$ and 2.00 ms.

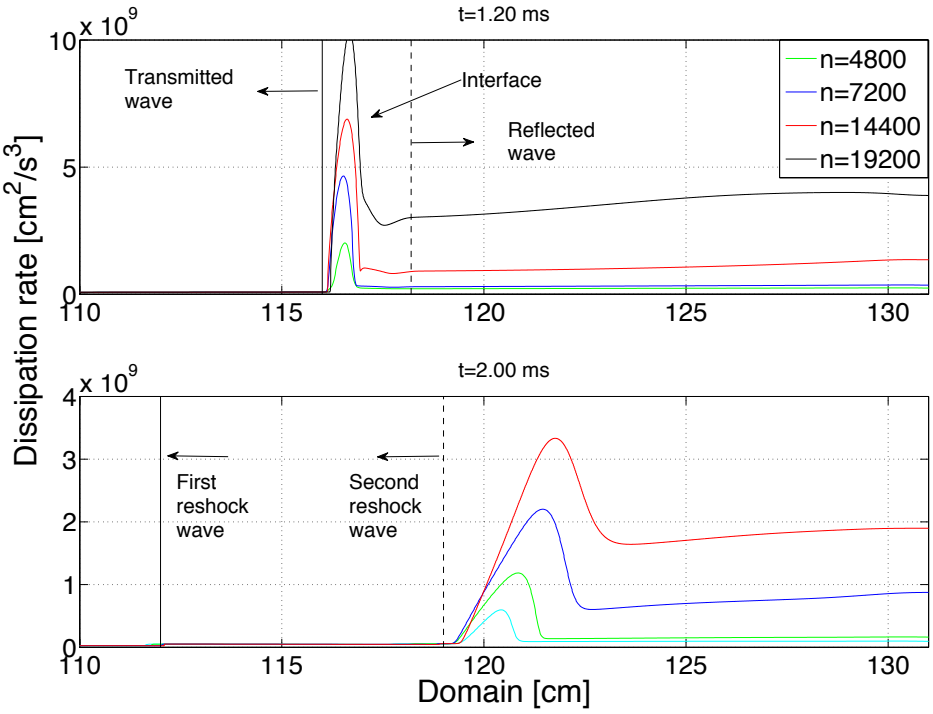

Figure 3.47: Turbulent kinetic energy dissipation rate convergence for $Ma_s = 1.45$ and $At = -0.67$ at $t = 1.20$ and 2.00 ms.

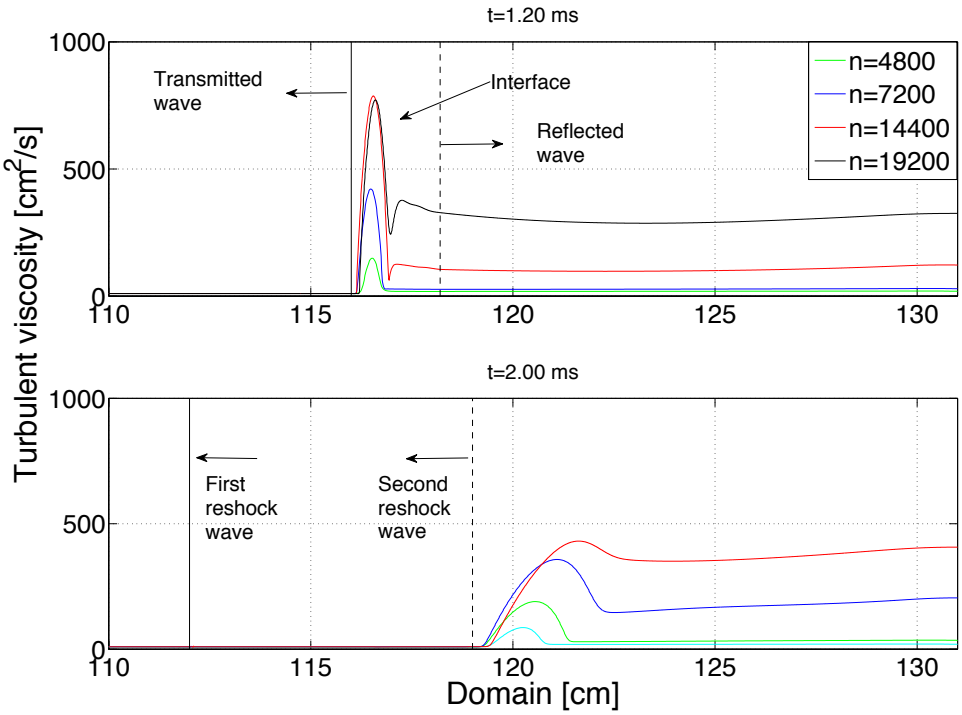

Figure 3.48: Turbulent viscosity convergence for $Ma_s = 1.45$ and $At = -0.67$ at $t = 1.20$ and 2.00 ms.

interface interaction results in a slower rate of convergence up to the test section endwall. The turbulent kinetic energy and dissipation rate demonstrate similar behavior, but with a slower rate of convergence at the interface. At $t = 2.00$ ms, the second reshock has just occurred and the progression of the reflected wave shows that passage of this secondary wave delays convergence from the interface to the test section endwall.

3.6 Chapter Summary

Variations in the turbulent kinetic energy seed K_0 affect turbulent mixing before and after reshock through the production and dissipation mechanisms. Larger K_0 values lead to increased mixing at early times prior to reshock through the buoyancy and shear production terms with turbulent kinetic energy spread through diffusion. Larger values of K_0 also result in a stronger compression during reshock, and corre-

spondingly stronger dissipation of the turbulent kinetic energy leading to less efficient mixing at later times. However, smaller K_0 values compress the interface to a lower degree at reshock, but prolong the mixing process to later times. The dissipation and diffusion terms dissipate and spread turbulent kinetic energy after reshock. The arrival of the expansion wave modestly increases turbulent mixing. The diffusion is insensitive to initial conditions at later times, and this mechanism is nearly the same for all values of K_0 upon interaction with the expansion wave. Variations in the initial perturbation wavelength λ_{rms} were also considered. This initial condition principally affects early-time mixing, but has minimal effect on post-reshock mixing.

Sensitivity of the model predictions to variations in shock Mach number was also examined. Turbulent mechanisms prior to reshock demonstrate sensitivity to these variations. As the shock travels faster at larger shock Mach numbers, reflection from the test section endwall, and therefore reshock, occur earlier. The post-reshock mixing layer growth rate is also affected by changes in Ma_s. Turbulent mixing increases significantly by reshock. During compression, the shock speed is reduced and shear production decreases as energy is dissipated into heat. The buoyancy production enhances turbulent mixing as density and pressure gradients from reshock result in larger turbulent viscosity and diffusion spreads turbulent kinetic energy during mixing. Finally, sensitivity to the buoyancy production model coefficients σ_ρ and $C_{\epsilon 0}$ was considered. This production mechanism influences post-reshock mixing but not early mixing prior to reshock. As σ_ρ appears reciprocally in the buoyancy production, smaller σ_ρ values resulted in larger turbulent kinetic energy and turbulent viscosity, resulting in larger diffusion and enhanced mixing. As the turbulent kinetic energy increased, larger shock speeds were also predicted. Similarly, mixing was also enhanced with smaller values of $C_{\epsilon 0}$ as there was less production of dissipation. Conversely, larger $C_{\epsilon 0}$ values produced larger dissipation of turbulent kinetic energy and smaller widths. As $C_{\epsilon 0}$ increased and the mixing layers were smaller, shocks emerged from

the layers with faster speeds as less energy was lost during compression.

Grid refinement studies demonstrated that convergence is generally achieved between $n = 7200$ and 9600 points for the mixing layer width and mean density, pressure, velocity, and heavy mass fraction. Small deviations are evident near the shock and in the vicinity of the mixing layer due to material interfaces. However, as the grid is refined, these deviations become smaller. The turbulent fields show stronger sensitivity to grid resolution and a slower convergence rate compared to the mean fields. Interactions between the interface and the endwall with secondary expansion and rarefaction waves are also responsible for slower convergence. However, better convergence is achieved as waves progress away from these boundaries.

CHAPTER IV

Application of the Model to Richtmyer–Meshkov Instability Under Variable Reshock Times

The model was applied to reshocked Richtmyer–Meshokov instability in Chapter III for a variety of incident shock Mach numbers Ma_s, Atwood numbers At, and test section lengths δ. Parametric studies were conducted to test the sensitivity of the model to variations in initial conditions, incident shock Mach number, and buoyancy production model coefficients. One important aspect of the present work is that of better understanding turbulent mixing processes following reshock. It was observed in the previous chapter that Ma_s variations influence the time of reshock, where stronger shocks result in earlier compression of the interface. Another way in which reshock is influenced is by changing the test section length. This parameter was discussed in Chapter III, and a systematic approach is used here to understand its effects on reshock timing.

A set of six test section lengths, δ = 23.5, 19.9, 17.2, 13.1, 9.8, and 8 cm with constant $Ma_s = 1.20$ and $At = 0.67$ is considered. Experimental measurements and three-dimensional numerical simulations performed by Leinov *et al.* (12) along with self-similar predictions prior to reshock are used to further evaluate the accuracy of the model. As the values for δ and Ma_s in this study are smaller than those in Chapter III, a modified coefficient set is used for this specific study. A general set

of coefficients applicable to a broader range of parameters is also developed. The evolution of turbulent production and dissipation mechanisms is compared between the two sets of coefficients. Finally, convergence under grid refinement is considered for the mean and turbulent fields in addition to mixing layer widths for each of the six test section lengths.

4.1 Initializing the Model

The model is initialized as discussed in Chapter II for these studies. The six test section lengths used to simulate the experiments are $\delta = 23.5$, 19.9, 17.2, 13.1, 9.8, and 8 cm. The domain is adjusted to smaller lengths in conjunction with decreasing values of δ. It was found that the domain length used in Chapter III for positive Atwood numbers, $X = 161$ cm, was too long for most of the simulations in this chapter, and difficulties were experienced in maintaining stability at lower resolutions. Table 4.1 lists the domains and test section lengths along with simulated experimental times for each of the six cases.

Case		1	2	3	4	5	6
δ	cm	23.5	19.9	17.2	13.1	9.8	8
X	cm	161	121	101	101	71	61
t_{end}	$\times 10^{-3}$ s	3	2.6	2.6	2.2	1.4	1.7

Table 4.1: Test section length δ, domain X, and simulated experimental time t_{end} for $Ma_s = 1.20$ with $At = 0.67$, $K_0 = 0.10$, and $\lambda_{rms} = 0.25$ cm.

The incident shock Mach number and Atwood number are $Ma_s = 1.20$ and $At = 0.67$; air fills the driver section while SF_6 fills the test section. Initial conditions for the turbulent kinetic energy seed and initial perturbation wavelength used in the simulations are $K_0 = 0.10$ and $\lambda_{rms} = 0.25$ cm, respectively. In comparison to simulations discussed in Chapter III, λ_{rms} is reduced to 0.25 cm. This value is comparable to the random perturbations found on the membrane of the experiments,

which have an average wavelength of 0.10 cm (12; 24). This information on the membrane was not available for experiments conducted by Vetter and Sturtevant (10) and Poggi *et al* (11). Three-dimensional numerical data is available only for three of the Leinov *et al.* experiments with test section lengths $\delta = 23.5$, 17.2, and 8 cm. The cases with $\delta = 19.9$, 13.1, and 9.8 cm do not have numerical results for comparison.

The mixing layer width following reshock evolves differently as a result of decreasing δ and Ma_s. The model coefficients used in simulating the experiments in Chapter III do not accurately predict turbulent mixing for the present cases, and the need to introduce a modified coefficient set arises. Table 4.2 compares values for σ_ρ and $C_{\epsilon 0}$ used to simulate the present experiments with those used to predict experiments by Vetter and Sturtevant (10) and Poggi *et al.* (11). Table 4.2 additionally includes a third set of coefficients applicable to a broader range of values for Ma_s, At, and δ; these values are listed as the *General* coefficients. This second coefficient set may not provide as optimal predictions as those intended for specific investigations, but results generated when applied to general studies provide better predictions. The model coefficients, $C_{\epsilon 1}$–$C_{\epsilon 4}$, C_μ, σ_m, σ_U, σ_K, and σ_ϵ, remain unchanged.

Coefficient	Leinov	Vetter, Poggi	General
σ_ρ	0.20	0.90	0.60
$C_{\epsilon 0}$	0.95	0.90	0.90

Table 4.2: Comparison of model coefficients for simulated experiments.

4.2 Model Predictions with Optimal and General Coefficients

The test section lengths used in experiments by Vetter and Sturtevant (10) and Poggi *et al.* (11) ranged between $\delta = 30$ and 110 cm, while those used in experiments by Leinov *et al.* are shorter. Decreasing the test section length affects reshock timing as the distance between the interface and the test section endwall is shortened. To

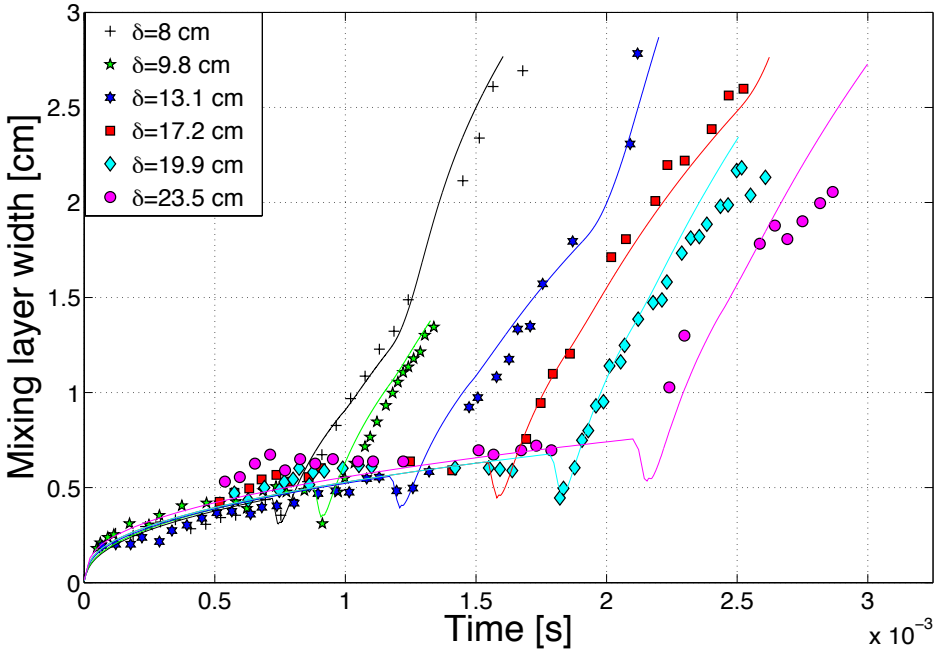

δ	cm	8	9.8	13.1	17.2	19.9	23.5	Mean
$\dot{h}$ (experiment)	$\times 10^3$ cm/s	2.4	2.5	2.2	2.8	2.4	2.1	2.4
$\dot{h}$ (RANS)	$\times 10^3$ cm/s	2.3	2.8	1.8	2.8	2.6	2.6	2.5
τ_R	ms	0.74	0.87	1.16	1.52	1.78	2.10	–

Figure 4.1: Mixing layer widths, growth rate estimates $\dot{h}$ shortly after reshock, and reshock times τ_R for $\delta = 8$, 9.8, 13.1, 17.2, 19.9, 23.5 cm with $Ma_s = 1.20$, $At = 0.67$, $K_0 = 0.10$, $\lambda_{rms} = 0.25$ cm, $\sigma_\rho = 0.20$, and $C_{\epsilon 0} = 0.95$. The experimental data are from Ref. (12).

illustrate the change in reshock timing due to a gradual shortening of the test section, Fig. 4.1 compares model predictions with experimental data for each of the six cases. As expected, the reshock time is delayed as δ increases, where τ_R ranges from 0.72 to 1.78 ms for $\delta = 8$ to 23.5 cm, respectively. In addition to reshock timing variations, the growth rate of the mixing layer width in the post-reshock regime is also of interest. The table compares experimental and model post-reshock growth rates; the mean experimental and model growth rates are 2.4×10^3 and 2.5×10^3 cm/s, respectively. These estimates are calculated as the ratio of the difference in mixing layer width shortly after reshock to the time elapsed.

Predictions using both coefficient sets are presented and discussed in Figs. 4.2–

4.4. Results using $\sigma_\rho = 0.20$ with $C_{\epsilon 0} = 0.95$ and $\sigma_\rho = 0.60$ with $C_{\epsilon 0} = 0.90$ are considered together when evaluating simulated experiments to compare and test the accuracy of each coefficient set. Figure 4.2 shows model predictions, experimental data, and available three-dimensional simulation data for $\delta = 23.5$ and 19.9 cm, respectively. In both cases, using $\sigma_\rho = 0.20$ with $C_{\epsilon 0} = 0.95$ results in a slightly larger early-time mixing width prior to reshock in comparison to $\sigma_\rho = 0.60$ with $C_{\epsilon 0} = 0.90$, as a smaller value in σ_ρ results in additional turbulent mixing due to buoyancy production. The largest difference (≈ 0.05 cm) between widths occurs before reshock. In comparisons with experimental data, a smaller width is predicted at early times with improved agreement closer to reshock. Results for three-dimensional simulations illustrate similar behavior; both numerical approaches follow the evolution of the self-similar solution.

Following reshock, simulations using coefficients specific to the Leinov *et al.* experiments better predict experimental measurements for the mixing layer. The $\delta = 23.5$ cm case in Fig. 4.2 shows the evolution of the mixing layer developing more rapidly using $\sigma_\rho = 0.20$ as smaller values in σ_ρ increase the rate of turbulent kinetic energy generated via buoyancy production. However, dissipative effects can be noted by the slight negative curvature of the width as $C_{\epsilon 0} = 0.95$ also increases the rate at which buoyancy production dissipation is dissipated. Conversely, as σ_ρ increases and $C_{\epsilon 0}$ decreases, the opposite effects occur. Simulations with $\sigma_\rho = 0.60$ and $C_{\epsilon 0} = 0.90$ predict a more gradual development of turbulent mixing after reshock followed by a linear-like evolution indicating prolonged turbulent mixing. The more gradual evolution is due to the larger value of σ_ρ, and weaker dissipation effects are due to the smaller value of $C_{\epsilon 0}$. Many Richtmyer–Meshkov instability experiments, analytical models, and semi-analytical models have predicted a growth linear in time following reshock (37; 58). Similar behavior is also present for $\delta = 19.9$ cm in Figure 4.2. Turbulent mixing between coefficient sets develops in a similar fashion following reshock,

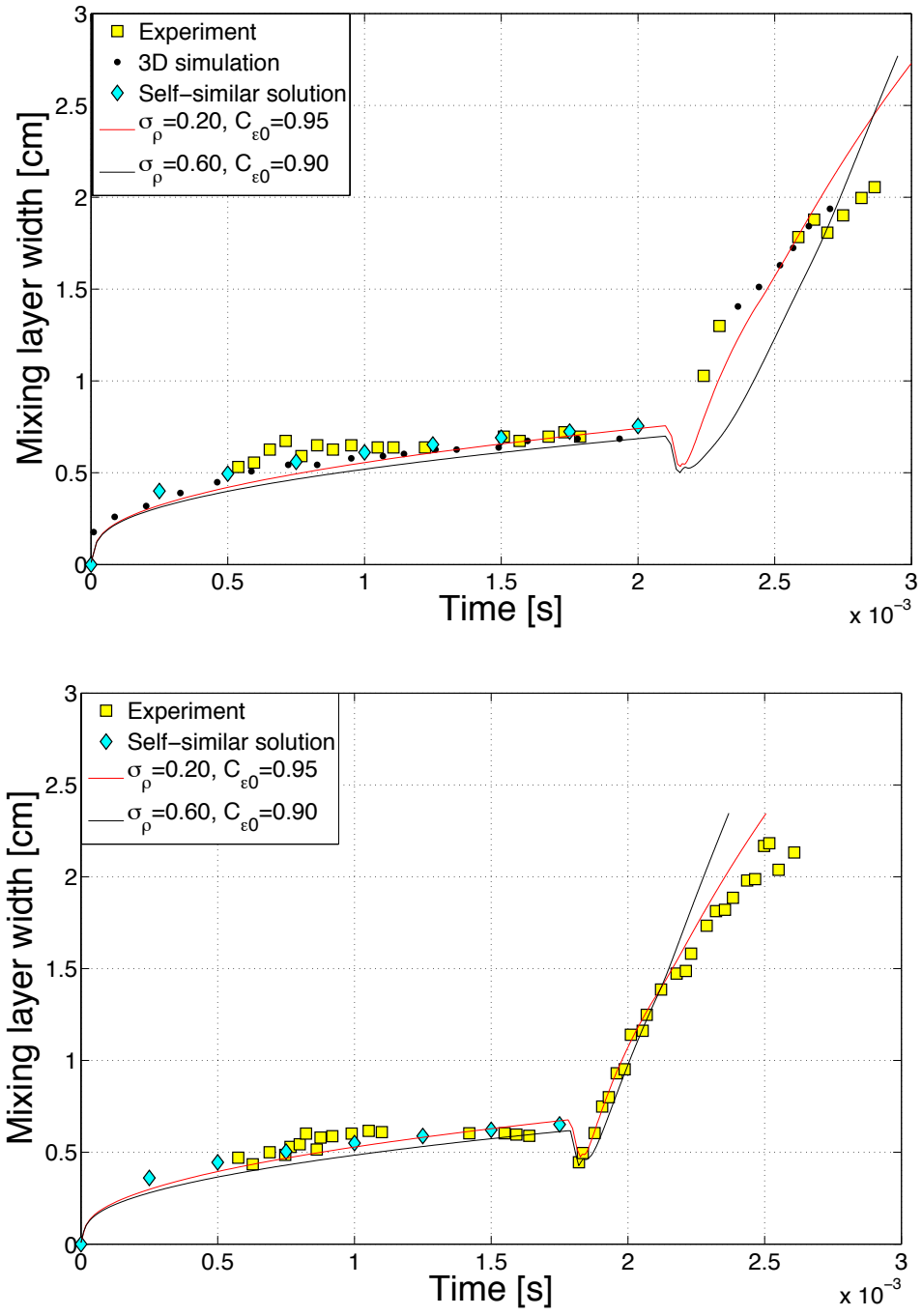

Figure 4.2: Mixing layer widths for $\delta = 23.5$ cm (top) and $\delta = 19.9$ cm (bottom) with $Ma_s = 1.20$, $At = 0.67$, $K_0 = 0.10$, $\lambda_{rms} = 0.25$ cm, $X = 161$ and 121 cm, and $n = 14400$ with $\Delta x = 0.01$ and 0.008 cm. The experimental and simulation data are from Ref. (12) and the self-similar solution is from Eq. (2.27).

and it is not until $t \approx 2.10$ ms that dissipative effects start to become more apparent for $\sigma_\rho = 0.20$ and $C_{\epsilon 0} = 0.95$.

Some differences between the predictions using the two coefficient sets is observed for the intermediate test section lengths. Figure 4.3 illustrates results for $\delta = 17.2$ and 13.1 cm, respectively. Simulations using $\sigma_\rho = 0.20$ and $C_{\epsilon 0} = 0.95$ again produce results agreeing well with experimental data, indicating the rapid growth rate following reshock and dissipative effects shortly thereafter. The model predicts a slightly smaller early-time width for $\delta = 17.2$ cm, but good agreement after reshock. Moreover, three-dimensional simulations and those of the K–ϵ model show nearly the same behavior with minor deviations at later times. The $\delta = 13.1$ cm simulation generates results that accurately predict the turbulent mixing before reshock and agree well with experimental data. For this case, the arrival of the expansion wave can be seen by the increase in the mixing layer width at $\tau_E \approx 2$ ms. By comparison, simulations using the second set of coefficients, $\sigma_\rho = 0.60$ and $C_{\epsilon 0} = 0.90$, produce results that less accurately match experimental data. The early-time mixing width still agrees well with experimental data. However, deviations from the experimental growth rate after reshock are evident. For $\delta = 17.2$ cm, the post-reshock mixing layer begins to evolve similarly to the widths generated with the first coefficient set, but due to the smaller value in $C_{\epsilon 0}$, the turbulent kinetic energy dissipation is weaker and enhanced mixing at later times is seen. Furthermore, the $\delta = 13.1$ cm case shows that the general coefficient set predicts a more gradual mixing layer growth rate after reshock than simulations using the first coefficient set due to the larger value of σ_ρ.

Findings for the two shortest test sections lengths, $\delta = 9.8$ and 8 cm, are shown in Fig. 4.4. For these two cases, the use of both coefficient sets generates good results when simulating these experiments. For the $\delta = 8$ cm case, simulations using both coefficient sets predict slightly less early-time mixing than the experimental data. After reshock, simulation results are very similar and predict the experimental

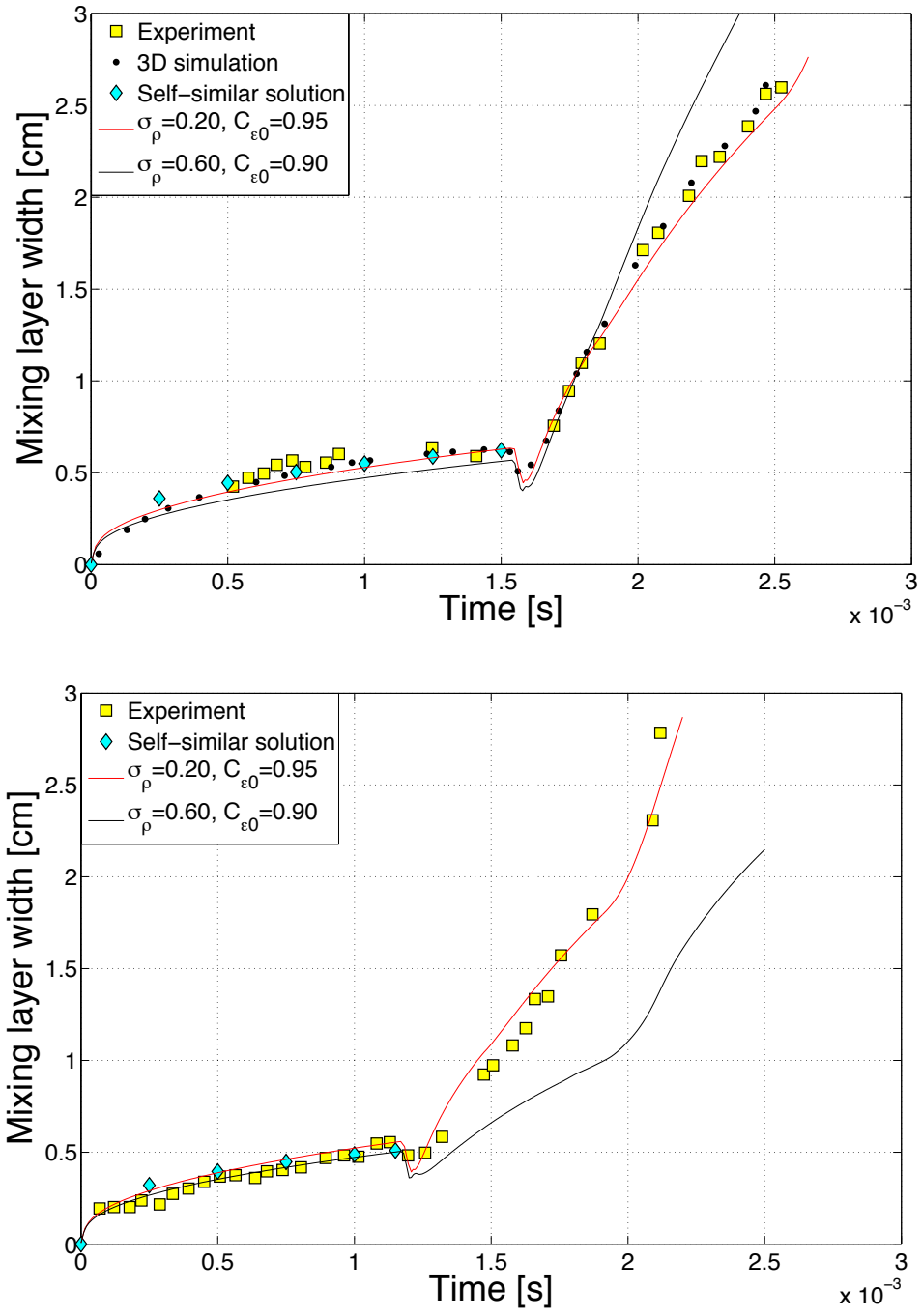

Figure 4.3: Mixing layer widths for $\delta = 17.2$ cm (top) and $\delta = 13.1$ cm (bottom) with $Ma_s = 1.20$, $At = 0.67$, $K_0 = 0.10$, $\lambda_{rms} = 0.25$ cm, $X = 101$ cm, and $n = 14400$ with $\Delta x = 0.007$ cm. The experimental and simulation data are from Ref. (12) and the self-similar solution is from Eq. (2.27).

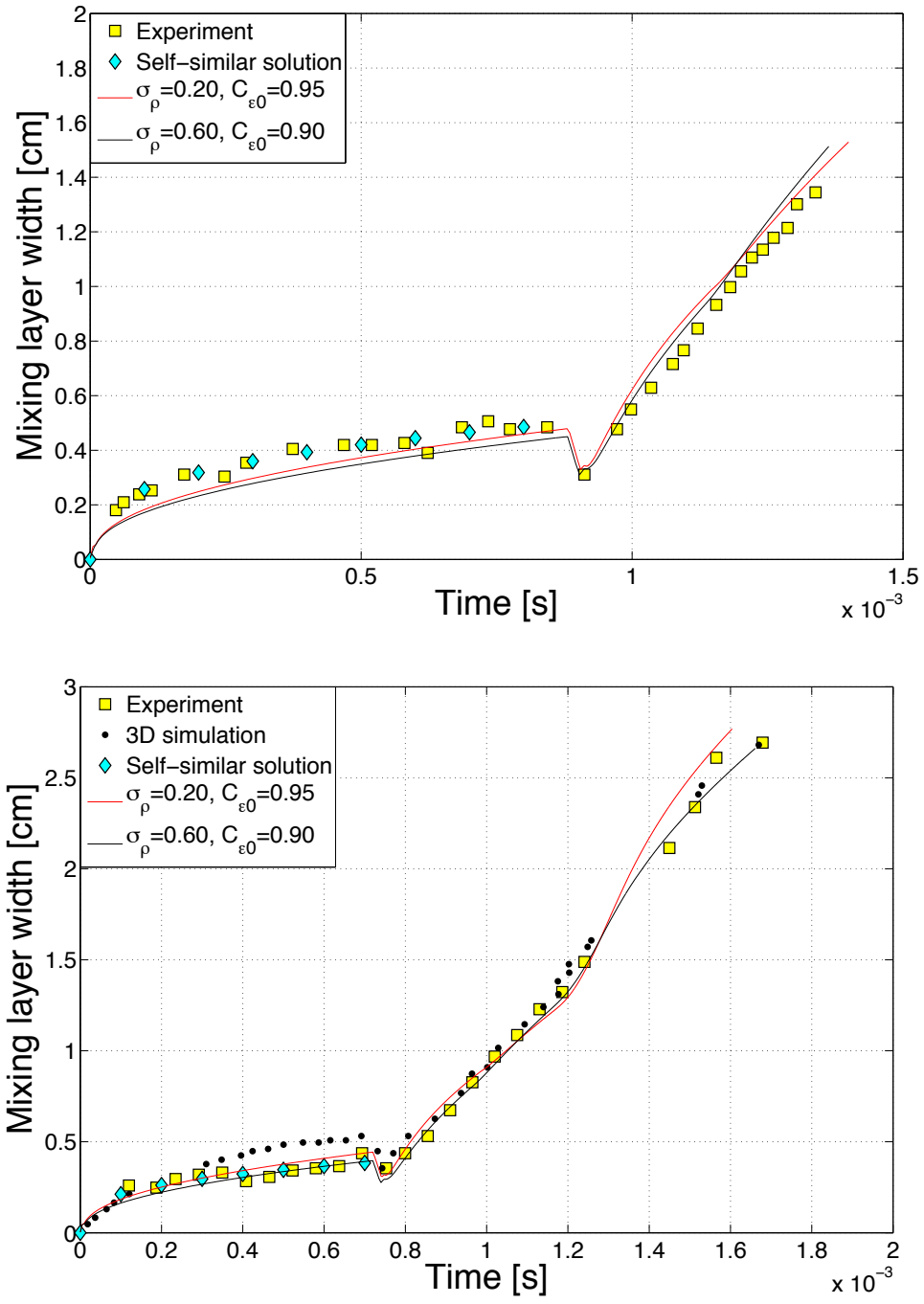

Figure 4.4: Mixing layer widths for $\delta = 9.8$ cm (top) and $\delta = 8$ cm (bottom) with $Ma_s = 1.20$, $At = 0.67$, $K_0 = 0.10$, $\lambda_{rms} = 0.25$ cm, $X = 71$ and 61 cm, and $n = 19200$ with $\Delta x = 0.004$ and 0.003 cm. The experimental and simulation data are from Ref. (12) and the self-similar solution is from Eq. (2.27).

evolution with a slightly larger width. The best results in simulating the mixing layer width were obtained for $\delta = 8$ cm. Both coefficient sets agree with the experimental data; the three-dimensional simulation slightly overpredicts early-time mixing but matches the mixing layer well after reshock. However, there is a small deviation between the widths after reshock. The first is due to the arrival of the expansion wave at $\tau_E \approx 0.97$ ms and the second is due to the rarefaction wave at $\tau_F \approx 1.27$ ms, where the first coefficient set predicts a slightly larger growth rate. Due to the smaller test sections, simulations for $\delta = 9.8$ and 8 cm were conducted with finer grids using $n = 19200$ points, in comparison to the first four cases with $n = 14400$ points. Convergence under grid refinement for each case is discussed in Sec. 4.5.

4.3 Extension of the Model to Accommodate Various Atwood and Shock Mach Numbers

Section 4.2 presented and discussed simulation results using both coefficient sets for the Leinov *et al.* experiments (12). The model is extended to a broader range of shock Mach numbers, Atwood numbers, and test section here by reconsidering the experiments by Vetter and Sturtevant (10) and Poggi *et al.* (11) presented in Chapter III: an optimal set of coefficients was obtained with values listed in Table 4.2. Simulations using these values produced results in good agreement with experimental data. Figures 3.2, 3.11, and 3.19 compare model predictions with experimental measurements for $Ma_s = 1.24$, 1.50, and 1.98 with $\delta = 110$, 61, and 49 cm, respectively, and $At = 0.67$. Results for $Ma_s = 1.45$ with $At = -0.67$ and $\delta = 30$ cm are available in Figure 3.25.

Figure 4.5 summarizes mixing layer evolutions for the $At = 0.67$ cases listed above using $\sigma_\rho = 0.90$ with $C_{\epsilon 0} = 0.90$ (dashed lines) and $\sigma_\rho = 0.60$ with $C_{\epsilon 0} = 0.90$ (solid lines). The buoyancy production of the dissipation rate is scaled by $C_{\epsilon 0}$ for both co-

efficient sets, but more turbulent mixing is expected with $\sigma_\rho = 0.60$. Moreover, recall that from Sec. 3.3 changes in these coefficients have minimal influence on early-time mixing. Therefore, differences between predictions are expected mainly in the post-reshock region. The initial conditions and remaining model coefficients remain unchanged for each case. The mixing layer width for $Ma_s = 1.20$ with $\delta = 8$ cm is additionally included as a reference for comparing results from Sec. 4.2. For $Ma_s = 1.98$ with $\delta = 49$ cm, both coefficient sets produce very similar results that agree well with experimental data. This is indicative of the ability to apply the general coefficient set to a case with δ approximately twice as long as the longest test section used in the Leinov *et al.* experiments with an $\approx 60\%$ increase in Mach number, and still obtain accurate predictions. As the test section is increased to $\delta = 61$ cm for the $Ma_s = 1.50$ case, reshock occurs later in time. Predictions between coefficient sets are similar during early-time mixing. However, following compression of the interface, differences in the predicted growth rates are apparent: turbulent mixing is enhanced via buoyancy production by decreasing σ_ρ from 0.90 to 0.60 and additional turbulent kinetic energy is produced after reshock. Although results generated using $\sigma_\rho = 0.60$ are not as accurate in matching the experimental data as those with $\sigma_\rho = 0.90$, the model still predicts the evolution of the mixing layer width fairly well, but with a slightly larger mixing rate. Similar behavior is seen for the $Ma_s = 1.24$ case. Simulations using the optimal coefficient set are in good agreement with experimental data, while the predictions using $\sigma_\rho = 0.60$ predict slightly more mixing after reshock. Comparing these three cases, small deviations from experimental data gradually increase when using the general coefficient set, but a larger range of applicability is demonstrated.

Similarly, Fig. 4.6 shows the predicted mixing layer width for $Ma_s = 1.45$ with $At = -0.67$ and $\delta = 30$ cm. For this set of simulations the initial conditions are $K_0 = 0.10$ and $\lambda_{rms} = 1.25$ cm. Using these initial conditions results in good agreement between the predicted width and experimental data before reshock. However, the

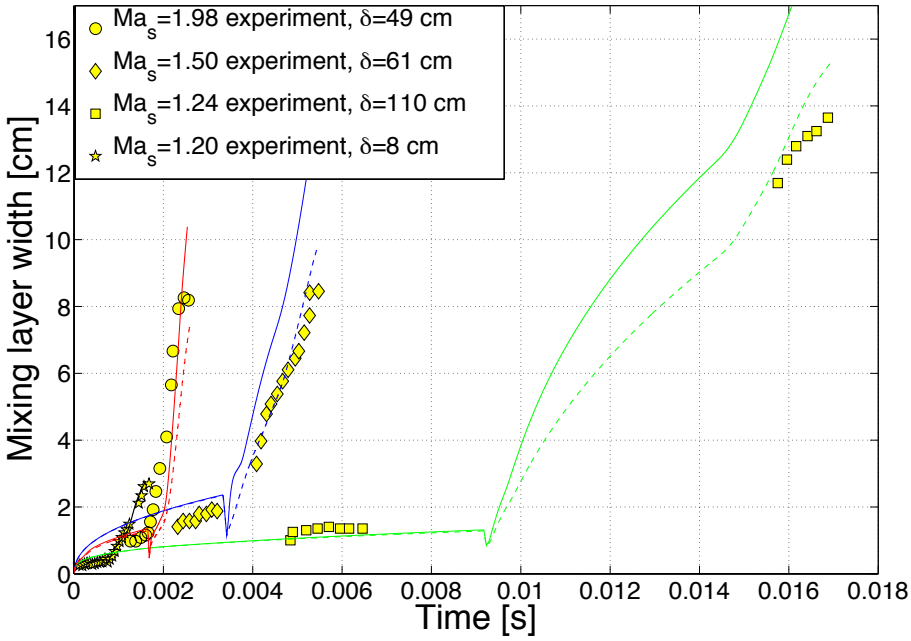

Figure 4.5: Comparison of mixing layer widths for $Ma_s = 1.20$, 1.24, 1.50, 1.98 with $\delta = 8$, 110, 61, 49 cm, respectively, and $At = 0.67$, $\sigma_\rho = 0.60$ (solid lines) and 0.90 (dashed lines), and $C_{\epsilon 0} = 0.90$. The experimental data are from Refs. (10; 12).

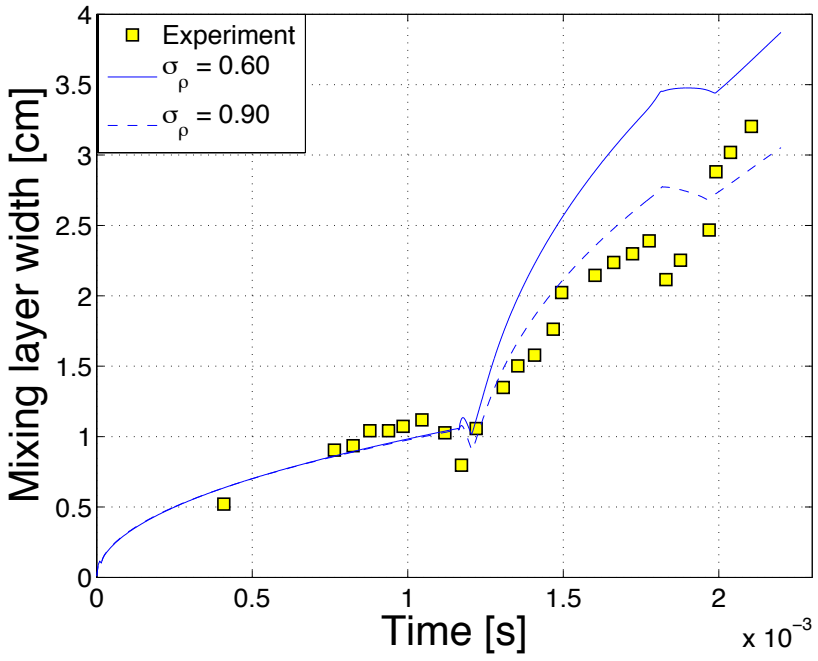

Figure 4.6: Comparison of mixing layer widths for $Ma_s = 1.45$ with $\delta = 30$ cm and $At = -0.67$, $\sigma_\rho = 0.60$ (solid) and 0.90 (dashed), and $C_{\epsilon 0} = 0.90$. The experimental data are from Ref. (11).

post-reshock width overpredicts the experimental data when using $\sigma_\rho = 0.60$ in the extended coefficient set. This occurs for the same reason as discussed above for the $Ma_s = 1.50$ and 1.24 cases. The original width generated after reshock with the optimal value $\sigma_\rho = 0.90$ qualitatively follows the behavior seen in the experiment. Attempting to establish a general set of model coefficients that accommodates a wide range of δ, At, and Ma_s is challenging, and will likely provide predictions that are less optimal for some cases that are very well predicted using a specific set of coefficients.

To further understand differences in the predictions between simulation sets, Table 4.3 lists approximate mixing layer growth rates $\dot{h}$ following reshock for each case. As expected, the growth rate is generally larger for $\sigma_\rho = 0.60$ as the buoyancy production generates a larger turbulent kinetic energy for mixing. The mixing rate also increases with larger shock Mach numbers, which has already been discussed in Sec. 3.2. Finally, a third way to increase the post-reshock mixing layer growth rate is by reversing the order of the gases, such that the denser gas occupies the driver section: as the shock is generated very close to the interface, minimal energy is deposited within the original gas at the onset of the simulation. This results in a front of the denser gas accelerating the lighter gas in the test section. As the shock travels in the test section after crossing the interface, it requires less energy to travel through a lighter gas, resulting in less energy expended in reflecting from the endwall and reshocking the interface. Therefore, the shock arrives in a more energetic state, and more turbulent kinetic energy is available for mixing. Table 4.3 also shows that the growth rate for $Ma_s = 1.45$ is very close to that of $Ma_s = 1.98$ for simulations with $\sigma_\rho = 0.60$. However, using $\sigma_\rho = 0.90$ would result in more confidence when making such comparisons, as this value is part of an optimal coefficient set for the $Ma_s = 1.98$, 1.50, 1.45, and 1.24 experiments.

Ma_s		1.98	1.50	1.24	1.20	1.45
At		0.67	0.67	0.67	0.67	-0.67
$\dot{h}_{\sigma_\rho=0.90}$	$\times 10^3$ cm/s	13	2	1.3	–	5
$\dot{h}_{\sigma_\rho=0.60}$	$\times 10^3$ cm/s	13	2.7	3.4	2.2	10

Table 4.3: Approximate mixing layer growth rates after reshock for $\sigma_\rho = 0.60$ and 0.90, $C_{\epsilon 0} = 0.90$, and $Ma_s = 1.98$, 1.50, 1.24, 1.20 with $At = 0.67$ and $Ma_s = 1.45$ with $At = -0.67$.

4.4 Evaluation of Production and Dissipation Mechanisms

Simulation sets for predicting the mixing layer width were compared in Sec. 4.2, while the generalized set of coefficients was applied to a broader range of experiments in Sec. 4.3. The mechanisms contributing to the production and dissipation of turbulent kinetic energy for experiments conducted by Leinov *et al.* (12) are evaluated in this section. The study with $\delta = 8$ cm is considered due to the various events that are observed during the experiment. Compression of the interface at reshock and arrival of the expansion wave occur at $\tau_R \approx 0.74$ and $\tau_E \approx 0.97$ ms, respectively, while development of the rarefaction wave can be seen at $\tau_F \approx 1.27$ ms. Budgets for the turbulent kinetic energy and dissipation rate are considered at $t = 0.80$, 1.0, 1.2, and 1.4 ms to examine the evolution of the mechanisms throughout these events. Note that the interface has been reshocked and the waves are propagating to the left, away from the test section endwall.

Figure 4.7 shows the terms in the turbulent kinetic energy budgets. The top two rows show the evolution of the turbulent kinetic energy buoyancy production (solid lines) and diffusion (dashed lines). Prior to reshock the majority of the buoyancy production is concentrated in the vicinity of the shock. At $t = 0.80$ ms immediately after reshock, this behavior can still be seen in both simulation sets. Contributions with larger magnitudes are seen for $\sigma_\rho = 0.20$, as expected. Diffusive effects can also be observed as turbulent kinetic energy generated by the buoyancy term is spread to enhance turbulent mixing. Diffusion is also stronger for $\sigma_\rho = 0.20$. At $t = 1.00$

ms, the magnitudes of these terms remain relatively unchanged because additional turbulent kinetic energy is supplied by the arrival of the expansion wave at $\tau_E \approx 0.97$ ms. This can be seen in the turning point of the slope of the mixing layer at this time (the effect is more easily seen for the $\sigma_\rho = 0.20$ case). As time progresses to $t = 1.20$ ms, the magnitudes of these terms decrease as the turbulent kinetic energy is diffused and dissipated. In addition to the smaller magnitudes, the area under the profiles has increased, indicating that the spreading of turbulent kinetic energy is increasing as time progresses. This is further supported by noting that the mixing layer width continues to grow with time in Fig. 4.4. Finally at $t = 1.4$ ms, these terms continue to decrease in magnitude and spread spatially as the turbulent kinetic energy continues to supply the mixing process.

The bottom two rows in Fig. 4.7 show the shear production (solid lines) and dissipation rate (dashed lines) of turbulent kinetic energy. Immediately after reshock at $t = 0.80$ ms, the enhanced turbulent mixing has not yet fully developed. Recall that changes in σ_ρ and $C_{\epsilon 0}$ have minimal effect on early-time mixing; thus, the structure and magnitude of the shear production is very similar despite variations in σ_ρ and $C_{\epsilon 0}$. After reshock, the shear production has a secondary role in turbulent mixing (and evolution of the mixing layer width) as much of the mixing is initiated from changes in pressure and density due to shock compression of the layer. Mixing from shear production contributions are due to changes in velocity after compression of the interface. Comparing the magnitudes of the shear production to the buoyancy production, the former accounts for $\approx 5\%$ of the turbulent kinetic energy supply after reshock. The dissipation rate has an even smaller role: Fig. 4.7 shows that this term is negligible in comparison to the other terms. From prior observations, dissipation is large behind the shock front: as the shock progresses, a trail of energy dissipates as it heats the gas in its path. Furthermore, a significant amount of energy is dissipated and converted into heat as the interface is compressed.

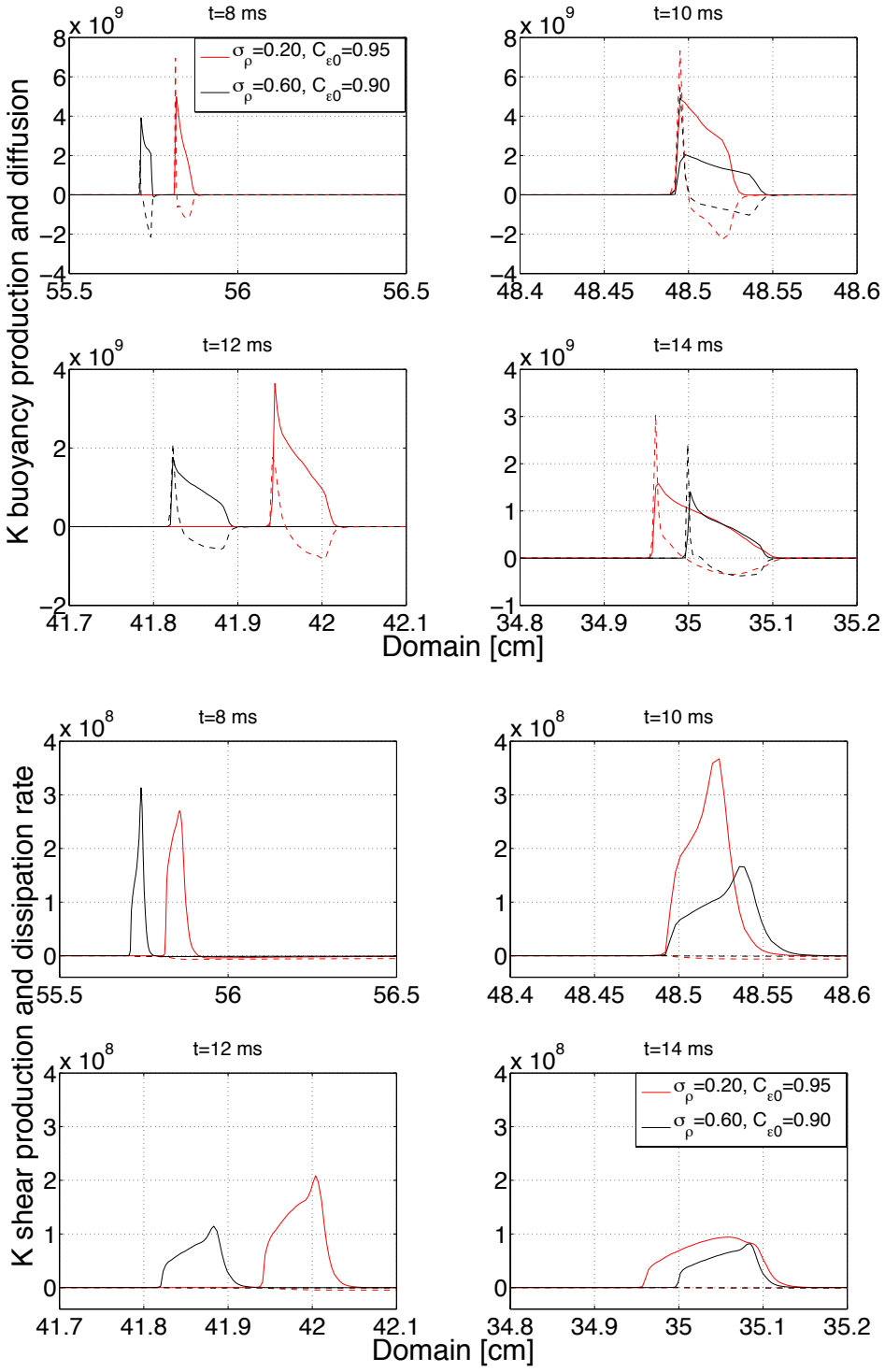

Figure 4.7: Turbulent kinetic energy budgets [g/cm-s^3] for $Ma_s = 1.20$, $At = 0.67$, and $\delta = 8$ cm, $\sigma_\rho = 0.20$ and 0.60, and $C_{\epsilon 0} = 0.90$ and 0.95. The buoyancy and shear production terms are represented by solid lines and diffusion and dissipation terms are represented by dashed lines.

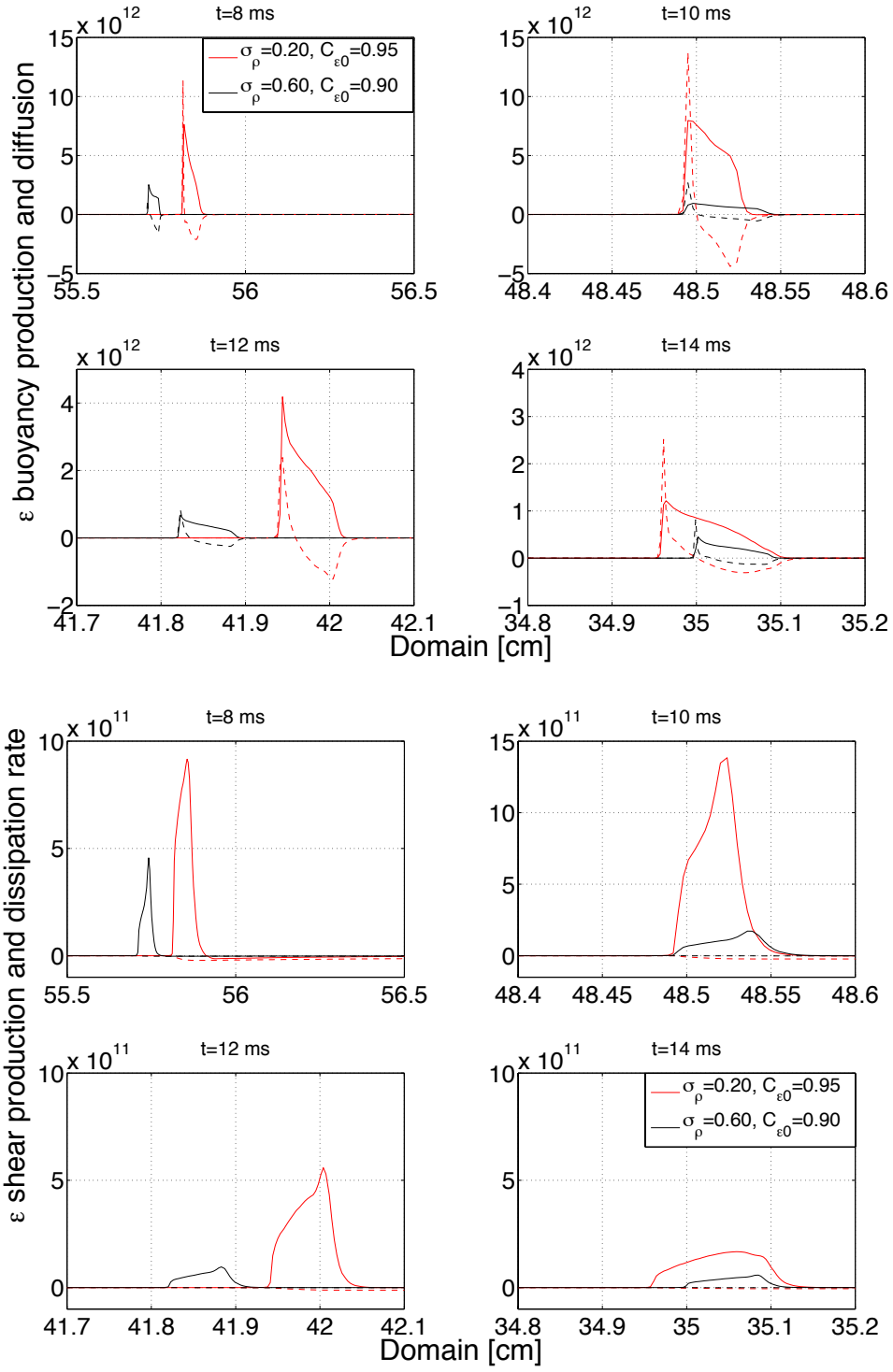

Figure 4.8: Turbulent kinetic energy dissipation rate budgets [g/cm-s^4] for $Ma_s = 1.20$, $At = 0.67$, and $\delta = 8$ cm, $\sigma_\rho = 0.20$ and 0.60, and $C_{\epsilon 0} = 0.90$ and 0.95. The buoyancy and shear production terms are represented by solid lines and diffusion and dissipation terms are represented by dashed lines.

The production, diffusion, and dissipation terms for the turbulent kinetic energy dissipation rate are presented in Fig. 4.8. The evolution and profiles of the terms are similar to those of the turbulent kinetic energy in Fig. 4.7 due to the proportionality relating ϵ to K. However, differences between coefficients sets are more apparent for the dissipation rate as this quantity is directly affected by both σ_ρ and $C_{\epsilon 0}$, whereas the turbulent kinetic energy is not directly affected by $C_{\epsilon 0}$. As the model is more sensitive to changes in $C_{\epsilon 0}$ as discussed in Sec. 3.3, dissipative effects become larger as this model coefficient increases from 0.90 to 0.95.

4.5 Convergence Under Grid Refinement

Convergence studies for each of the six experiments performed by Leinov *et al.* (12) are presented here. Results for the mean and turbulent fields in addition to the mixing layer widths are presented and discussed. These studies were conducted for the optimal set of coefficients using $\sigma_\rho = 0.20$ and $C_{\epsilon 0} = 0.95$, which are specific to these experiments. Furthermore, as the different domains can vary between cases, Table 4.4 gives the grid spacings for each domain used.

Number of points, n		4800	7200	9600	14400	19200
Δx_{161}	cm	0.034	0.022	0.017	0.011	0.008
Δx_{121}	cm	0.025	0.017	0.013	0.008	0.006
Δx_{101}	cm	0.021	0.014	0.011	0.007	0.005
Δx_{71}	cm	0.015	0.010	0.007	0.005	0.004
Δx_{61}	cm	0.013	0.008	0.006	0.004	0.003

Table 4.4: Grid resolutions for the Leinov *et al.* simulations with domain lengths $X = 161$, 121, 101, 71, and 61 cm.

4.5.1 Mixing layer widths

Convergence results for the $\delta = 23.5$ and 19.9 cm cases are presented in Fig. 4.9. Using a coarse mesh with $n = 4800$ points does not accurately represent the mixing

layer width, and some inaccuracy is still evident when using $n = 7200$ and 9600 points. A finer grid using $n = 14400$ and 19200 points is necessary for the width to approach convergence for both cases. Profiles generated using these resolutions produce similar results prior to reshock and for some times after reshock. A small divergence is noted at later times after the arrival of the expansion wave.

Figure 4.10 illustrates mixing layer width convergence results for the intermediate test section lengths, $\delta = 17.2$ and 13.1 cm. Similarly, using $n = 4800$, 7200, and 9600 points does not accurately predict the experimental mixing layer width. Simulations with $n = 14400$ and 19200 points produce a small loss of accuracy in the early-time width. In the post-reshock regime, a divergence between profiles similar to that in Fig. 4.9 is evident, but occurs earlier in time: as the test section is progressively decreased in length, the arrival of the expansion wave occurs at earlier times. Moreover, convergence is more difficult to achieve at the interface due to the strong mixing processes. Given the closer proximity of the interface to the test section endwall with shorter test section lengths, oscillations from secondary wave interactions can overlap, inhibiting convergence.

Finally, results for the $\delta = 9.8$ and 8 cm cases are presented in Fig. 4.11. As the test section length is reduced further to these values, difficulty in achieving convergence for the mixing layer width becomes more apparent. Although simulations using $n = 14400$ and 19200 points generate similar early-time widths, the rate of convergence is slower in the post-reshock region due to secondary waves reflecting from the test section endwall and interacting with the interface, which is now situated closer compared to the larger δ cases. For example, the $\delta = 8$ cm case experiences reshock and arrival of the expansion wave at $\tau_R \approx 0.74$ and $\tau_E \approx 0.97$ ms, respectively. Shock and secondary wave interactions with the interface and the reflecting boundary at the endwall in such a short time frame can inhibit convergence of the mixing layer width.

Similar results were observed in the convergence investigations of Sec. 3.5. The

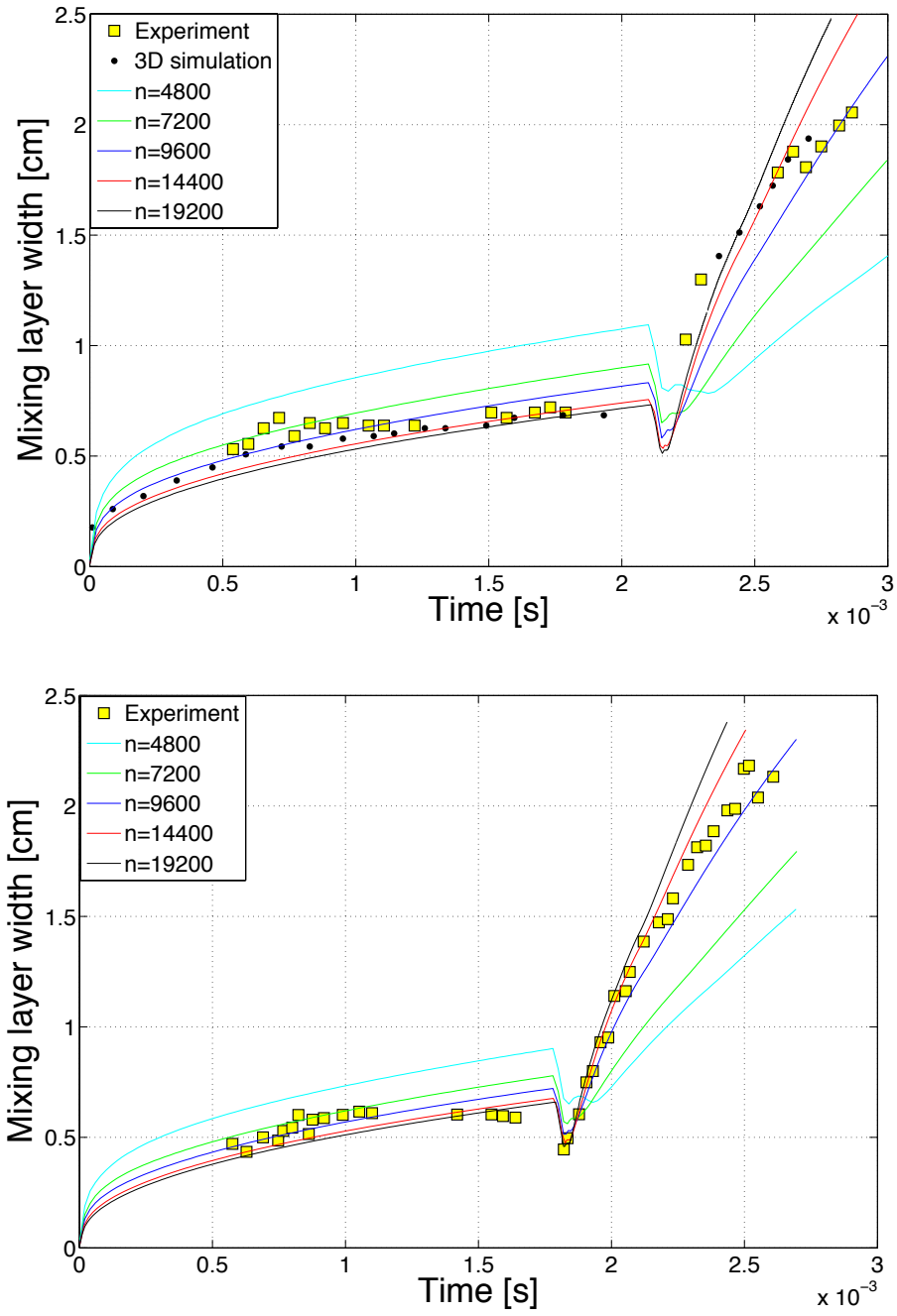

Figure 4.9: Mixing layer convergence for $\delta = 23.5$ cm (top) and $\delta = 19.9$ cm (bottom) with $Ma_s = 1.20$, $At = 0.67$, $K_0 = 0.10$, $\lambda_{rms} = 0.25$ cm, $\sigma_\rho = 0.20$, and $C_{\epsilon 0} = 0.95$. The experimental and simulation data are from Ref. (12).

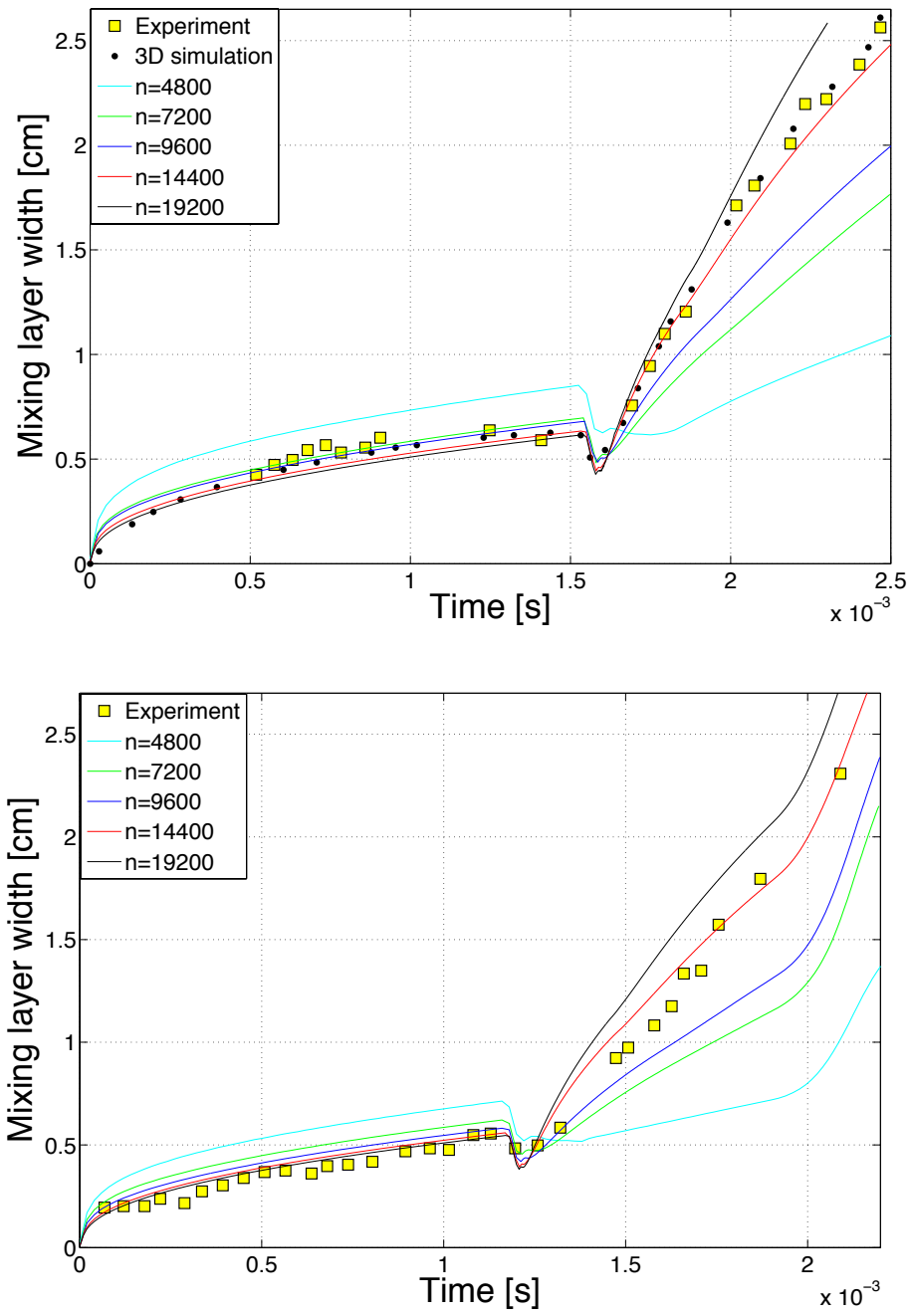

Figure 4.10: Mixing layer convergence for $\delta = 17.2$ cm (top) and $\delta = 13.1$ cm (bottom) with $Ma_s = 1.20$, $At = 0.67$, $K_0 = 0.10$, $\lambda_{rms} = 0.25$ cm, $\sigma_\rho = 0.20$, and $C_{\epsilon 0} = 0.95$. The experimental and simulation data are from Ref. (12).

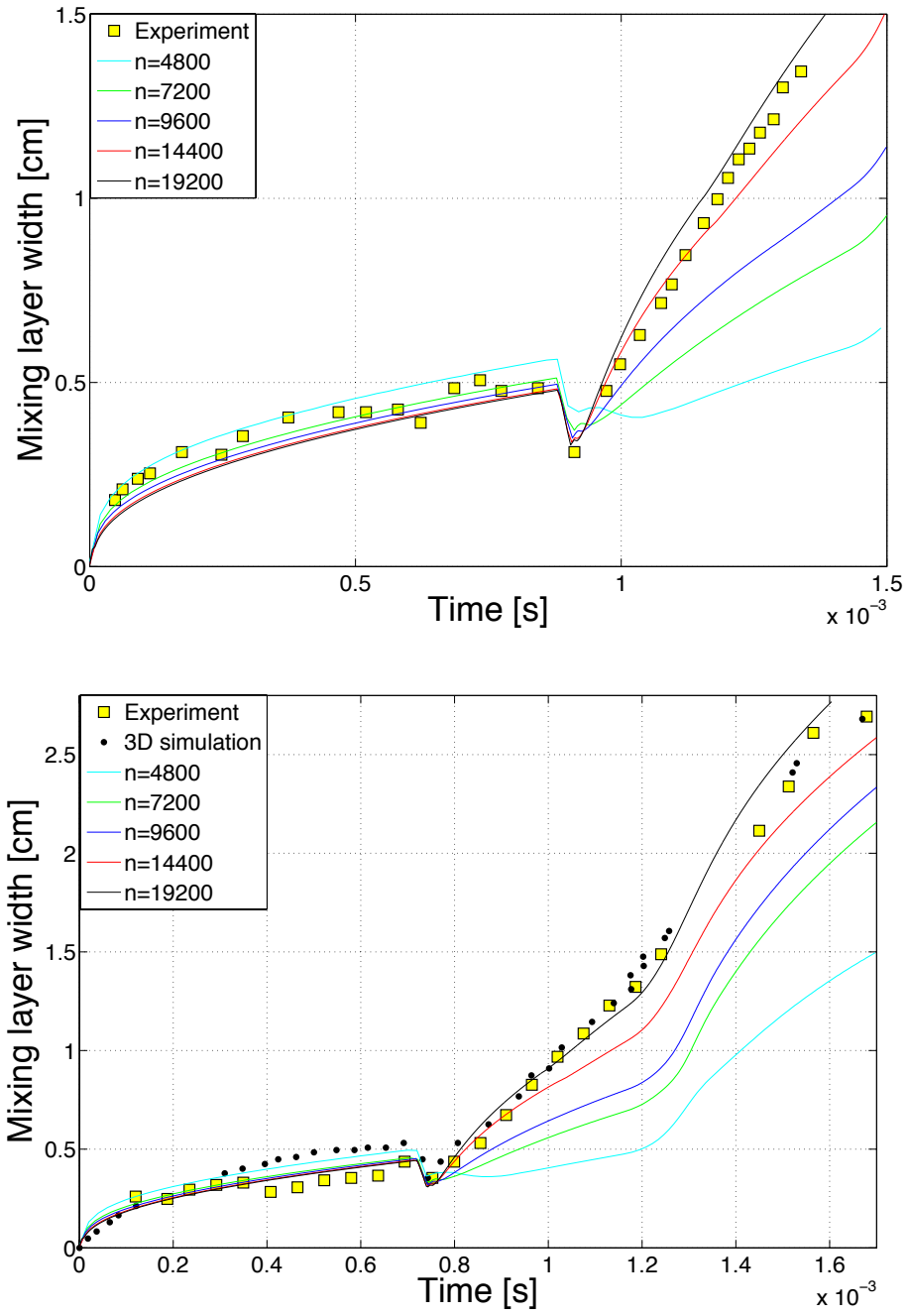

Figure 4.11: Mixing layer convergence for $\delta = 9.8$ cm (top) and $\delta = 8$ cm (bottom) with $Ma_s = 1.20$, $At = 0.67$, $K_0 = 0.10$, $\lambda_{rms} = 0.25$ cm, $\sigma_\rho = 0.20$, and $C_{\epsilon 0} = 0.95$. The experimental and simulation data are from Ref. (12).

$Ma_s = 1.50$ and 1.24 experiments (10) had test section lengths, $\delta = 61$ and 110 cm, respectively. Convergence was achieved for these cases between $n = 7200$ and 9600 points with minimal error. As the test section length decreased further to $\delta = 49$ cm for the $Ma_s = 1.98$ case, the rate of convergence decreased. The $Ma_s = 1.45$ investigation had the smallest test section length in Chapter III, where $\delta = 30$ cm. Similar diverging behavior following reshock observed for this case is also evident in the present studies. These cases further show that shortening the test section length inhibits convergence due to the closer proximity of the interface to the endwall and secondary wave interactions within shorter time intervals.

4.5.2 Convergence of the mean fields

Mean field studies under grid refinement consider a time after reshock for each of the six cases in the Leinov *et al.* experiments. As variations in reshock timing via test section length adjustments and post-reshock mixing are of interest, grid refinement for the mean fields is evaluated at different times following reshock. Figure 4.12 shows convergence results for the mean density, pressure, heavy mass fraction, and velocity for the $\delta = 23.5$ and 19.9 cm cases. The reshock times for these experiments are $\tau_R \approx$ 2.10 and 1.78 ms, respectively, and convergence for these cases is evaluated at $t = 2.50$ and 2.00 ms. In both cases, the density and heavy mass fraction require less points for convergence: using $n = 9600$ points for these two fields shows good agreement with results generated using $n = 14400$ and 19200 points. The pressure and velocity profiles similarly demonstrate that away from the interface, good agreement is established with $n = 9600$ points. However, in the vicinity of the interface, convergence is delayed and additional points are necessary to achieve convergence. This effect can be partly due to the transmitted and reflected waves departing from the interface following the compression at reshock. Behind these waves, convergence is also approached at a slower rate. Grids with $n = 4800$, 7200, and 9600 points demonstrate difficulty in

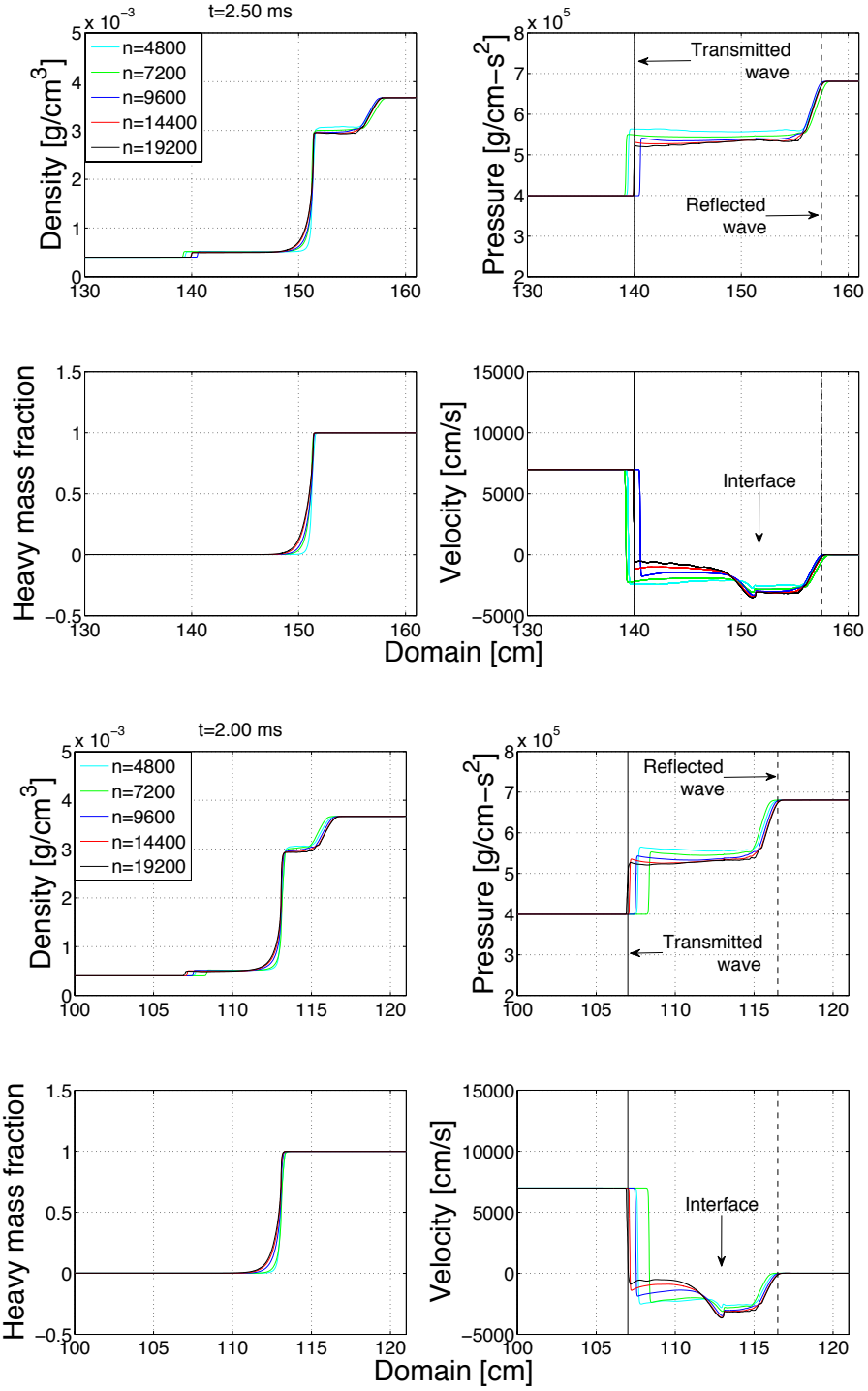

Figure 4.12: Mean field convergence for $\delta = 23.5$ cm at $t = 2.50$ ms (top) and $\delta = 19.9$ cm at $t = 2.00$ ms (bottom) with $Ma_s = 1.20$, $At = 0.67$, $K_0 = 0.10$, $\lambda_{rms} = 0.25$ cm, $\sigma_\rho = 0.20$, and $C_{\epsilon 0} = 0.95$.

accurately predicting the evolutions near the mixing region.

Results for the intermediate cases with $\delta = 17.2$ and 13.1 cm are shown in Fig. 4.13. Reshock for these cases occurs at $\tau_R \approx 1.52$ and 1.16 ms, respectively. Corresponding times are taken at 2.00 and 1.60 ms to evaluate convergence properties following reshock. Similar results to those presented in Fig. 4.12 for the density and heavy mass fraction are obtained in these cases, where good agreement is achieved with $n = 9600$ points. The $\delta = 17.2$ cm case shows the reflected wave from reshock approaching the test section endwall and initiating the first stages of the expansion wave. At the right boundary, initial oscillations are evident as the wave reflects from the endwall. Furthermore, although interface convergence occurs at a slower rate, good agreement is reestablished as the transmitted and reflected waves become more distant from the interface. The velocity profiles also demonstrate a slower rate of convergence, primarily behind the transmitted wave. The $\delta = 13.1$ cm case is an example showing where the expansion wave has arrived. The pressure profile at the right boundary exhibits further oscillations from secondary wave interactions with the reflecting boundary. The velocity demonstrates additional oscillation behind the shock in comparison with the $\delta = 17.2$ cm case. However, the velocity displays minimal oscillation from interaction with the reflecting endwall in comparison to the pressure in both cases.

Convergence of simulations for $\delta = 9.8$ and 8 cm is shown in Fig. 4.14. Reshock times are $\tau_R \approx 0.87$ and 0.74 ms, respectively, and convergence is considered at $t =$ 1.00 and 0.80 ms. Like results for the mixing layer width in Fig. 4.11, grid refinement is necessary to achieve convergence for these shorter test sections, particularly near the mixing region. This is seen in the pressure and velocity profiles as the transmitted and reflected waves emerge from the mixing layer after reshock. It is expected that as the reflected wave approaches the endwall, additional oscillations will develop. However, it is also expected that convergence will improve as the waves become more

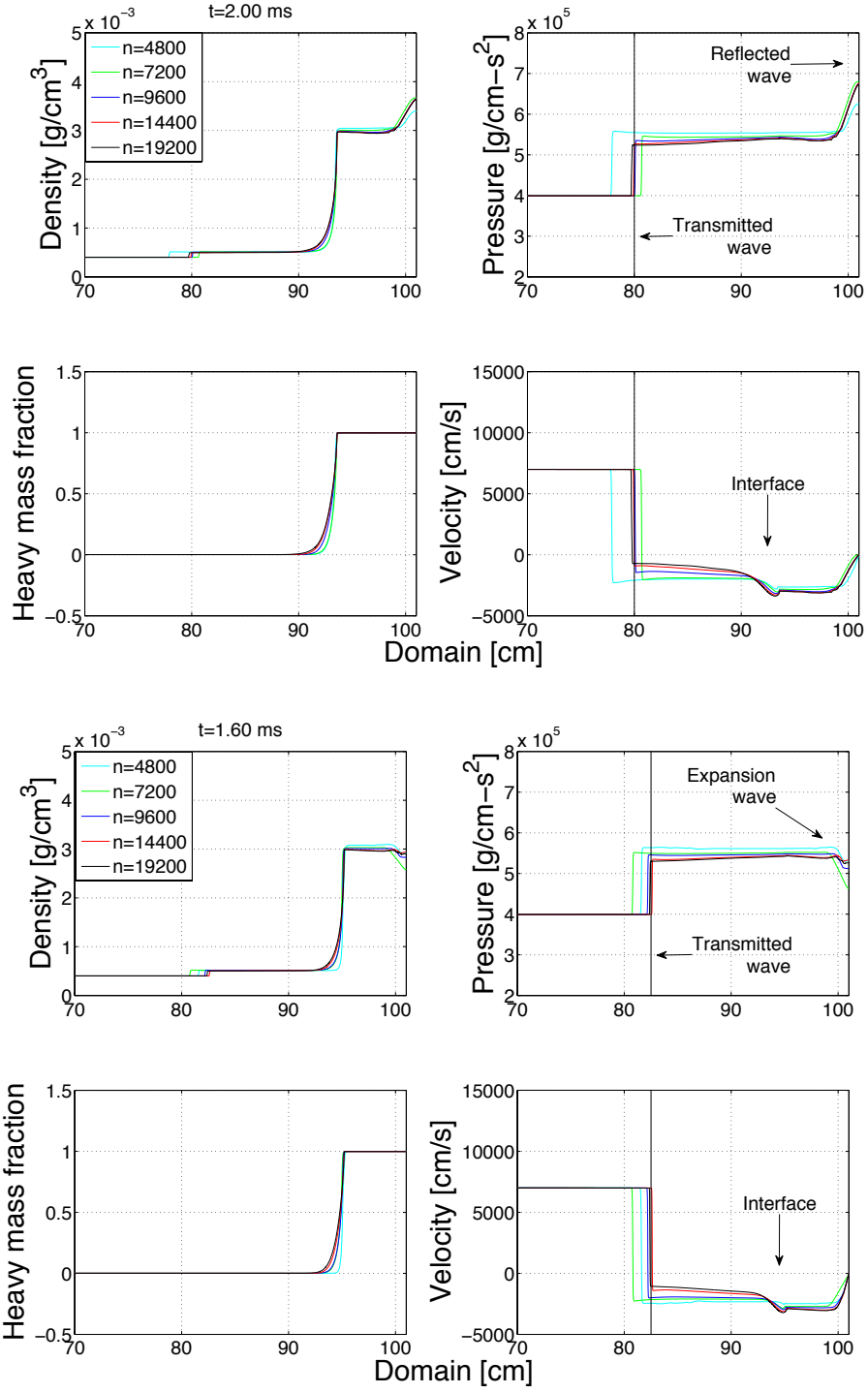

Figure 4.13: Mean field convergence for $\delta = 17.2$ cm at $t = 2$ ms (top) and $\delta = 13.1$ cm at $t = 1.6$ ms (bottom) with $Ma_s = 1.20$, $At = 0.67$, $K_0 = 0.10$, $\lambda_{rms} = 0.25$ cm, $\sigma_\rho = 0.20$, and $C_{\epsilon 0} = 0.95$.

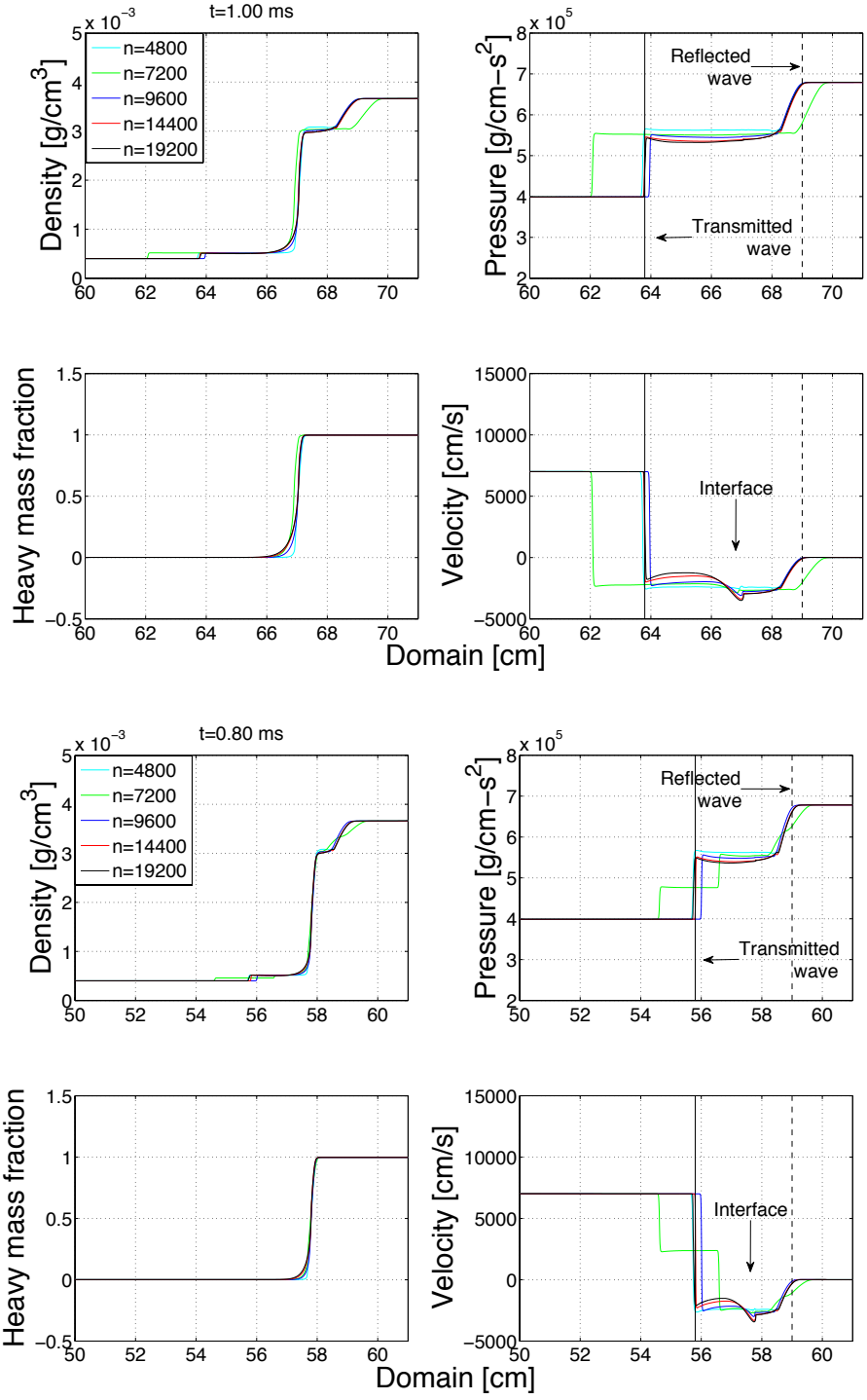

Figure 4.14: Mean field convergence for $\delta = 9.8$ cm at $t = 1$ ms (top) and $\delta = 8$ cm at $t = 0.8$ ms (bottom) with $Ma_s = 1.20$, $At = 0.67$, $K_0 = 0.10$, $\lambda_{rms} = 0.25$ cm, $\sigma_\rho = 0.20$, and $C_{\epsilon 0} = 0.95$.

distant from the interface.

4.5.3 Convergence of the turbulent fields

Turbulent field convergence is evaluated at the same times after reshock for each case considered. The quantities considered are the turbulent kinetic energy K, the turbulent kinetic energy dissipation rate ϵ, and the turbulent viscosity ν_T.

Studies for $\delta = 23.5$ and 1.99 cm are presented in Fig. 4.15. Turbulence effects after reshock principally occur between the transmitted wave and the interface where mixing is enhanced. Turbulent effects ahead of the transmitted wave and in the unmixed region in the test section are minimal. Figure 4.15 further shows that convergence is more difficult to achieve near the mixing region, but as the transmitted wave becomes more distant, convergence improves. For example, in the $\delta = 23.5$ cm case the transmitted shock is ≈ 12 cm away from the interface at $t = 2.50$ ms, and gradual convergence is apparent. Conversely, in the $\delta = 19.9$ cm case, the transmitted wave is ≈ 6 cm away from the interface at $t = 2.00$ ms, and weak convergence is apparent. Moreover, the dissipation rate converges slower than the turbulent kinetic energy and turbulent viscosity. Convergence results for the intermediate test section lengths, $\delta = 17.2$ and 13.1 cm are shown in Fig. 4.16. Similar convergence properties are seen as in the preceding two cases illustrated in Fig. 4.15: the turbulent kinetic energy and the turbulent viscosity show more rapid convergence than the dissipation rate, with converging behavior away from the interface. Grid refinement for $\delta = 9.8$ and 8 cm is considered in Fig. 4.17, where the turbulent kinetic energy and dissipation rate appear to approach convergence when using $n = 14400$ and 19200 points. However, the turbulent viscosity shows slower convergence.

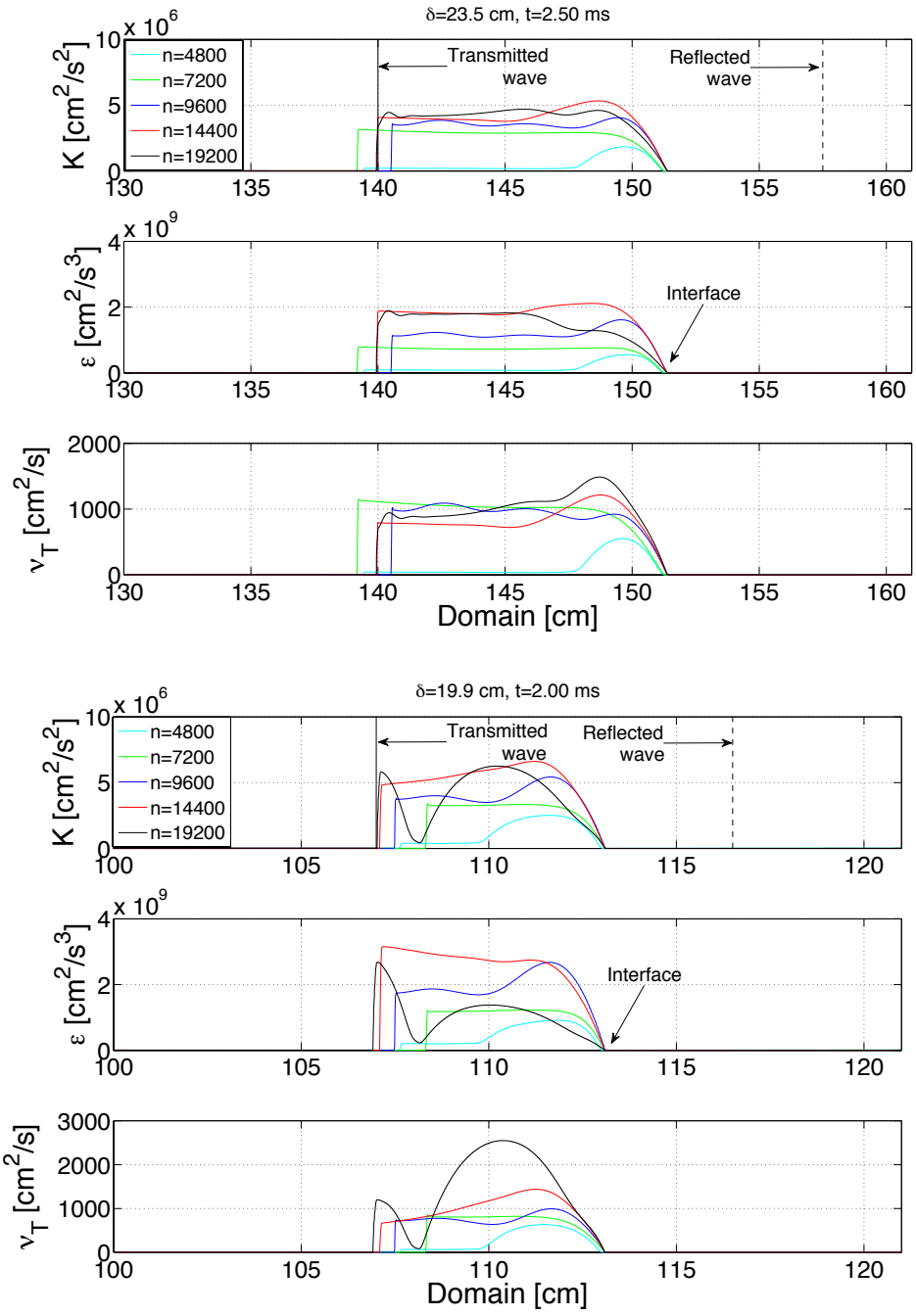

Figure 4.15: Convergence of the turbulent fields for $\delta = 23.5$ cm at $t = 2.5$ ms (top) and $\delta = 19.9$ cm at $t = 2$ ms (bottom) with $Ma_s = 1.20$, $At = 0.67$, $K_0 = 0.10$, $\lambda_{rms} = 0.25$ cm, $\sigma_\rho = 0.20$, and $C_{\epsilon 0} = 0.95$.

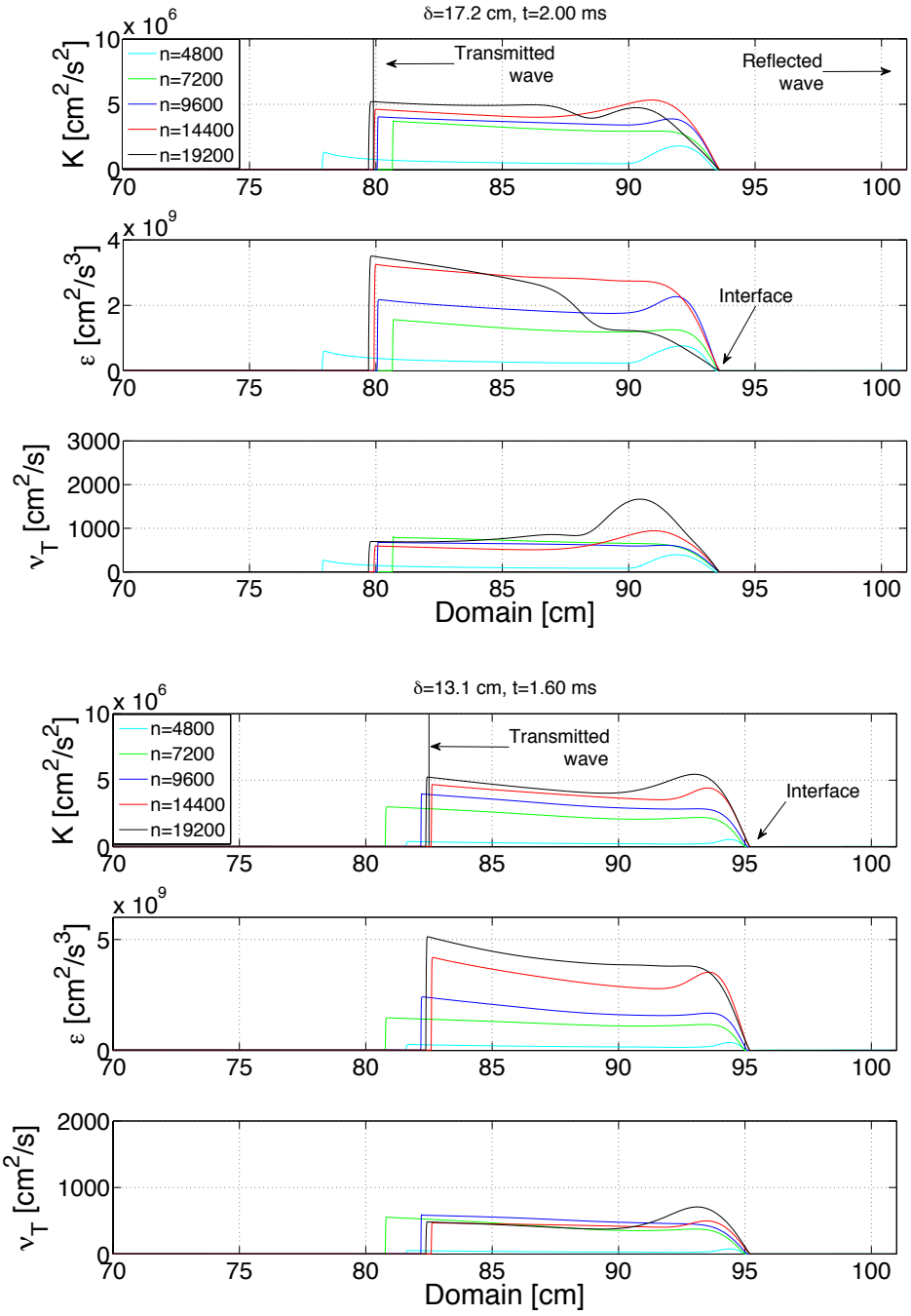

Figure 4.16: Convergence of the turbulent fields for $\delta = 17.2$ cm at $t = 2$ ms (top) and $\delta = 13.1$ cm at $t = 1.6$ ms (bottom) with $Ma_s = 1.20$, $At = 0.67$, $K_0 = 0.10$, $\lambda_{rms} = 0.25$ cm, $\sigma_\rho = 0.20$, and $C_{\epsilon 0} = 0.95$.

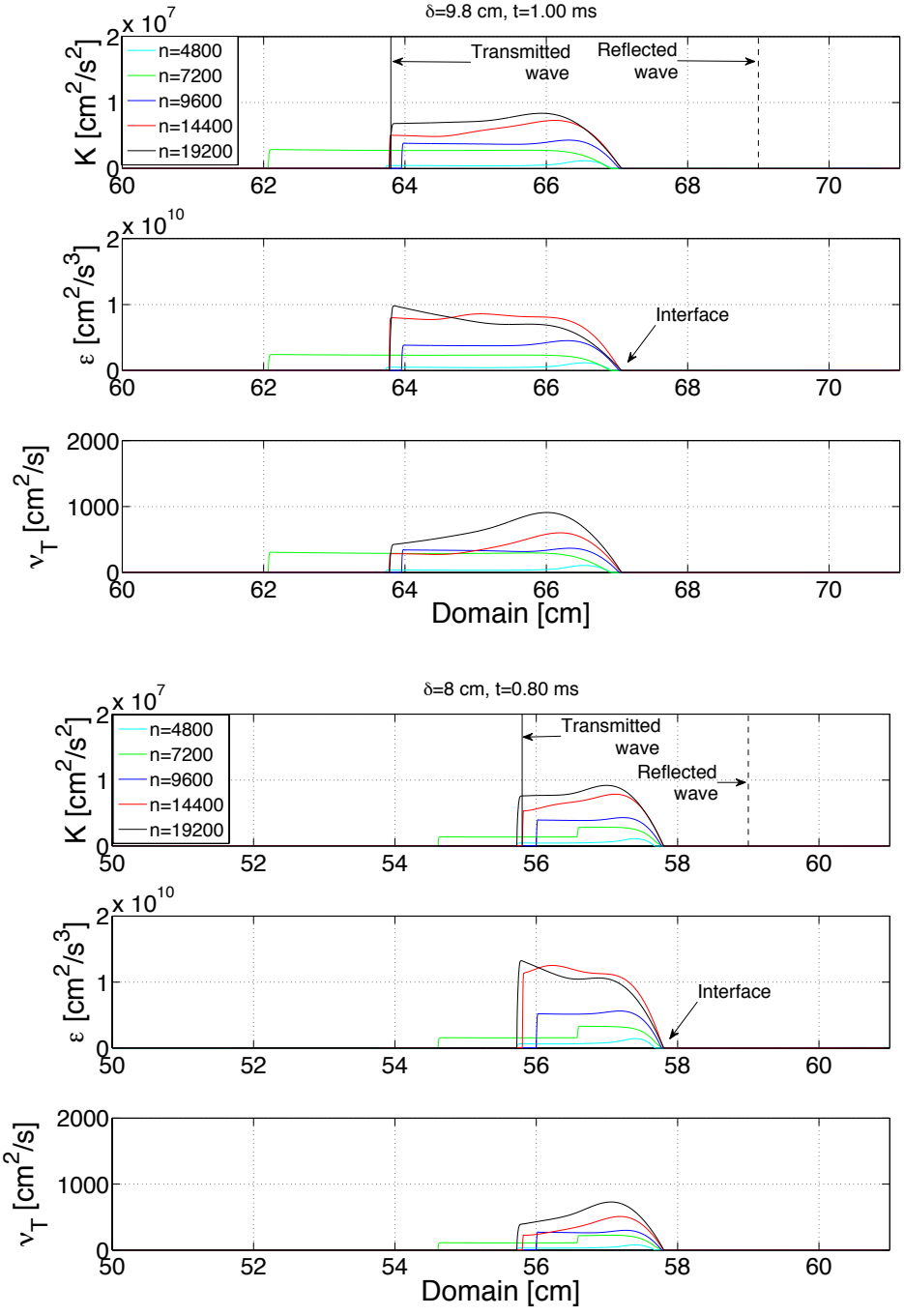

Figure 4.17: Convergence of the turbulent fields for $\delta = 9.8$ cm at $t = 1$ ms (top) and $\delta = 8$ cm at $t = 0.8$ ms (bottom) with $Ma_s = 1.20$, $At = 0.67$, $K_0 = 0.10$, $\lambda_{rms} = 0.25$ cm, $\sigma_\rho = 0.20$, and $C_{\epsilon 0} = 0.95$.

4.6 Chapter Summary

Reshocked Richtmyer–Meshkov instability under different reshock times was considered. Reshock occurred earlier for shorter test section lengths. Early-time mixing was minimally affected by variations in the reshock times. The post-reshock mixing layer growth rate generally varied from previous studies with longer test sections, and a new set of coefficients was established to accurately model the turbulent mixing. Good agreement was established between model predictions and the Leinov *et al.* (12; 31) experimental and three-dimensional simulation data. To the author's knowledge, this is the first published application of a Reynolds-averaged model to simulate these experiments. A general set of coefficients applicable to a broader range of shock Mach numbers, Atwood numbers, and test section lengths was also established. To evaluate the accuracy of the model, the general coefficient set was used to simulate the Vetter and Sturtevant (10) and Poggi *et al.* (11) experiments. Comparisons were made with simulations using the optimal coefficient set for these experiments. Good agreement was generally established when using the general coefficient set, but a small loss of accuracy was seen as the test section increased to $\delta = 110$ cm for the $Ma_s = 1.24$ case. The production and dissipation mechanisms for the turbulent kinetic energy and dissipation rate were considered to further investigate differences in the predictions between coefficient sets.

Grid refinement studies demonstrated that convergence was generally achieved between $n = 7200$ and 9600 points for the mean fields. However, the mixing layer width and the turbulent fields required finer grid resolution to achieve convergence. In all cases, convergence was slower in the vicinity of the mixing layer due to strong mixing and material discontinuities. Interactions between the interface and the end-wall with secondary expansion and rarefaction waves were also responsible for slower convergence. However, better convergence was achieved as waves progressed away from these boundaries.

CHAPTER V

Application of the Model to Reshocked Richtmyer–Meshkov Instability for Varying Atwood Numbers

Investigations of reshocked Richtmyer–Meshkov instability in Chapters III and IV were limited to air and sulfur hexafluoride (SF_6) gas combinations corresponding to Atwood numbers $At = \pm 0.67$. In Chapter III, parametric studies investigating the sensitivity of the model to changes in key model coefficients and initial conditions were conducted for shock Mach numbers $1.24 \leq Ma_s \leq 1.98$ with $At = \pm 0.67$ and a variety of test section lengths. Chapter IV considered the application of the model to reshocked Richtmyer–Meshkov instability under different reshock times with test section lengths $\delta = 8$, 9.8, 13.1, 17.2, 19.9, and 23.5 cm while $Ma_s = 1.20$ and $At = 0.67$ were held constant. Relatively little experimental work has been conducted for cases different from $At = \pm 0.67$. Therefore, the RANS model is further applied here to model a set of six different Atwood number cases for which previous LES data are available (37) with $At = \pm 0.21$, ± 0.67, and ± 0.87 corresponding to combinations of air with CO_2, SF_6, and H_2, respectively.

5.1 Mean Field and Mixing Layer Comparisons for Positive and Negative Atwood Numbers

The six investigations for both positive and negative Atwood numbers used domain length, shock location, and interface location $X = 162$ cm, $x_s = 99.75$ cm, and $x_i = 100$ cm, respectively; this resulted in a test section length $\delta = 62$ cm, as also used in LES (37). Mean and turbulent fields were initialized as discussed in Sec. 2.1.5. The $Ma_s = 1.50$, $At = 0.67$ case is very similar to that investigated experimentally by Vetter–Sturtevant (10), for which model predictions agreeing well with measurements were achieved in Sec. 3.2. The only difference is that the Vetter–Sturtevant experiment used $\delta = 61$ cm. This small change causes reshock to occur slightly later with minimal effect on early-time mixing and post-reshock growth rate of the mixing layer. Thus, the same initial conditions, $K_0 = 0.10$ and $\lambda_{rms} = 1.0$ cm, and principal model coefficients, $\sigma_\rho = 0.90$ and $C_{\epsilon 0} = 0.90$, were used in the present simulations. Table 5.1 lists the gas pairs resulting in positive Atwood numbers, where the shock accelerates the light gas towards the denser gas. The negative Atwood numbers are obtained by reversing the gas order, where the shock is introduced in the heavy gas to impulsively accelerate the lighter gas.

Gas pairs	air–CO_2	air–SF_6	H_2–air
At	0.21	0.67	0.87

Table 5.1: Gas pairs for positive Atwood numbers.

Figure 5.1 shows the mean density, pressure, heavy mass fraction, and velocity profiles in the vicinity of the initial shock and interface at the onset of the simulations. Comparisons are made between the three Atwood numbers, $At = 0.21$, 0.67, and 0.87. The density plot in Fig. 5.1 shows that the change in density in the post-shock region is much less apparent when using H_2 in the driver section when compared with cases where the shock is generated in air. Figure 5.2 similarly shows the mean fields for the

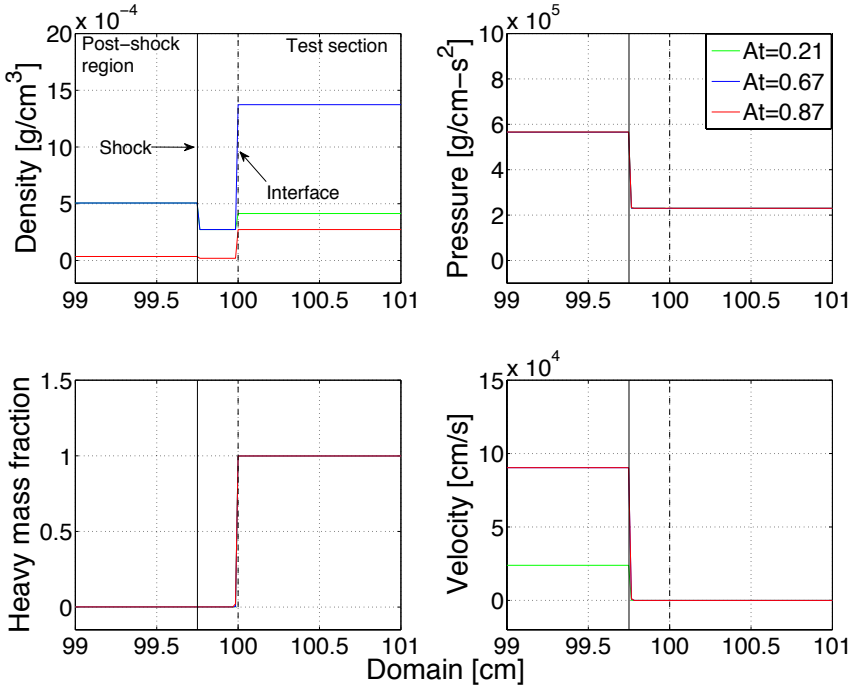

Figure 5.1: Mean density, pressure, heavy mass fraction, and velocity profiles in the post-shock, driver, and test section regions at the onset of simulations for $At > 0$.

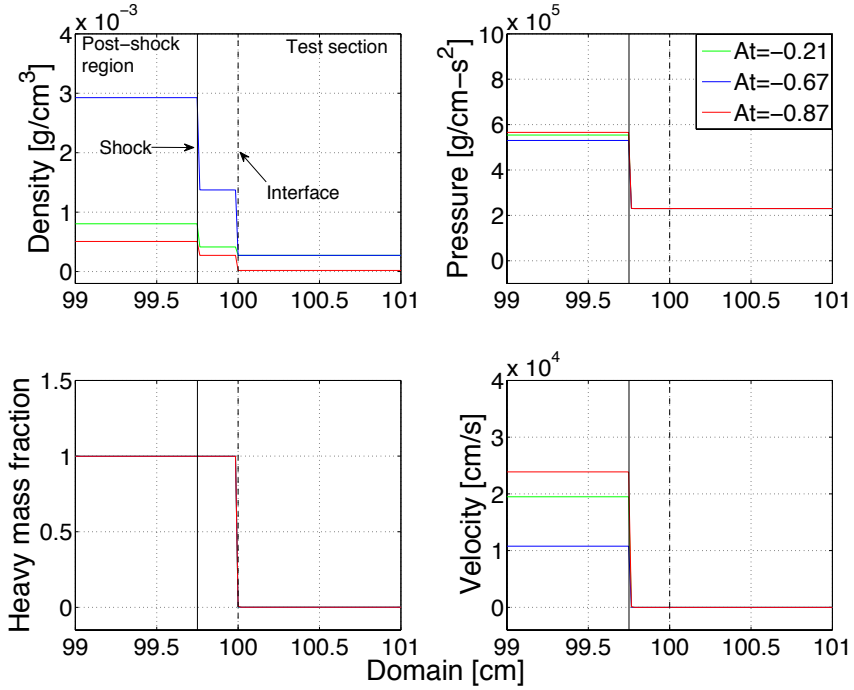

Figure 5.2: Mean density, pressure, heavy mass fraction, and velocity profiles in the post-shock, driver, and test section regions at the onset of simulations for $At < 0$.

negative Atwood numbers. In comparison to Fig. 5.1, the denser gases occupy the driver section while the lighter gas is situated in the test section. This is seen in the density and heavy mass fraction plots of Fig. 5.2. The pressure and velocity again have the same initial conditions in the cold region. For both positive and negative Atwood number, jumps in the pressure and velocity are noted in the post-shock region due to the passage of the shock while the initial conditions are seen in the unshocked (cold) regions. There is no shock-induced jump in the heavy mass fraction as this quantity shows the interface and regions occupied by the different gases. Table 5.2 lists thermodynamic properties and initial post-shock values for the mean fields. The first set of post-shock values corresponds to studies with $At > 0$ where the shock is introduced in air or H_2; thus, values are not listed for CO_2 and SF_6. The second set of post-shock values corresponds to studies with $At < 0$, where H_2 is not used in the driver section as it is the lightest of the gases used.

Property	Units	air	SF_6	CO_2	H_2
Atwood number with air, $\|At\|$		0	0.67	0.21	0.87
Polytropic index, γ		1.40	1.09	1.29	1.41
Molecular weight	g/mol	28.97	146.06	44.01	2.02
Density	$\times 10^{-3}$ g/cm^3	0.2723	1.3731	0.4137	0.0190
Post-shock density	$\times 10^{-3}$ g/cm^3	0.5067	–	–	0.0352
Post-shock pressure	$\times 10^{5}$ g/(cm-s^2)	5.656	–	–	5.664
Post-shock velocity	$\times 10^{4}$ cm/s	2.5	–	–	9.0
Post-shock density	$\times 10^{-3}$ g/cm^3	0.5067	2.9267	0.8366	–
Post-shock pressure	$\times 10^{5}$ g/(cm-s^2)	5.656	5.3028	5.5391	–
Post-shock velocity	$\times 10^{4}$ cm/s	2.5	1.0	1.95	–

Table 5.2: Gas properties at onset of simulation for positive Atwood numbers. The densities are calculated at $p = 2.3 \times 10^5$ g/(cm-s^2) and $T = 294$ K.

Figure 5.3 shows mixing layer widths for $At = \pm 0.21$, ± 0.67, and ± 0.87. Initial positive Atwood number configurations generally result in a reflected expansion wave after reshock that interacts with the interface (37), while reverse configurations typically result in a second reshock. Thus, times of reshock τ_R, arrival of the expansion

wave τ_E, and second reshock τ_{R2} are listed in addition to the mixing layer growth rates $\dot{h}$ shortly after reshock. The turbulent mixing widths generally evolve differently, especially after reshock, due to differences in the gas densities. For $At = 0.21$ and 0.67 (air is the light gas in both cases), the early-time width shows a weak dependence on At. However, a significant difference in reshock times is observed as more time is required for the shock to reflect from the endwall and reshock the layer for $At = 0.67$. A larger width is observed post-reshock for $At = 0.67$ due to a denser gas reshocking the interface. Reshock occurs earliest and mixing occurs at a higher rate after reshock with $At = 0.87$ for the same reasons.

Similar behavior is observed for the $At < 0$ cases. Although all of the gases in the driver section are different, similarities in initial mixing can be seen between $At = -0.87$ and -0.21 as the difference in densities is smaller. The turbulent mixing layer widths also grow more rapidly as compared to the $At > 0$ cases. As mentioned above, a result of reversing the gas order is that a second reshock is often observed as opposed to an expansion wave. These secondary waves can be seen in Fig. 5.3, where the first reshock induces turbulent mixing, and as time progresses a second reshock results in an increased mixing rate. Similar behavior was observed in the $Ma_s = 1.45$ Poggi *et al.* study in Sec. 3.4, which was also performed with $At = -0.67$.

The predicted mixing layer widths are also compared with LES data (37). The mixing layer behavior generally agrees well with the LES results throughout, but small differences are evident in the widths. For $At = \pm 0.67$ and ± 0.87, mixing layer results generated by the K–ϵ model give an early-time width slightly smaller than predicted by LES. RANS and LES results agree better after reshock, especially for $At = \pm 0.67$. Similar results were also observed in comparisons with LES data (15) for the Vetter and Sturtevant experiments in Chapter III. For $At = \pm 0.21$, a similar pattern is observed prior to reshock, but the RANS model predicts a larger post-reshock width. Again, there are no experimental data available with which to

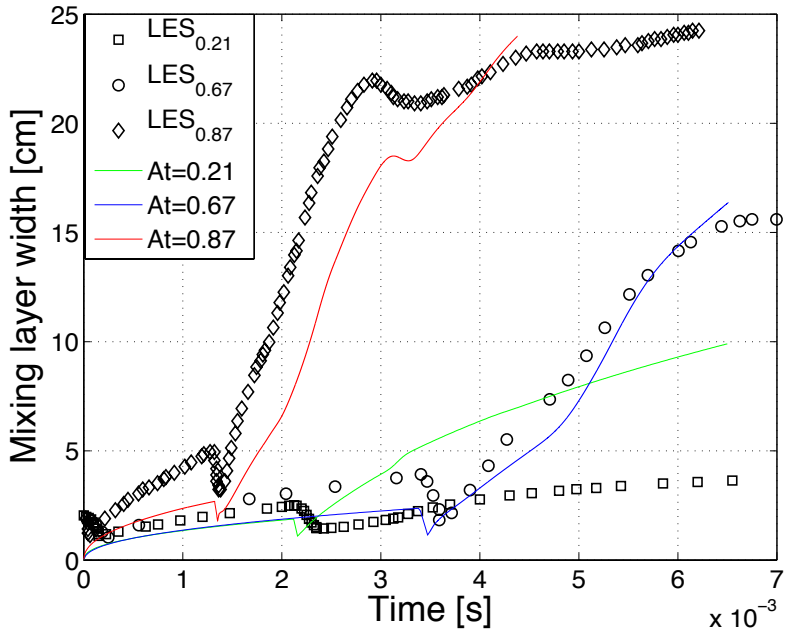

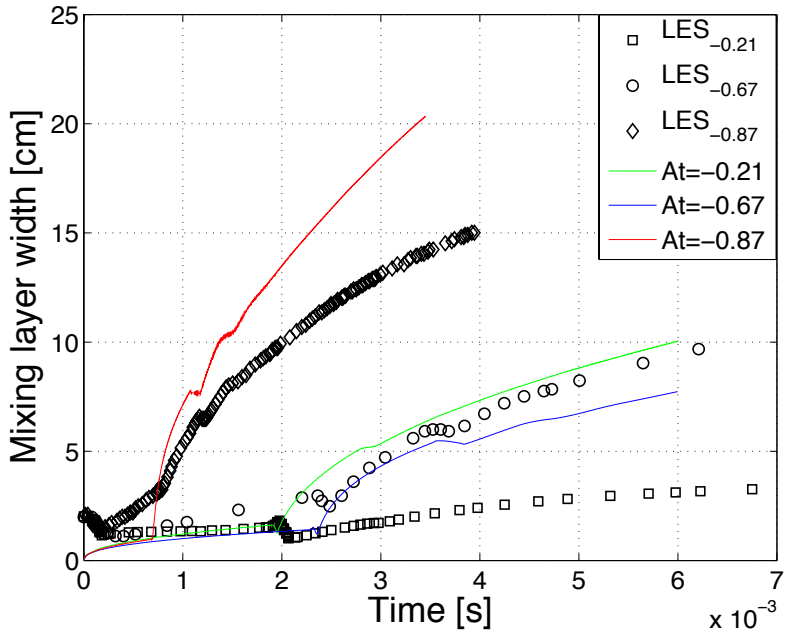

At		0.21	0.67	0.87	-0.21	-0.67	-0.87
$\dot{h}$ (LES)	cm/s	0.8×10^3	5.0×10^3	17.0×10^3	0.9×10^3	3.0×10^3	8.5×10^3
$\dot{h}$ (RANS)	cm/s	3.0×10^3	3.6×10^3	8.0×10^3	5.1×10^3	6.6×10^3	31.9×10^3
τ_R	ms	2.18	3.487	1.354	1.939	2.321	0.689
τ_E or τ_{R2}	ms	3.178	4.255	1.925	2.927	3.782	1.15

Figure 5.3: Mixing layer widths, growth rates $\dot{h}$ shortly after reshock, and reshock times τ_R for $At = \pm 0.21$, ± 0.67, and ± 0.87 with $Ma_s = 1.50$, $\delta = 62$ cm, $K_0 = 0.10$, $\lambda_{rms} = 0.25$ cm, $\sigma_\rho = 0.90$, and $C_{\epsilon 0} = 0.90$ and $\Delta x = 0.02$ cm. The LES data with $\Delta x = 0.21$ cm are from Ref. (37).

compare results. However, the $Ma_s = 1.50$ with $At = 0.67$ case is very similar to that investigated experimentally by Vetter–Sturtevant (10), for which model predictions agreeing well with data were achieved. Therefore, studies for the remaining Atwood numbers were conducted similarly. Convergence studies in Sec. 5.4 also elucidate differences between RANS and LES results.

5.2 Turbulent Budget Studies for Positive Atwood Numbers

Referring to Fig. 5.3, the times of reshock and arrival of the expansion wave occur at $\tau_R \approx 1.354$ and $\tau_E \approx 1.925$ ms, respectively, for the $At = 0.87$ case. The turbulent kinetic energy and dissipation rate budgets consider times shortly before and after τ_{R1} and τ_E. Considering the turbulent kinetic energy budgets in Fig. 5.4, large amounts of turbulent kinetic energy are concentrated in the vicinity of the shock shortly before reshock at $t = 1.20$ ms. The buoyancy production mechanism (pressure work) generates larger amounts of turbulent kinetic energy than the shear production. Some spreading of turbulent kinetic energy is also seen due to diffusion, while the dissipation rate is negligible. Upon reshocking the interface, energy is deposited during compression of the mixing layer and turbulent mixing is enhanced. At $t = 1.40$ ms, ≈ 0.05 ms after reshock, a clear distinction between the transmitted and reflected waves is seen. Buoyancy production decreases significantly as diffusion spreads the turbulent kinetic energy during mixing. Similarly, the dissipation reduces the turbulent kinetic energy from shear production as the interface is compressed and heated. As the speed of the shock slows from compressing the interface, turbulent kinetic energy from shear production decreases and is dissipated. After reshock, turbulent mixing continues but will diminish as turbulence dissipates without a sustained source. Comparing the budgets at $t = 1.80$ and $t = 2.20$ ms, the arrival of the expansion wave supplies additional turbulent kinetic energy via buoyancy production for additional mixing from changes in density and pressure. The diffusion remains relatively unchanged

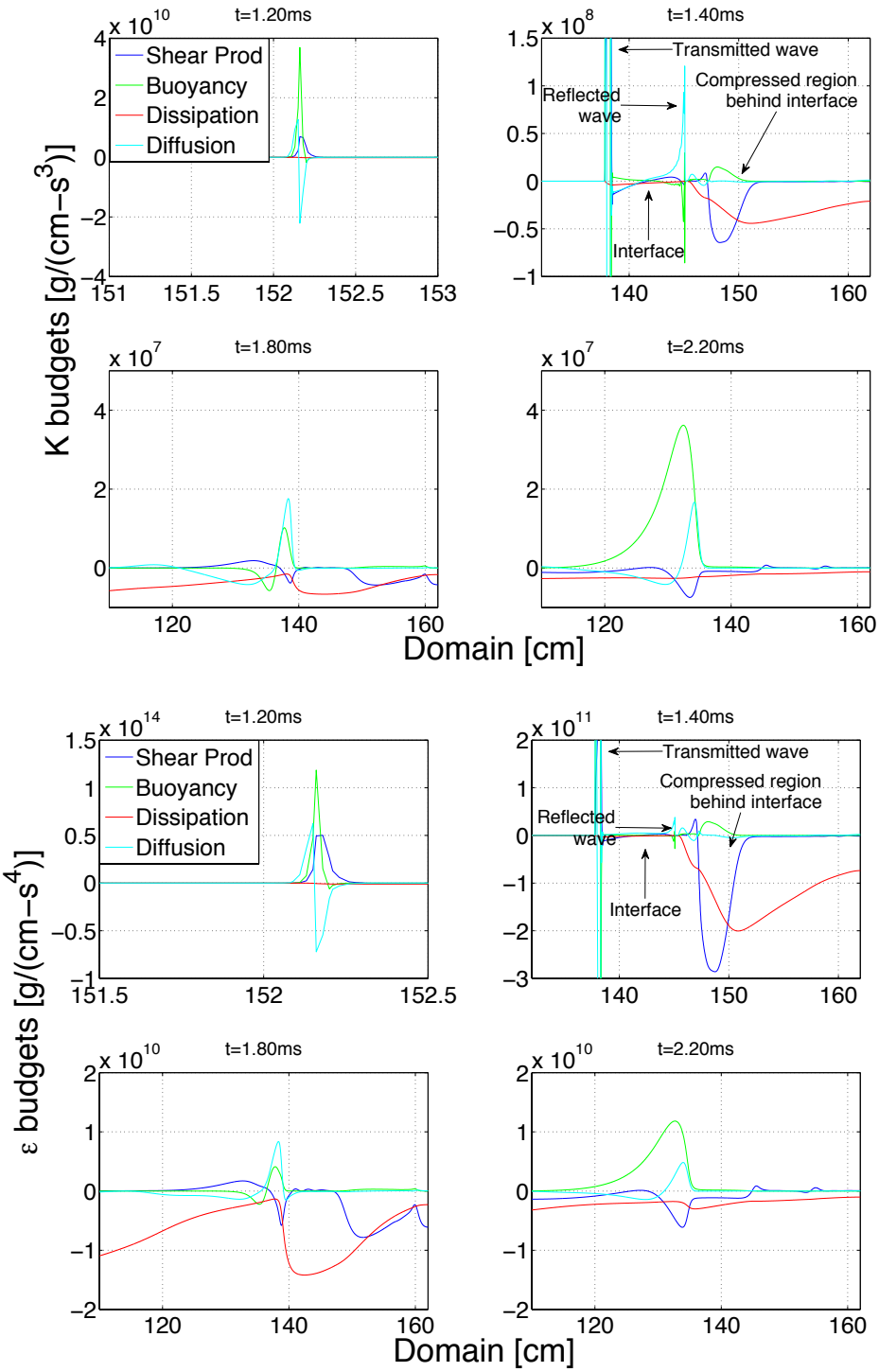

Figure 5.4: Turbulent kinetic energy and dissipation rate budgets for $At = 0.87$ and $Ma_s = 1.50$ at $t = 1.20$, 1.40, 1.80, and 2.20 ms. The times of reshock and arrival of expansion wave are $\tau_R \approx 1.354$ and $\tau_E \approx 1.925$ ms, respectively.

while contributions from the dissipation rate decrease. The turbulent kinetic energy dissipation rate budgets evolve similarly as the dissipation rate is proportional to the turbulent kinetic energy. Prior to reshock, the terms maintain similar profiles near the vicinity of the shock. Shortly after reshock the dissipation rate is larger as the gas is compressed, resulting in turbulent kinetic energy dissipation. Similar behavior is observed at $t = 1.80$ ms, and an increase in the production terms is seen after the arrival of the expansion wave.

Similar to the $At = 0.87$ case, Fig. 5.5 shows times shortly before and after reshock and the arrival of the expansion wave, $\tau_R \approx 3.487$ and $\tau_E \approx 4.255$ ms, respectively. Comparisons can be made between cases despite the different gases used in each case. Prior to reshock, production of turbulent kinetic energy is concentrated primarily near the shock, with larger contributions from the buoyancy production. Smaller diffusion is seen at this time also, as the shock initiating reshock is further away from the interface in comparison to the $At = 0.87$ case in the first plot. After reshock, the transmitted and reflected waves are seen, where both waves diffuse turbulent kinetic energy as they propagate through the gas. As the transmitted wave progresses at $t = 4.00$ ms, the dissipation of turbulent kinetic energy becomes larger behind the shock as it heats the gas in its path. Additional turbulent kinetic energy is produced by the arrival of the expansion wave at approximately $t = 4.40$ ms. Dissipative effects becomes weaker, and diffusion spreads the turbulent kinetic energy over a broader region behind the transmitted wave. Moreover, the generally lower magnitudes for $At = 0.67$ in comparison to $At = 0.87$ indicate that the rate of turbulent kinetic energy production is lower. This is in agreement with Fig. 5.3, as the post-reshock mixing layer growth rate is lower for $At = 0.67$, where $\dot{h}_{0.67}/\dot{h}_{0.87} \approx 0.30$. As the ϵ equation is proportional to the K equation, the turbulent kinetic energy dissipation rate displays similar behavior and the magnitudes of the budgets are also lower.

The last case in the positive Atwood number studies corresponds to $At = 0.21$.

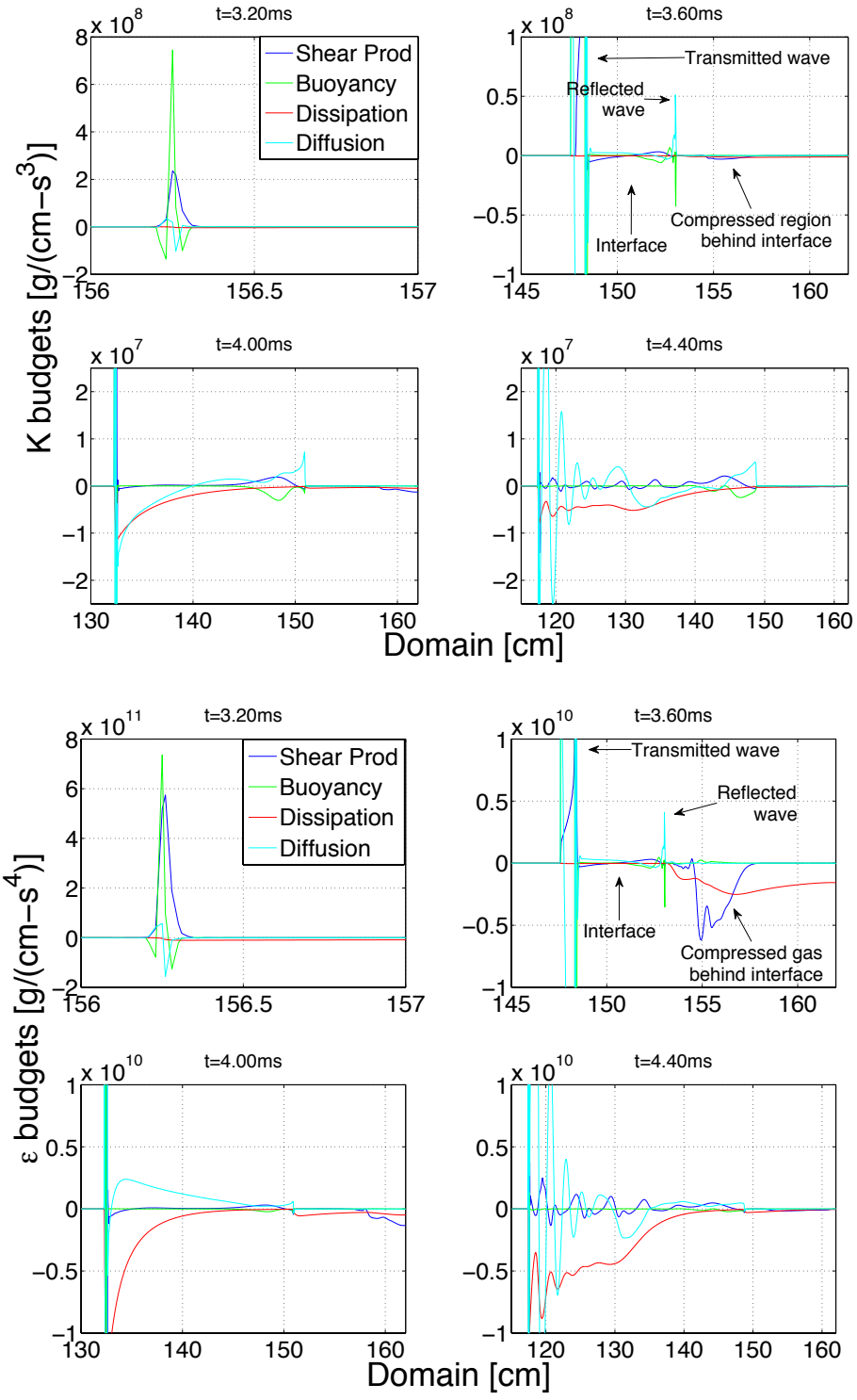

Figure 5.5: Turbulent kinetic energy and dissipation rate budgets for $At = 0.67$ and $Ma_s = 1.50$ at $t = 3.20$, 3.60, 4.00, and 4.40 ms. The times of reshock and arrival of expansion wave are $\tau_R \approx 3.487$ and $\tau_E \approx 4.255$ ms, respectively.

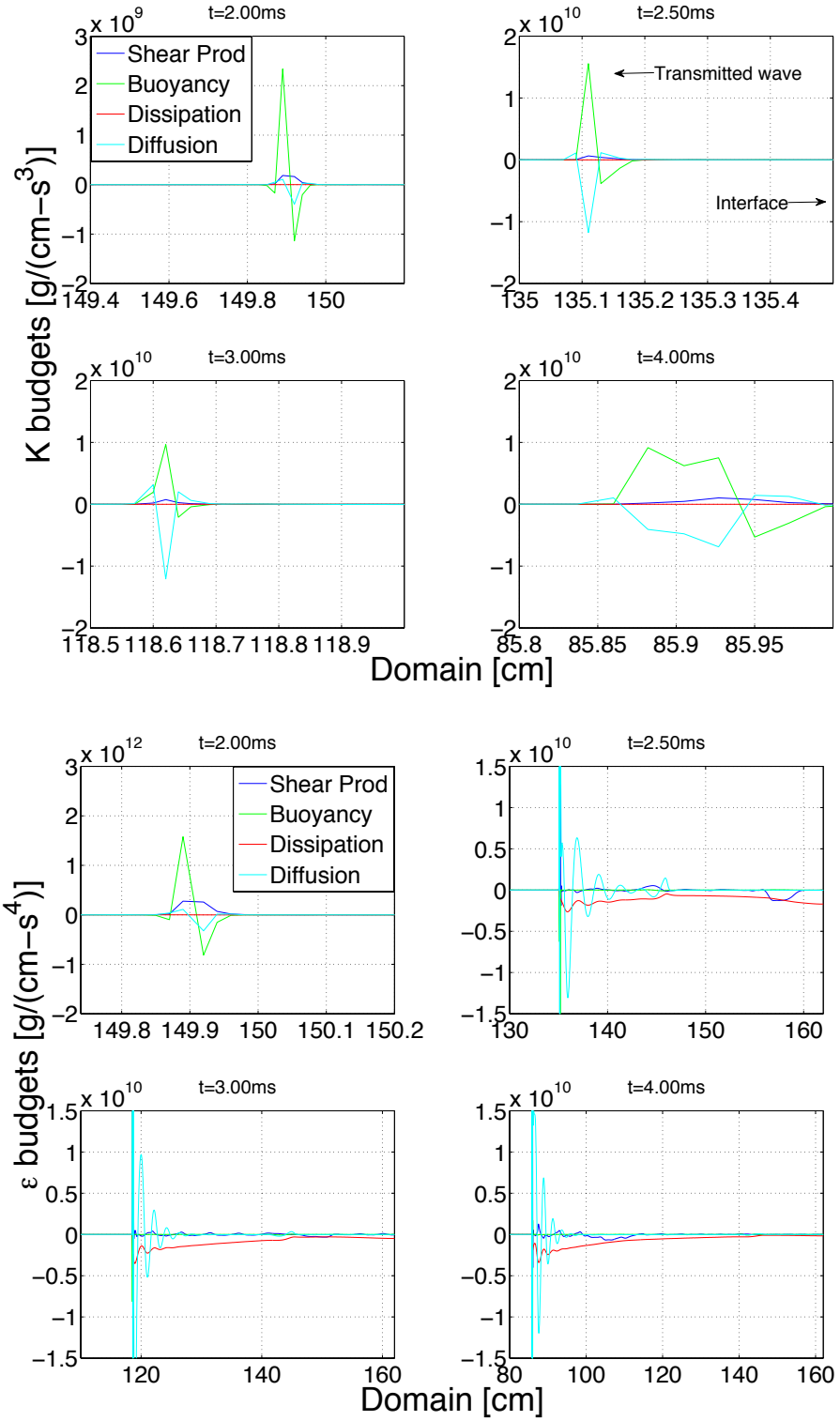

Figure 5.6: Turbulent kinetic energy and dissipation rate budgets for $At = 0.21$ and $Ma_s = 1.50$ at $t = 2.00$, 2.50, 3.00, and 4.00 ms. Times of reshock and arrival of expansion wave are $\tau_R \approx 2.18$ and $\tau_E \approx 3.18$ ms, respectively.

As shown in the previous two cases, the turbulent kinetic energy and dissipation rate budgets show similar evolutions. Therefore, the turbulent kinetic energy budgets are used to focus on the transmitted shock to elucidate its structure. Following the transmitted wave in time, similar profiles are maintained after reshock. Contributions from diffusion are larger as post-reshock mixing evolves. At later times the diffusion of turbulent kinetic energy remain relatively constant; the profiles spatially broaden as mixing continues. The turbulent kinetic energy dissipation rate budgets consider the collective evolution of the production, diffusion, and dissipation terms. Similar behavior is seen as in the previous cases. The transmitted wave generates turbulent kinetic energy, which is diffused during the mixing. Shear production makes secondary contributions to the mixing. Dissipation is largest behind the shock as the gas is heated, and gradually becomes smaller in regions where the gas begins to expand after passage of the shock.

5.3 Turbulent Budget Studies for Negative Atwood Numbers

As discussed above, reshocked Richtmyer–Meshkov instability with negative Atwood numbers typically experiences a second reshock. Budgets for the turbulent kinetic energy and dissipation rate are considered at times when both the first and second reshock occur.

Figure 5.7 shows three times for the turbulent kinetic energy and dissipation rate budgets with $At = -0.87$. The first time is at $t = 0.80$ ms, shortly after the first reshock, $\tau_R \approx 0.689$ ms. At this time, the transmitted and reflected waves from the first reshock are seen. The former wave is traveling in air, while the latter is traveling in H_2 (in the direction of the test section endwall). Buoyancy production is the dominant term near the shocks due to the density and pressure gradients from compression of the interface, while diffusion of turbulent kinetic energy is small. The second plot at $t = 0.80$ ms minimizes the range so that the structure of the mixing

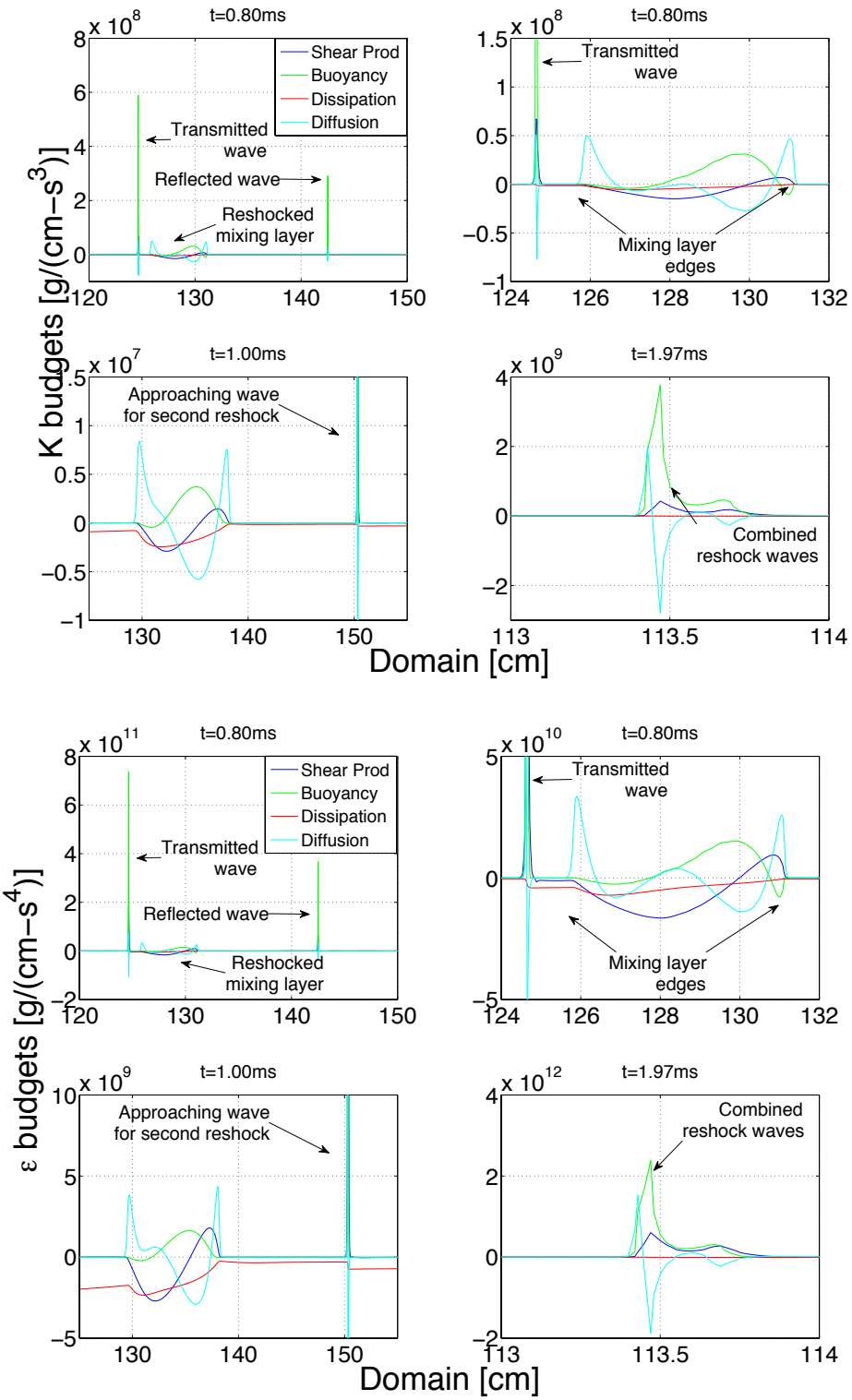

Figure 5.7: Turbulent kinetic energy and dissipation rate budgets for $At = -0.87$ and $Ma_s = 1.50$ at $t = 0.80$, 1.00, and 1.97 ms, respectively. The times of first and second reshock are $\tau_R \approx 0.689$ and $\tau_{R2} \approx 1.15$ ms, respectively.

layer width can be elucidated; the diffusion term is strongest in spreading turbulent kinetic energy at the mixing layer edges as it grows. Additional turbulent kinetic energy is generated via buoyancy production and diffused within the mixing layer; the shear production and dissipation terms make small contributions. The distance between the edges of the mixing layer show that it is $\approx$ 6 cm thick, which is in agreement with the width in Fig. 5.3 for $At = -0.87$ at $t \approx 0.80$ ms.

At $t = 1.00$ ms, shortly before the second reshock, the diffusion and buoyancy production terms retain their earlier structure. The dissipation of turbulent kinetic energy has spread across the mixing layer as the gas was heated by passage of the shock; the shear production is still relatively small. Diffusion of turbulent kinetic energy is large near the second wave as it approaches the interface for the second reshock. Finally, at $t \approx 1.97$ ms, the transmitted wave from the second reshock coalesces with the transmitted wave from first reshock to form a single wave. In the process, the evolution of the budgets are similar to those of the initial shock prior to first reshock. The dominant terms are once again the buoyancy production and diffusion of turbulent kinetic energy, while the shear production is smaller and the dissipation term is negligible. The budget evolution for the turbulent kinetic energy dissipation rate is very similar, as expected. The orders of magnitude between the K and ϵ budgets are different.

The $At = -0.67$ case in Fig. 5.8 considers times before and after the first and second reshock. Shortly before reshock at $t = 2.20$ ms, early-time mixing is very similar to the behavior seen for the positive Atwood number cases. Buoyancy production is the principal mechanism for generating turbulent kinetic energy with smaller contributions from shear production. The turbulent kinetic energy is spread by diffusion in small amounts near the shock as turbulent mixing occurs, while the dissipation is negligible. Approximately 0.50 ms after first reshock at $t = 2.80$ ms, the transmitted and reflected waves can be discerned by the localized turbulent kinetic energy production

traveling in opposite directions. Diffusion is again prominent at the edges of the mixing layer as turbulent mixing is enhanced and the layer becomes larger. Within the mixing layer, shear and buoyancy production make comparable contributions while the dissipation serves as a sink. Similar behavior as described in previous cases is seen for the secondary wave reflecting from the test section endwall and reshocking the interface a second time at $t = 3.40$ and 4.00 ms. Comparisons between $t = 3.40$ and 4.00 ms show that the shock loses considerable energy in reshocking the interface the second time. The diffusion of turbulent kinetic energy is much smaller at the shock front, indicating that the transmitted wave spreads less turbulent kinetic energy. However, an increase in the shear production is also seen due to the change in velocity the transmitted wave experiences upon exiting the mixing layer. Another observation to make in Fig. 5.8 is the growth of the mixing layer. Between the first and second reshocks, the mixing layer grows ≈ 2 cm; at $t = 2.80$ and 4 ms, $h(t) \approx 4$ and ≈ 6 cm, respectively. These results are in agreement with the mixing layer for $At = -0.67$ in Fig. 5.3, and show the evolution of the mixing layer as reshock enhances turbulent mixing.

The final budget studies for the turbulent kinetic energy and dissipation rate are for $At = -0.21$. The first time considered in Fig. 5.9 is $t = 2.20$ ms, approximately 0.25 ms after first reshock. Some observations can be made when using CO_2 to impulsively accelerate air in comparison with the $At = -0.87$ and -0.67 cases. The transmitted wave shows that the buoyancy production and diffusion of turbulent kinetic energy are the dominant terms as the wave exits the mixing layer and enters pure CO_2. The change in density as the shock crosses boundaries results in larger buoyancy production and diffusion. However, note that for the reflected wave the dominant contributions arise from shear production rather than buoyancy production: the wave is traveling in the compressed region behind the mixing layer where mixing is occurring, and the difference in densities is smaller. Thus, the change in density from

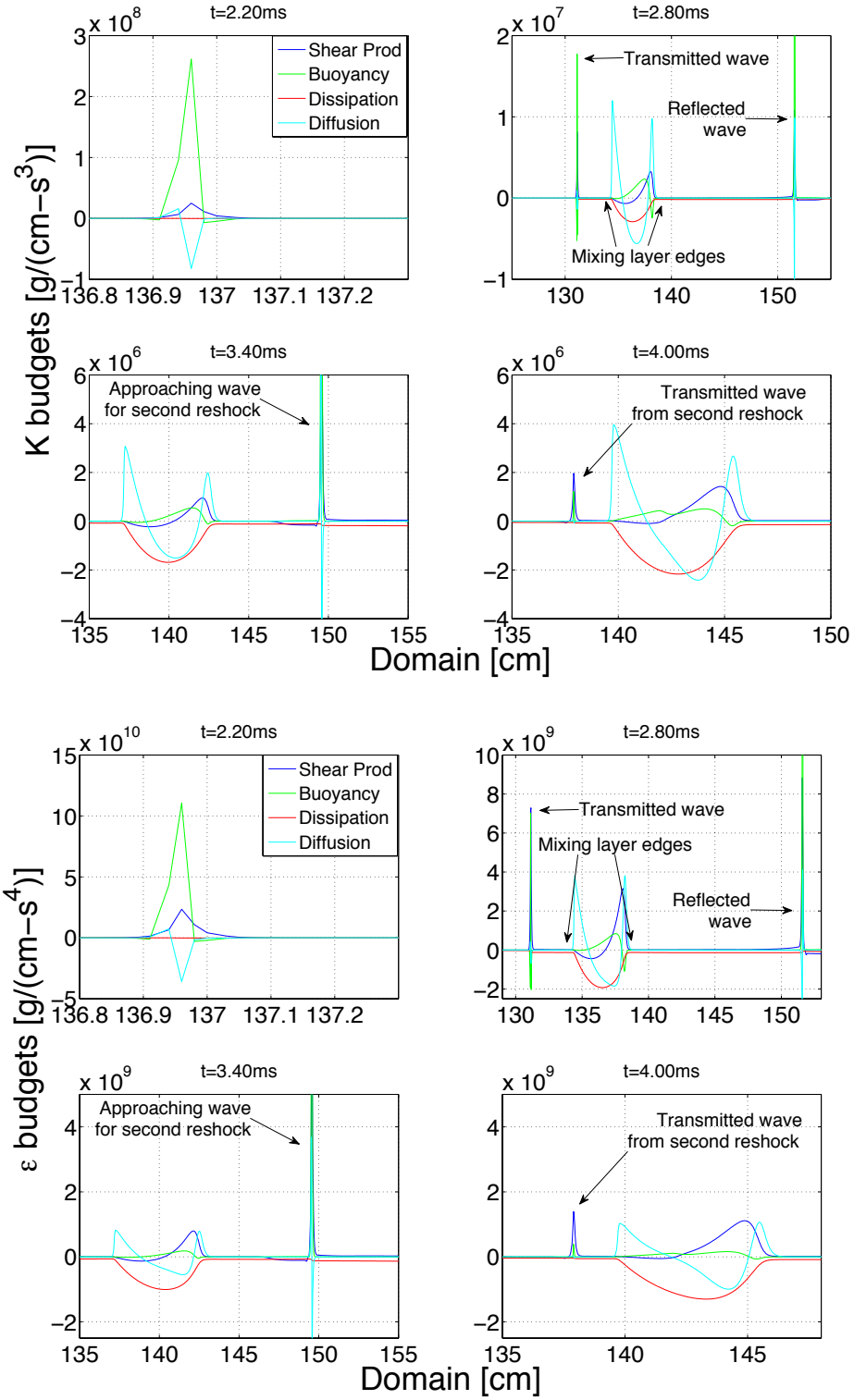

Figure 5.8: Turbulent kinetic energy and dissipation rate budgets for $At = -0.67$ and $Ma_s = 1.50$ at $t = 2.20$, 2.80, 3.40, and 4.00 ms, respectively. The times of first and second reshock are $\tau_R \approx 2.321$ and $\tau_{R2} \approx 3.712$ ms, respectively.

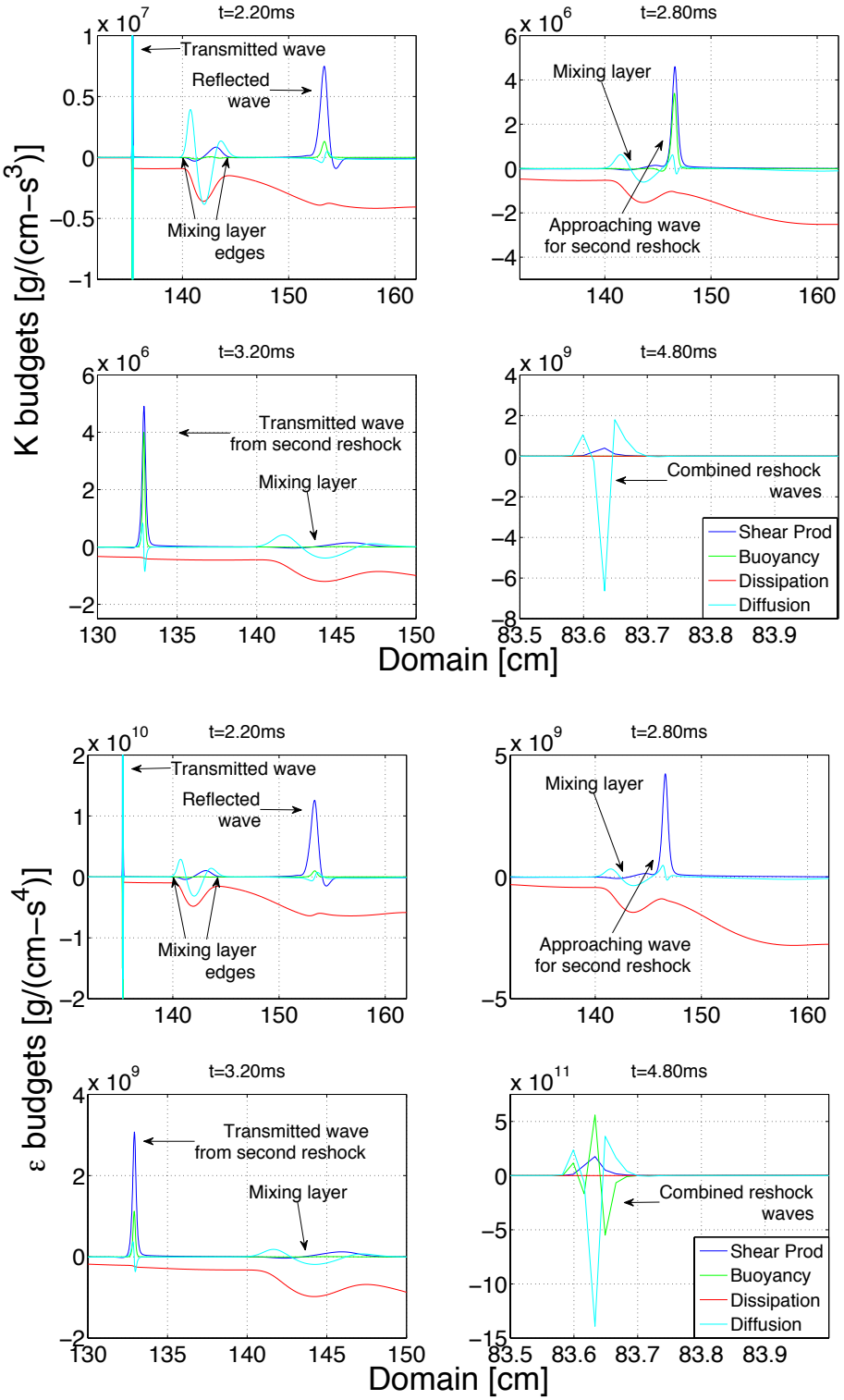

Figure 5.9: Turbulent kinetic energy and dissipation rate budgets for $At = -0.21$ and $Ma_s = 1.50$ at $t = 2.20$, 2.80, 3.20, and 4.80 ms. The times of first and second reshock are $\tau_R \approx 1.939$ and $\tau_{R2} \approx 2.927$ ms, respectively.

compression of the interface is smaller during reshock, and the buoyancy production is also smaller. Smaller buoyancy production also results in less diffusion of turbulent kinetic energy. This is different from the $At = -0.87$ and -0.67 cases, where the difference in densities is larger. Turbulent kinetic energy dissipation is prominent behind the transmitted wave from the first reshock as the gas is heated as the shock propagates. Furthermore, dissipation is also large in the compressed region behind the interface, where energy is dissipated and transformed into heat. The mixing layer grows between the first and second reshocks between $t = 2.20$ and 3.20 ms. As with the previous cases, comparisons showing good agreement can be made with Fig. 5.3. After the second reshock at $t = 3.20$ ms, the buoyancy production and diffusion increase near the transmitted wave as it enters the region with pure CO_2. The transmitted waves from the first and second reshocks coalesce at $t \approx 4.81$ ms, resulting in an increase in buoyancy production and diffusion of turbulent kinetic energy. The structure and evolution of the budgets for the turbulent kinetic energy dissipation rate are similar to those for the turbulent kinetic energy.

5.4 Convergence Under Grid Refinement

Convergence properties under grid refinement are considered for the mixing layer widths along with the mean and turbulent fields for each of the six Atwood numbers. The mean fields are the density, pressure, heavy mass fraction, and velocity; the turbulent fields are the turbulent kinetic energy, turbulent kinetic energy dissipation rate, and turbulent viscosity. Mixing layer widths predicted by the K–ϵ model are compared with LES data with grid spacing $\Delta x = L_y/128 = 0.21$ cm, where $L_y = 27$ cm (37). Convergence results were not presented or discussed for the LES investigations. Depending on the study, grid refinement for the RANS simulations included $n = 2400$, 4800, 7200, 9600, and 14400 points, which correspond to grid spacings $\Delta x = 0.0675$, 0.0338, 0.0225, 0.0169, and 0.0113 cm, respectively.

5.4.1 Mixing layer widths

The grid refinement study was initiated with a coarse grid of $n = 2400$ points and progressively increased to $n = 4800$, 7200, and 9600 points. In some cases it was necessary to refine the grid further to $n = 14400$ points. Convergence is generally achieved between $n = 7200$ and 9600 points. Figures 5.10–5.12 illustrate mixing layer convergence results for $At = 0.87$, 0.67, and 0.21, respectively. Simulations using $n = 7200$ and 9600 points for $At = 0.87$ generated nearly identical results. Similar results were obtained for 0.67, but some divergence is seen starting at $t \approx 5$ ms. As discussed in Sec. 3.5, this is due to secondary waves. For $At = 0.21$, convergence is achieved at early times between $n = 4800$ and 7200 points while comparisons between the post-reshock profiles show similar results with small loss of accuracy. In these three cases the converged RANS results predict smaller early-time mixing than the LES predictions. Comparisons after reshock vary. For $At = 0.87$, the post-reshock RANS width is smaller but RANS and LES results are comparable after reshock for $At = 0.67$. For $At = 0.21$, LES predictions are quite similar to RANS results for the coarsest grid of $n = 2400$ points: this is a potential indication that the LES were underresolved.

Figures 5.13–5.15 present mixing layer convergence results for the corresponding negative Atwood numbers. The $At = -0.87$ case shows that convergence is achieved for the early-time mixing between $n = 7200$ and 9600 points. After reshock, convergence is maintained but a small divergence between profiles starts at $t \approx 0.75$ ms due to the second reflected wave from the test section endwall approaching the interface for second reshock. However, the diverging behavior does not grow significantly, and predictions with $n = 7200$ and 9600 points are similar with small loss of accuracy. The early-time RANS width is again smaller than the LES width. After reshock, the LES widths lie between the RANS widths for $n = 2400$ and 4800 points. Results for $At = -0.67$ are illustrated in Fig. 5.14. Unlike all previous cases, nonmonotonic

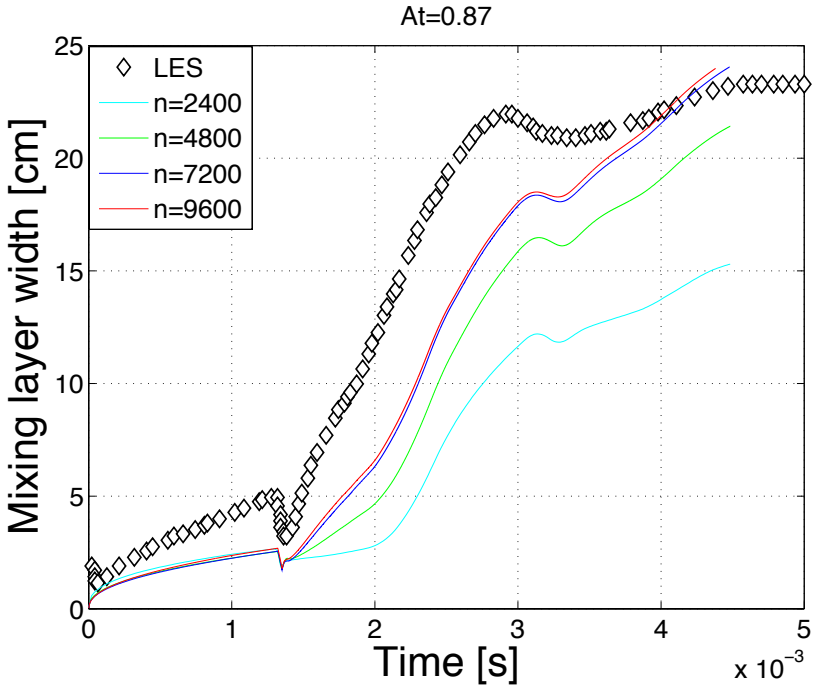

Figure 5.10: Mixing layer convergence for $At = 0.87$ and $Ma_s = 1.50$. The LES data are from Ref. (37).

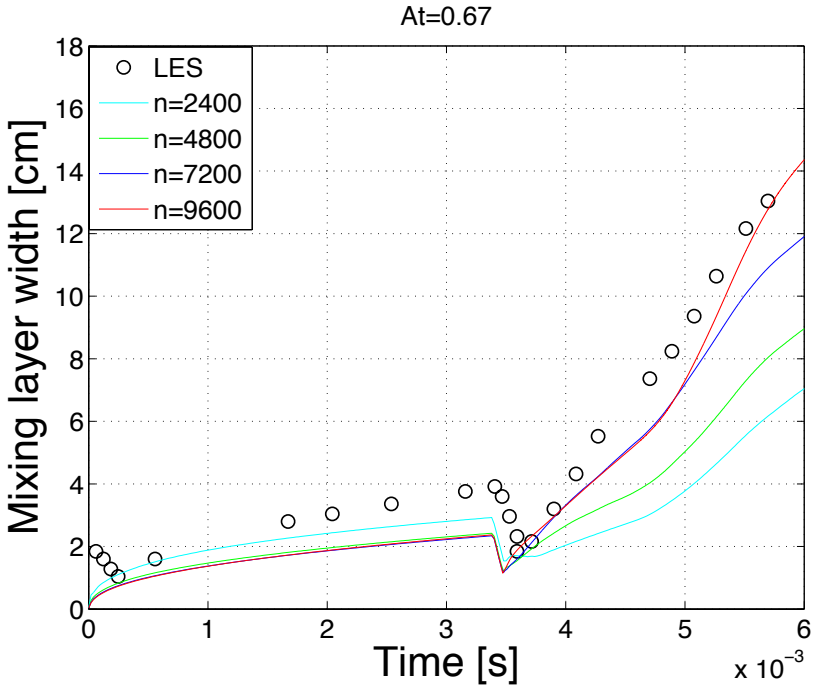

Figure 5.11: Mixing layer convergence for $At = 0.67$ and $Ma_s = 1.50$. The LES data are from Ref. (37).

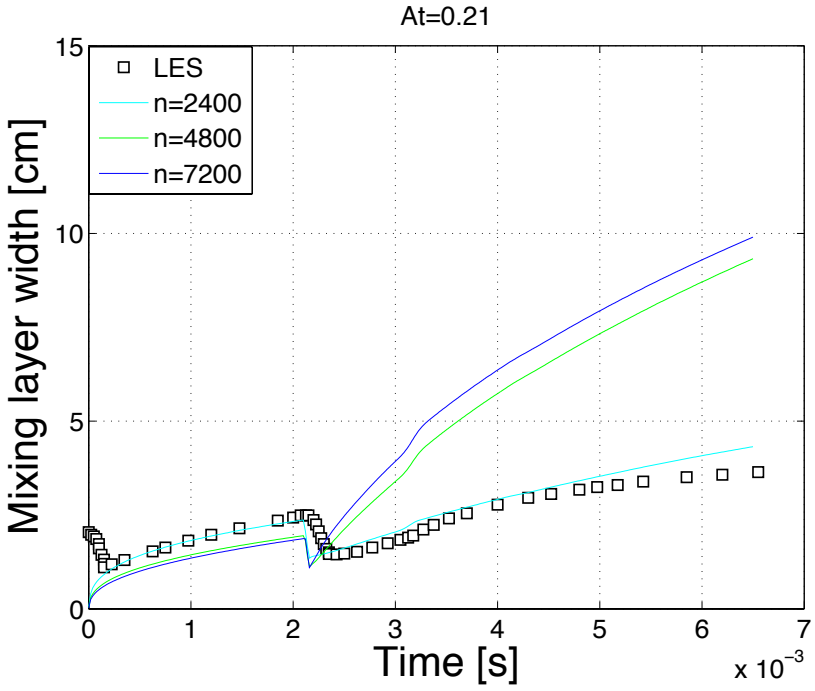

Figure 5.12: Mixing layer convergence for $At = 0.21$ and $Ma_s = 1.50$. The LES data are from Ref. (37).

behavior is seen starting at $n = 7200$ points, where rather than converging, the profile with $n = 9600$ points grows farther away. Finally, using $n = 14400$ points leads to converging results with $n = 7200$ points. LES and RANS approaches produce similar results after reshock for $n = 9600$ points, but considering the nonmonotonic behavior demonstrated by the RANS model, convergence is uncertain. Finally, convergence findings for $At = -0.21$ in Fig. 5.15 show converged results between $n = 7200$ and $n = 9600$ points. As with the $At = 0.21$ case, the LES width most closely matches the RANS width on the coarsest grid with $n = 2400$ points.

5.4.2 Convergence of the mean fields

Grid refinement studies for the mean fields were conducted at different times after reshock for each case to evaluate post-reshock convergence. As with the mixing layer widths, the mean density, pressure, heavy mass fraction, and velocity generally achieved convergence between $n = 7200$ and 9600 points. Simulations using $n = 4800$

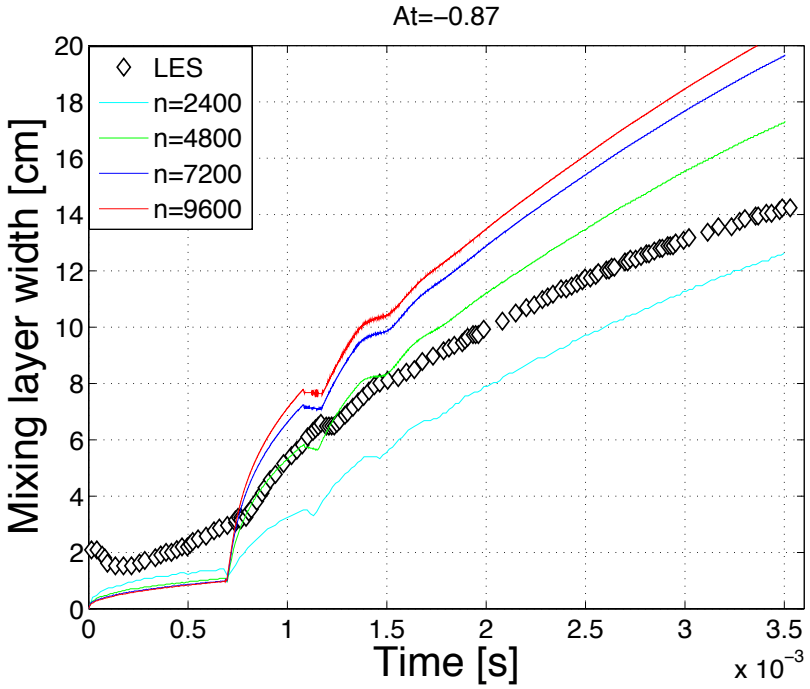

Figure 5.13: Mixing layer convergence for $At = -0.87$ and $Ma_s = 1.50$. The LES data are from Ref. (37).

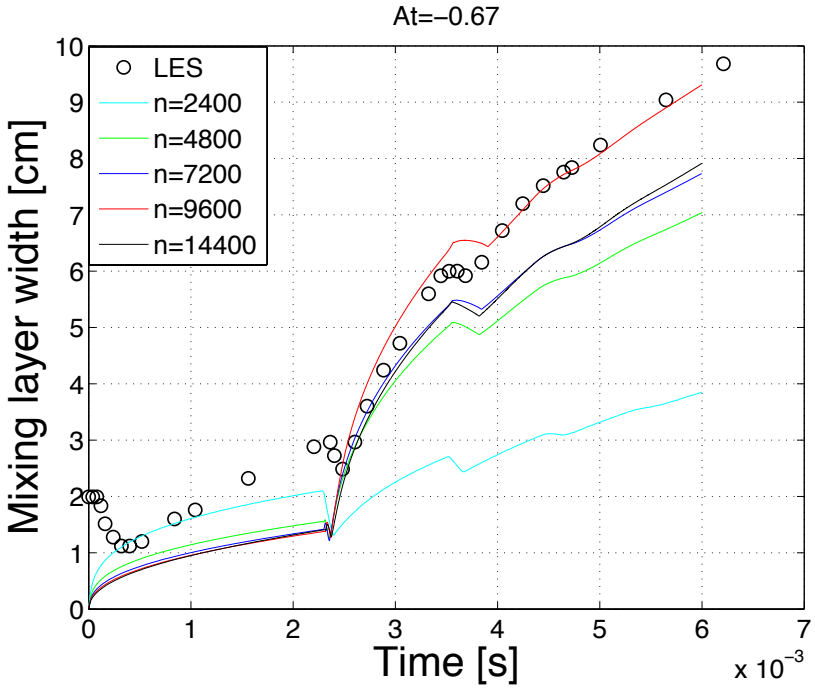

Figure 5.14: Mixing layer convergence for $At = -0.67$ and $Ma_s = 1.50$. The LES data are from Ref. (37).

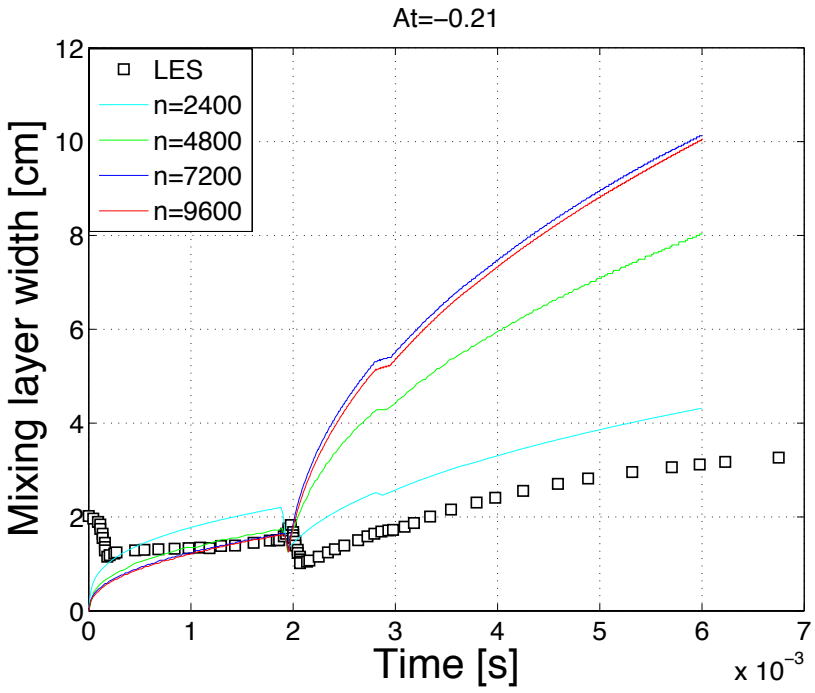

Figure 5.15: Mixing layer convergence for $At = -0.21$ and $Ma_s = 1.50$. The LES data are from Ref. (37).

points also capture the profile behavior well, but a small loss of accuracy can be seen near the mixing layer width and the shock. As discussed in Sec. 1.3.3, this is due to the material discontinuities in these regions. Slightly larger loss of accuracy occurs when using a coarse grid with $n = 2400$ points.

Figures 5.16–5.18 show convergence results for $At = 0.87$, 0.67, and 0.21 at $t =$ 1.40, 4.80, and 5.00 ms, respectively. Reshock times for each case are listed in Fig. 5.3. As time evolves after reshock, the progression of transmitted and reflected waves can be followed. It can also be seen that convergence was achieved faster and with less error as the Atwood number decreased. Whereas simulations with $n = 4800$ points still introduced error near the shock for $At = 0.87$, convergence was achieved between $n = 4800$ and 7200 points for $At = 0.21$. Moreover, recall that a small lack of convergence was noted in the mixing layer widths for $At = 0.67$ and 0.21 cases after reshock. Such lack of convergence was not seen in the mean fields.

Similarly, Figs. 5.19–5.21 illustrate convergence results for the negative Atwood

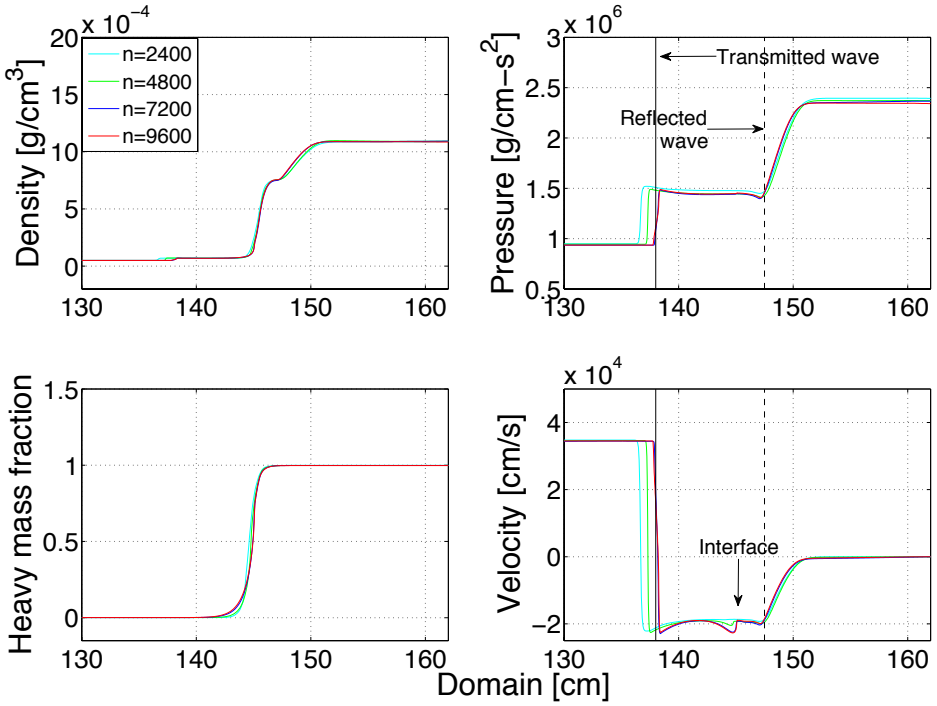

Figure 5.16: Mean field convergence for $At = 0.87$ and $Ma_s = 1.50$ at $t = 1.40$ ms.

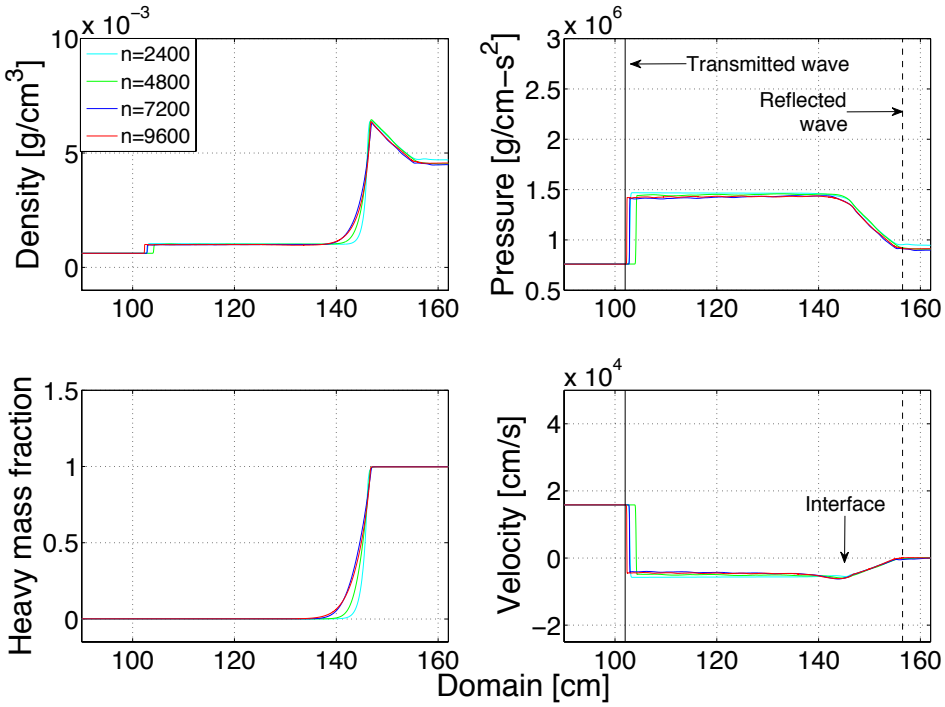

Figure 5.17: Mean field convergence for $At = 0.67$ and $Ma_s = 1.50$ at $t = 4.80$ ms.

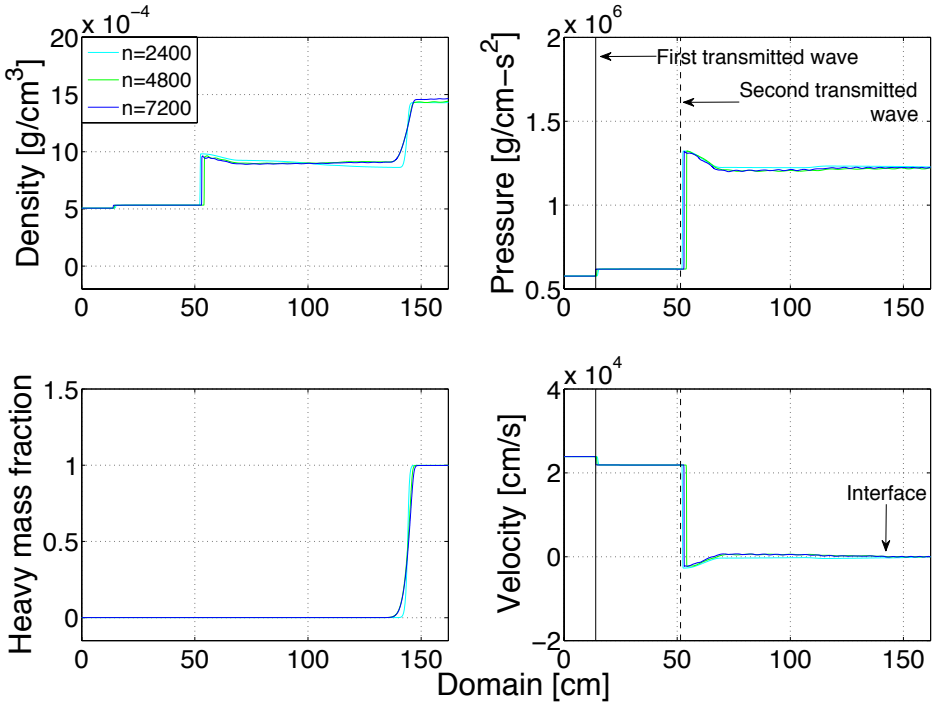

Figure 5.18: Mean field convergence for $At = 0.21$ and $Ma_s = 1.50$ at $t = 5.00$ ms.

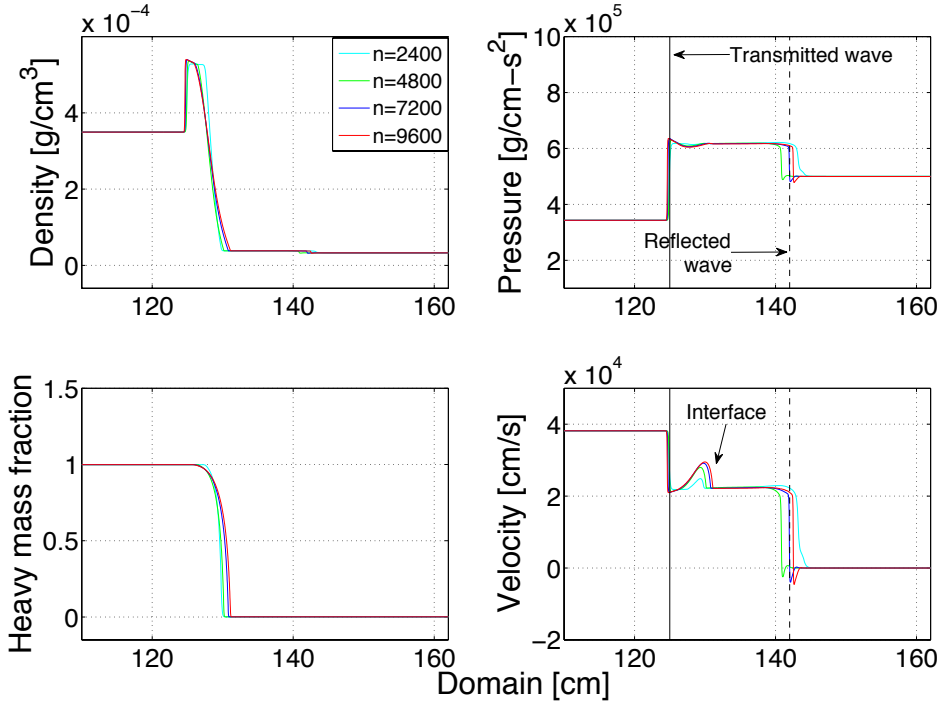

Figure 5.19: Mean field convergence for $At = -0.87$ and $Ma_s = 1.50$ at $t = 0.80$ ms.

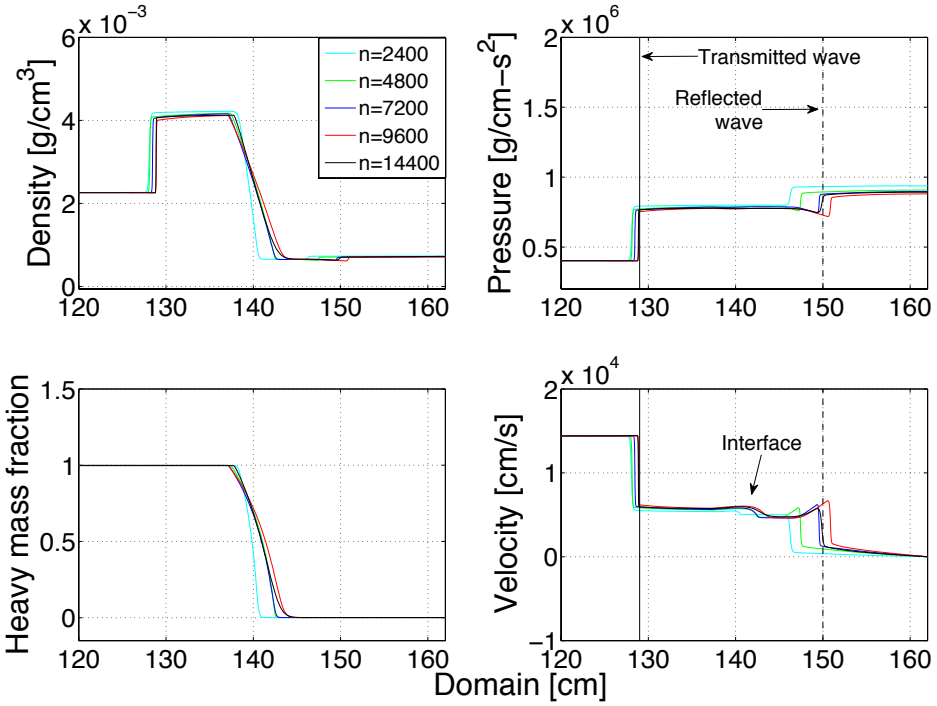

Figure 5.20: Mean field convergence for $At = -0.67$ and $Ma_s = 1.50$ at $t = 3.40$ ms.

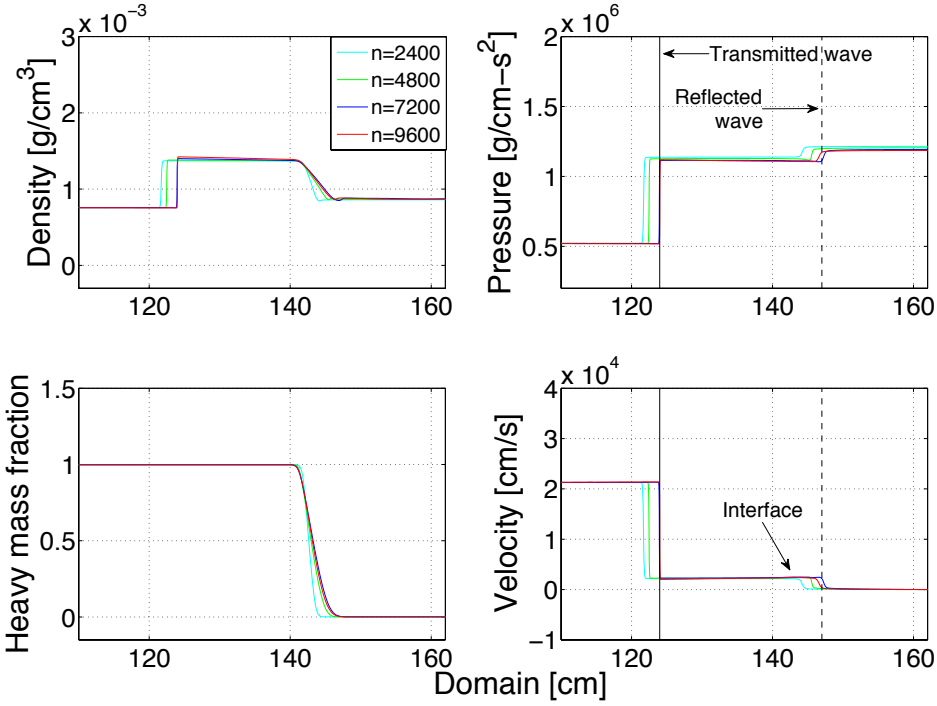

Figure 5.21: Mean field convergence for $At = -0.21$ and $Ma_s = 1.50$ at $t = 2.80$ ms.

number cases $At = -0.87$, -0.67, and -0.21 at times $t = 0.80$, 3.40, and 2.80 ms, respectively. Although the negative cases require slightly higher resolution than the positive Atwood number cases, convergence is generally achieved between $n = 7200$ and 9600 points. This is the case for $At = -0.87$ and -0.21, where using $n = 2400$ and 4800 points show small loss of accuracy primarily in the vicinity of the interface and both transmitted and reflected waves after reshock. For $At = -0.87$, less error is evident near the interface and shock front. In comparison, the $At = -0.21$ case demonstrates slightly more loss of accuracy for coarser grids near the fronts and interface.

Finally, recall that nonmonotonic behavior was observed in the convergence of the mixing layer width for $At = -0.67$. This is also seen in the mean fields, primarily near the reflected wave from the interface after reshock in the pressure and velocity profiles. It is also seen to a lesser extent in the density and heavy mass fraction profiles near the interface. This nonmonotonicity can be due to the significantly higher density of SF_6. Unlike the positive case with $At = 0.67$, where the denser gas impacted the interface during *reshock*, the lighter gas impacts the much denser gas during reshock in the corresponding negative case. Thus, the wave traveling in the air interacts with the SF_6 interface as a boundary or a wall as it reflects. Furthermore, the interface is not static, and the interaction of this additional boundary with secondary waves can make convergence difficult to achieve. After reshock, the reflected wave travels toward the test section endwall, where lack of convergence is most notable near the wave front. However, convergence results for both the mixing layer width and mean fields show that despite this behavior, simulation profiles using $n = 14400$ points decrease in magnitude and match results with $n = 7200$ points.

5.4.3 Convergence of the turbulent fields

Convergence of the turbulent fields was considered at the same times as the mean fields. However, unlike the mean fields where a single time was considered, convergence studies of the turbulent fields were extended to later times.

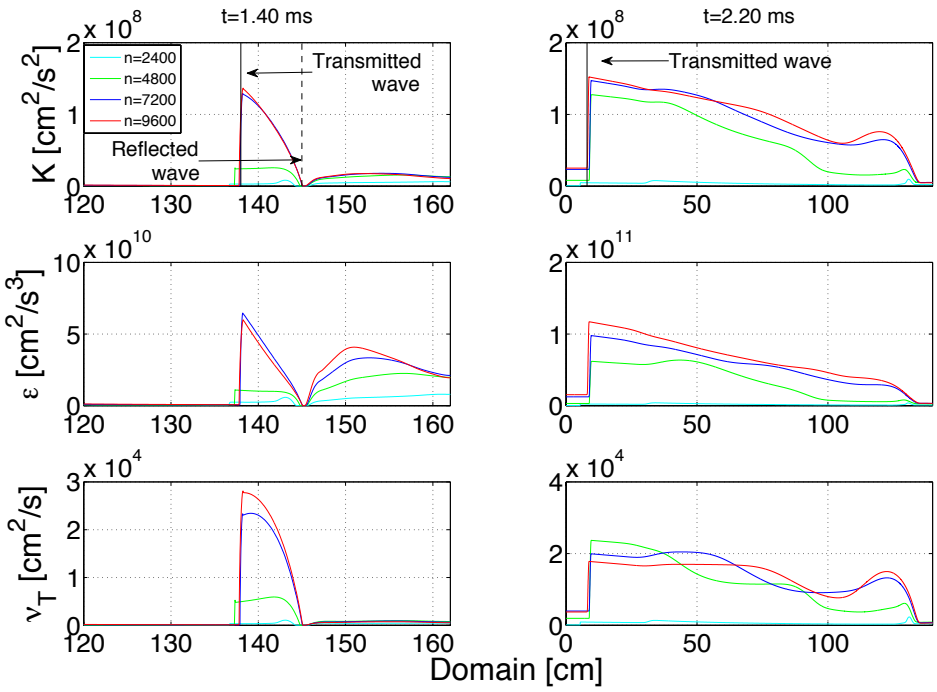

Figure 5.22: Turbulent field convergence for $At = 0.87$ and $Ma_s = 1.50$ at $t = 1.40$ and 2.20 ms.

The first case considered is for $At = 0.87$, with results illustrated in Fig. 5.22. As with the mixing layer width and the mean fields, convergence for the turbulent kinetic energy, turbulent kinetic energy dissipation rate, and turbulent viscosity is achieved between $n = 7200$ and 9600 points, where the turbulent viscosity converges slower than the other turbulent fields. Refinement at these levels still results in small differences between profiles, but loss of accuracy is small. However, unlike the mean fields, simulations using coarser grids with $n = 2400$ and 4800 points do not predict the turbulent fields adequately. Lack of convergence for the turbulent fields appears to grow for $At = 0.67$, which appears to be strongest in the vicinity of the interface where

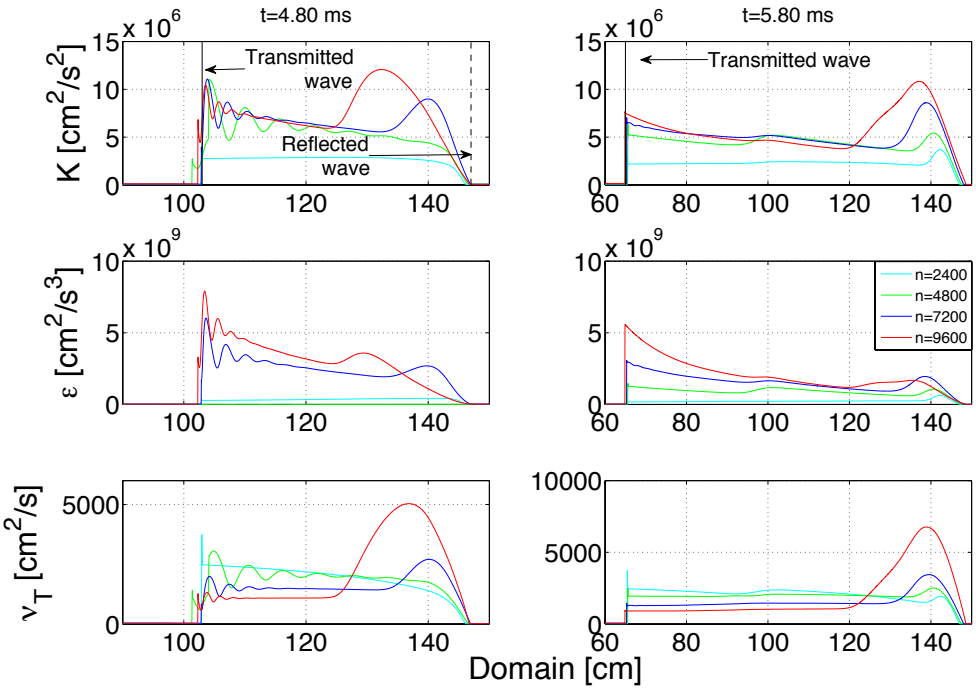

Figure 5.23: Turbulent field convergence for $At = 0.67$ and $Ma_s = 1.50$ at $t = 4.80$ and 5.80 ms.

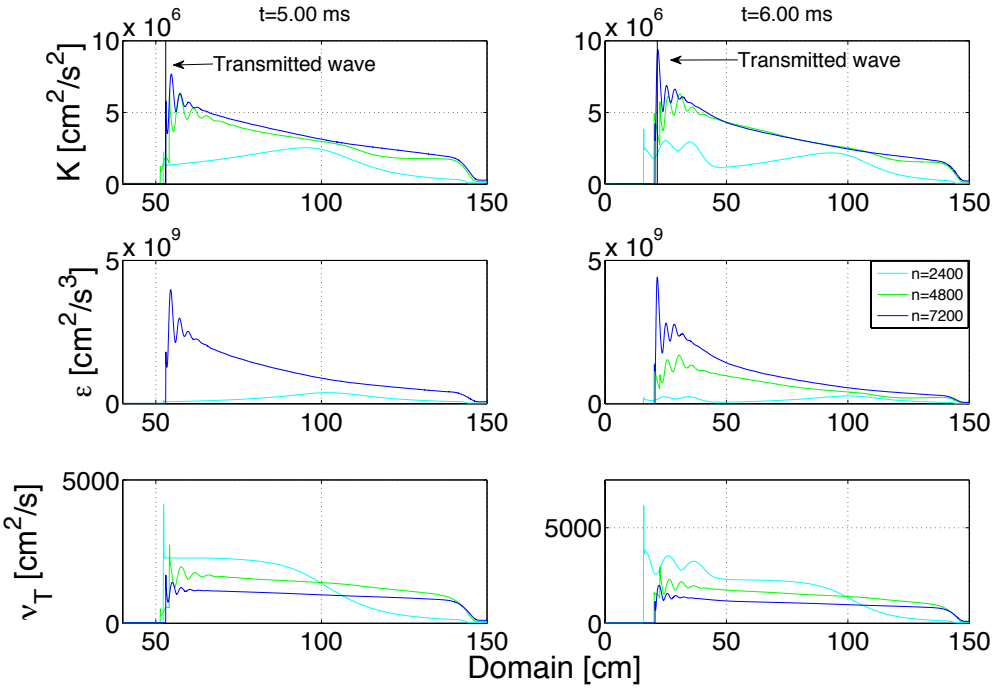

Figure 5.24: Turbulent field convergence for $At = 0.21$ and $Ma_s = 1.50$ at $t = 5.00$ and 6.00 ms.

mixing is most active. Oscillatory behavior is also observed behind the transmitted wave as illustrated in Fig. 5.23, which may be due to the higher density of SF_6; recall that SF_6 impacts air during reshock and progresses past the interface after compressing the interface. As SF_6 is denser, it proceeds past the interface and the mixing of the two gases continues behind the shock as well. Thus, simulating this behavior can cause numerical difficulties as the code calculates higher-order terms for rapidly varying quantities. However, as the transmitted wave becomes more distant from the interface, the profiles show converging behavior. The last case is $At = 0.21$. For this case, convergence of the mixing layer width and the mean fields was achieved between $n = 4800$ and 7200 points. This is also the case with the turbulent fields, with faster convergence achieved for the turbulent kinetic energy. The dissipation rate and turbulent viscosity also approach convergence more slowly. The rate of convergence appears to remains constant between $t = 5$ and 6 ms.

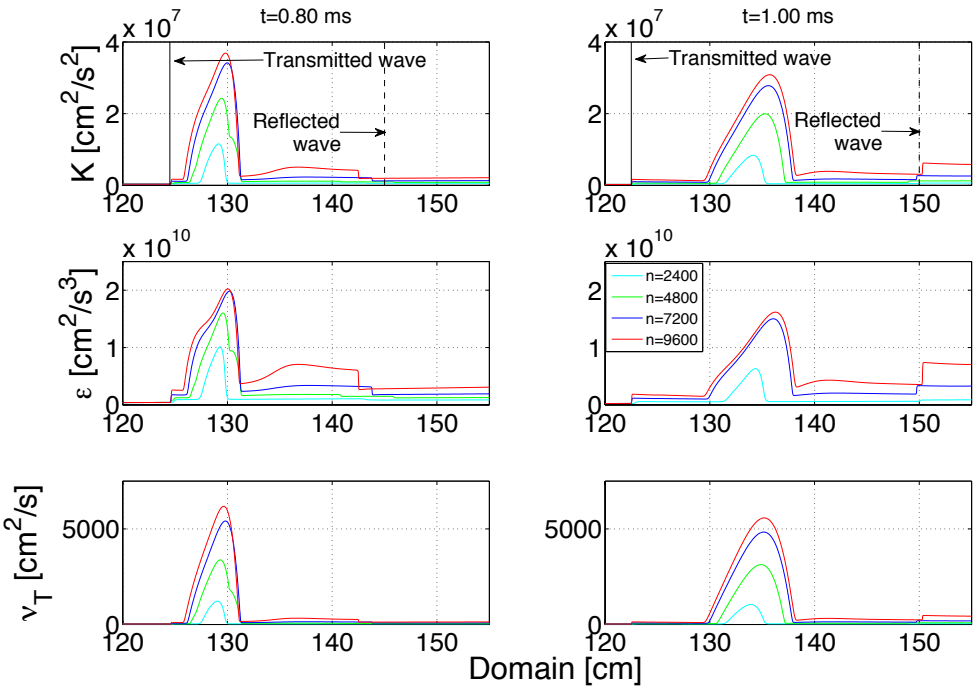

Figure 5.25: Turbulent field convergence for $At = -0.87$ and $Ma_s = 1.50$ at $t = 0.80$ and 1.00 ms.

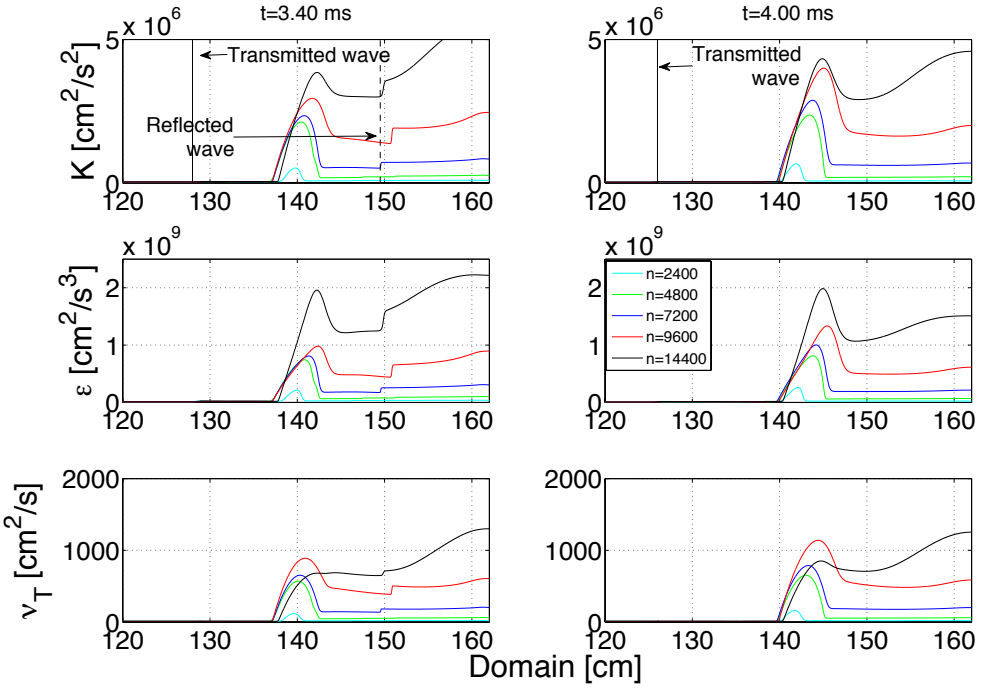

Figure 5.26: Turbulent field convergence for $At = -0.67$ and $Ma_s = 1.50$ at $t = 3.40$ and 4.00 ms.

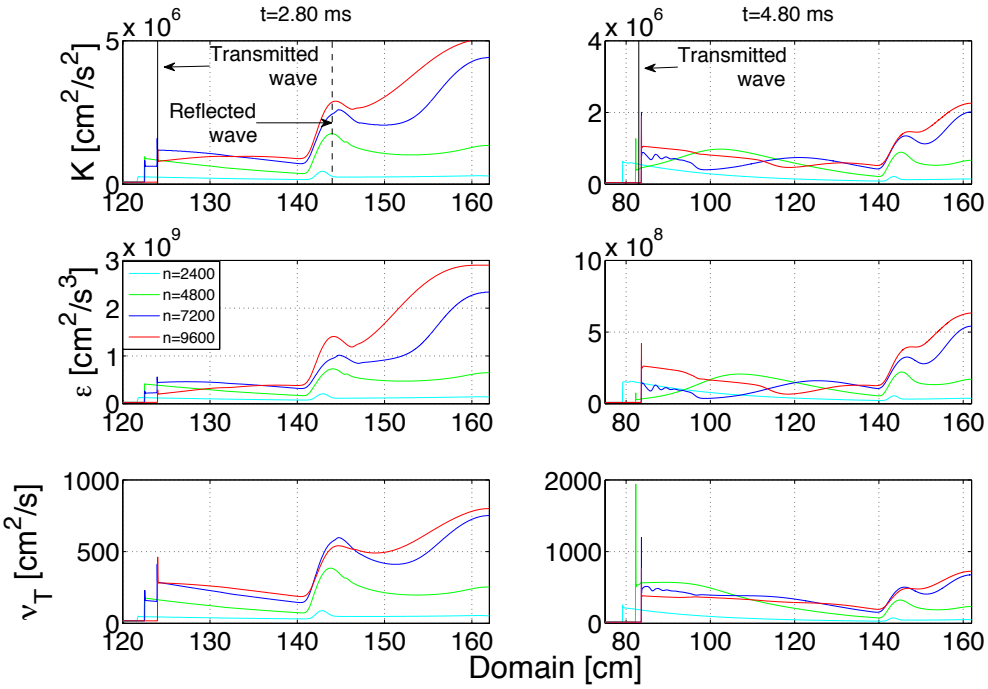

Figure 5.27: Turbulent field convergence for $At = -0.21$ and $Ma_s = 1.50$ at $t = 2.80$ and 4.80 ms.

Finally, convergence results for the turbulent fields with $At = -0.87$, -0.67, and -0.21 are presented in Figs. 5.25–5.27. Like the previous studies, the $At = -0.87$ case shows that convergence is achieved between $n = 7200$ and 9600 points, while using coarser grids with $n = 2400$ and 4800 points results in lack of accuracy for turbulent field predictions. The dissipation rate demonstrates a slower rate of convergence in the vicinity of the reflected wave after reshock. The $At = -0.67$ study demonstrated nonmonotonic behavior for the mixing layer width and mean fields. Related behavior is observed in the turbulent fields as illustrated in Fig. 5.26. As with the mixing layer, it appears that the turbulent fields approach convergence between $n = 4800$ and 7200 points. Convergence is observed as the grid is refined further to $n = 9600$ points. However, unlike mixing layer widths and mean fields, where simulations with $n = 14400$ points converge again to match the $n = 7200$ profile, profiles for the turbulent fields continue to diverge as the grid is refined further. It appears that this behavior originates from the reflected wave following reshock, where the interface is principally affected. Away from these interactions, convergence is achieved in the cold region and also in the vicinity of the transmitted wave from reshock. The reflected wave from reshock appears to also affect convergence of the last case, $At = -0.21$. Again, the transmitted shock travels away from the interface and the turbulent field profiles appear to converge in this region. However, lack of convergence is evident in the region between the interface and the test section endwall, where the secondary wave is located. This effect seems to be more prominent earlier where both transmitted and reflected waves are closer to the mixing region. As the waves become more distant as time progresses, all three turbulent profiles show converging behavior. Thus, convergence appears to be most difficult to achieve near the interface, where material discontinuities are present and mixing is most intense.

5.5 Chapter Summary

Reshocked–Richtmyer–Meshkov instability was considered for $At = \pm 0.87$, ± 0.67, and ± 0.21 corresponding to combinations of air with H_2, SF_6, and CO_2, respectively. Post-reshock turbulent mixing for larger Atwood numbers showed larger growth rates of the mixing layer. For negative Atwood numbers, where the denser gas impulsively accelerates the light gas, larger growth rates also resulted after reshock in comparison with the corresponding positive cases. Early-time mixing was independent of the Atwood number between cases using the same gas in the driver section. However, the Atwood number significantly affected the reshock times in addition to the post-reshock growth rates. Expansion waves were generally seen as the post-reshock secondary waves for positive Atwood numbers, while the negative Atwood cases experienced second reshocks. The evolution of the turbulent kinetic energy and dissipation rate budgets were considered for each of the six Atwood numbers. Buoyancy production and diffusion were generally the dominant terms, with smaller contributions from the shear production and dissipation. Estimates of the widths from the budget plots were in good agreement with the mixing layer width data.

The RANS mixing layer widths were compared with LES data (37). The RANS model generally predicted smaller early-time widths than LES, but comparisons varied after reshock. However, both the RANS and LES predictions were qualitatively similar. Convergence studies were performed for the RANS simulations, with convergence generally achieved between $n = 7200$ and 9600 points for the mixing layer widths and the mean fields. Simulations using coarser grids with $n = 2400$ and 4800 points allowed for small deviations in the mean fields. The mixing layer widths did not converge at this grid resolution, and more refinement was necessary. However, the mixing layer widths at the lower resolution agreed well with LES. This is a possible indication that the LES were underresolved. The turbulent fields showed slow convergence near secondary waves and boundaries, but converging behavior was seen away

from these regions. Nonmonotonicity was seen for the $At = -0.67$ case. However, the mixing layer width and the mean fields eventually converged, but the turbulent fields diverged. Convergence for this particular case is uncertain.

CHAPTER VI

Application of the Model to Reshocked Richtmyer–Meshkov Simulations for Larger Mach Numbers

Investigations in the previous chapters have focused on reshocked Richtmyer–Meshkov instability for moderate incident shock Mach numbers $1.20 \leq Ma_s \leq 1.98$, which constitute flows ranging from transonic to supersonic speeds. Parametric studies, variations in reshock timing, and the shock-induced acceleration of perturbed material interfaces with different gas combinations have been presented and discussed. Transonic speeds exist in the range $0.80 \leq Ma_s \leq 1.20$, while the supersonic range encompasses Mach numbers $1.20 \leq Ma_s \leq 5.00$ (56). Table 6.1 enumerates different sonic regimes with corresponding shock Mach numbers and speeds. Investigations considered to this point have focused on low energy supersonics. Simulations for the Vetter and Sturtevant $Ma_s = 1.24$ (10) and the Leinov *et al.* $Ma_s = 1.20$ (12) experiments border the transonic regime. Simulations for the $Ma_s = 1.50$ and 1.98 Vetter–Sturtevant and $Ma_s = 1.45$ Poggi *et al.* (11) experiments are in the lower supersonic regime.

A principal reason for the larger number of investigations at lower supersonic speeds is that experimental measurements and numerical simulations for larger Mach

Regime	v/c_s	Speed [$\times 10^4$cm/s]
Subsonic	≤ 0.8	≤ 2.70
Transonic	0.8–1.2	2.70–4.10
Supersonic	1.2–5.0	4.10–17.10
Hypersonic	5.0–10.0	17.10–34.15
High hypersonic	10–25	34.15–84.65
Re-entry speeds	≥ 25	≥ 84.65

Table 6.1: Regimes ranging from subsonic to re-entry speeds. The data are from Ref. (56).

numbers are sparse. Lombardini (38) performed LES for $Ma_s = 3.00$ and 5.00, but did not consider reshock, focusing instead on singly-shocked Richtmyer–Meshkov instability and the transition to turbulence. The lack of experimental and numerical data can make validating RANS models in new regimes a difficult task. Considered in this chapter is the application of the RANS model to reshocked Richtmyer–Meshkov instability at supersonic speeds bordering the hypersonic regime with $Ma_s = 3.00$ and 5.00, and Atwood numbers $At = -0.87$, -0.67, and -0.21. For positive Atwood numbers, *freeze out* is observed, in which turbulent mixing after reshock evolves very slowly, and the mixing layer appears to *freeze* rather than grow (57; 58; 59). This topic is not considered in the thesis. Thus, only negative Atwood numbers are investigated where multiple reshocks occur and the evolution of turbulent mixing can be more clearly investigated. Flows at larger Mach numbers begin to be affected by dissociation of molecules and gas ionization (56). The current RANS model does not consider these effects.

6.1 Initializing the Model for $Ma_s = 3.00$ and 5.00

As demonstrated in previous chapters, simulations using the current RANS model have been compared with a variety of experimental, numerical, and theoretical results for various Mach numbers and gas configurations. An approach similar to initializing the Vetter–Sturtevant $Ma_s = 1.98$ case (10) is used to initialize the simulations here

for two reasons. The $Ma_s = 1.98$ case is the study with the largest shock Mach number for which experimental and numerical results are available, and the RANS simulations produced results matching well with experimental data using both optimal and general sets of coefficients (see Chapter IV). In addition to matching experimental data well, confidence in the predictions has been further established through convergence studies. Although the rate of convergence for the turbulent fields was slow for $Ma_s = 1.98$, the mean fields and mixing layer width demonstrated convergence at resolutions with $n = 7200$ and 9600 points. Therefore, simulations for $Ma_s = 3.00$ were conducted under similar conditions: a test section length $\delta = 49$ cm, domain $X = 161$ cm, and initial conditions $K_0 = 0.10$ and $\lambda_{rms} = 0.50$ cm. The general coefficient set with $\sigma_\rho = 0.60$ and $C_{\epsilon 0} = 0.90$ was selected, while the remaining model coefficients were unchanged.

6.2 Turbulent Mixing at Larger Mach Numbers

To better understand the dynamics of impulsively-accelerated interfaces at larger Mach numbers, consider the $At = -0.67$ case with $Ma_s = 3.00$. Figure 6.1 illustrates the mixing layer width, where different events during the turbulent mixing process are indicated; Fig. 6.2 shows the mean heavy mass fraction as different times. Figures 6.3–6.5 show the mean fields and budgets for the turbulent kinetic energy and turbulent kinetic energy dissipation rate at $t = 1.25$ ms. The impulsive acceleration of the interface initiates mixing between SF_6 and air; the interface follows the shock with the width spreading as mixing evolves. After the shock initially reflects from the endwall, the first reshock occurs at $\tau_R \approx 0.95$ ms. The shock does not stop the interface from progressing towards the endwall, but is sufficiently energetic to compress the mixing layer so that the width decreases; as a result, the pressure and density in the compressed region increase. As the interface progresses, the distance to the endwall is shorter, and the reflected wave from the first reshock travels a shorter

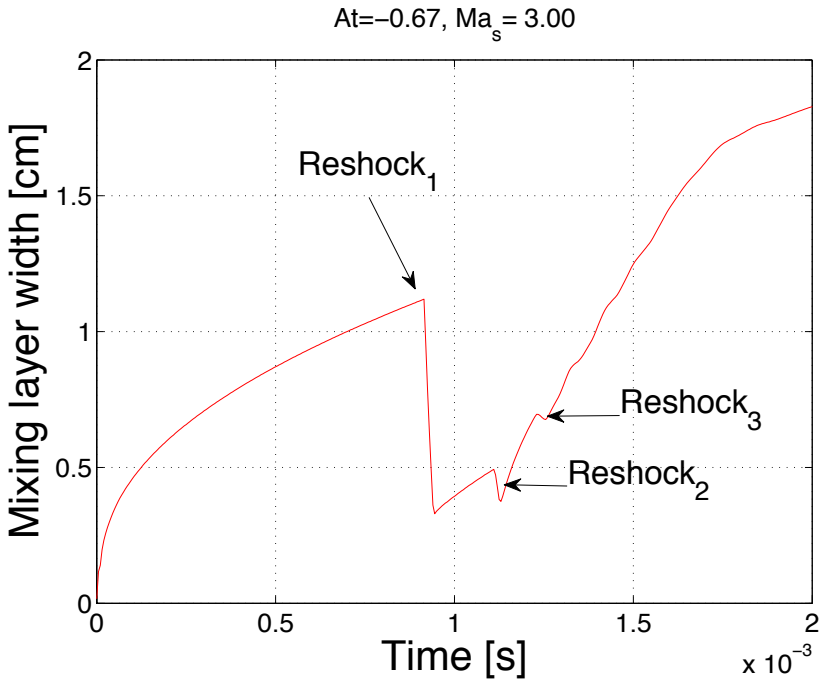

Figure 6.1: Mixing layer width for $At = -0.67$ and $Ma_s = 3.00$. The reshock times are $\tau_R \approx 0.95$, 1.15, and 1.30 ms.

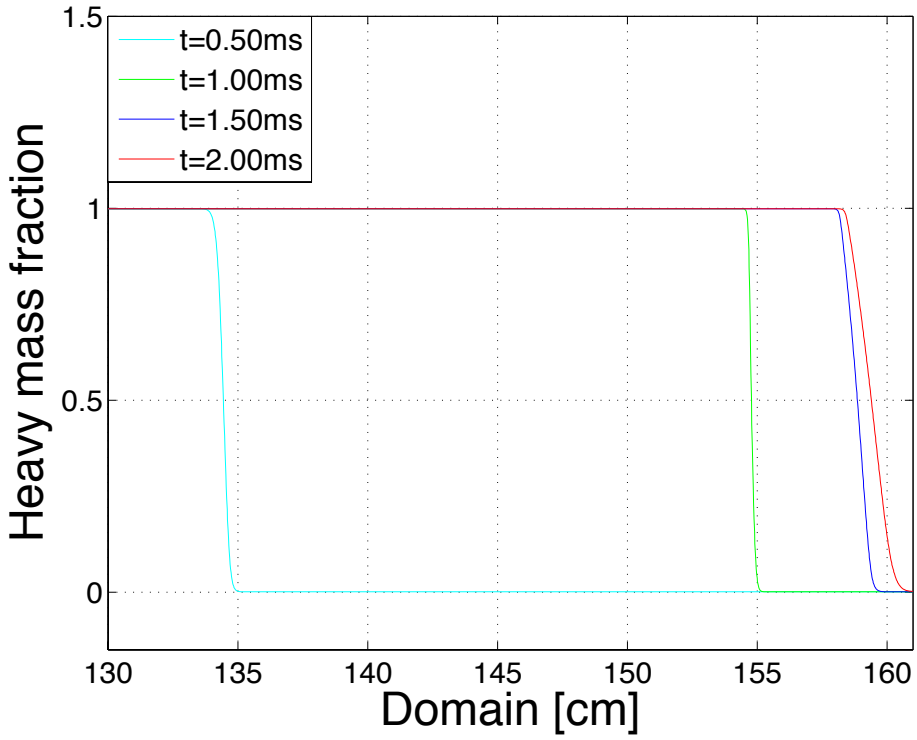

Figure 6.2: Evolution of the heavy mass fraction for $At = -0.67$ and $Ma_s = 3.00$ at $t = 0.50$, 1.0, 1.5, and 2 ms.

distance to reshock the mixing layer a second time (see Figs. 6.1 and 6.2). Turbulent mixing is inhibited as the newly compressed mixing layer does not have time to expand before it is reshocked a second time. Thus, the mixing layer appears to *freeze*, while the pressure and density behind the mixing region increase further after the second reshock. However, the second reshock slows the bulk of the compressed material. With the third reshock, the gas behind the interface finally starts moving away from the endwall, and the gas begins to expand and mix once again, resulting in renewed growth of the mixing layer. These phenomena are not manifested at smaller shock Mach numbers due to the lower energy of the shock. Instead of inhibited mixing accompanied by shrinking of the mixing layer, turbulent mixing at smaller shock Mach numbers continues to evolve and the density and pressure decrease with the expansion of the gas, as the interface is not *frozen*.

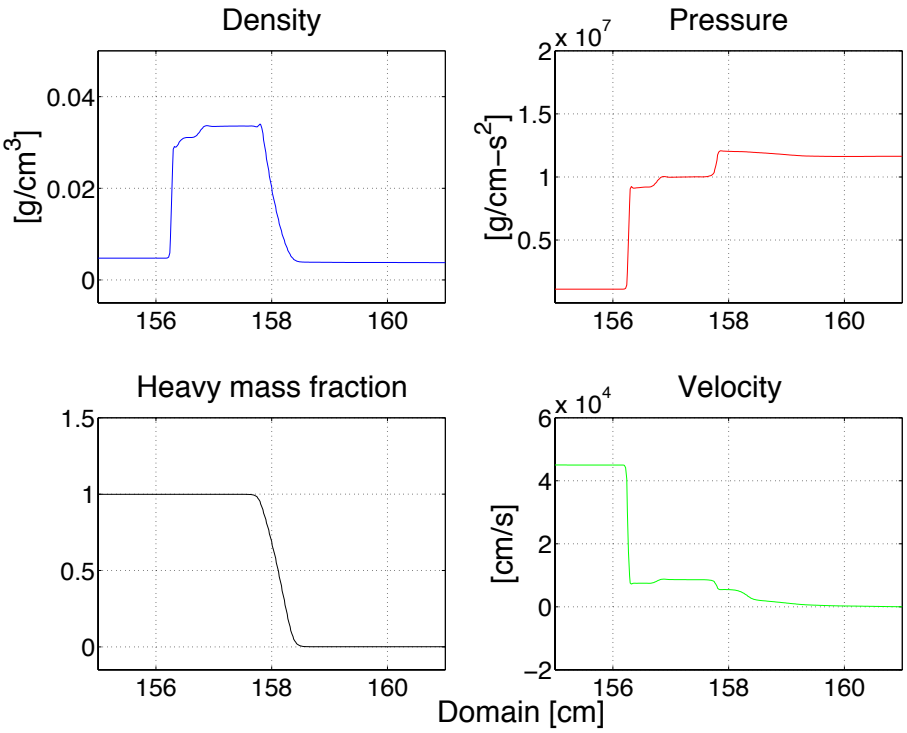

Figure 6.3: Mean fields for $At = -0.67$ and $Ma_s = 3.00$ at $t = 1.25$ ms.

At $t = 1.25$ ms, the transmitted wave from second reshock is leaving the com-

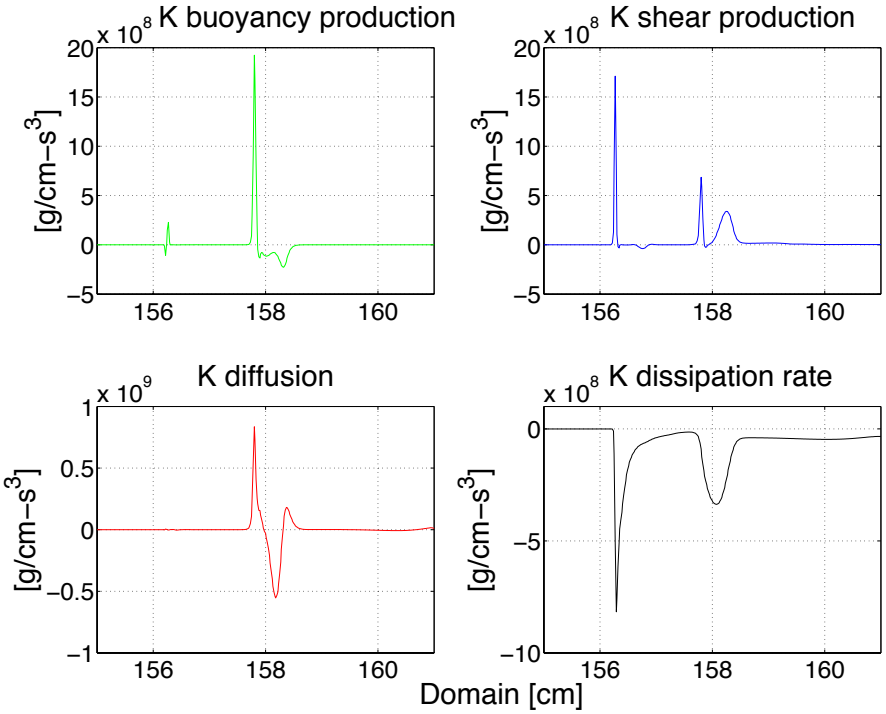

Figure 6.4: Turbulent kinetic energy budget for $At = -0.67$ and $Ma_s = 3.00$ at $t = 1.25$ ms.

pressed mixing layer. This is noted at $x \approx 156$ cm by the decrease in density and pressure and corresponding increase in velocity as the shock leaves the concentrated, denser compressed gas behind the layer in Fig. 6.3. Simultaneously, the wave initiating the third reshock has impacted the interface at $x \approx 158$ cm, as shown by the increase in pressure and density with decrease in velocity as the wave enters the denser region. Moreover, comparing the mean heavy mass fraction at $t = 1.25$ ms with earlier times in Fig. 6.2 shows the continued development of the mixing layer after third reshock. Figure 6.4 for the turbulent kinetic energy budgets similarly shows the decrease in buoyancy production as the transmitted wave from the second reshock exits the mixing layer at $x \approx 156$ cm. The decrease in pressure and density results in a decrease of buoyancy production. Conversely, as the mixing layer is reshocked a third time near $x \approx 158$ cm, a significant increase in buoyancy production occurs due to density and pressure gradients. Diffusion is most active in the mixing layer as

turbulent kinetic energy is supplied for turbulent mixing.

Conversely, the shear production increases as the transmitted wave from the second reshock exits the mixing layer due to the increase in velocity as the wave enters a region of lower density. Shear production similarly decreases as the wave reshocking the mixing layer the third time loses speed by entering the denser region. The spread of shear production over a wider region in the vicinity of the interface represents a more gradual production of turbulent kinetic energy. The dissipation of turbulent kinetic energy is principally localized behind the shock front, with additional dissipation in the mixing layer as the interface is compressed and turbulent kinetic energy is dissipated into heat.

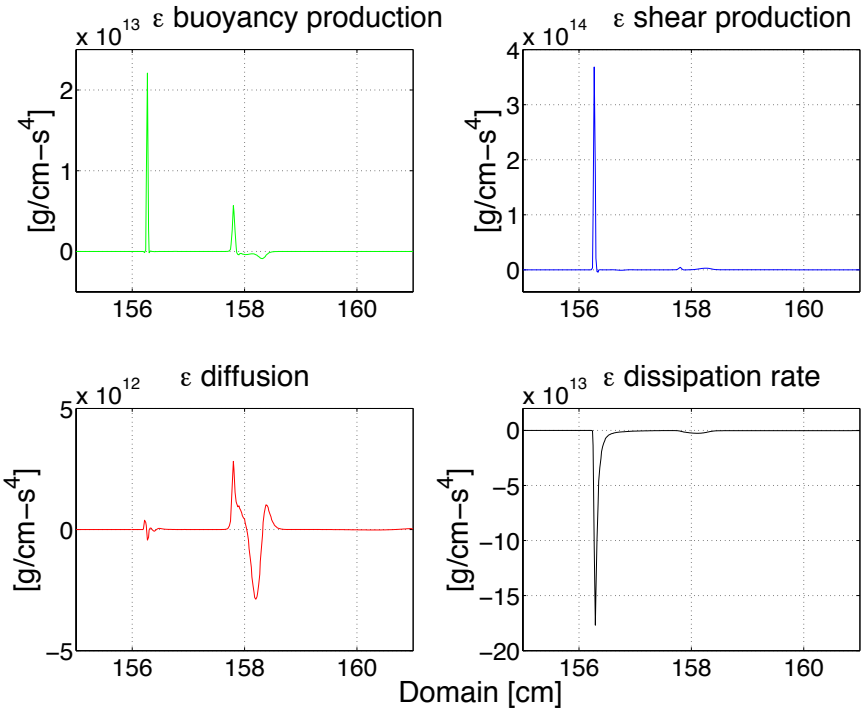

Figure 6.5: Turbulent kinetic energy dissipation rate budget for $At = -0.67$ and $Ma_s = 3.00$ at $t = 1.25$ ms.

The budgets for the turbulent kinetic energy dissipation rate in Fig. 6.5 reflect processes of the turbulent kinetic energy. As turbulent kinetic energy via buoyancy production decreases as it leaves the mixing layer, the dissipation rate increases, and

vice versa. Similarly, diffusion is most active near the interface, but decreases as the shock departs the mixing layer. Furthermore, as the wave from second reshock exits the compact and denser region, its speed increases, leading to an increase in buoyancy production. Contributions from the shear production of the dissipation rate form within the mixing layer, but are minimal as the shear production of turbulent kinetic energy has a secondary role in this region. Similar effects are noted in the turbulent kinetic energy dissipation rate.

6.3 Simulations for $At = -0.87$, -0.67, and -0.21 with $Ma_s = 3.00$

Section 6.2 discussed shocked-induced turbulent mixing for $At = -0.67$ initiated by a shock with $Ma_s = 3.00$. The investigation is extended here to additionally consider $At = -0.87$ and -0.21. Figure 6.6 (top) shows mixing layer widths for the three Atwood numbers with $Ma_s = 3.00$, and that shock-induced turbulent mixing is more effective for larger Atwood numbers. Similar results were presented in Fig. 5.3 for $Ma_s = 1.50$ with $\delta = 62$ cm. The enhanced growth rate for larger Atwood numbers is due to greater differences in densities between the gases in the driver and test sections. Larger density gradients lead to larger buoyancy production of turbulent kinetic energy. As the Atwood number decreases and the difference in densities is smaller, the buoyancy production produces less turbulent kinetic energy and turbulent mixing after reshock is smaller, as seen in the $At = -0.21$ case. The mixing layer width for $At = -0.87$ shows behavior similar to that discussed in Sec. 6.2 for $At = -0.67$, but the post-reshock growth rates are larger for reasons just discussed. The first and second reshocks occur at $\tau_R \approx 0.31$ and $\tau_{R2} \approx 0.46$ ms, respectively, within $\Delta t = 0.15$ ms of each other. Table 6.2 gives times of the multiple reshocks for each of the Atwood number cases.

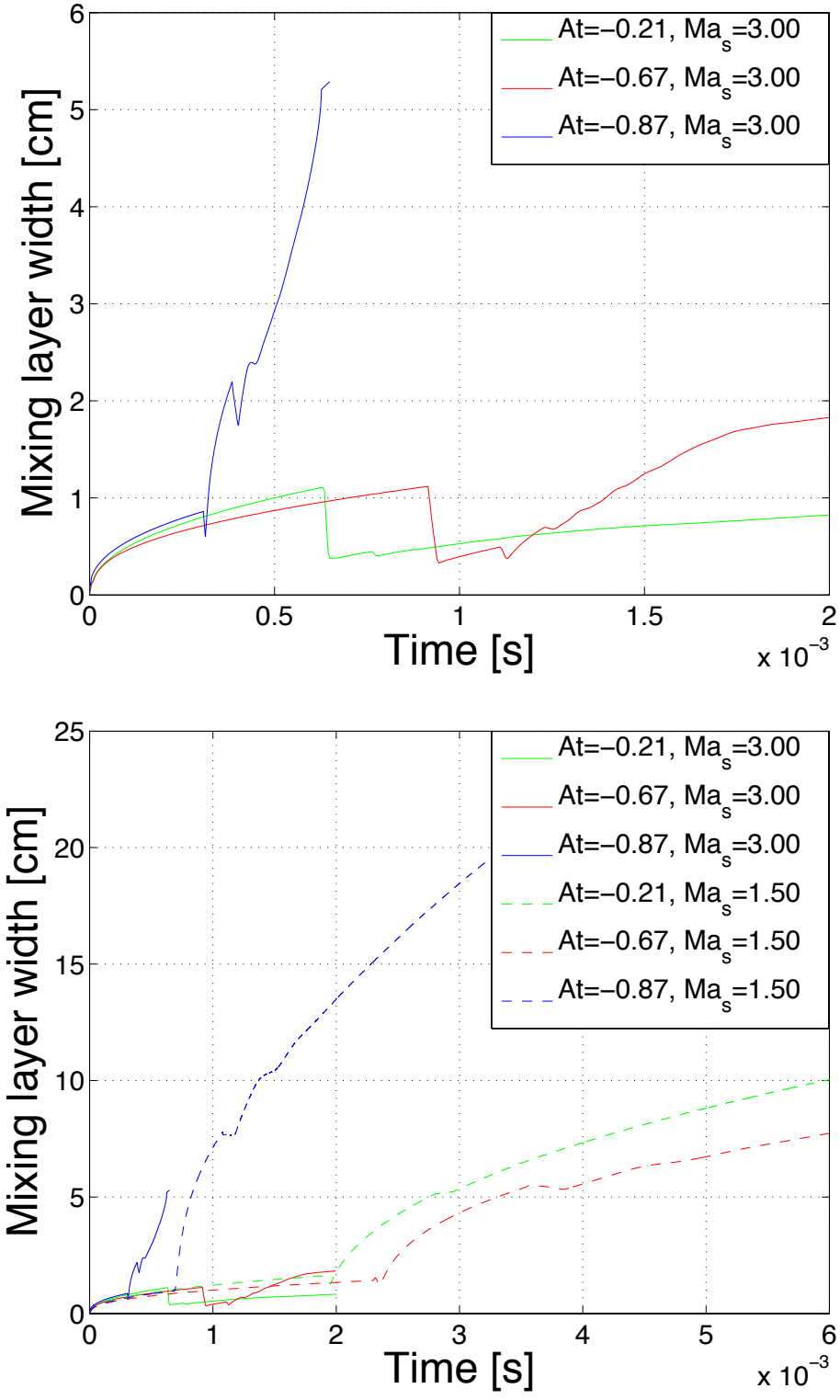

Figure 6.6: Mixing layer widths for $At = -0.21$, -0.67, and -0.87 with $Ma_s = 3.00$, $\delta = 49$ cm and $Ma_s = 1.50$, $\delta = 62$ cm.

At		-0.21	-0.67	-0.87
τ_R	ms	0.65	0.95	0.31
τ_{R2}	ms	0.75	1.15	0.46
τ_{R3}	ms	–	1.30	–
$\dot{h}$ $(Ma_s = 1.50)$	cm/s	5.1×10^3	6.6×10^3	31.9×10^3
$\dot{h}$ $(Ma_s = 3.00)$	cm/s	0.9×10^3	3.0×10^3	8.5×10^3

Table 6.2: Reshock times and growth rates after *first* reshock for $At = -0.21$, -0.67, and -0.87 with $Ma_s = 3.00$, $\delta = 49$ cm and $Ma_s = 1.50$, $\delta = 62$ cm.

Comparisons of the mixing layer growth rates after the *first* reshock are also made between the $Ma_s = 3.00$ and 1.50 (see Chapter V) cases. Despite the 13 cm difference in test section lengths, it is useful to compare cases between the different shock Mach numbers; recall from Chapter IV that variations in δ affect the reshock time, but minimally affect the post-reshock growth rate. Therefore, differences in the post-reshock mixing layer widths are primarily a result of the difference in Mach numbers. As a comparative reference, widths are included in the bottom plot of Fig. 6.6. In comparing widths between shock Mach numbers in Fig. 6.6, the results further indicate that turbulent mixing prior to reshock is not significantly affected by differences in Ma_s. Similar findings were presented in Sec. 3.2, where variations of $\pm 3\%$ from $Ma_s = 1.50$ were considered. While reshock times and growth rates after reshock vary with Ma_s, the general behavior and structure remain similar. Reshock occurs earlier in time due to the corresponding increase in shock speed for larger Mach numbers, as expected. However, an important result is that in increasing the initial shock strength to $Ma_s = 3.00$, turbulent mixing is less effective for the three Atwood numbers at later times: this is primarily due to the successive reshocks in relatively short periods of time. While reshock increases turbulent mixing, the successive compression of the interface by reflected shocks in short time intervals suppresses turbulent mixing. Thus, the constantly decreasing distance between the interface and endwall in conjunction with larger Ma_s inhibits turbulent mixing. By comparison, a weaker shock results in slower progression of the interface and longer

periods between successive reshocks; this allows the mixing layer to further evolve before the second reshock enhances turbulent mixing.

6.4 Turbulent Mixing for $At = -0.67$ and $Ma_s = 5.00$

The RANS model is also applied to reshocked Richtmyer–Meshkov instability with $At = -0.67$ and $Ma_s = 5.00$. The dynamics of early-time mixing at $Ma_s = 5.00$ are generally similar to those discussed in Sec. 6.2 for $Ma_s = 3.00$, but there are differences between these cases in the post-reshock mixing. Figure 6.7 shows that mixing is initiated by the initial shock, and the first reshock occurs at $\tau_R \approx 0.56$ ms. Like the $Ma_s = 3.00$ case, the mixing layer progresses towards the test section endwall. However, there is no transmitted wave after the first reshock. Part of the energy imparted during reshock compresses the gas and shrinks the mixing layer, which results in an increase in pressure and density; the remaining energy is carried by the reflected wave. The mixing layer remains in this compressed state as it progresses towards the endwall, decreasing the distance between the interface and wall boundary: this is seen in the evolution of the mean heavy mass fraction in Fig. 6.8. The second reshock occurs at $\tau_{R2} \approx 0.64$ ms, resulting in an additional increase of the density and pressure within the mixing layer. Unlike the $Ma_s = 3.00$ case, the mixing layer does not slow down after the second reshock, but continues progressing towards the endwall. After the second reshock, a secondary expansion wave is seen rather than a reflected wave (that eventually would result in a third reshock). Furthermore, the density of the gas within the mixing layer is significantly larger than the density in the downstream region, and a rarefaction wave develops as the denser gas within the layer pushes the lighter gas. The rarefaction and expansion waves coalesce close to the endwall at $t \approx 0.66$ ms, and mixing is enhanced. This is seen in the growth of the mixing layer width in Fig. 6.7 and in the evolution of the mean heavy mass fraction in Fig. 6.8. During the 0.04 ms interval, the mixing layer is still progressing towards

the endwall. By $t \approx 0.70$ ms, all of the air in the test section is mixed as the mean heavy mass fraction reaches the endwall.

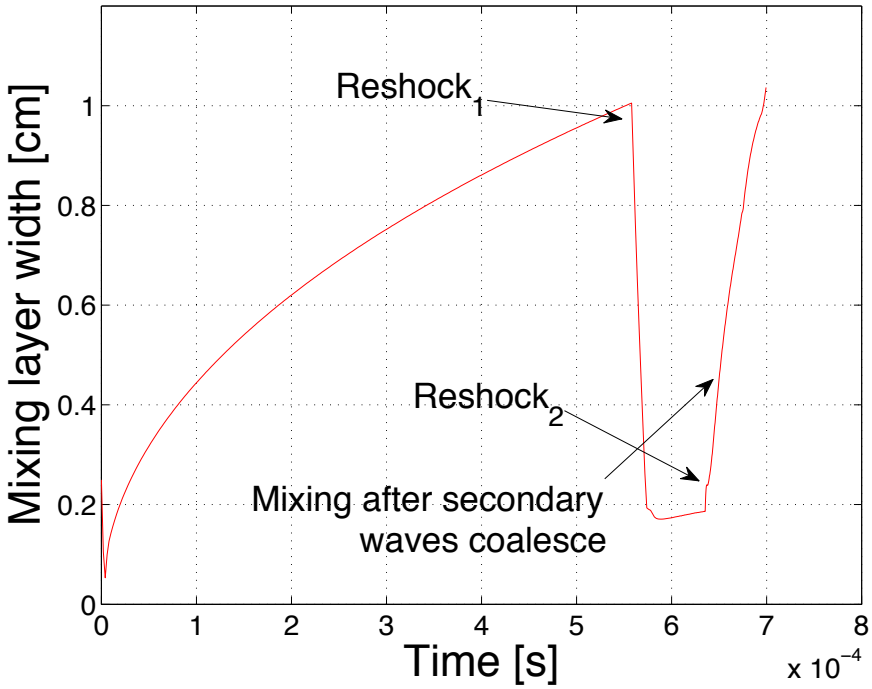

Figure 6.7: Mixing layer widths for $At = -0.67$ and $Ma_s = 5.00$.

Reshocked Richtmyer–Meshkov instability for $At = -0.67$ with $Ma_s = 5.00$ significantly inhibits turbulent mixing. This is further shown in Fig. 6.9, where turbulent mixing for $At = -0.67$ with $Ma_s = 1.50$, 3.00, and 5.00 is considered. As the incident shock Mach number increases, post-reshock turbulent mixing is reduced. Reshock times are earlier for larger shock Mach numbers, as expected. Moreover, the early-time width increases with Ma_s due to the additional turbulent kinetic energy supplied by the turbulent pressure. However, changes in the early-time width are small. Reshocked Richtmyer–Meshkov instability for $At = -0.87$ and -0.21 is not considered in this thesis, but is a topic of interest for future work. Monotonic behavior is seen in Fig. 6.9 for $At = -0.67$. It is reasonable to expect similar evolutions and structures for the other Atwood numbers. Larger growth rates are expected for $At = -0.87$, but a more gradual evolution of the mixing layer width is expected for $At = -0.21$.

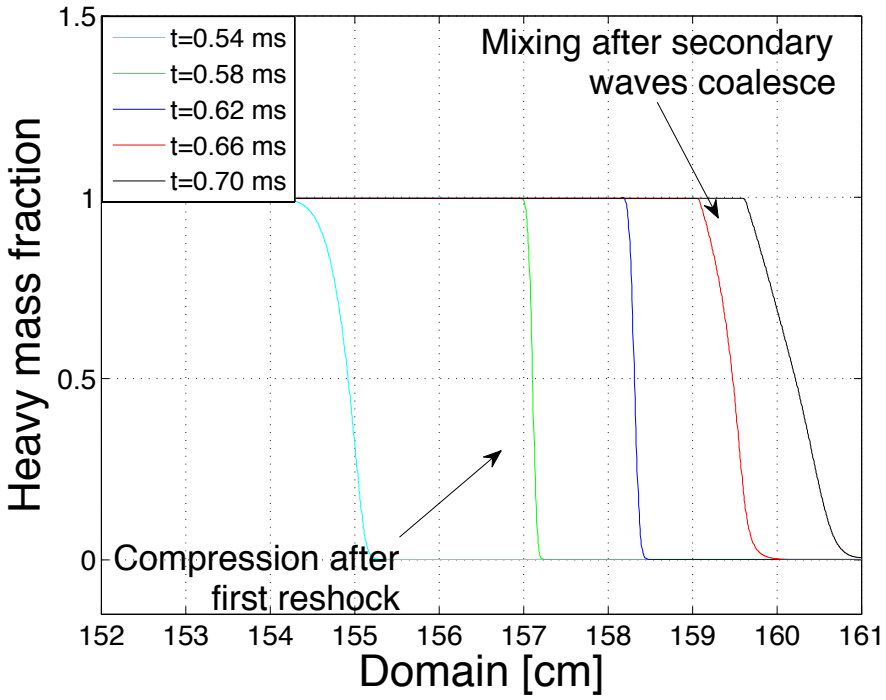

Figure 6.8: Evolution of the mean heavy mass fraction for $At = -0.67$ and $Ma_s = 5.00$ at $t = 0.54$, 0.58, 0.62, 0.66, and 0.70 ms.

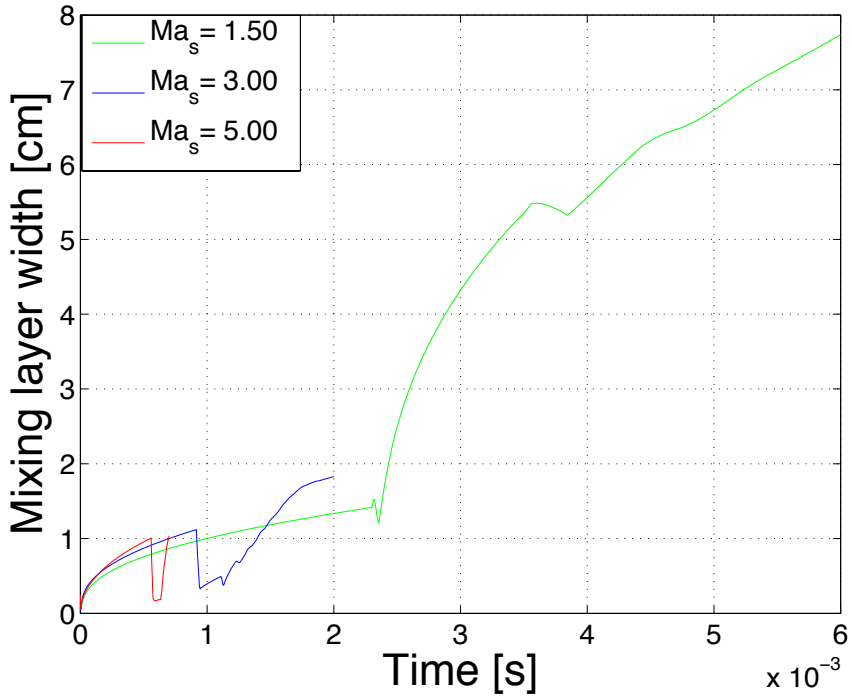

Figure 6.9: Mixing layer widths for $At = -0.67$ and $Ma_s = 1.50$, 3.00, and 5.00.

6.5 Convergence Under Grid Refinement

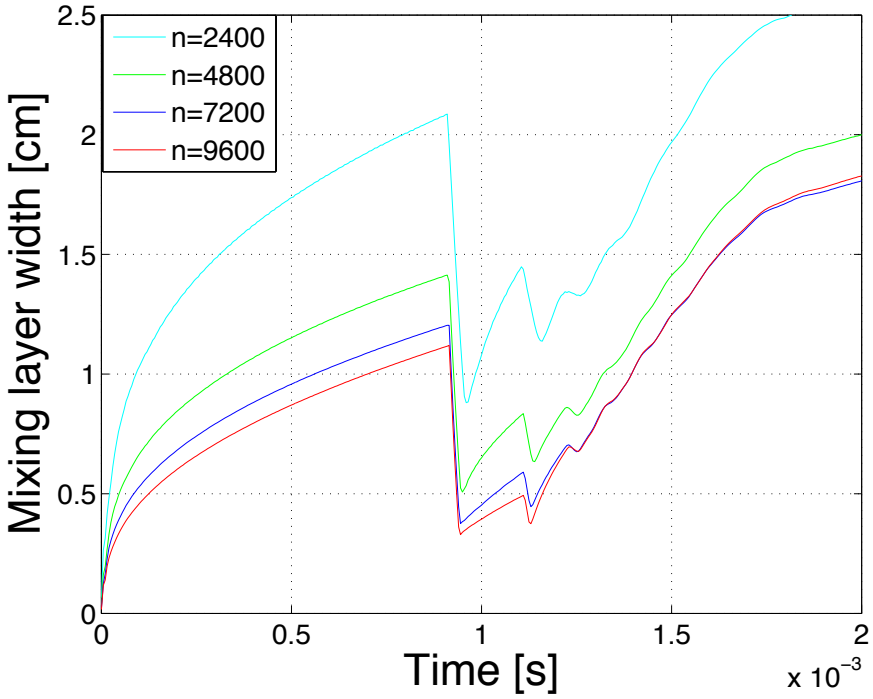

Figure 6.10: Mixing layer width convergence for $At = -0.67$ and $Ma_s = 3.00$.

Convergence was considered for the cases discussed in Secs. 6.2–6.4. Grid refinement for the RANS simulations included $n = 2400$, 4800, 7200, 9600, 14400, 19200, and 28800 points, which correspond to grid spacings $\Delta x = 0.067$, 0.034, 0.022, 0.017, 0.011, 0.008, and 0.006 cm, respectively. For $At = -0.67$ with $Ma_s = 3.00$, Figs. 6.10–6.12 show that the mixing layer width and the mean and turbulent fields converge between $n = 7200$ and 9600. A small loss of accuracy is seen in the early-time width and before the second reshock, but quantities converge as mixing evolves after the second reshock. Convergence for the mean and turbulent fields is considered at $t = 1.25$ ms; at this time the transmitted wave from the second reshock enters the pure SF_6 region while the mixing layer is simultaneously reshocked a third time. Figures 6.11 and 6.12 show that simulations using coarser grids with $n = 2400$ and 4800 points inaccurately predict the fields as waves enter and exit the mixing layer due

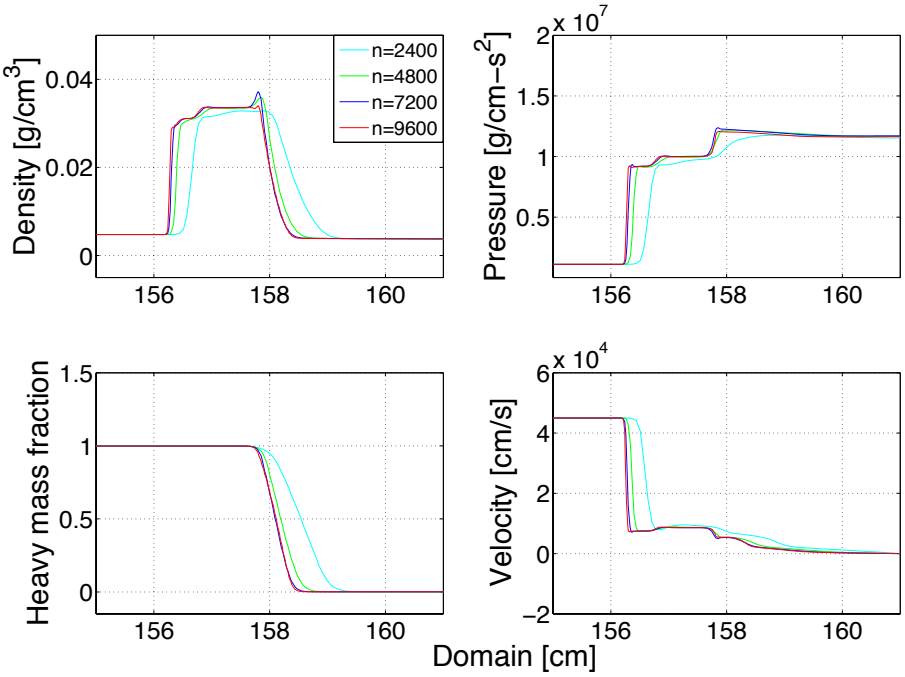

Figure 6.11: Mean field convergence for $At = -0.67$ and $Ma_s = 3.00$ at $t = 1.25$ ms.

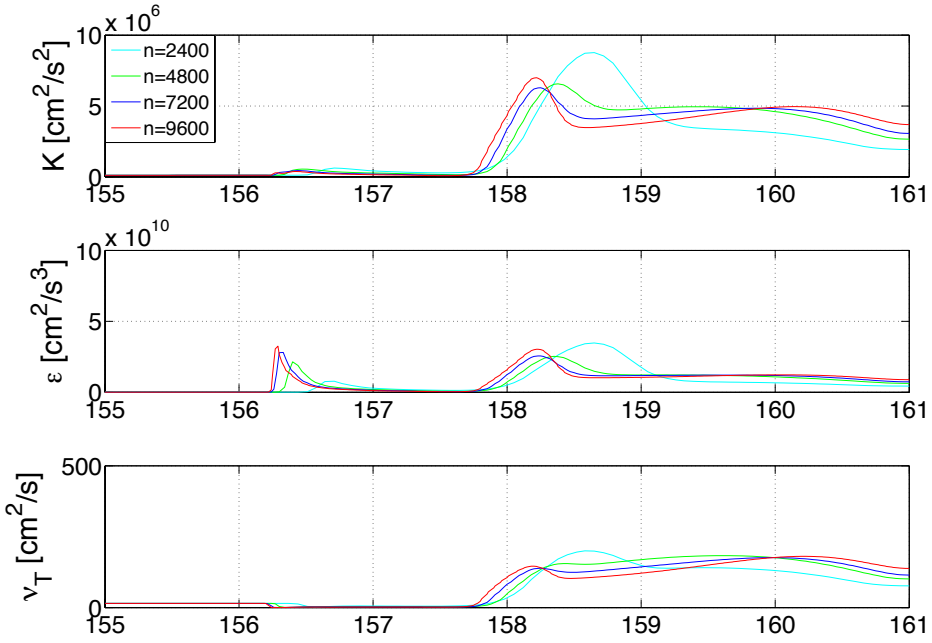

Figure 6.12: Turbulent field convergence for $At = -0.67$ and $Ma_s = 3.00$ at $t = 1.25$ ms.

to material discontinuities. Increasing the resolution shows converging behavior with $n = 7200$ and 9600 points.

Studies for $At = -0.87$ with $Ma_s = 3.00$ show nonmonotonic converging behavior for the mixing layer width and the mean and turbulent fields. Figure 6.13 shows that the mixing layer approaches convergence as the grid is refined from $n = 2400$ to 7200 points. However, divergence is seen as the resolution increases to $n = 9600$ points. As the grid is refined further to $n = 14400$ points, the width converges to results with $n = 7200$ points. Similar behavior was seen in Sec. 5.4 for the $At = -0.67$ case, where it is possible that the nonmonotonicity was due to the material discontinuities. Convergence is considered for the mean and turbulent fields at $t = 0.40$ ms, approximately the same time of the second reshock. Figure 6.14 shows the increase in pressure and density and corresponding decrease in shock speed as the wave reshocks the mixing layer. Figure 6.15 shows that the turbulent fields are largest in the turbulent mixing layer. Simulations with $n = 2400$ points are not adequate to correctly represent the mean and turbulent fields. Converging behavior is seen between $n = 4800$ and 7200 points, but the profiles diverge with $n = 9600$ points. Like the mixing layer, the fields show converging behavior between $n = 7200$ and 14400 points.

Simulations for $At = -0.21$ and $Ma_s = 3.00$ generally required additional resolution to achieve convergence. The mixing layer width in Fig 6.16 shows converging behavior for early-time mixing between $n = 14400$ and 19200 points, while the post-reshock width shows a small loss of accuracy between these resolutions. Convergence for the mean fields was considered at $t = 0.70$ ms, where the transmitted and reflected waves after the first reshock are distinguishable in Fig. 6.16. Results show that the mean fields required less resolution as convergence was reached between $n = 4800$ and 7200 points. However, the turbulent fields required as much resolution as the mixing layer width to show converging behavior. Figure 6.18 shows the turbulent ki-

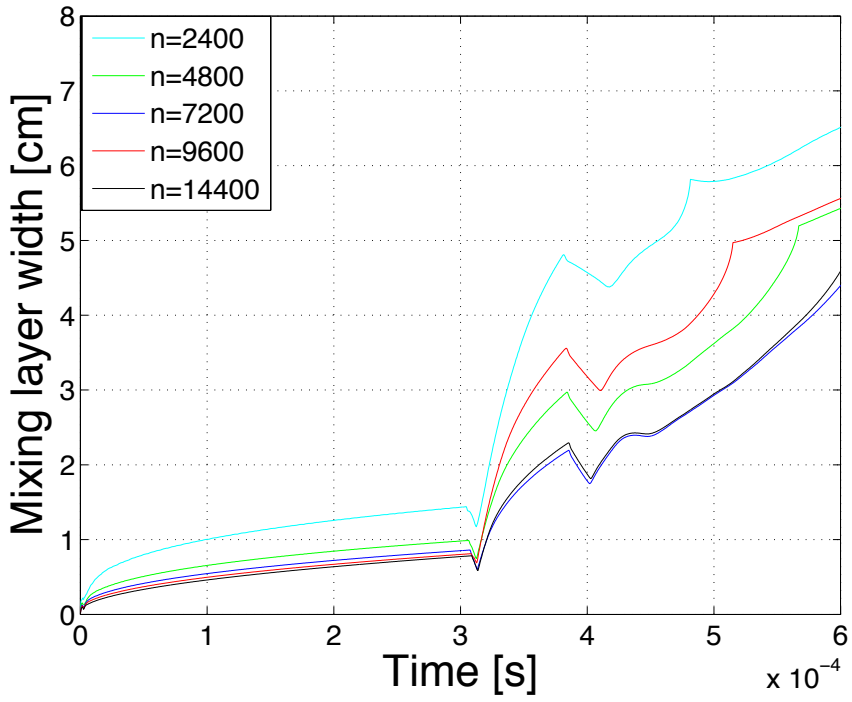

Figure 6.13: Mixing layer width convergence for $At = -0.87$ and $Ma_s = 3.00$.

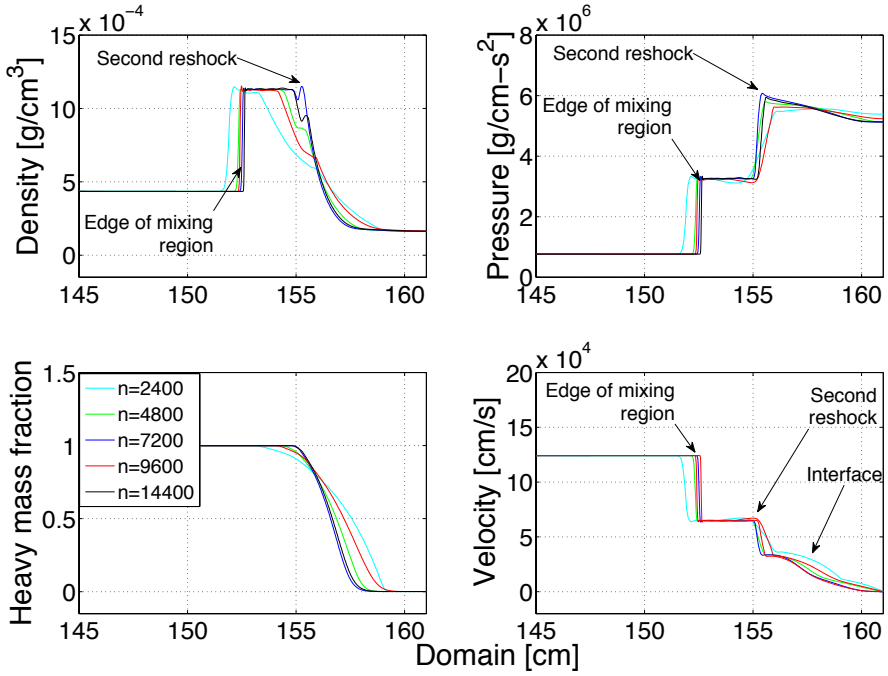

Figure 6.14: Mean field convergence for $At = -0.87$ and $Ma_s = 3.00$ at $t = 0.40$ ms.

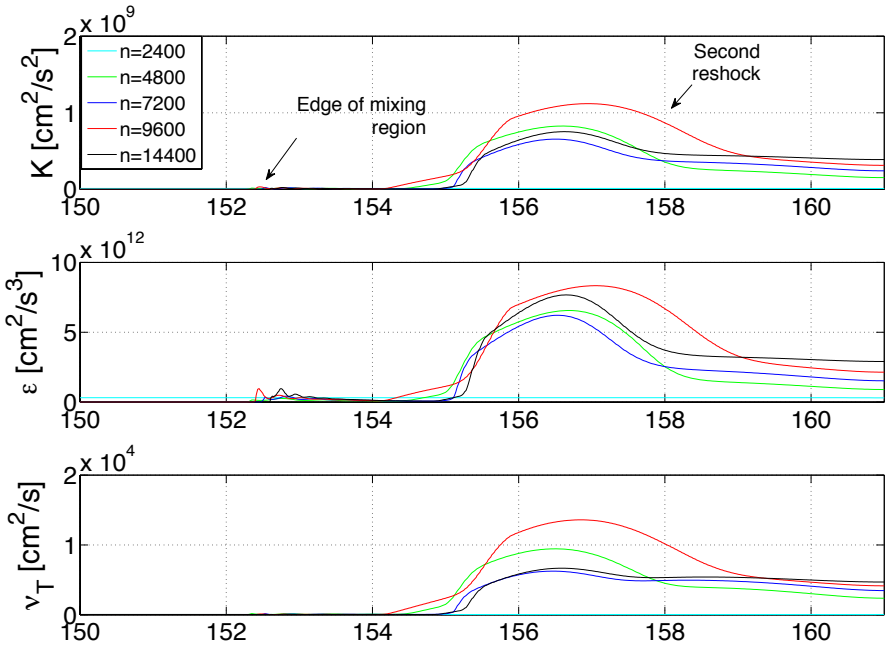

Figure 6.15: Turbulent field convergence for $At = -0.87$ and $Ma_s = 3.00$ at $t = 1.25$ ms.

netic energy, dissipation rate, and turbulent viscosity within the mixing layer as the transmitted and reflected waves travel in opposite directions after the first reshock. The slow convergence behind the transmitted wave is due to the rapid variations in the turbulent fields as mixing of the gases evolves. Ahead of the transmitted wave, turbulence is minimal and convergence is achieved sooner.

Finally, convergence for $At = -0.67$ with $Ma_s = 5.00$ required the largest resolution to approach convergence. Figure 6.19 shows that the early-time mixing layer converges between $n = 19200$ and 28800 points. However, the width shows lack of convergence after reshock for two possible reasons. As the density of SF_6 is larger in comparison to the downstream region and no energy is transmitted after reshock, the interface acts as an additional boundary with which the wave interacts, thus leading to boundary–wave instabilities. Also, this additional boundary is not static as it progresses towards the interface rapidly behind the reflected wave as discussed in Sec. 6.4. Thus, convergence can be inhibited in modeling additional moving discontinuities in

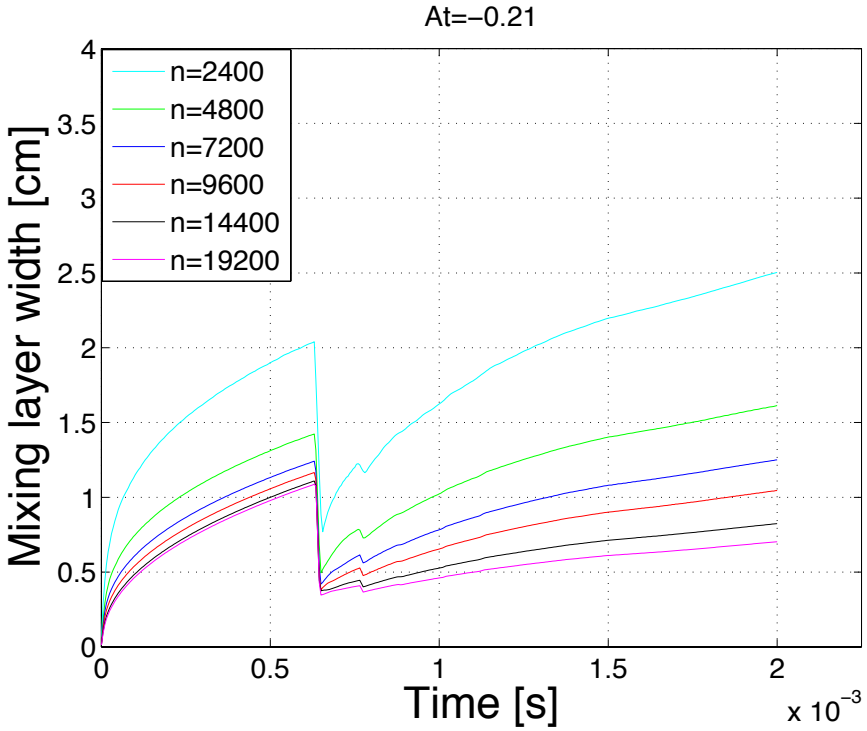

Figure 6.16: Mixing layer width convergence for $At = -0.21$ and $Ma_s = 3.00$ at $t = 0.70$ ms.

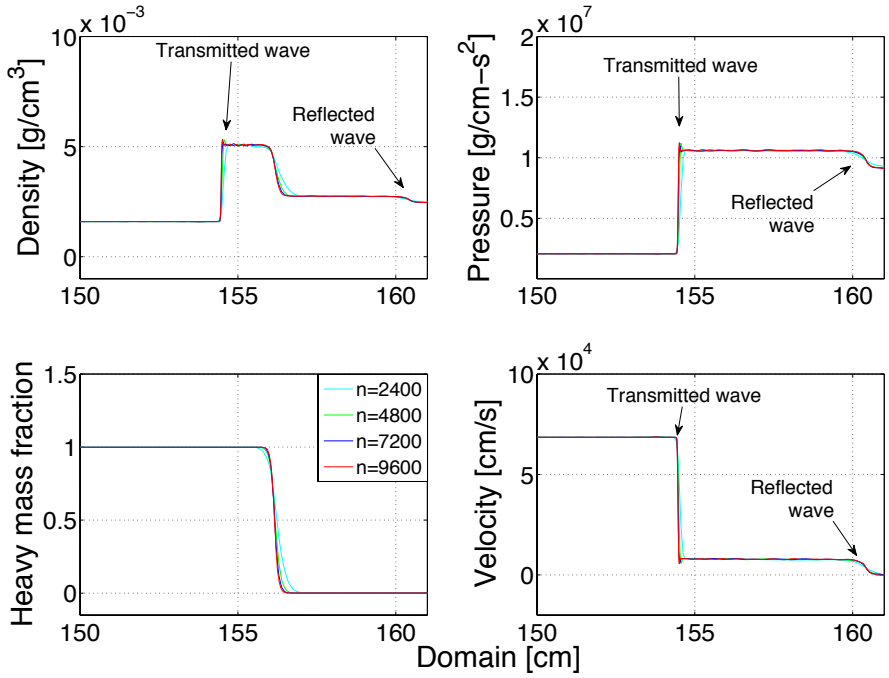

Figure 6.17: Mean field convergence for $At = -0.21$ and $Ma_s = 3.00$ at $t = 0.70$ ms.

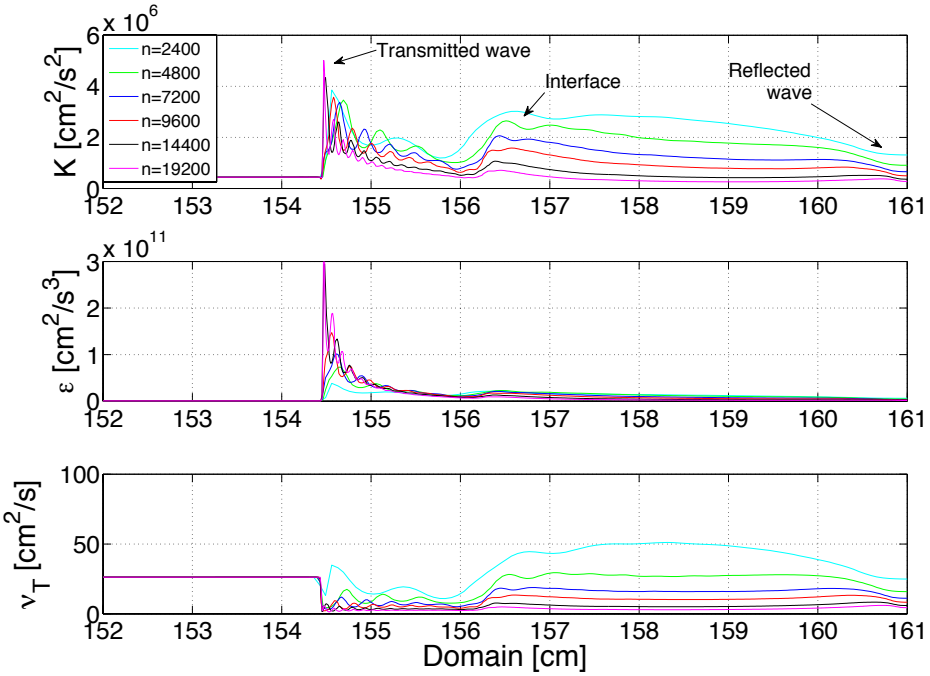

Figure 6.18: Turbulent field convergence for $At = -0.21$ and $Ma_s = 3.00$ at $t = 0.70$ ms.

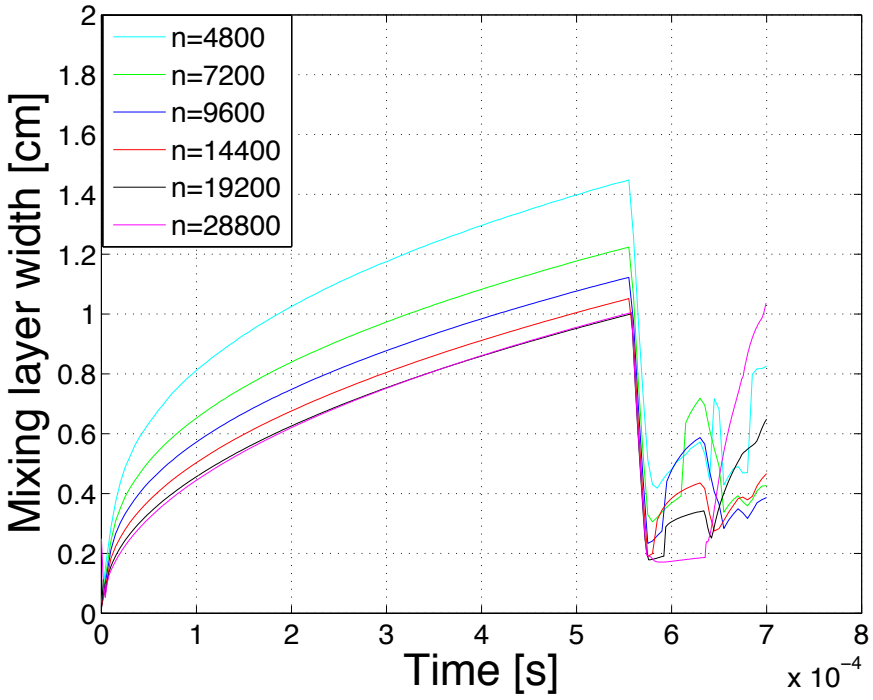

Figure 6.19: Mixing layer width convergence for $At = -0.67$ and $Ma_s = 5.00$.

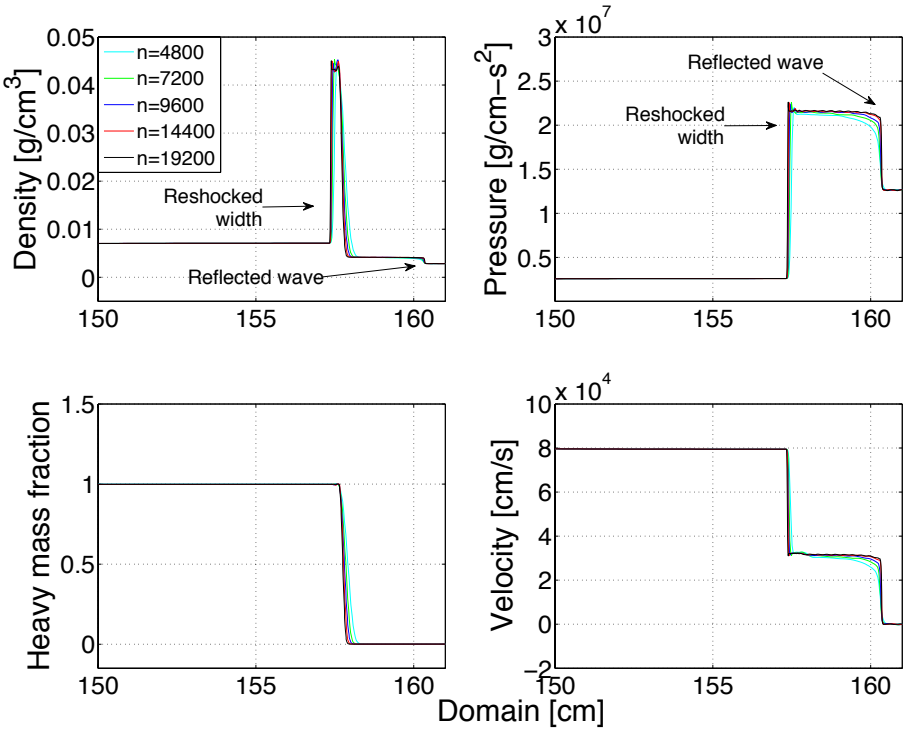

Figure 6.20: Mean field convergence for $At = -0.67$ and $Ma_s = 5.00$ at $t = 0.60$ ms.

addition to the shocks. Furthermore, monotonic behavior is seen in the post-reshock mixing layer width. Convergence for the mean and turbulent fields was considered at $t = 0.60$, shortly after the first reshock. The rise in density and pressure of the mixing layer width due to reshock are seen in Fig. 6.20; approaching the endwall is the reflected wave. The density in the compressed layer is approximately ten times larger than in the downstream region; the density of the compressed region grows larger after the second reshock. Similarly, the pressure in the compressed layer is also larger than in the downstream region. The mean fields require lower resolution than the mixing layer width, as convergence is achieved between $n = 14400$ and 19200 points. The mean fields can be modeled using $n = 9600$ points, but using $n = 4800$ and 7200 points results in some error near the shock fronts and the gas interface. Moreover, the mean fields do not show the same nonmonotonic behavior seen in Fig. 6.19. Like the mixing layer width, the turbulent fields require additional resolution to achieve

convergence. The turbulent kinetic energy, turbulent kinetic energy dissipation rate, and turbulent viscosity show converging behavior in Fig. 6.21. The fields are larger within the mixing layer after reshock, indicating enhanced mixing. The active mixing of gases in this region requires additional resolution for convergence. However, unlike the mixing layer width, the turbulent fields do not show nonmonotonic behavior.

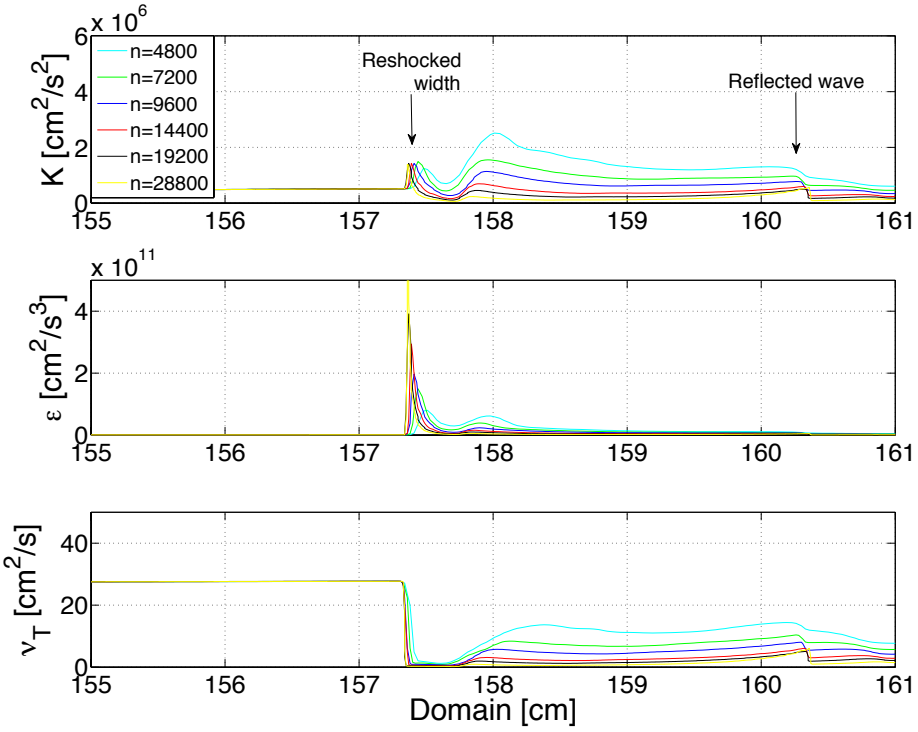

Figure 6.21: Turbulent field convergence for $At = -0.67$ and $Ma_s = 5.00$ at $t = 0.60$ ms.

6.6 Chapter Summary

The RANS model was applied to reshocked Richtmyer–Meshkov instability for $At = -0.87$, -0.67, and -0.21 with $Ma_s = 3.00$ and $At = -0.67$ with $Ma_s = 5.00$. Comparisons were made for the $Ma_s = 3.00$ cases with $Ma_s = 1.50$ results from Chapter V. The $Ma_s = 3.00$ cases showed similar evolution of the mixing layer widths. However, turbulent mixing was significantly inhibited for the larger shock Mach numbers due to the continuous progression of the interface towards the endwall

and the successive reshocks in short time intervals that prevented the mixing layer width from growing. As the shock Mach number was increased further to $Ma_s = 5.00$, turbulent mixing became even more inhibited. The early-time width was minimally affected by the variations in the shock Mach number. Furthermore, in using a $\delta = 49$ cm test section with larger shock Mach numbers, all of the gas in the test section became mixed as the edge of the interface reached the test section endwall.

Convergence studies were performed for the mixing layer width and mean and turbulent fields. The mixing layer and turbulent fields generally required slightly higher resolution to achieve convergence, while the mean fields converged at lower resolution. Nonmonotonicity in the mixing layer width was seen for $At = -0.87$ with $Ma_s = 3.00$ and $At = -0.67$ with $Ma_s = 5.00$. The nonmonotonic behavior was also seen in the mean and turbulent fields for the $Ma_s = 3.00$ case, which made convergence uncertain. However, nonmonotonicity was not seen in the mean and turbulent fields for the $Ma_s = 5.00$ case.

CHAPTER VII

Conclusions and Future Work

Systematic Reynolds-averaged Navier–Stokes (RANS) studies of reshocked Richtmyer–Meshkov instability were performed with shock Mach numbers $1.20 \leq Ma_s \leq 5.00$, Atwood numbers $At = \pm 0.21$, ± 0.67, and ± 0.87, and test section lengths $8 \leq \delta \leq 110$ cm to elucidate and better understand shock-driven turbulent mixing. Rather than using the Reynolds-averaged Euler equations, the multicomponent RANS equations including mixture molecular transport and thermodynamic coefficients were used. The RANS equations were coupled to a two-equation K–ϵ turbulence model for the turbulent kinetic energy and turbulent kinetic energy dissipation rate. The equations were solved using a third-order conservative finite-difference weighted essentially nonoscillatory (WENO) shock-capturing method and a characteristic projection formulation. The model was used to elucidate several aspects of reshocked Richtmyer–Meshkov instability for which experimental and numerical simulation data are sparse.

The Vetter and Sturtevant (10) and Poggi *et al.* (11) experiments were considered to perform parametric studies with variations in buoyancy production model coefficients, initial conditions, incident shock Mach numbers $1.24 \leq Ma_s \leq 1.98$, and air–SF_6 configurations with Atwood numbers $At = \pm 0.67$. An optimal coefficient set was established; simulations using $\sigma_\rho = 0.90$ and $C_{\epsilon 0} = 0.90$ predicted mixing layer widths agreeing well with the Vetter–Sturtevant and Poggi *et al.* experimental data.

It was found that these coefficients influence early-time and post-reshock turbulent mixing. The mixing was affected before and after reshock by the initial seed K_0 as it scaled the amount of turbulent kinetic energy introduced initially. The initial perturbation wavelength scaled the initial dissipation rate and principally affected early-time mixing, while post-reshock mixing was minimally affected. Post-reshock mixing was sensitive to variations in the buoyancy model coefficients σ_ρ and $C_{\epsilon 0}$, while early-time mixing was minimally affected. Variations in σ_ρ scaled the amount of turbulent kinetic energy and its dissipation rate generated via buoyancy production, while $C_{\epsilon 0}$ scaled the turbulent kinetic energy dissipation rate of buoyancy production. Post-reshock mixing was highly sensitive to changes in $C_{\epsilon 0}$. Reshock times varied with $\pm 3\%$ changes in the shock Mach number Ma_s. Variations in these coefficients and initial conditions also affected the growth rate of the mixing layer after reshock. Results were additionally compared with LES (15) and BHR model (29) predictions and the early-time power-law self-similar solution. LES generally agreed well with experimental data after reshock, but overpredicted early-time mixing. The BHR model agreed with experimental data for early-time mixing, but underpredicted post-reshock mixing. The converged RANS model predictions in the present study agreed well with experimental data throughout the mixing evolution and with the early-time power-law growth in these cases.

The RANS model was also applied to the Leinov *et al.* (12) experiments, in which reshocked Richtmyer–Meshkov instability was considered under different reshock times. The reshock times were varied by adjusting the distance between the interface and the endwall, δ. A set of six experiments was considered with test section lengths $\delta = 8$, 9.8, 13.1, 17.2, 19.9, and 23.5 cm. Like variations in Ma_s, changes in δ influenced the reshock times, but the early-time width and post-reshock growth rate were not significantly affected. An optimal set of coefficients was also established for these six experiments: $\sigma_\rho = 0.20$ and $C_{\epsilon 0} = 0.95$. RANS simulations agreed well with experi-

mental data in all cases. Good agreement was also achieved with three-dimensional simulations for the $\delta = 8$, 17.2, and 23.5 cm cases and the early-time self-similar solution. A *general* coefficient set ($\sigma_\rho = 0.60$ and $C_{\epsilon 0} = 0.90$) applicable to a broader range of Ma_s, At, and δ values was also established so that the Vetter and Sturtevant, Poggi *et al.*, and Leinov *et al.* experiments could be simulated using a single coefficient set while generally varying only the initial conditions. The deviation from experimental data was more apparent *after reshock* for the case with the longest test section, $\delta = 110$ cm. This represents the first application of a multicomponent RANS model to systematically investigate these experiments.

As experimental and simulation data are sparse for reshocked Richtmyer–Meshkov instability for Atwood numbers different from $At = \pm 0.67$, the RANS model was applied to elucidate turbulent mixing for different gas combinations. Cases with $At = \pm 0.21$, ± 0.67, and ± 0.87 corresponding to combinations of air with CO_2, SF_6, and H_2, respectively, were considered with $Ma_s = 1.50$. Larger post-reshock growth rates of the mixing layer width were obtained for larger Atwood numbers. Cases with negative Atwood numbers also showed larger post-reshock growth rates in comparison with the positive cases. Studies with $At > 0$ also showed that when the same gas was used in the driver section (in this case air), the use of different gases in the test section did not affect early-time mixing. However, differences were observed in the reshock time. Furthermore, cases with $At > 0$ experienced secondary expansion waves, while cases with $At < 0$ experienced secondary reshocks due to the gas order during reshock compression. The RANS predictions were compared with LES data, which were qualitatively similar. LES generally predicted larger early-time widths, and post-reshock predictions varied between the RANS and LES approaches.

The negative Atwood cases, $At = -0.87$, -0.67, and -0.21, were also considered with larger shock Mach numbers, $Ma_s = 3.00$ and $Ma_s = 5.00$. Singly-shocked Richtmyer–Meshkov instability was studied previously by others, but data on *reshocked*

mixing with larger shock Mach numbers are sparse. In these cases, the mixing layer also experienced multiple reshocks, but unlike flows with smaller shock Mach numbers, mixing was inhibited. The multiple reshocks in short time intervals and the progression of the mixing layer towards the endwall prevented the mixing layer from growing. These effects were more evident for $Ma_s = 5.00$ as mixing was significantly inhibited. For $Ma_s = 3.00$, the multiple reshocks eventually stopped the mixing layer width from progressing towards the endwall, as energy from the third reshock was finally transmitted and mixing evolved. For $Ma_s = 5.00$, there was no energy transmitted past the compressed gas in the mixing layer. Instead the energy was either stored within the compressed gas as the pressure and density increased or carried by the reflected wave.

The turbulent kinetic energy and dissipation rate budgets were considered for the cases discussed above. Generally, the shear and buoyancy production contributed to early-time mixing. However, the buoyancy production was dominant after reshock, while the shear production had a secondary role. The enhanced mixing after reshock from buoyancy production was due to the density and pressure gradients from compression of the mixing layer. These effects were more evident for larger Atwood numbers as the difference in densities between gases in the driver and test sections was larger. As the Atwood number became smaller, the density gradients became smaller and less turbulent kinetic energy was generated from buoyancy production. In these cases, the shear and buoyancy production were comparable. Diffusion was also larger after reshock, as turbulent kinetic energy was spread during mixing; the dissipation rate was relatively smaller. However, stronger dissipative effects were seen behind the shock and near the mixing layer as energy was dissipated into heat during compression of the gas. Budgets for the turbulent kinetic energy dissipation rate were generally similar as the K and ϵ equations are proportional.

Finally, convergence under grid refinement was also considered. This topic is often

neglected in turbulence studies or is too computationally expensive to perform when using multidimensional numerical simulations. In all cases, the mean density, mean pressure, mean heavy mass fraction, and mean velocity converged faster than the mixing layer and turbulent fields. For smaller shock Mach numbers, convergence of the mean fields was generally achieved with $n = 7200$ points. Somewhat higher resolution was necessary for cases with shorter test sections as material discontinuities and boundaries were in closer proximity to each other. Secondary wave interactions with these boundaries typically resulted in slower convergence in these regions. Furthermore, higher resolution was also necessary for larger incident shock Mach numbers. The mixing layer width and turbulent fields generally required more resolution to approach convergence. For smaller shock Mach numbers, converging behavior for the mixing layer could be seen between $n = 7200$ and 9600 points, but for cases with smaller test section lengths or larger shock Mach numbers, resolutions with $n = 14400$ and 19200 points were needed at times. The turbulent kinetic energy, turbulent kinetic energy dissipation rate, and turbulent viscosity were particularly sensitive where mixing was strongest. In several cases, it was shown that the RANS predictions with coarse resolutions generally agreed well with LES and the BHR model results. As discussed above, it is possible that the LES and BHR model predictions were underresolved. This is an important topic to investigate as these modeling approaches are used to investigate processes in high-energy-density environments such as ICF and high-energy laser experiments.

Additional work for reshocked Richtmyer–Meshkov instability is planned. The present investigations were conducted with a third-order WENO method. Although higher-order methods are more accurate, the third-order predictions showed good agreement with experimental data. However, it would be instructive to compare turbulent flow predictions and convergence rates between the present model and higher-order WENO methods.

The Reynolds-averaged Euler equations have been used in previous studies modeling turbulent flows. The present RANS model includes mixture molecular transport and thermodynamic coefficients. Predictions between the two approaches are planned to more closely evaluate molecular transport and enthalpy diffusion effects. Initial investigations for small shock Mach number $Ma_s = 1.20$ and $At = 0.67$ show minimal differences between these approaches. However, a systematic study considering positive and negative Atwood numbers and larger incident shock Mach numbers is planned.

Additional research is also needed to better understand reshocked Richtmyer–Meshkov instability with different Atwood numbers and larger incident shock Mach numbers. As experimental data is limited for cases different from $At = 0.67$ and $Ma_s < 2.00$, systematic parametric studies will be conducted in a similar fashion to those presented in Chapters III and IV. For larger Ma_s values, positive Atwood number cases will also be considered as this thesis only considered negative Atwood number cases. Detailed investigations will help elucidate the *freezeout* reported in previous studies.

The model will also be extended to include the density variance and density variance dissipation rate transport equations. In addition to the turbulent budgets, these quantities will further elucidate scalar turbulent mixing properties (such as molecular mixing) for a broader range of applications. Furthermore, studies with different approaches to initializing the turbulent fields are planned. It is important to further understand the sensitivity of early-time and post-reshock turbulent mixing to changes in initialization techniques. This work can possibly help understand the early-time mixing behavior seen in LES. Quantitative measurements for mixing layer comparisons and convergence rates, as well as different reshock models, will also be considered.

Hydrodynamic instability-induced turbulent mixing has a primary role in many

science and engineering applications. Elucidating reshocked Richtmyer–Meshkov instability is important for improving current techniques in predicting turbulence in complex flows and advancing many areas of high-energy-density physics.

APPENDICES

APPENDIX A

Derivation of the Model Transport Equations and Numerical Methods

A.1 The Unaveraged Multicomponent Navier–Stokes Equations

The unaveraged multicomponent Navier–Stokes equations for the transport of mass, momentum, total energy, and the heavy mass fraction are

$$\frac{\partial \rho}{\partial t} + \frac{\partial}{\partial x_j}(\rho\, v_j) = 0\,, \tag{A.1}$$

$$\frac{\partial}{\partial t}(\rho\, v_i) + \frac{\partial}{\partial x_j}(\rho\, v_i\, v_j) = \rho\, g_i - \frac{\partial p}{\partial x_i} + \frac{\partial \sigma_{ij}}{\partial x_j}\,, \tag{A.2}$$

$$\frac{\partial}{\partial t}(\rho\, e) + \frac{\partial}{\partial x_j}(\rho\, e\, v_j) = \rho\, g_i\, v_i - \frac{\partial}{\partial x_j}(p\, v_j) + \frac{\partial}{\partial x_j}(\sigma_{ij}\, v_i) + \frac{\partial}{\partial x_j}\left(\kappa\, \frac{\partial T}{\partial x_j} + H_j\right), \tag{A.3}$$

$$\frac{\partial}{\partial t}(\rho\, m_H) + \frac{\partial}{\partial x_j}(\rho\, m_H\, v_j) = \frac{\partial}{\partial x_j}\left(\rho\, D\, \frac{\partial m_H}{\partial x_j}\right), \tag{A.4}$$

respectively, where $e = v^2/2 + U$ is the total energy, $U = p/[\rho\,(\gamma - 1)] = c_v\, T$ is the internal energy, $\sigma_{ij} = \mu\,(\partial v_i/\partial x_j + \partial v_j/\partial x_i - \frac{2}{3}\delta_{ij}\partial v_k/\partial x_k)$ is the viscous stress tensor, and g_i is a constant gravitational acceleration (included here for generality, and is zero for the present Richtmyer–Meshkov instability study). The heavy and

light mass fractions are related by $m_H = 1 - m_L$. Unlike the equations used in Ref. (15), the present equations include enthalpy diffusion.

The enthalpy diffusion, $H_j = -\sum_{r=1}^{2} h_r J_{r,j}$, depends on the enthalpy and diffusive flux of gas r,

$$h_r = U_r + \frac{p_r}{\rho_r} \quad , \quad J_{r,j} = -\rho\, D_r \frac{\partial m_r}{\partial x_j} \,, \tag{A.5}$$

respectively. Indices 1 and 2 refer to H and L. The transport coefficients for the dynamic viscosity μ, thermal conductivity κ, and mass diffusivity D are calculated using the binary mixture relation

$$\phi = \frac{\phi_H\, m_H/\sqrt{MW_H} + \phi_L\,(1 - m_H)\,/\sqrt{MW_L}}{\widetilde{m}_H/\sqrt{MW_H} + (1 - m_H)\,/\sqrt{MW_L}} \quad , \quad \phi = \mu, \kappa, D \,. \tag{A.6}$$

The Euler equations do not include these mixture molecular transport and thermodynamic terms.

A.2 Reynolds and Favre Averaging

In deriving statistically-averaged flow equations, it is necessary to first introduce Reynolds and Favre averaging along with related properties. Reynolds averaging can take a variety of forms, including temporal, spatial, ensemble, and phase averaging (32). Time averaging is commonly employed,

$$\Phi(\mathbf{x}) = \lim_{\tau \to \infty} \frac{1}{\tau} \int_{t}^{t+\tau} \phi(\mathbf{x}, t)\, \mathrm{d}t \,, \tag{A.7}$$

where $\phi(\mathbf{x}, t)$ and $\Phi(\mathbf{x}) = \overline{\phi}(\mathbf{x})$ are instantaneous and time-averaged flow fields, respectively. Flow variables are sums of mean and fluctuating components, $\phi = \overline{\phi} + \phi'$. If Φ is interpreted as a time-averaged field, then the Reynolds average of the fluctu-

ating component of a flow field is zero,

$$\overline{\phi'} = \lim_{\tau\to\infty} \frac{1}{\tau} \int_{t}^{t+\tau} \left[\phi(\mathbf{x},t) - \overline{\phi}\,\right] \mathrm{d}t = \Phi - \overline{\phi} = 0\,. \tag{A.8}$$

In Reynolds averaging the product of two quantities, α and β, the product of mean and fluctuating components is zero since fluctuating components have zero average. Conversely, the product of two mean or fluctuating components is not zero,

$$\overline{\alpha\,\beta} = \overline{(\overline{\alpha}+\alpha')\big(\overline{\beta}+\beta'\big)} = \overline{\alpha}\,\overline{\beta} + \overline{\alpha'\,\beta'}\,, \tag{A.9}$$

where $\overline{\alpha'\,\beta'}$ necessitates a closure approximation. In computing derivatives of scalars and vectors, the following properties hold:

$$\overline{\frac{\partial\alpha}{\partial x_j}} = \frac{\partial\overline{\alpha}}{\partial x_j} \quad , \quad \overline{\frac{\partial\beta_j}{\partial x_j}} = \frac{\partial\overline{\beta_j}}{\partial x_j}\,. \tag{A.10}$$

Similarly, a Favre average is a density- (or mass-) weighted average. Scalar and vector Favre averages are defined as

$$\overline{\rho}\,\widetilde{\alpha} = \lim_{T\to\infty} \frac{1}{T} \int_{t}^{t+T} \rho(\mathbf{x},t)\,\alpha(\mathbf{x},t)\,\mathrm{d}t = \overline{\rho\,\alpha} \quad , \quad \overline{\rho}\,\widetilde{\beta}_i = \lim_{T\to\infty} \frac{1}{T} \int_{t}^{t+T} \rho(\mathbf{x},t)\,\beta_i(\mathbf{x},t)\,\mathrm{d}t = \overline{\rho\,\beta_i}\,, \tag{A.11}$$

respectively, with the Reynolds-averaged density $\overline{\rho}$, and Favre-averaged scalars and vectors, $\widetilde{\alpha}$ and $\widetilde{\beta}_i$, respectively. As with Reynolds averaging, vector and scalar fields are also decomposed into mean and fluctuating parts. For example, to Favre average the velocity, it is first decomposed as $v_i = \widetilde{v}_i + v_i''$, multiplied by the density, and Reynolds averaging is performed to obtain $\overline{\rho\,v_i} = \overline{\rho}\widetilde{v}_i + \overline{\rho v_i''}$. Combining this result with the definition of a Favre-averaged quantity results in $\overline{\rho\,v_i''} = 0$. Furthermore,

Reynolds averaged Favre-averaged fluctuating components do not equal zero:

$$\overline{v_i''} = \overline{v_i - \widetilde{v}_i} = -\frac{\overline{\rho'\, v_i'}}{\overline{\rho}}\,. \tag{A.12}$$

Just as the product of two Reynolds averaged fluctuating quantities required a closure approximation, so does the average of a fluctuating component, $\overline{v_i''}$.

A.3 Mean Continuity and Momentum Conservation Equations

Following Reynolds–Favre averaging rules, the Reynolds-averaged density equation is

$$\frac{\partial \overline{\rho}}{\partial t} + \frac{\partial}{\partial x_j}(\overline{\rho}\,\widetilde{v}_j) = 0\,. \tag{A.13}$$

Averaging the momentum equation gives

$$\overline{\frac{\partial}{\partial t}[\rho\,(\widetilde{v}_i + v_i'')]} + \overline{\frac{\partial}{\partial x_j}\big[\rho\,(\widetilde{v}_i + v_i'')\big(\widetilde{v}_j + v_j''\big)\big]} = \overline{\rho\, g_i} - \overline{\frac{\partial}{\partial x_i}(\overline{p} + p')} + \overline{\frac{\partial \sigma_{ij}}{\partial x_j}} \tag{A.14}$$

or

$$\frac{\partial}{\partial t}(\overline{\rho}\,\widetilde{v}_i) + \frac{\partial}{\partial x_j}(\overline{\rho}\,\widetilde{v}_i\,\widetilde{v}_j) = \overline{\rho}\, g_i - \frac{\partial \overline{p}}{\partial x_i} - \frac{\partial \tau_{ij}}{\partial x_j} + \frac{\partial \overline{\sigma}_{ij}}{\partial x_j}\,, \tag{A.15}$$

where the Reynolds stress tensor is $\tau_{ij} = \overline{\rho v_i'' v_j''}$.

A.4 Mean Kinetic and Internal Energy Equations

The mean kinetic energy equation is obtained by first multiplying (A.15) by $\widetilde{v}_i$,

$$\widetilde{v}_i\,\overline{\rho}\,\frac{\partial \widetilde{v}_i}{\partial t} + \overline{\rho}\,\widetilde{v}^2\,\frac{\partial \widetilde{v}_j}{\partial x_j} = \overline{\rho}\, g_i\,\widetilde{v}_i - \widetilde{v}_i\left(\frac{\partial \overline{p}}{\partial x_j} + \frac{\partial \tau_{ij}}{\partial x_j} - \frac{\partial \overline{\sigma}_{ij}}{\partial x_j}\right). \tag{A.16}$$

Using the relation

$$\frac{\partial}{\partial t}\left(\frac{\overline{\rho}\,\widetilde{v}^2}{2}\right) = \overline{\rho}\,\frac{\partial}{\partial t}\left(\frac{\widetilde{v}^2}{2}\right) + \frac{\widetilde{v}^2}{2}\,\frac{\partial \overline{\rho}}{\partial t} \;\equiv\; \overline{\rho}\,\widetilde{v}_i\,\frac{\partial \widetilde{v}_i}{\partial t} - \frac{\widetilde{v}^2}{2}\,\frac{\partial}{\partial x_j}(\overline{\rho}\,\widetilde{v}_j)\,, \tag{A.17}$$

the mean kinetic energy equation is

$$\frac{\partial}{\partial t}\left(\frac{\overline{\rho}\,\widetilde{v}^2}{2}\right) + \frac{\partial}{\partial x_j}\left(\frac{\overline{\rho}\,\widetilde{v}^2\,\widetilde{v}_j}{2}\right) = \overline{\rho}\,g_j\,\widetilde{v}_j - \widetilde{v}_j\,\frac{\partial \overline{p}}{\partial x_j} - \widetilde{v}_j\,\frac{\partial \tau_{ij}}{\partial x_i} + \widetilde{v}_j\,\frac{\partial \overline{\sigma}_{ij}}{\partial x_j}\,. \tag{A.18}$$

Averaging the internal energy equation gives

$$\begin{aligned}\overline{\frac{\partial}{\partial t}\Big[\rho\left(\widetilde{U}+U''\right)\Big]} + \overline{\frac{\partial}{\partial x_j}\Big[\rho\left(\widetilde{U}+U''\right)\left(\widetilde{v}_j+v_j''\right)\Big]} &= -\overline{(\overline{p}+p')\,\frac{\partial}{\partial x_j}\left(\widetilde{v}_j+v_j''\right)} \\ &\quad + \overline{\sigma_{ij}\,\frac{\partial v_i}{\partial x_j}}\end{aligned} \tag{A.19}$$

or

$$\begin{aligned}\frac{\partial}{\partial t}\left(\overline{\rho}\,\widetilde{U}\right) + \frac{\partial}{\partial x_j}\left(\overline{\rho}\,\widetilde{U}\,\widetilde{v}_j\right) &= -\overline{p}\,\frac{\partial \widetilde{v}_j}{\partial x_j} - \overline{p}\,\frac{\partial \overline{v_j''}}{\partial x_j} - \overline{p'\,\frac{\partial v_j''}{\partial x_j}} + \overline{\sigma_{ij}\,\frac{\partial v_i}{\partial x_j}} \\ &\quad - \frac{\partial}{\partial x_j}\left(\overline{\rho\,U''\,v_j''}\right)\,.\end{aligned} \tag{A.20}$$

Summing the mean kinetic and internal energy equations gives the mean energy equation,

$$\begin{aligned}\frac{\partial}{\partial t}\left[\overline{\rho}\left(\frac{\widetilde{v}^2}{2}+\widetilde{U}\right)\right] + \frac{\partial}{\partial x_j}\left\{\left[\overline{\rho}\left(\frac{\widetilde{v}^2}{2}+\widetilde{U}\right)+\overline{p}\right]\widetilde{v}_j\right\} &= \overline{\rho}\,g_j\,\widetilde{v}_j - \widetilde{v}_j\,\frac{\partial \tau_{ij}}{\partial x_i} - \overline{p}\,\frac{\partial \overline{v_j''}}{\partial x_j} \\ &\quad - \overline{p'\,\frac{\partial v_j''}{\partial x_j}} + \overline{\sigma_{ij}\,\frac{\partial v_i}{\partial x_j}} \\ &\quad - \frac{\partial}{\partial x_j}\left(\overline{\rho\,U''\,v_j''}\right)\,.\end{aligned} \tag{A.21}$$

A.5 Turbulent Kinetic and Total Energy Equations

The turbulent kinetic energy equation is obtained by averaging the product of the velocity fluctuation and the total momentum equation. Setting $v_j'' \, v_j'' = v''^{\,2}$, the first step in the derivation of the turbulent kinetic energy equation gives (32)

$$\underbrace{\overline{\rho \, v_j'' \, \frac{\partial}{\partial t}\left(\widetilde{v}_j + v_j''\right)}}_{i} + \underbrace{\overline{\rho \left(\widetilde{v}_i + v_i''\right) v_j'' \frac{\partial}{\partial x_i}\left(\widetilde{v}_j + v_j''\right)}}_{ii} + \underbrace{\overline{v_j'' \, \frac{\partial}{\partial x_j}(\overline{p} + p')}}_{iii} = \underbrace{\overline{v_j'' \, \frac{\partial \sigma_{ij}}{\partial x_i}}}_{iv} \tag{A.22}$$

or

$$\underbrace{\frac{\partial}{\partial t}\left(\overline{\frac{\rho \, v''^2}{2}}\right) - \overline{\frac{v''^2}{2} \, \frac{\partial \rho}{\partial t}}}_{i} + \underbrace{\overline{\rho \, v_i'' \, v_j''} \, \frac{\partial \widetilde{v}_j}{\partial x_i} + \frac{\partial}{\partial x_i}\left[\overline{\rho \left(\widetilde{v}_i + v_i''\right) \frac{v''^2}{2}}\right] - \overline{\frac{v''^2}{2} \, \frac{\partial}{\partial x_i}(\rho \, v_i)}}_{ii} \tag{A.23}$$

$$+ \underbrace{\overline{v_j''} \, \frac{\partial \overline{p}}{\partial x_j} + \frac{\partial}{\partial x_j}\left(\overline{p' \, v_j''}\right) - \overline{p' \, \frac{\partial v_j''}{\partial x_j}}}_{iii} = \underbrace{\frac{\partial}{\partial x_i}\left(\overline{\sigma_{ij} \, v_j''}\right) - \overline{\sigma_{ij} \, \frac{\partial v_j''}{\partial x_i}}}_{iv} .$$

Defining $\overline{\rho v''^2/2} = \overline{\rho} K$ and noting that $\overline{v''^2 \left[\partial \rho / \partial t + \partial \left(\rho \, v_i\right)/\partial x_i\right]} = 0$, the mean turbulent kinetic energy equation becomes

$$\begin{aligned} \frac{\partial}{\partial t}(\overline{\rho} \, K) + \frac{\partial}{\partial x_j}(\overline{\rho} \, K \, \widetilde{v}_j) \;\; = \;\; & -\overline{v_j''} \, \frac{\partial \overline{p}}{\partial x_j} - \tau_{ij} \, \frac{\partial \widetilde{v}_i}{\partial x_j} + \overline{p' \, \frac{\partial v_j''}{\partial x_j}} - \overline{\sigma_{ij} \, \frac{\partial v_i''}{\partial x_j}} \\ & + \frac{\partial}{\partial x_j}\left(\overline{\sigma_{ij} \, v_i''} - \overline{\frac{\rho \, v''^2 \, v_j''}{2}} - \overline{p' \, v_j''}\right) . \end{aligned} \tag{A.24}$$

The terms on the right side represent the buoyancy and shear production of turbulent kinetic energy, pressure–dilatation, and dissipation of turbulent kinetic energy. The terms on the second line represent molecular and turbulent diffusion. Summing the mean kinetic, mean internal, and turbulent kinetic energy equations and defining the

total energy density as $\overline{\rho}\,\widetilde{e} = \overline{\rho}\left(\widetilde{v}^2/2 + \widetilde{U} + K\right)$ gives the total energy equation,

$$\frac{\partial}{\partial t}(\overline{\rho}\,\widetilde{e}) + \frac{\partial}{\partial x_j}[(\overline{\rho}\,\widetilde{e} + \overline{p})\,\widetilde{v}_j] = \overline{\rho}\,g_j\,\widetilde{v}_j - \frac{\partial}{\partial x_j}(\tau_{ij}\,\widetilde{v}_i) - \frac{\partial}{\partial x_j}\left(\overline{p}\,\overline{v_j''}\right) \qquad \text{(A.25)}$$
$$-\frac{\partial}{\partial x_j}\left(\,\overline{\rho\,U''\,v_j''}\,\right) + \frac{\partial}{\partial x_j}\left(\overline{\sigma_{ij}\,v_i''} - \frac{\overline{\rho\,v''^2\,v_j''}}{2} - \overline{p'\,v_j''}\right).$$

An additional equation for the turbulent kinetic energy dissipation rate ϵ is needed. The present study treats the ϵ equation as proportional to the K equation by the the inverse of the large–eddy turnover time, K/ϵ. Therefore, the ϵ equation is determined once the K equation is closed. To do so, gradient–diffusion closure approximations are needed.

A.6 Numerical Flux and Eigenstructure

In conservative form, the conservative fields $\mathbf{u}$ and numerical flux $\mathbf{f}$ in one dimension are

$$\mathbf{u} = \begin{bmatrix} \overline{\rho} \\ \overline{\rho}\,\widetilde{v} \\ \overline{\rho}\,\widetilde{e} \\ \overline{\rho}\,\widetilde{m}_H \\ \overline{\rho}\,K \\ \overline{\rho}\,\epsilon \end{bmatrix}, \qquad \mathbf{f} = \begin{bmatrix} \overline{\rho}\,\widetilde{v} \\ \overline{\rho}\,\widetilde{v}^2 + \overline{p} + \frac{2}{3}\,\overline{\rho}\,K \\ (\overline{\rho}\,\widetilde{e} + \overline{p} + \frac{2}{3}\,\overline{\rho}\,K)\,\widetilde{v} \\ \overline{\rho}\,\widetilde{m}_H\,\widetilde{v} \\ \overline{\rho}\,K\,\widetilde{v} \\ \overline{\rho}\,\epsilon\,\widetilde{v} \end{bmatrix}, \qquad \text{(A.26)}$$

respectively. Note that the turbulent pressure $p_T = (2/3)\overline{\rho}\,K$ is included in the flux. Defining the mean enthalpy $\widetilde{h} = \widetilde{e} + \overline{p}/\overline{\rho} + (2/3)K$, the Jacobian (see Ref. (52)) is

$$A = \begin{bmatrix} 0 & 1 & 0 & 0 & 0 & 0 \\ \frac{\overline{\gamma}-3}{2}\,\widetilde{v}^{\,2} - \widetilde{m}_H\,\frac{\partial\overline{\gamma}}{\partial\widetilde{m}_H}\,\frac{\overline{p}}{\overline{\rho}\,(\gamma-1)} & (3-\overline{\gamma})\,\widetilde{v} & \overline{\gamma}-1 & \frac{\partial\overline{\gamma}}{\partial\widetilde{m}_H}\,\frac{\overline{p}}{\overline{\rho}(\gamma-1)} & -(\overline{\gamma}-\frac{5}{3}) & 0 \\ -\Big[\widetilde{h} - \frac{(\overline{\gamma}-1)\,\widetilde{v}^{\,2}}{2} + \widetilde{m}_H\,\frac{\partial\overline{\gamma}}{\partial\widetilde{m}_H}\,\frac{\overline{p}}{\overline{\rho}\,(\overline{\gamma}-1)}\Big]\widetilde{v} & \widetilde{h} - (\overline{\gamma}-1)\,\widetilde{v}^{\,2} & \overline{\gamma}\,\widetilde{v} & \frac{\partial\overline{\gamma}}{\partial\widetilde{m}_H}\,\frac{\overline{p}}{\overline{\rho}\,(\overline{\gamma}-1)}\,\widetilde{v} & -(\overline{\gamma}-\frac{5}{3})\,\widetilde{v} & 0 \\ -\widetilde{m}_H\,\widetilde{v} & \widetilde{m}_H & 0 & -\widetilde{v} & 0 & 0 \\ -K\,\widetilde{v} & K & 0 & 0 & -\widetilde{v} & 0 \\ -\epsilon\,\widetilde{v} & \epsilon & 0 & 0 & 0 & -\widetilde{v} \end{bmatrix}. \tag{A.27}$$

The eigenvalues are

$$\lambda = \widetilde{v} - c_s, \widetilde{v}, \widetilde{v} + c_s, \widetilde{v}, \widetilde{v}, \widetilde{v}\,, \tag{A.28}$$

and the Roe-averaged right and left eigenvectors are

$$R = \begin{bmatrix} 1 & 1 & 1 & 0 & 0 & 0 \\ \widetilde{v} - c_s & \widetilde{v} & \widetilde{v} + c_s & 0 & 0 & 0 \\ \frac{\widetilde{v}^{\,2}}{2} + \frac{c_s^2}{\overline{\gamma}-1} - \widetilde{v}\,c_s + \frac{(\overline{\gamma}-\frac{5}{3})}{(\overline{\gamma}-1)}\,K & \frac{\widetilde{v}^{\,2}}{2} + \frac{(\overline{\gamma}-\frac{5}{3})}{(\overline{\gamma}-1)}\,K & \frac{\widetilde{v}^{\,2}}{2} + \frac{c_s^2}{\overline{\gamma}-1} + \widetilde{v}\,c_s + \frac{(\overline{\gamma}-\frac{5}{3})}{(\overline{\gamma}-1)}\,K & \frac{(\overline{\gamma}-\frac{5}{3})}{(\overline{\gamma}-1)}\,K & \frac{(\overline{\gamma}-\frac{5}{3})}{(\overline{\gamma}-1)}\,K & 0 \\ \widetilde{m}_H & \widetilde{m}_H & \widetilde{m}_H & \widetilde{m}_H & \widetilde{m}_H & \widetilde{m}_H \\ K & K & K & K & K & 0 \\ \epsilon & \epsilon & \epsilon & \epsilon & 0 & 0 \end{bmatrix}, \tag{A.29}$$

$$L = \begin{bmatrix} \frac{\widetilde{v}}{2\,c_s^2}\left[c_s + (\overline{\gamma}-1)\,\frac{\widetilde{v}}{2}\right] & -\frac{c_s+(\overline{\gamma}-1)\,\widetilde{v}}{2\,c_s^2} & \frac{\overline{\gamma}-1}{2\,c_s^2} & 0 & -\frac{\overline{\gamma}-\frac{5}{3}}{2\,c_s^2} & 0 \\ \frac{c_s^2-(\overline{\gamma}-1)\,\frac{\widetilde{v}^2}{2}}{c_s^2} & \frac{(\overline{\gamma}-1)\,\widetilde{v}}{c_s^2} & -\frac{\overline{\gamma}-1}{c_s^2} & 0 & \frac{\overline{\gamma}-\frac{5}{3}}{c_s^2} & 0 \\ -\frac{\widetilde{v}}{2\,c_s^2}\left[c_s - (\overline{\gamma}-1)\,\frac{\widetilde{v}}{2}\right] & \frac{c_s-(\overline{\gamma}-1)\,\widetilde{v}}{2\,c_s^2} & \frac{\overline{\gamma}-1}{2\,c_s^2} & 0 & -\frac{\overline{\gamma}-\frac{5}{3}}{2\,c_s^2} & 0 \\ -1 & 0 & 0 & 0 & 0 & \frac{1}{\epsilon} \\ -1 & 0 & 0 & 0 & \frac{1}{K} & -\frac{1}{\epsilon} \\ -1 & 0 & 0 & \frac{1}{\widetilde{m}_H} & -\frac{1}{K} & 0 \end{bmatrix}. \tag{A.30}$$

These eigenvalues are used to transform the numerical fluxes between physical and characteristic spaces, with the WENO reconstruction performed in characteristic space.

BIBLIOGRAPHY

BIBLIOGRAPHY

[1] Chassaing, P., Antonia, R.A., Anselmet, F., Joly, L., Sarkar, S.: Variable Density Fluid Turbulence, Fluid Mechanics and its Applications Vol. 69, Kluwer Academic (2002)

[2] Zhou, Y., Remington, B.A., Robey, H.F., Cook, A.W., Glendinning, S.G., Dimits, A., Buckingham, A.C., Zimmerman, G.B., Burke, E.W., Peyser, T.A., Cabot, W., Eliason, D.: Progress in understanding turbulent mixing induced by Rayleigh–Taylor and Richtmyer–Meshkov instabilities. Phys. Plasmas **10**, 1883–1886 (2003)

[3] Grun, J., Stamper, J., Manka, C., Resnick, J., Burris, R., Crawford, J., Ripin, B.H.: Instability of Taylor–Sedov blast waves propagating through a uniform gas. Phys. Rev. Lett. **66**, 2738–2741 (1991)

[4] Brouillette, M.: The Richtmyer-Meshkov instability. Annu. Rev. Fluid Mech. **34**, 445–468 (2002)

[5] Schilling, O., Jacobs, J.W.: Richtmyer-Meshkov instability and re-accelerated inhomogeneous flows. Scholarpedia **3**, 6090 (2008)

[6] Collins, B.D., Jacobs, J.W.: PLIF flow visualization and measurements of the Richtmyer–Meshkov instability of an air/SF_6 interface. J. Fluid Mech. **464**, 113–136 (2002)

[7] Atzeni, S., Meyer-ter-Vehn, J.: The Physics of Inertial Fusion: Beam Plasma Interaction, Hydrodynamics, Hot Dense Matter, International Series of Monographs on Physics Vol. 125, Oxford University Press (2004)

[8] Lindl, J.D.: Inertial Confinement Fusion: The Quest for Ignition and Energy Gain Using Indirect Drive, AIP Press (1998)

[9] Brouillette, M., Sturtevant, B.: Experiments on the Richtmyer-Meshkov instability: single-scale perturbations on a continuous interface. J. Fluid Mech. **263**, 271–292 (1994)

[10] Vetter, M., Sturtevant, B.: Experiments on the Richtmyer-Meshkov instability of an air/SF_6 interface. Shock Waves **4**, 247–252 (1995)

[11] Poggi, F., Thorembey, M.-H., Rodriguez, G.: Velocity measurements in turbulent gaseous mixtures induced by Richtmyer-Meshkov instability. Phys. Fluids **10**, 2698–2700 (1998)

[12] Leinov, E., Malamud, G., Elbaz, Y., Levin, L.A., Ben-Dor, G., Shvarts, D., Sadot, O.: Experimental and numerical investigation of the Richtmyer–Meshkov instability under re-shock conditions. J. Fluid Mech. **626**, 449–475 (2009)

[13] Balakumar, B.J., Orlicz, G.C., Ristorcelli, J.R., Balasubramanian, S., Prestridge, K.P., Tomkins, C.D.: Turbulent mixing in a Richtmyer–Meshkov fluid layer after reshock: velocity and density statistics. J. Fluid Mech. **696**, 67–93 (2012)

[14] Weber, C., Haehn, N., Oakley, J., Anderson, M., Bonazza, R.: Richtmyer–Meshkov instability on a low Atwood number interface after reshock. Shock Waves **22**, 317–325 (2012)

[15] Hill, D.J., Pantano, C., Pullin, D.I.: Large-eddy simulation and multiscale modeling of a Richtmyer–Meshkov instability with reshock. J. Fluid Mech. **557**, 29–61 (2006)

[16] Latini, M., Schilling, O., Don, W.S.: Effects of WENO flux reconstruction order and spatial resolution on reshocked two-dimensional Richtmyer–Meshkov instability. J. Comput. Phys. **221**, 805–836 (2007)

[17] Schilling, O., Latini, M., Don, W.S.: Physics of reshock and mixing in single-mode Richtmyer-Meshkov instability. Phys. Rev. E **76**, 026319 (2007); Erratum, Phys. Rev. E **85**, 049904 (2012)

[18] Schilling, O., Latini, M.: High-order WENO simulations of three-dimensional reshocked Richtmyer–Meshkov instability to late times: Dynamics, dependence on initial conditions, and comparisons to experimental data. Acta Mech. Scientia **30B**, 595–620 (2010)

[19] Grinstein, F.F., Gowardhan, A.A., Wachtor, A.J.: Simulations of Richtmyer–Meshkov instabilities in planar shock-tube experiments. Phys. Fluids **23**, 034106 (2011)

[20] Hahn, M., Drikakis, D., Youngs, D.L., Williams, R.J.R.: Richtmyer–Meshkov turbulent mixing arising from an inclined material interface with realistic surface perturbations and reshocked flow. Phys. Fluids **23**, 046101 (2011)

[21] Thornber, B., Drikakis, D., Youngs, D.L., Williams, R.J.R.: Growth of a Richtmyer-Meshkov turbulent layer after reshock. Phys. Fluids **23**, 095107 (2011)

[22] Morán-López, J.T., Schilling, O.: Multicomponent Reynolds-averaged Navier–Stokes simulations of reshocked Richtmyer–Meshkov instability-induced mixing. High Energy Density Physics **9**, 112–121 (2013)

[23] Morán-López, J.T., Holloway, J.P., Schilling, O.: Application of a K-ϵ Turbulence Model to Reshocked Richtmyer–Meshkov Instability Corresponding to a Heavy-to-Light Gas Transition. Seventh International Conference on Computational Fluid Dynamics (ICCFD7) Conference Proceedings (2012)

[24] Morán-López, J.T., Schilling, O.: Multicomponent Reynolds-averaged Navier–Stokes simulations of Richtmyer–Meshkov instability and mixing induced by reshock at different times. Shock Waves, submitted (2013)

[25] Gauthier, S., Bonnet, M.: A k-ϵ model for turbulent mixing in shock-tube flows induced by Rayleigh–Taylor instability. Phys. Fluids A **2**, 1685–1694 (1990)

[26] Grégoire, O., Souffland, D., Gauthier, S.: A second-order turbulence model for gaseous mixtures induced by Richtmyer–Meshkov instability. Journal of Turbulence **6**, 29 (2005)

[27] Dimonte, G., Tipton, R.: K-L turbulence model for the self-similar growth of Rayleigh-Taylor and Richtmyer-Meshkov instabilities. Phys. Fluids **18**, 085101 (2006)

[28] Chiravalle, V.P.: The k-L turbulence model for describing buoyancy-driven fluid instabilities. Laser and Particle Beams **24**, 381–394 (2006)

[29] Banerjee, A., Gore, R.A., Andrews, M.J.: Development and validation of a turbulent-mix model for variable density and compressible flows. Phys. Rev. E **82**, 046309 (2010)

[30] Schwarzkopf, J.D., Livescu, D., Gore, R.A., Rauenzahn, R.M., Ristorcelli, J R.: Application of a second-moment closure model to mixing processes involving multicomponent miscible fluids. Journal of Turbulence **12**, 49 (2011)

[31] Malamud, G., Elbaz, Y., Leinov, E., Sadot, O., Shvarts, D., Ben-Dor, G.: Bubble dynamics effects in re-shock system. Proceedings of the Eleventh International Workshop on the Physics of Compressible Turbulent Mixing (IWPCTM) (2008)

[32] Wilcox, D.C.: Turbulence Modeling for CFD, second edition, DCW Industries (2006)

[33] Pope, S.B.: Turbulent Flows, Cambridge University Press (2000)

[34] Cloutman, L.D.: A new estimate of the mixing length and convective overshooting in massive stars. Astrophys. J. **313**, 699–710 (1987)

[35] Cloutman, L.D.: Compressibility corrections to closure approximations for turbulent flow simulations. Lawrence Livermore National Laboratory Report UCRL-ID-147757 Rev. 1 (2002)

[36] Latini, M., Schilling, O., Don, W.S.: High-resolution simulations and modeling of reshocked single-mode Richtmyer-Meshkov instability: Comparison to experimental data and to amplitude growth model predictions. Phys. Fluids **19**, 024104 (2007)

[37] Lombardini, M., Hill, D.J., Pullin, D.I., Meiron, D.I.: Atwood ratio dependence of Richtmyer–Meshkov flows under reshock conditions using large-eddy simulations. J. Fluid Mech. **670**, 439–480 (2011)

[38] Lombardini, M., Pullin, D.I., Meiron, D.I.: Transition to turbulence in shock-driven mixing: a Mach number study. J. Fluid Mech. **690**, 203–226 (2012)

[39] Kim, J., Moin, P., Moser, R.: Turbulence statistics in fully developed channel flow at low Reynolds number. J. Fluid Mech. **177**, 133–166 (1987)

[40] Reid, R.C., Prausnitz, J.M., Polling, B.E.: The Properties of Gases and Liquids, McGraw–Hill (1987)

[41] Mihalas, D., Weibel–Mihalas, B.: Foundations of Radiation Hydrodynamics, Dover (1999)

[42] Zel'dovich, Y.B., Raizer, Y.P.: Physics of Shock Waves and High-Temperature Hydrodynamic Phenomena, Dover (2002)

[43] X.-D. Liu, S. Osher, T. Chan, Weighted essentially non-oscillatory schemes. J. Comput. Phys. **115** 200–212 (1994)

[44] C.-W. Shu, High order weighted essentially nonoscillatory schemes for convection dominated problems. SIAM Rev. **51** 82–126 (2009)

[45] Landau, L.D., Lifshitz, E.M.: Fluid Mechanics: Course of Theoretical Physics Vol. 6, Elsevier (1987)

[46] Anderson, D.A., Tannehill, J.C., Pletcher, R.H.: Computational Fluid Mechanics and Heat Transfer, Hemisphere (1997)

[47] Hinze, J.O.: Turbulence, McGraw–Hill (1975)

[48] Richtmyer, R.D.: Taylor instability in shock acceleration of compressible fluid. Comm. Pure Appl. Math. **13**, 297–319 (1960)

[49] Meshkov, E.E.: Instability of the interface of two gases accelerated by a shock wave. Sov. Fluid Dyn. **4**, 101–108 (1969)

[50] Liepmann, H.W., Roshko, A., Coles, D., Sturtevant, B.: A 17-inch diameter shock tube for studies in rarefied gas dynamics. Rev. Sci. Instrum. **33**, 625 (1962)

[51] Mügler, C., Gauthier, S.: Two-dimensional Navier–Stokes simulations of gaseous mixtures induced by Richtmyer–Meshkov instability. Phys. Fluids **12**, 1783–1798 (2000)

[52] Laney, C.B.: Computational Gasdynamics, Cambridge University Press (1998)

[53] Larsson, J., Lele, S.K.: Direct numerical simulation of canonical shock/turbulence interaction. Phys. Fluids **21**, 126101 (2009)

[54] Grinstein, F.F., Margolin, L.G., Rider, W.J. eds.: Implicit Large Eddy Simulation: Computing Turbulent Fluid Dynamics, Cambridge University Press (2007)

[55] Ukai, S., Genin, F., Srinivasan, S., Menon, S.: Large eddy simulation of reshocked Richtmyer-Meshkov instability, AIAA Paper 2009-944 (2009)

[56] Anderson, J.D.: Hypersonic and High-Temperature Gas Dynamics, McGraw–Hill (1989)

[57] Oakley, J.G.: Experimental Study of Shocked Gas Interfaces with Visualized Initial Conditions. Ph.D. dissertation, University of Wisconsin, Madison (2001)

[58] Mikaelian, K.O.: Richtmyer–Meshkov instabilities in stratified flows. Phys. Rev. A **31**, 410–419 (1985)

[59] Charakhch'yan, A.A.: Reshocking at the non-linear stage of Richtmyer–Meshkov instability. Plasma Phys. Control. Fusion **43**, 1169–1179 (2001)

[60] Tennekes, H., Lumley, J.L.: A First Course in Turbulence, Massachusetts Institute of Technology Press (1972)

[61] Valerio, E., Jourdan, G., Houas, L., Zeitoun, D.: Modeling of Richtmyer–Meshkov instability-induced turbulent mixing in shock tube experiments. Phys. Fluids **11**, 214–225 (1999)

[62] Schilling, O., Mueschke, N.J.: Analysis of turbulent transport and mixing in transitional Rayleigh–Taylor unstable flow using direct numerical simulation data. Phys. Fluids **22**, 105102 (2010)

[63] Branch, D., Tamman, G.A.: Type Ia supernovae as standard candles. Annu. Rev. Astronomy and Astrophysics **30**, 359–389 (1992)

[64] Woosley, S. E., Almgren, A., Bell, J.B., Glatzmaier, G., Kasen, D., Kerstein, A.R., Ma, H., Nugent, P., Ropke, F., Sankaran, V., Zingale, M.: Type Ia supernovae. J. of Phys: Conference Series **78**, 1–10 (2007)

[65] Cabot, W. H. Cook, A.W.: Reynolds number effects on Rayleigh–Taylor instability with possible implications for Type-Ia Supernovae. Nature Phys. **2**, 562–568 (2006)

[66] Gritschneder, T. Naab, T., Walch, S., Burkert, A., and Heitsch, F.: Driving turbulence and triggering star formation by ionizing radiation. Astrophys. J. **694**, L26–L30 (2009)

[67] Woosley, S. E., Wunsch, S., Kuhlen, M.: Carbon ignition in Type Ia supernovae: An analytic model. Astrophys. J. **607**, 921–930 (2004)

[68] Reighard, A. B.: Collapsing Radiative Shock Experiments on the Omega Laser, Ph.D. dissertation, University of Michigan (2007)

[69] Hogan, W. J., Moses, E.I., Warner, B.E., Sorem, M.S., Soures, J.M.: The National Ignition Facility. Nuclear Fusion **41**, 567–573 (2001)

[70] Landen, O. L. *et al.*: The first target experiments on the National Ignition Facility. European Phys. J. **44**, 273–281 (2007)

[71] Kuranz, C. C., Drake, R.P., Leibrandt, D.R., Harding, E.C., Robey, H.F., Miles, A.R., Blue, B.E., Hansen, J.F., Louis, H., Bono, M., Knauer, J., Arnett, D., Meakin, C.A.: Progress toward the study of laboratory scale, astrophysically relevant, turbulent plasmas. Astrophys. Space Sci. **298**, 9–16 (2004)

[72] Hurricane, O. A. *et al.*: Validation of a turbulent Kelvin–Helmholtz shear layer model using a high-energy-density OMEGA laser experiment. Phys. Rev. Letters **109**, 155004 (2012)

[73] Bradley, P.A. *et al.*: Role of shocks and mix caused by capsule defects. Phys. Plasmas **19**, 092703 (2012)

[74] Amendt, P. *et al.*: Indirect-drive non cryogenic double-shell ignition targets for the National Ignition Facility: Design and analysis. Phys. Plasmas **9**, 2221–2233 (2002)

[75] Smagorinsky, J.: General circulation experiments with the primitive equations. Monthly Weather Rev. **91**, 99–164 (1963)

[76] Aspden, A.J., Nikiforakis, N., Dalziel S.B., and Bell. J.B.: Analysis of implicit LES methods. Comm. Appl. Math. Comput. Sci. **3**, 103–126 (2008)